Hygrothermal performance assessment of damaged building materials

Simon Rouchier

N° d'ordre 194-2012 Année 2012

THÈSE DE L'UNIVERSITÉ DE LYON

Délivrée par

L'UNIVERSITÉ CLAUDE BERNARD LYON 1

École doctorale :

Mécanique, Énergétique, Génie Civil, Acoustique

DIPLÔME DE DOCTORAT

soutenue publiquement le **19 octobre 2012** par

Simon ROUCHIER

Ingénieur

Titre

HYGROTHERMAL PERFORMANCE ASSESSMENT OF DAMAGED BUILDING MATERIALS

EVALUATION DES PERFORMANCES HYGROTHERMIQUES DES MATÉRIAUX DE CONSTRUCTION ENDOMMAGÉS

Jury

Jean-Michel Torrenti	Professeur	IFSTTAR	Président du jury
Alain Sellier	Professeur	INSA Toulouse	Examinateur
Francis Allard	Professeur	Université de La Rochelle	Rapporteur
Jan Carmeliet	Professeur	ETH Zürich	Rapporteur
Jean-Jacques Roux	Professeur	INSA Lyon	Directeur de thèse
Monika Woloszyn	Professeur	Université de Savoie	Encadrante
Geneviève Foray	Maître de Conférences	INSA Lyon / UCBL	Encadrante
Hans Janssen	Professeur	Katholieke Universiteit Leuven	Invité
Carsten Rode	Professeur	Danmarks Tekniske Universitet	Invité

CETHIL - UMR CNRS 5008 - Université Claude-Bernard Lyon 1
9, rue de la Physique, 69621 Villeurbanne Cedex (FRANCE)
MATEIS - UMR CNRS 5510 - INSA de Lyon
7, avenue Jean Capelle, 69621 Villeurbanne Cedex (FRANCE)

Abstract

An important matter in the field of building physics is the questioning of how well buildings sustain ageing, and how their overall efficiency evolves over their lifetime. Many causes for degradation are carried by moisture transfer through these porous materials. Indeed, infiltrated water may transport chemicals, alter mechanical properties, and cause freeze thaw damage or mould development. It may also affect thermal properties and energetic efficiency, as well as the health and comfort of the occupants. The understanding of how moisture transfer properties evolve during the lifespan of building materials is however far from complete. The pore structure of a material itself may change over time, or be altered by cracks and defects caused by mechanical loading and aggravated by moisture-induced degradation. All sizes of fractures may have a strong impact on heat and moisture flow in the building envelope, and their influence is to be accounted for in any long-term performance assessment, not only of building and building components, but of any built structure in general. A considerable amount of work has already been performed in order to allow predicting the hygrothermal behaviour of buildings over longer periods of time. However, an accurate prediction of all ranges of damage in a building component, from microscopic to macroscopic cracks, supposes an extensive knowledge of all damage-inducing, time-varying boundary conditions of the problem during the simulation time. This also implies high computational costs, as well as important needs for material characterisation.

As a complement to these predictive methods, a new approach was undertaken, combining experimental characterisation of crack patterns and numerical simulations of coupled heat and moisture transfer. First, a preliminary study was conducted, consisting of measurements of the water vapour permeability of diffusely damaged construction materials. This allowed identifying the experimental and numerical requirements of the remainder of the work, which aimed at providing measurements of fracture network geometries for their explicit modelling in heat and moisture transfer simulations. Digital image correlation and acoustic emission monitoring were then performed during the degradation of cementitious materials, in order to obtain quantitative data on crack pattern geometries, and to assess the possibilities for damage monitoring at the building scale. The optical technique, along with an appropriate image processing procedure, was found suitable for providing precise measurements of fracture networks. A method was also proposed for the interpretation of acoustic emission recordings in terms of damage quantification, localisation and identification.

Then, a new model for coupled heat and moisture modelling in cracked porous media was developed, that allows including such measurements of fracture patterns into a finite element mesh, and simulating flow accordingly. This model was validated on the basis of experimental measurements: digital image correlation was performed during the fracturing of concrete samples, in which moisture uptake was then monitored using X-ray radiography. A good accordance was found between experimental and numerical results in terms of 2-dimensional moisture concentration distributions. The

validated code was then used for the simulation of test cases, in order to assess the hygrothermal performance of damaged multi-layered building components subjected to real climatic conditions. The consequences of fractures on the moisture accumulation in walls, on the amplitude of sorption/desorption cycles and on the thermal performance, were observed.

KEYWORDS: building materials, fractured porous media, characterisation, non destructive testing, coupled heat and moisture transfer, modelling, durability

Résumé

Les transferts d'humidité dans les matériaux de construction ont une influence importante sur leur durabilité et sur les performances hygriques et thermiques des bâtiments. De nombreux mécanismes d'endommagement chimiques et physiques de ces matériaux sont en effet dus à l'infiltration d'eau. En conséquence, leur structure poreuse peut évoluer au cours du temps, et des fissures microscopiques comme macroscopiques peuvent s'y développer. La description des matériaux à l'échelle microscopique est cependant une source d'erreur importante dans les codes de simulation actuels des transferts d'humidité et de chaleur, notamment en raison du fait que les milieux sont considérés comme homogènes, et que les effets du vieillissement des matériaux sont négligés. Il importe donc de trouver un moyen d'inclure les effets de l'endommagement dans les simulations de transferts d'humidité et de chaleur à l'échelle du bâtiment. Des méthodes existent pour la prédiction du comportement de milieux soumis à des sollicitations hygriques et mécaniques, mais supposent que l'ensemble des facteurs extérieurs influant sur l'endommagement soient connus tout au long des simulations.

Une nouvelle méthodologie est proposée ici pour compléter ces approches prédictives, en combinant des mesures expérimentales d'endommagement avec la simulation de transferts couplés d'humidité et de chaleur. Une étude préliminaire a d'abord été menée, consistant à mesurer la perméabilité vapeur équivalente d'éprouvettes de mortier multi-fissurées. Cette démarche a permis d'identifier les besoins expérimentaux et numériques de la suite du travail, visant à modéliser les écoulements dans un réseau discret de fissures sur la base de leur caractérisation. Une méthodologie expérimentale combinant corrélation d'images numériques et émissions acoustiques a ensuite été développée, permettant de disposer de cartographies d'endommagement et de proposer une démarche pour la mesure de réseaux de fissures dans les matériaux de construction en place. La méthode optique, associée à une procédure de traitement d'images, a permis de disposer de données précises de la géométrie de réseaux de fissures. De plus, une méthode a été proposée pour permettre l'interprétation des mesures d'émissions acoustiques en termes de quantification, localisation et identification des phénomènes d'endommagement.

Un code de simulation a ensuite été écrit, permettant d'intégrer ces mesures de fissuration dans la modélisation des écoulements couplés d'humidité et de chaleur en milieu poreux. Ce modèle a été validé sur la base de mesures expérimentales : la corrélation d'images numériques a été appliquée durant la fracturation d'éprouvettes de béton, dans lesquelles l'infiltration d'eau a ensuite été suivie par radiographie aux rayons X. Les résultats numériques obtenus sont en bonne conformité avec les mesures expérimentales en termes de prédiction de la concentration d'eau en deux dimensions. Enfin, la méthodologie a été appliquée à une série de cas test, dans le but de modéliser les performances hygrothermiques de parois multi-couches, incluant des matériaux endommagés, soumises à des conditions climatiques réelles. On a ainsi pu estimer les

conséquences potentielles de l'endommagement sur l'accumulation d'eau dans des parois, sur l'amplitude des cycles de sorption et de séchage, ainsi que sur les transferts thermiques.

KEYWORDS: matériaux de construction, milieux poreux fracturés, mesures non destructives, caractérisation, transferts couplés humidité et chaleur, modélisation

Synthèse

Introduction

Les transferts d'humidité dans les matériaux de construction ont une influence importante sur leur durabilité, sur les performances hygriques et thermiques des bâtiments et sur la santé des occupants. Cependant, les codes de calcul pour les transferts couplés dans les parois se basent généralement sur des hypothèses d'homogénéité et d'isotropie des matériaux, et négligent les effets de leur vieillissement. L'évolution des propriétés de transfert de ces matériaux au cours de leur cycle de vie est encore mal comprise, et n'est pas incluse dans les codes de simulation actuels.

Les fractures sont présentes dans les matériaux cimentaires dès leur mise en place [BAZ 82]. Leur endommagement progressif est ensuite causé par un ensemble de facteurs mécaniques (chargement), physiques (gradients thermiques) ou chimiques (corrosion, carbonatation). L'effet des fractures sur les transferts d'humidité est connu. Des développements récents [MOO 09] permettent de coupler une modélisation mécanique à la modélisation des transferts d'humidité et de chaleur, afin de prédire les écoulements dans un milieu soumis à un chargement mécanique. Cependant, la diversité des causes d'endommagement rend la prédiction des réseaux de fissures microscopiques et macroscopiques difficile sur le long terme. C'est pourquoi une démarche alternative est proposée dans le travail présenté ici : on cherche à modéliser les transferts couplés sur la base de la mesure expérimentale des réseaux de fractures, plutôt que sur leur prédiction.

Dans un premier temps, on a mesuré les perméabilités équivalentes d'éprouvettes fissurées de mortier fibré pour déterminer à quelle échelle d'observation les fractures doivent être considérées dans une simulation à l'échelle de l'enveloppe. Ensuite, la fissuration du matériau a été suivi par corrélation d'images et émissions acoustiques afin de mettre en place une procédure de caractérisation non destructive in situ des fractures dans les matériaux de construction. Ces données de fracturation, combinées à des mesures d'infiltration d'eau par rayons X dans des éprouvettes de béton fracturé, ont servi au développement et à la validation d'un modèle éléments finis pour les transferts couplés humidité/chaleur en milieu poreux fracturé. Ce modèle, une fois validé, a enfin été utilisé pour la simulation de parois multi-couches afin d'estimer l'effet de l'apparition de fractures sur les performances de l'enveloppe du bâtiment. L'ensemble de cette procédure vide à permettre l'estimation des propriétés hygrothermiques in situ des composants d'une paroi sur la base de la détection des fractures suivie de simulations numériques. La démarche peut notamment servir à identifier les besoins de rénovation énergétique d'une enveloppe.

Chapitre 2 : étude préliminaire

La représentation d'un milieu poreux fracturé pour la modélisation des transferts hygriques peut suivre deux principales stratégies : une approche continue consistant

à assigner au matériau des propriétés macroscopiques équivalentes, et une approche discrète consistant à représenter individuellement chaque fracture et leur impact sur les écoulements. Dans la première partie du travail, on a cherché à déterminer si l'approche continue était adéquate pour caractériser les fissures des matériaux de construction endommagés, en vue de la modélisation des transferts d'humidité. La démarche complète est exposée dans [ROU 12a].

Une formulation de mortier d'enduit fibré pour l'isolation thermique par l'extérieur a été élaborée sous la forme de plaques de dimensions 300x100x10 mm. Ce matériau a été conçu pour développer un endommagement progressif sous la forme de microfissures avant l'initiation d'une fracture macroscopique [CHA 10b]. La méthode de caractérisation hygrique est résumée en figure 1.

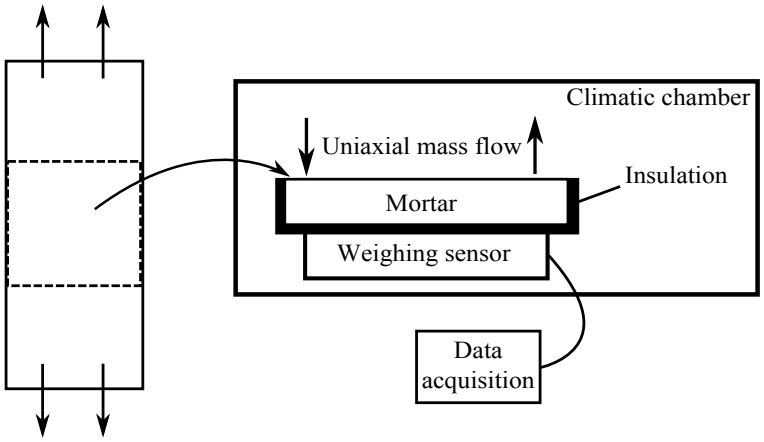

Figure 1: Dispositif expérimental de l'étude préliminaire

Après maturation, les éprouvettes ont été endommagées par un chargement en traction uniaxiale. La partie centrale en a été ensuite extraite pour être placée sur des dispositifs de suivi de masse en continu, à l'intérieur d'une enceinte climatique recréant des cycles d'humidité pendant 3 à 7 jours entre 33% et 75% d'humidité relative. Les profils de prise d'eau ainsi mesurés permettent de calculer la perméabilité à la vapeur d'eau de chaque éprouvette, endommagée ou intacte, à partir d'une méthode inverse consistant à ajuster une solution analytique de l'équation de transfert d'humidité sur les profils expérimentaux.

La procédure a été répétée sur un ensemble d'éprouvettes présentant divers degrés d'endommagement diffus (défini de manière similaire à [PIJ 09]). La perméabilité à la vapeur d'eau en fonction de cet endommagement, normée sur la valeur mesurée du matériau intact, est présentée en figure 2.

On constate une légère augmentation de la perméabilité à la vapeur des éprouvettes avec l'endommagement, du fait de microfissures parcourant le milieu poreux et facilitant le déplacement de l'eau. En revanche, la dispersion des valeurs mesurées de perméabilité pour une même valeur d'endommagement indique qu'une description macroscopique des fissures ne permet pas une prédiction précise des écoulements.

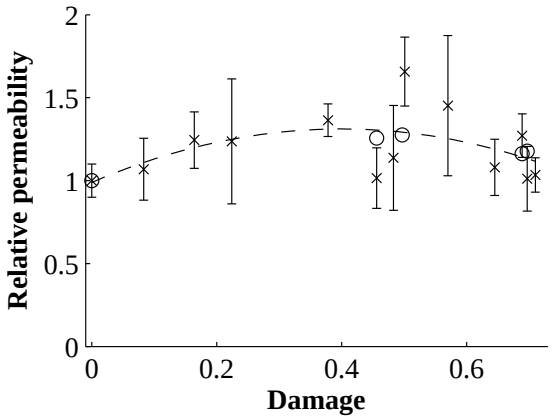

Figure 2: Mesures de perméabilité vapeur relative en fonction de l'endommagement diffus d'éprouvettes de mortier fibré

Une caractérisation plus avancée est donc nécessaire pour permettre une modélisation des transferts couplés humidité/chaleur en tenant compte des caractéristiques géométriques réelles des fractures (approche discrète mentionnée ci-dessus).

Chapitre 3 : mesures non destructives

L'étude préliminaire a permis d'identifier les besoin expérimentaux et numériques de la suite du travail, visant à modéliser les écoulements dans des réseau discret de fissures sur la base de leur mesure expérimentale. La caractérisation des fractures et de l'endommagement des matériaux de construction peut notamment se faire par méthodes optiques ou acoustiques. Une procédure a été mise en place, consistant à coupler les méthodes de corrélation d'images numériques et de mesure d'émissions acoustiques, dans le but de remplir deux objectifs principaux : disposer de cartographies d'endommagement pour alimenter un modèle de prédiction des écoulements, et permettre l'interprétation de signaux acoustiques pour la mesure de réseaux de fissures dans des matériaux de construction en place. La démarche de cette étude expérimentale est exposée dans [ROU 13].

La formulation de mortier fibré étudiée précédemment a de nouveau été soumise à un chargement en traction uniaxiale. La fissuration du matériau a été suivie conjointement par une caméra CCD à focale fixe et 4 capteurs acoustiques placés autour de la zone d'endommagement entre les entailles. La figure 3 montre un schéma de la procédure.

Les images obtenues par la caméra tout au long de l'essai ont ensuite été traitées par le logiciel Icasoft pour la corrélation d'images numériques. La technique permet le calcul du champ de déformations sur l'ensemble de la surface visible de l'éprouvette [HIL 06]. Les capteurs acoustiques sont connectés à un système d'acquisition MISTRAS. Les formes d'ondes enregistrées peuvent être décrites sur la base de plusieurs

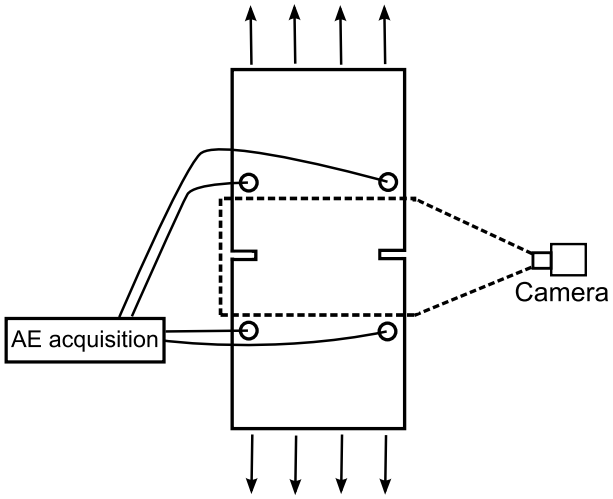

Figure 3: Dispositif expérimental pour le suivi d'endommagement du mortier fibré

descripteurs permettant la classification des signaux [GOD 06].

La figure 4(a) montre un exemple de cartographie de déformations obtenue en appliquant l'algorithme de corrélation d'images numériques à partir d'une image prise au pic de chargement d'une éprouvette de mortier.

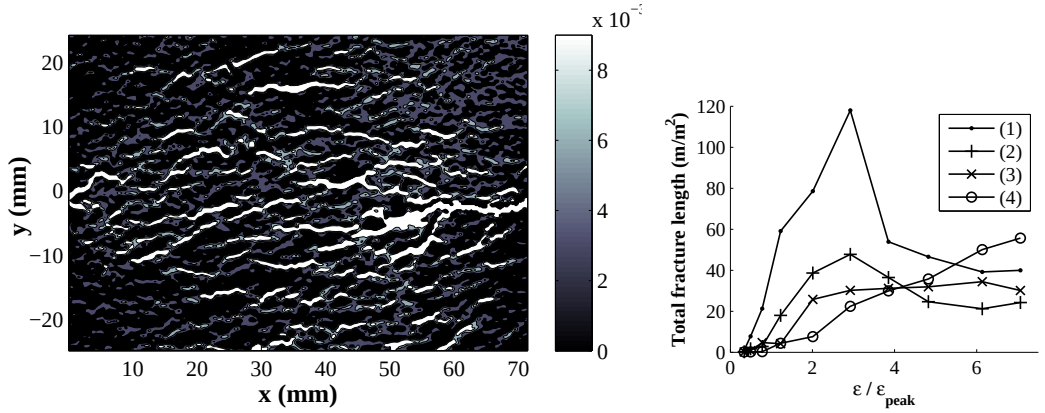

(a) (b)

Figure 4: Exemple de cartographie de l'endommagement, et partitionnement des échelles de fissuration

L'image montre un réseau de microfissures indiquées par des valeurs élevées de la déformation longitudinale (fort gradient de déplacement entre deux éléments adjacents de la grille). Le dispositif utilisé permet de détecter les fissures apparentes jusqu'à l'ordre de grandeur de 10^{-6} m, sur une zone d'observation de l'ordre de 10^{-2} à 10^{-1} m. Ces cartographies peuvent servir de base pour quantifier l'ensemble des échelles d'endommagement : les fissures visibles peuvent être mesurées par traitement d'image sur toutes les cartographies de déformations prises au long d'un es-

sai. On peut ainsi suivre l'évolution de la longueur totale de fractures par intervalle de largeur d'ouverture, en fonction de la déformation globale ϵ. La figure 4(b) montre un exemple de cette évolution, pour des fractures de largeur (1) inférieure à 5 μm, (2) entre 5 et 10 μm, (3) entre 10 et 50 μm et (4) supérieure à 50 μm. On peut ainsi, à tout moment du chargement d'une éprouvette, connaître la distribution des largeurs de fissures. On voit, entre autres observations, que les fissures microscopiques se développent d'abord, puis ont tendance à se refermer lors du passage d'une fracture macroscopique se propageant dans le milieu pour les fortes valeurs de la déformée ϵ. Ces mesures remplissent le premier objectif de cette partie de l'étude : on dispose d'un moyen d'acquérir l'ensemble des paramètres géométriques de réseaux de fractures en cours d'endommagement.

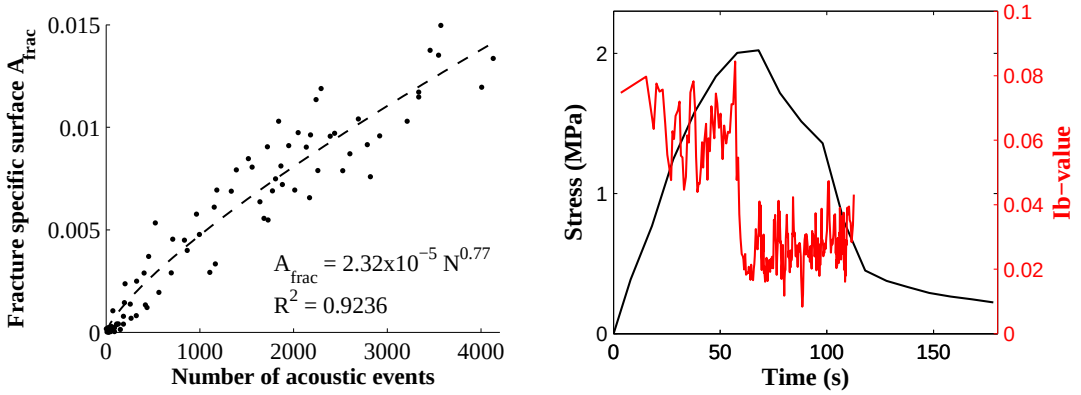

Figure 5: Quantification de l'endommagement et prédiction de la fracturation par émissions acoustiques

Après avoir développé cette méthodologie pour quantifier automatiquement les réseaux de fissure par traitement d'images, on a cherché à mettre en relation ces résultats avec les mesures acoustiques. La figure 5(a) montre la relation entre la surface spécifique de fracture observée par corrélation d'images (issue de la procédure de traitement d'images), et le nombre cumulé de signaux acoustiques localisés, à chaque instant des essais portant sur une série d'éprouvettes. La bonne correspondance entre les deux techniques permet d'établir que les mesures acoustiques, après une phase de calibration, peuvent être un outil efficace pour la quantification de l'endommagement à toutes les échelles. La localisation en deux dimensions des sources acoustiques, grâce à l'utilisation de plusieurs capteurs, peut par ailleurs fournir des cartographies d'endommagement similaires à celles obtenues par méthodes optiques.

Une tentative d'identification des mécanismes d'endommagement sur la base des formes d'ondes mesurées a par ailleurs été menée. En particulier, l'analyse des distributions d'amplitudes des signaux acoustiques permet de distinguer les émissions causées par des microfissures ou par des fractures macroscopiques. La figure 5(b) montre l'évolution d'un indice prédictif Ib [SHI 94] basé sur cette analyse, permettant

d'anticiper la transition entre un régime de microfissuration diffuse (valeur Ib élevée) et l'initiation d'une fracture macroscopique dans le matériau (chute soudaine de la valeur Ib).

Des pistes ont été avancées pour permettre la quantification et la localisation de l'endommagement, ainsi que l'identification des échelles de fissuration, par mesures acoustiques. Après calibration de ces mesures sur la base de résultats optiques, on peut ensuite envisager l'utilisation des émissions acoustiques de façon autonome à l'échelle de l'enveloppe, dans le but d'obtenir une cartographie des perméabilités à l'eau des matériaux.

Chapitre 4 : suivi et modélisation de l'infiltration d'eau

Une fois la procédure pour la caractérisation non destructive de fissures établie, il a fallu développer et valider un modèle permettant d'inclure ces mesures de fissuration dans des simulations de transferts couplés. Le travail présenté dans cette section a été réalisé au département génie civil de l'université technique de Copenhague (DTU Byg) et est présenté dans [ROU 12b]. La démarche expérimentale est résumée sur la figure 6.

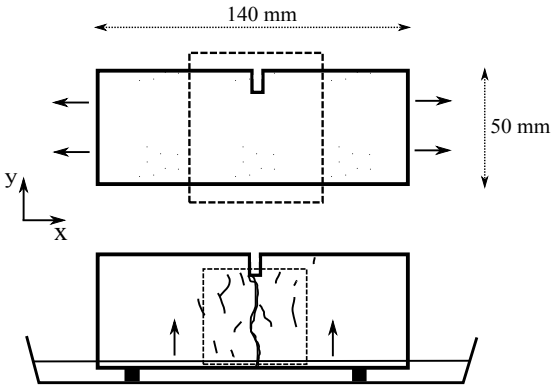

Figure 6: Disposition des éprouvettes de béton pendant le chargement et le suivi d'infiltration d'eau

Des éprouvettes de béton (ciment Portland Aalborg à 330 kg/m^3) renforcé par des fibres d'acier ont été fracturées et suivies par corrélation d'images. La démarche de traitement d'images prédédemment développée a permis d'extraire les principales propriétés géométriques de l'ensemble des fissures ainsi générées. Les éprouvettes ont ensuite été placées au contact d'une surface d'eau à l'intérieur d'un appareil de radiographie aux rayons X, permettant d'y observer la cartographie de la concentration en eau pendant son infiltration dans le milieu poreux et les fractures. L'ensemble de ces mesures constitue un jeu de données suffisant pour valider un modèle de prévision des écoulements en milieu poreux fracturé. Un exemple est donné sur la figure 7(a) mon-

trant la superposition des fractures mesurées (lignes de niveau) et de la distribution de la concentration d'eau (normalisée) pendant l'essai.

En plus de ces mesures, une caractérisation hygrique de cette formulation de béton a été réalisée. L'isotherme de sorption a été mesurée dans le domaine hygroscopique par dessiccateurs et dans le domaine sur-hygroscopique (humidité relative supérieure à 97%) par extracteurs. La diffusivité liquide a été calculée par méthode de Boltzmann appliquée à des profils d'infiltration par capillarité, mesurés par rayons X dans des éprouvettes non fracturées. Ces mesures constituent une caractérisation hygrique complète du matériau.

Une fois les données de validation et de caractérisation disponibles, un code de calcul par éléments finis a été développé, dont la base théorique suit la procédure présentée par [JAN 07]. Ce modèle a été écrit de sorte à pouvoir inclure des mesures de réseaux de fissures dans un maillage éléments finis, et prédire les transferts couplés d'humidité et de chaleur en conséquence : un tenseur de perméabilité anisotrope est assigné aux parties du maillage correspondant aux fractures. Leur contribution aux phénomènes de sorption comme de séchage est prise en compte. La procédure de développement du code de calcul est résumée en annexe B.

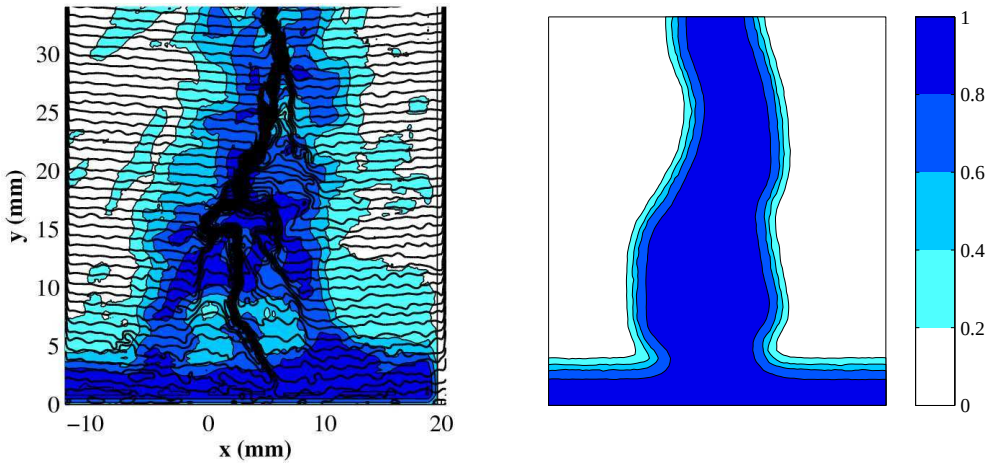

(a) (b)

Figure 7: (a) Mesure par rayons X et (b) simulation de la concentration en eau dans une éprouvette fracturée de béton, 10 minutes après contact avec une surface d'eau

Le modèle a ensuite été utilisé pour recréer les conditions des mesures effectuées sous rayons X. Un exemple est présenté en figure 7, montrant une bonne correspondance entre les mesures et les prédictions de profils d'humidité en deux dimensions. Ainsi, le modèle développé permet une bonne prévision des écoulements en milieux poreux fracturés, sur la base de la caractérisation de leurs réseaux de fissures. Par ailleurs, une étude de sensibilité au maillage a été menée, permettant d'établir avec quelle densité les fissures doivent être discrétisées pour fournir une bonne prédiction quantitative des écoulements.

Chapitre 5 : application du modèle

Le code de calcul a été validé pour le cas de transferts isothermes d'humidité en milieu poreux fracturé. La dernière partie de l'étude a consisté à l'appliquer pour l'estimation des conséquences potentielles de l'endommagement sur les performances hygrothermiques des matériaux à l'échelle de l'enveloppe.

Tout d'abord, les performances du modèle pour les simulations de transferts couplés d'humidité et de chaleur ont été mises à l'épreuve: ses résultats ont été comparés à ceux obtenus par 6 autres instituts dans la simulation des benchmarks du projet *Hamstad*. On a pu constater que le modèle est en mesure de simuler correctement le comportement de parois multi-couches soumises à des conditions climatiques variables.

Le modèle a ensuite été appliqué à la simulation à long terme de parois types. Un ensemble de géométries de parois a été défini dans le but de remplir trois objectifs : estimer les conséquences des fissures sur l'accumulation d'humidité dans une paroi et sur ses propriétés thermiques ; déterminer si ces conséquences sont aggravées en présence de matériaux isolants sensibles à l'humidité dans la paroi ; montrer dans quelle mesure une isolation thermique par l'extérieur avec un enduit hygrophobe permet de corriger les problèmes de durabilité causés par les fissures. Ces parois sont montrées en figure 8. Trois cas ont été définis : un mur non isolé, un mur isolé par l'intérieur et un mur isolé par l'extérieur. Dans chaque cas, les calculs ont été menés avec des matériaux intacts, ou avec une couche de béton fracturé.

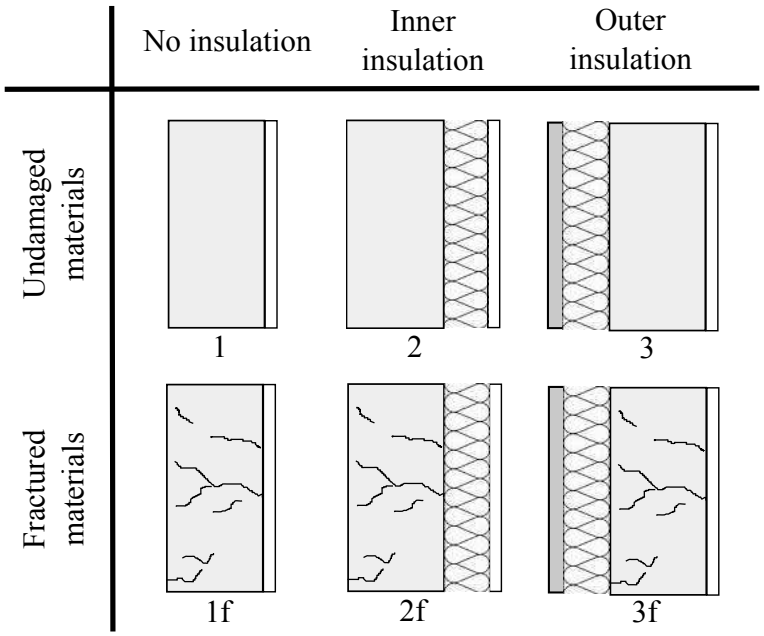

Figure 8: Définition des cas de simulation

Des données climatiques mesurées à Lyon ont ensuite été intégrées au code de calcul pour la simulation du comportement de chaque enveloppe pendant plusieurs mois

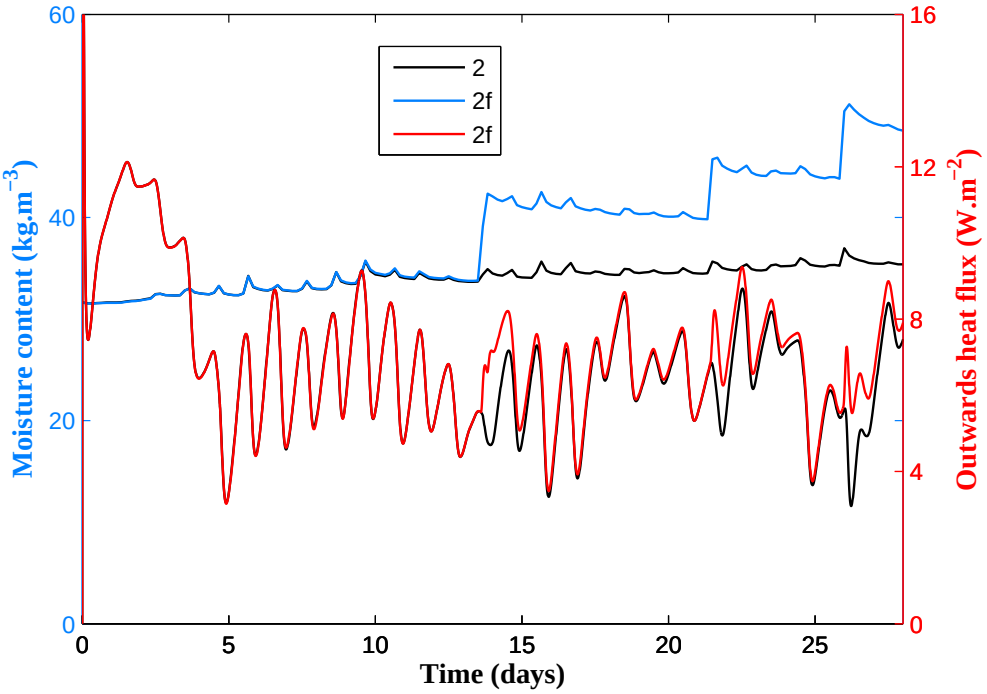

Figure 9: Comportement hygrique et thermique d'une paroi isolée par l'intérieur pendant le mois de février

avec un pas de temps de 10 minutes. Les phénomènes d'ensoleillement, de vent et de pluie ont été pris en compte pour l'expression des échanges entre l'environnement et la paroi à tout instant des simulations. Une étude de sensibilité aux conditions climatiques a d'abord été menée, dans le but de déterminer les conditions des calculs ultérieurs : les temps de calcul étant relativement longs pour la simulation de parois endommagées, il a fallu réduire le nombre de cas à traiter. Les simulations sont alors menées pour des parois orientées vers l'ouest pendant les mois de février et juillet.

Un exemple de résultat obtenu par une simulation mensuelle est montré en figure 9. Le comportement de la paroi isolée par l'intérieur, non fracturée, est montré par les lignes noires, et le comportement de la même paroi intégrant une couche fracturée de béton est montré par les lignes bleue et rouge. On constate que la présence de fissures implique de brusques hausses de concentration d'eau dans la paroi en cas d'averse : cette eau s'infiltre en profondeur dans le matériau, dont le temps de séchage est très élevé. Une accumulation d'eau a alors lieu dans la paroi. Ce phénomène, additionné à une augmentation de l'amplitude des cycles journaliers de sorption et de désorption, est une atteinte potentiellement importante à la durabilité du matériau. De plus, on observe une légère influence de cette accumulation d'eau sur les transferts thermiques à travers la paroi, étant donné que la conductivité thermique du béton augmente en présence d'eau.

Contents

Introduction

Background

While matters such as building durability and thermal comfort have long been taken in consideration in the design process of buildings, the reduction of their energetic consumption has gained a critical importance with the rising environmental concerns. Indeed, buildings are responsible for nearly 40% of the primary fuel consumption in France, and are a potentially important contribution to the overall reduction in fossil fuel consumption. This explains a rapidly increasing interest in building physics studies over the past few decades. The field of building physics includes a set of methods and techniques designed to enhance the overall performance of buildings in terms of energy efficiency, durability and sustainability, feasibility and cost reduction, indoor air quality, health and comfort... Studies can for instance include elements of fluid mechanics, civil engineering, material sciences, and often stand at the boundary between these fields.

An important matter in the domain is the questioning of how well buildings sustain ageing, and how their overall efficiency evolves over their lifetime. All types of construction materials are subjected to either biological, physical or chemical degradation processes. Many of these causes for degradation are carried by moisture transfer through these porous materials. Indeed, infiltrated water may transport chemicals such as chloride ions or carbon dioxide, alter mechanical properties, and cause freeze thaw damage or mould development. It may also affect the thermal properties and energetic efficiency, as well as the health and comfort of the occupants. All these issues justify the current increasing interest in the hygrothermal performance assessment of structures. The modelling of coupled heat and moisture transfer in construction materials is now a common practice, and can be integrated into the larger frame of building scale simulations.

Any analysis of moisture transfer requires dependable moisture transfer properties, for the characterisation of which various experimental techniques can be implemented. Lab measurements are commonly carried as to provide necessary material parameters for transfer simulations at the building scale. However, the understanding of how these properties evolve during the lifespan of building materials is far from complete. The pore structure of a material itself may change over time, or be altered by cracks and defects caused by mechanical loading and aggravated by moisture-induced

degradation. Several years after their installation, building materials such as concrete present signs of ageing in the form of fractures, caused by a large variety of factors, and covering a wide range of sizes, from microscopic to macroscopic cracks. All these types of fractures can have a strong impact on heat and moisture flow in the building envelope, and their influence is to be accounted for in any long-term performance assessment, not only of building and building components, but of any built structure in general.

As in any other scientific field, knowledge is gradually gained by conducting experimental investigations, which serve as a basis for the development of numerical models. These models can then be used to investigate in conditions that cannot be reached in laboratory studies. This methodology has been conducted during the last century for the understanding of the thermodynamics of deformable porous media. Although the understanding of chemical degradation processes is still undergoing improvement, new methods are being proposed for the numerical implementation of models and the reduction of computational costs, allowing increasingly comprehensive simulations for the service-life prediction of construction materials and building components.

Objectives and outline

A considerable amount of work has been recently performed in order to allow predicting the hygrothermal behaviour of buildings over longer periods of time, on the basis of a set of equations describing the coupled mechanical, hygric and thermal behaviour of porous materials. However, such a fully predictive approach has limitations: indeed, an accurate prediction of all ranges of damage in a building component, from microscopic to macroscopic cracks, supposes an extensive knowledge of all damage-inducing, time-varying boundary conditions of the problem during the simulation time. Such requirements can be met for life-cycle analyses and studies performed ahead of the building design. This is however not the case when considering simulating the hygrothermal behaviour of existing buildings, of which causes for degradation have not been monitored over time.

The present work aims at offering a complement to predictive methods. A new approach is proposed, based on experimental damage monitoring and numerical transfer simulations. The objectives of such an approach are:

- to summarise and complete the current knowledge in the field of flow and transport in damaged porous media,
- to observe the effects of damage on the microstructure of construction materials,
- to propose a methodology which allows identifying which existing building components are in need for renovation,
- to reduce characterisation needs and computational costs for numerical simulations.

In order to answer this questioning, a combined experimental and numerical methodology has been undertaken, in an attempt to relate microstructural observations to their consequences at the building scale. The study is centered on the development of a numerical tool for the hygrothermal performance assessment of existing building components, on the basis of the characterisation of their damage and fracture patterns rather than their prediction. Non-destructive techniques for damage monitoring were implemented during the degradation of cementitious materials, as to obtain quantitative data on crack pattern geometries. These geometries were then included into a newly developed simulation model for coupled heat and moisture modelling in cracked porous media. The model was then applied to a series of specified cases, in order to give an estimate of the potential consequences of cracking on the hygric and thermal performance of building components.

The work is presented as such: a bibliographic overview was assembled in Chap. 1, describing the general principles of heat and moisture transfer in damaged porous media, and the existing methods for damage and fracture monitoring and prediction. Chapter 2 presents an experimental investigation on the influence of diffuse damage on the water vapour permeability of fibre-reinforced mortar. The aim of this exploratory part of the work was to identify the needs for further damage characterisation and the methods to be used in transfer simulations. Chapter 3 then exposes the results of non-destructive damage monitoring techniques applied to the cracking of the same material. A methodology is proposed as to calibrate acoustic emission measurements as a tool for damage quantification, localisation, identification and prediction. Furthermore, quantitative measurements of fracture networks were performed, that can be supplied into a numerical model for heat and moisture transfer simulation in cracked porous media. Chapter 4 describes the development of such a model, and the procedure for the automated detection and implementation of crack measurements into its frame. The model was validated on the basis of X-ray radiography, by monitoring the moisture infiltration in fractures and comparing these measurements with the predictions of the code. Chapter 5 then shows the application of the model to case studies, as to investigate the effects of fractures on the hygrothermal performance of multi-layered building facades. The main results of the work, as well as suggestions and guidelines for future research, are then summed up in a conclusive section.

Frame of the work

The work presented in this manuscript has been performed in the frame of the RENOVBAT project, a cooperation between the CETHIL and MATEIS laboratories of the University of Lyon. It is a continuation of previous projects of the same cooperation, dealing with hygroscopic materials and their interaction with the environment, the most recent of which being the Ph.D. of J. Kwiatkowski [KWI 09]. The experimental equipment used in the first part of the study, covered by Chap. 2 and 3, is part of the MATEIS lab: the most notable assistance concerning this part of the project was brought by

Geneviève Foray in terms of material elaboration and characterisation, and by Nathalie Godin who helped analysing acoustic emission recordings. Monika Woloszyn and Jean-Jacques Roux of the CETHIL lab contributed to the numerical side of the work by helping identify the requirements and applications of the developed simulation code. Funding was provided for this project by the Rhône-Alpes region through the ARC Energies (Communauté de Recherche Académique).

In addition to this cooperation, a key contribution was that of the Department of Civil Engineering of the Technical University of Denmark (DTU Byg). The work covered by Chap. 4 was performed in this institute by the author, with the help of Carsten Rode and Kurt K. Hanssen on the experimental processes, and of Hans Janssen who helped in the development process of the numerical model.

Chapter 1

Heat and moisture transfer in fractured building materials

As a first step of the work, a bibliographic study was carried, as to estimate the current state of the art on the subject of the hygrothermal performance of damaged and fractured porous media. The present chapter summarises such an overview. A short survey was conducted on the basics of flow in porous media, on the derivation of the transport equations, on the detection and prediction of fractures, and on their influence on the flow. This overview allowed establishing the structure of the remainder of the work.

Contents

The importance of moisture transfer in the overall performance of buildings has already been underlined. Modelling is now common practice in the design process, in order to ensure that a given building meets all energy, comfort and durability criteria. Such an analysis can be performed prior to the construction as part of the design process, or after several years of use in order to identify an eventual need for renovation. However, only a fraction of new buildings are studied each year, and the performance of most existing ones could be enhanced through a thermal renovation.

The field of building physics simulation revolves around interactions between the environment and the constructions, represented as a group of zones and components. Simulations can run from the scale of the material microstructure to entire districts. The complexity of the phenomena at stake has generated a large variety of models and numerical methods, which can be combined for simulations including coupling effects between scales.

A widespread method for building scale simulations is the use of zonal models [KAL 07] which allow assembling a representation of a building as a group of components. Each of these components can be represented with various levels of complexity. For instance, the air volume of a room can either be represented by one node or by more complex CFD simulations, which can then be coupled to the multizonal model in order to study the interactions with the surrounding components. HAM modelling, although often restricted to the scale of hygroscopic building materials, can therefore be integrated in such a frame [STE 10] in order to estimate the interactions between the envelope and indoor air [QIN 09, QIN 12].

The present chapter is ordered as follows : in Sec. 1.1, the general principles of heat and moisture transfer in porous building materials are summed up. A brief literature survey addresses the matters of the scales of observation and the underlying mechanisms of heat and moisture transfer. In a second section 1.2, the full expression of the transport equations for anisotropic coupled transfer is displayed and discussed under the current simplification hypotheses. Sec. 1.3 then describes how fractures can influence the flow, and how they can be included in simulations.

1.1 General principles of flow in porous media

1.1.1 Derivation of the conservation equations

At the microscopic scale, a porous material is composed of a solid skeleton and of variously sized voids, filled with one or more fluid phases, each of which can be a mixture of several components. Bulk properties such as the mass density present high local fluctuations and discontinuities at interfaces between phases. In order to properly describe multi-phase flow at the scale of a building component, one first has to define an averaging region, i.e. the size of representative elementary volume (REV) in which quantities can be considered continuous [WHI 69].

The most commonly used theory for the derivation of the macroscopic conser-

vation equations is the averaging procedure introduced by Hassanizadeh and Gray [HAS 79a, HAS 79b]. This procedure consists in applying averaging theorems to the microscopic balance law of a thermodynamical property or quantity ψ in a phase α. When neglecting exchanges between phases, the general form of the resulting equation is:

$$\frac{\partial}{\partial t}\langle\rho\rangle_\alpha\overline{\psi}^\alpha + \nabla\cdot\left(\langle\rho\rangle_\alpha\overline{\mathbf{v}}^\alpha\overline{\psi}^\alpha\right) - \nabla\cdot\mathbf{i}^\alpha = \langle\rho\rangle_\alpha\left(\overline{f}^\alpha + \overline{g}^\alpha\right) \tag{1.1}$$

where the $\langle\cdot\rangle_\alpha$ and $\overline{\cdot}^\alpha$ operators respectively depict a volume and mass average operators [HAS 79a], $\overline{\mathbf{v}}^\alpha$ is the phase velocity and $\mathbf{i}^\alpha$, $\overline{f}^\alpha$ and $\overline{g}^\alpha$ are the surface flux vector, external supply and net production rate of the quantity $\overline{\psi}^\alpha$. Eq. 1.1 can be formulated into the conservation equations of mass, momentum, energy and entropy by appropriately setting the values of $\overline{\psi}^\alpha$ and of these variables. One can refer to [HAS 79b, HAS 86a] for a full derivation of these equations. This frame was also the basis for the development of studies on the deformation of porous media [LEW 87, COU 04] under mechanical, thermal and hygric loads.

In most building physics applications, only three equations are considered: mass conservation of the liquid and gas phases, and energy conservation: by assuming a local thermal equilibrium between phases, one does not need to express separate energy conservation equations for each phase [HAS 86a]. The liquid and gaseous momentum balances do not need to be explicitely calculated as their displacements can be modelled through Darcy's and Fick's laws [HAS 86b], which are recalled below.

On the scale of the REV, permeable porous materials are characterised by macroscopic parameters describing their transport properties and equilibrium potentials, for both hydraulic and thermal processes. These material characteristics can either be determined experimentally or estimated through structural models, and are necessary for subsequent building physics simulations including the concerned materials.

1.1.2 Water movement and storage in porous materials

1.1.2.1 Sorption isotherm

The equilibrium moisture content of a material is the concentration of water that is either adsorbed or condensed in its porous network once a steady state is reached. It is mostly a function of the ambient relative humidity (RH), but also of the wetting history of the material and the temperature. Its profile versus values of RH is the sorption isotherm, which entirely characterises the moisture storage capacity of the material.

The moisture storage mechanism in porous media follows several phases from low to high RH's. At first, water molecules are adsorbed to the pore surface by van der Waals forces. The layer of adsorbed molecules thickens with increasing RH. In this interval of humidity, materials with high specific surfaces present higher increases of volumetric moisture content. At higher values of RH, the quantity of adsorbed water reaches the point at which smaller pore spaces can be filled by capillary condensation. A meniscus is then formed at the interface between the gas a liquid phases, of which pressures,

respectively denoted p_g and p_l obey the Young-Laplace law:

$$p_g - p_l = 2\sigma H \tag{1.2}$$

where σ is the surface tension ($\sigma = 73 \cdot 10^{-3}$ N.m^{-1} for water) and H the mean curvature of the meniscus. For instance, in a cylindrical pore of radius r, with a water/solid contact angle of θ:

$$H = \frac{\cos\theta}{r} \tag{1.3}$$

The pressure jump at the gas/liquid interface arises, caused by the difference in the surface tension of the wetting and non-wetting fluids, is denoted as capillary pressure p_c:

$$p_c = p_l - p_g \tag{1.4}$$

According to this definition, the capillary pressure has a negative value for unsaturated conditions. Although this convention does not meet general consensus, its purpose is to guarantee physical consistency in the expression of the moisture flow, which occurs in the opposite direction of the pressure gradient.

The gas phase in contact with the water meniscus is a mixture of air and water vapour. As water coexists in two adjacent phases, the condition for equilibrium is that its partial pressure p_v follows Kelvin's law:

$$\frac{p_v}{p_s} = \phi = \exp\left(\frac{p_c M_{H_2O}}{\rho_l RT}\right), \tag{1.5}$$

where p_s is the water vapour saturation pressure in air, ϕ is the relative humidity, M_{H_2O} and ρ_l are the molar mass and density of water, and R is the universal gas constant. The Clausius-Clapeyron relation is commonly used to approximate the vapour saturation pressure:

$$\frac{\partial p_s}{\partial T} = \frac{L_{lv} M_{H_2O}}{RT^2} p_s, \tag{1.6}$$

where L_{lv} is the evaporation latent heat of water. Eq. 1.6 is assumed to hold for usual atmospheric conditions to which buildings are submitted. Eq. 1.5 discloses the equivalence between water vapour pressure and capillary pressure.

Fig. 1.1 shows the general shape of the sorption isotherm of two hygroscopic construction materials. The slope is higher over the hygroscopic range, near saturated conditions, due to an increasing concentration of capillary condensed water. The equilibrium moisture content of some materials can show an important hysteresis behaviour, i.e. a difference between sorption and desorption curves. This is due to the presence of remaining water in the material after drying, due to the presence of adjacent pores of different diameters. When this effect is important, a hysteresis model must be used to estimate the moisture content and capacity at a given value of relative humidity, as a function of eventual previous alternating processes of adsorption and desorption [MUA 74, MUA 76a, CAR 05a, DER 07]. The use of these models result in history-dependent sorption laws.

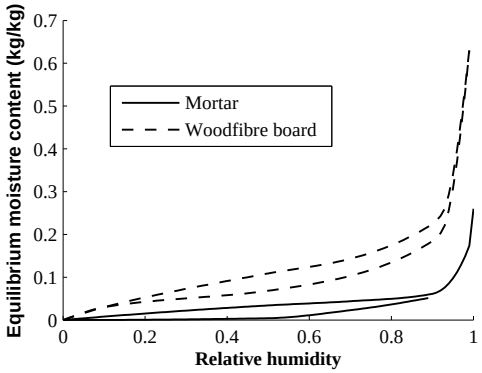

Figure 1.1: Examples of sorption and desorption isotherms (based on data from [KUM 02])

Experimental measurements of the equilibrium moisture content are now widespread : the sorption isotherm can be measured in the hygroscopic range with the desiccator method or climatic chamber method [ISOa], and in the over-hygroscopic range with the pressure plate method. In the present work, these techniques have been performed on concrete and mortar samples, and their procedures and results are discussed in Chap. 2 and 4 along with moisture flow measurements. These results are then approximated by the analytical laws recalled in Sec. 1.2.3.

1.1.2.2 Moisture transport

Similarly to moisture storage mechanisms, the movement of water in porous media undergoes two main stages. In the hygroscopic range, the displacement of water molecules is mostly caused by diffusion phenomena in the gaseous phase, driven by gradients of vapour pressure. The resulting pressure variations in the pore network causes local increases or decreases of the adsorbed layer of water molecules. The ability of a material to resist these diffusion phenomena is characterised by its water vapour permeability. This parameter can be experimentally measured either by means of the standardised cup method [ISOb] or by transient techniques [CRA 75, ARF 00, GAR 06, AND 08, GAR 10, ROU 12a]. More information on such methods is provided in Sec. 2.2.

Liquid flow in unsaturated porous media occurs under the effect of capillary pressure gradients. Where a meniscus is formed, “the movement of the fluid-fluid interface is governed by the balance of the forces exerted by the two fluids on the interface and the forces present within the interface” [HAS 93]. A simple measure for the ability of a material to resist or allow water infiltration is the so-called water absorption coefficient, or sorptivity [GUM 80, VEJ 09]. While this coefficient can be seen as a useful parameter to define free water suction of a building material, it is not sufficient for the prediction of flow in an unsaturated medium. For this purpose, the observation of two-dimensional moisture concentration distributions is preferred. This can be done using

gravimetric methods [DRC 03] or techniques such as nuclear magnetic resonance, γ-ray attenuation, capacitance method or X-ray projection [CER 02]. More information on such methods is provided in Sec. 4.1.3.

1.1.2.3 Network models

It can be argued that measurements of the moisture transport and storage properties of porous construction materials are time-consuming and do not offer a full comprehension of pore networks. Alternative approaches for the computation of the transport properties have been proposed.

The principle of network models is the construction of a porous network as an ensemble of simple interconnected geometries, in the prospects of deriving its transport or storage properties. The pore structure is approximated by a lattice of interconnected tubes, of which transport properties can be derived by calculating the Poiseuille flow [FAT 56]. Xu *et al.* [XU 97a] proposed a model for reconstructing multiscale porous structures on the basis of mercury intrusion porosimetry data. This method was applied to the prediction of transport properties of a series of materials [XU 97b, QUE 98]. Roels *et al.* [ROE 01] then proposed predicting the porosimetry results, by using image analysing techniques on SEM micrographs. By applying an earlier developed multiscale network model [CAR 99], the authors show how imaging techniques may serve as a basis for the derivation of transfer [CAR 01] or storage properties [CAR 02] of porous media.

An alternative approach relies on a more simplified description of the medium: bundle of tubes models [BUR 53] propose a formulation of moisture properties, based on the sole knowledge of the pore-size distribution function. These models, though more simple than fully comprehensive network models, are semi-empirical and require some adjustments as to fit with the considered materials [SCH 10].

1.1.3 Heat transfer

Heat transfer in permeable porous solids is caused by conduction, convection and radiation exchanges. The importance of each of these phenomena is greatly influenced by the nature of the considered material.

Conduction is the main cause of heat transfer in materials with relatively low porosity. At the scale of the REV, these materials are characterised by a macroscopic (or effective) thermal conductivity. Numerous models are available for its estimation, although most of them can only cover a specific type of porous structure [PRO 76]. One can for instance cite parallel or series models, the Maxwell-Eucken equation [LEV 81], the effective medium theory [CAR 05b], or a combination of these models [WAN 06]. The macroscopic thermal conductivity is greatly influenced by the nature of the fluid filling the voids of the porous network. As the conductivity of water is much higher than that of air, the moisture content of a building material is known to influence its overall conductivity [MNA 06]. This is one of the motivation behind the coupled resolution

of the transport equations for heat and moisture in such materials. The local heat capacity is a function of the local moisture content as well, but its estimation is more straightforward as it can be approached by a simple volume averaging.

Convection processes also occur inside the porous material, as well as on its external surface in case of air movement. Internal convection is caused by the heat carried by the air and water flowing in the material, and to the latent heat of the water vapour which can condensate on the pore surfaces. This phenomenon appears in the expression of the convective heat flux as explained in Sec. 1.2. External convection is the exchange of heat between the material and the ambient air.

The radiative heat exchange is composed of the short-wave and long-wave radiation exchanges between the surface, the atmosphere and the ground [JAN 07]. They are particularly important in case of solar exposure of a building facade. Radiation exchanges may also occur inside a porous material between pore surfaces. This phenomenon is of higher relative importance in highly porous insulation materials with high specific areas, in which conduction transfer can be very low. It is however not considered in the present study, which is focused on cementitious materials.

1.2 Conservation equations for building physics applications

Heat, air and moisture transfer modelling in building materials has gone through standardisation during the past decade. This has been the purpose of the Hamstad project [HAG 04, HAG 02b], which established a platform for the assessment of HAM simulation tools in building physics. The project includes a set of benchmarks [HAG 02a] designed to allow the validation of models for the prediction of flow in various combinations of materials and climatic conditions. It is however focused on the case of isotropic materials, of which transport and storage properties do not evolve over time.

The present section recapitulates the hypotheses allowing a simplified and accurate modelling of HAM transfer and formulates the transport equations which are to be implemented into the simulation code. A further mention to the Hamstad project is made in Sec. 5.1, as the benchmark cases are to be used for the validation of a simulation tool.

1.2.1 Hypotheses

All subsequent mentions to multi-phase flow in porous media in the present manuscipt refer to building materials filled with a liquid phase only composed of water, and a gaseous phase which is a mixture of dry air and water vapour. The expressions of the transport equations for heat, air and moisture are based on several assumptions, allowed by the operating conditions of buildings and the nature of the materials at stake.

- **Temperatures remain in a relatively narrow range**. Therefore, moisture storage is temperature-independent and the sorption isotherm is to be measured only

once at a reference temperature. Also, no ice is formed on the material surfaces nor in the pores, allowing neglecting the thermal and mechanical effects of water solidification.

- **Climatic loads are simplified**. Radiative heat transfer to and from a building facade is represented by an equivalent temperature which combines air temperature, long wave and short wave solar radiation. The expression of hygric loads caused by wind-driven rain is simplified as well.
- **No hysteresis effects** are considered.
- **No chemical reactions** are considered. Transport of salt, chloride ions or carbon dioxyde is therefore not calculated.
- **Damage processes** are not modelled. Although the influence of cracks on the flow is the main interest of this work, their initiation and propagation is not explicitely simulated, as stated earlier. Instead, fracture geometries are to be measured experimentally and then included into the simulation code.

1.2.2 Balance equations

HAM transport in building physics is a strongly coupled process. This means that the evolution of a variable field (pressure or temperature) is influenced by the state of other fields. The causes of coupling are the following:

- temperature and moisture concentration dependency of the transport coefficients,
- convective heat and water transport in gas and liquid phases,
- moisture dependency of heat storage,
- water movement driven by temperature gradients.

1.2.2.1 Air

Although often neglected in hygrothermal simulations of building components, air transfer can contribute markedly to the drying or wetting of hygroscopic materials through convective phenomena. Assuming the absence of fluctuations in air density, its conservation equation simply reads:

$$-\nabla \cdot \mathbf{g}_a = 0, \tag{1.7}$$

The air flow $\mathbf{g}_a$ [kg.m^{-2}.s^{-1}] is driven by a gradient of air pressure. In case of laminar flow, this term reads:

$$\mathbf{g}_a = -K_a \nabla p_a \tag{1.8}$$

where K_a is the unsaturated air permeability of the material.

1.2.2.2 Moisture

The mass conservation equation for water relates the temporal variations of its volumetric content w to the moisture flow in either vapour or liquid phase, respectively denoted $\mathbf{g}_v$ and $\mathbf{g}_l$:

$$\frac{\partial w}{\partial t} = -\nabla \cdot \left(\mathbf{g}_v + \mathbf{g}_l\right) \tag{1.9}$$

Water vapour transfer is caused by both diffusive and convective phenomena. The former follows Fick's law and is driven by a gradient of vapour pressure, while the latter is proportional to the air flow. Assuming water vapour obeys the ideal gas law,

$$\mathbf{g}_v = -\delta_p \nabla p_v + \frac{p_v}{\rho_a R_v T}\mathbf{g}_a \tag{1.10}$$

where δ_p is the water vapour permeability of the material, and R_v is the specific gas constant of water, i.e. the universal gas constant divided by water's molar mass. Liquid transport is driven by a gradient of capillary pressure, according to Darcy's law:

$$\mathbf{g}_l = -K_l \nabla p_c \tag{1.11}$$

where K_l is the liquid permeability of the material. In practical applications, only one pressure variable is used as a potential for moisture transfer. In order to guarantee the applicability of Eq. 1.9, the equivalence between ∇p_v and ∇p_c must be established. This equivalence can be formulated thanks to the Young-Laplace, Kelvin and Clausius-Clapeyron laws (Eq. 1.2, 1.5 and 1.6, respectively):

$$\nabla p_v = \frac{p_v}{\rho_l R_v T}\nabla p_c + \frac{p_v}{\rho_l R_v T^2}\left[\rho_l L_{lv} + p_c\left(\frac{T}{\sigma}\frac{\partial \sigma}{\partial T} - 1\right)\right]\nabla T \tag{1.12}$$

The derivation of this equation is not trivial, and has been detailed in appendix A.1. For simplification purposes, we can assume a negligible dependency of the surface tension to the temperature, i.e. $\partial\sigma/\partial T = 0$.

The left term of Eq. 1.9 represents temporal variations of the volumetric moisture content and can be decomposed as a function of the potentials p_c and T.

$$\frac{\partial w}{\partial t} = \frac{\partial w}{\partial p_c}\frac{\partial p_c}{\partial t} + \frac{\partial w}{\partial T}\frac{\partial T}{\partial t} \tag{1.13}$$

The term $\partial w/\partial p_c$ is the slope of the moisture retention curve and can be referred to as moisture capacity. The last term $\partial w/\partial T$ is often neglected as the equilibrium moisture content is considered temperature-independent.

An alternative way to write Eq. 1.9 is to use w as the driving potential for moisture transfer, which in the isothermal case reads:

$$\frac{\partial w}{\partial t} = -\nabla \cdot (-D_w \nabla w) \tag{1.14}$$

where D_w is the moisture diffusivity of dimension $[\mathrm{m}^2.\mathrm{s}^{-1}]$. Its expression follows from Eq. 1.9 to 1.12:

$$D_w = \frac{1}{\partial w/\partial p_c}\left[K_l + \delta_p \frac{p_v}{\rho_l R_v T}\right] \tag{1.15}$$

	Capacity	Permeability
Heat	$(c_m \rho_m)$	λ
Air		K_a
Moisture	$\partial w / \partial p_c$	K_l ; δ_p

Table 1.1: Recapitulation of material properties required for HAM modelling

1.2.2.3 Heat

The energy balance equation reads:

$$\frac{\partial E}{\partial t} = -\nabla \cdot \left(\mathbf{q}_{cond} + \mathbf{q}_{conv} \right) \tag{1.16}$$

where E is the internal energy:

$$E = c_m \rho_m T + c_l w T \tag{1.17}$$

where the subscripts m and l respectively indicate properties of the raw material and of water. The conductive heat transfer follows Fourier's law:

$$\mathbf{q}_{cond} = -\lambda \nabla T \tag{1.18}$$

where λ is the thermal conductivity, function of both the temperature and the moisture content. The convective heat transfer is driven by the flow of each fluid phase and of water vapour:

$$\mathbf{q}_{conv} = c_a T \cdot \mathbf{g}_a + c_l T \cdot \mathbf{g}_l + (c_v T + L_{lv}) \mathbf{g}_v \tag{1.19}$$

1.2.3 Transport and storage coefficients

From the balance equations 1.7, 1.9 and 1.16, it appears that a total of six material properties (transport and storage coefficients) need to be identified for modelling purposes. These variables are summed up in table 1.1.

The moisture retention curve is commonly described using van Genuchten functions [GEN 80]. These functions are flexible and depend on parameters which allow fitting with experimental measurements as to describe retention characteristics of various pore network geometries. In order to describe the retention curve arising from a heterogeneous porous medium with several pore sizes, Durner [DUR 94] proposed superimposing unimodal van Genuchten functions as to form a multimodal expression:

$$w\left(p_c\right) = w_{sat} \sum_i l_i \left[1 + \left(\alpha_i |p_c| \right)^{n_i} \right]^{-m_i} \tag{1.20}$$

where w_{sat} is the water concentration in the capillary saturated material, and i covers the number of subsystems. The set of parameters (l, α, m, n) can be estimated by fitting Eq. 1.20 on measurements. The number of modes is directly related to the level of

heterogeneity of the pore structure. Conductivity estimations for materials with heterogeneous pore systems can follow the general form of Mualem's model [MUA 76b] for the prediction of the relative hydraulic conductivity of soils [PRI 06]:

$$K_l = K_{sat}\, s^{\tau} \left[\frac{\int_0^s h(s)^{-q}\, \mathrm{d}s}{\int_0^1 h(s)^{-q}\, \mathrm{d}s} \right]^2 \tag{1.21}$$

where h is the pressure head, or capillary suction height, commonly used as driving potential in the field of soil sciences:

$$h = -\frac{p_c}{\rho_l g} \tag{1.22}$$

The introduction of Eq. 1.20 into 1.21 results in:

$$K_l = K_{l,sat}\, s^{\tau} \left[\frac{\sum_i l_i \alpha_i \left(1 - \left(1 - s_i^{1/m_i}\right)^{m_i}\right)}{\sum_i l_i \alpha_i} \right]^2 \tag{1.23}$$

where $K_{l,sat}$ is the water permeability of the saturated material, p and q are material parameters. The variable s denotes the non-dimensional saturation degree of the material $s = w/w_{sat}$, and s_i are the subcurves of the retention function:

$$s_i = \frac{w_i}{w_{sat}} = l_i \left[1 + \left(\alpha_i |p_c|\right)^{n_i}\right]^{-m_i} \tag{1.24}$$

The main asset of this formulation is its flexibility, allowing an accurate description of most materials for their implementation in building physics or soil science simulations. By using prescribed values of the parameters p and q [GEN 80], one can circumvent the need for a tedious measurement of the moisture permeability. However, this derivation is not always accurate, and the set of parameters (l, α, m, n) used in Eq. 1.23 often differs from that of Eq. 1.20 [ROU 12b].

According to Luckner *et al.* [LUC 89], the air permeability can be expressed in a similar fashion, by substituting the saturation permeability for that of air $K_{sat,a}$ and the liquid saturation degree by a nonwetting fluid saturation variable s_*:

$$K_a = K_{a,sat}\, s_*^{\tau} \left[\frac{\sum_i l_i \alpha_i \left(1 - \left(1 - s_{*i}^{1/m_i}\right)^{m_i}\right)}{\sum_i l_i \alpha_i} \right]^2 \tag{1.25}$$

The saturation permeabilities of both liquid and air phases can be related through the definition of the intrinsic permeability $K\ [\mathrm{m}^2]$

$$K = K_{l,sat}\frac{\eta_l}{\rho_l} = K_{a,sat}\frac{\eta_a}{\rho_a} \tag{1.26}$$

which is a material property. This theoretically allow characterising the unsaturated air permeability on the sole basis of the knowledge of the unsaturated liquid permeability.

1.2.4 Boundary transfer

Ambient or atmospheric boundary conditions can be implemented into HAM simulations with various levels of complexity. Basic approaches characterise heat and moisture exchange with the environment through simple convective transfer imposed as boundary conditions. The past decade has seen an increasing implementation of weather data (wind, rain and solar radiation) into simulation codes, and the development of mathematical formulations allowing integrating them into the calculations.

The general expressions of boundary heat and moisture flows are [HAG 04, JAN 07]:

$$\begin{array}{rcl} \mathbf{q} & = & \alpha\left(T_{eq}-T\right)\cdot\mathbf{n}+c_l T_a \mathbf{g}_{l,r}+\left(c_v T_a+L_{lv}\right)\mathbf{g}_v \\ \mathbf{g} & = & \mathbf{g}_v+\mathbf{g}_{l,r}=\beta\left(p_{v,a}-p_v\right)\cdot\mathbf{n}+\mathbf{g}_{l,r} \end{array} \tag{1.27}$$

where α and β denote the heat and mass surface transfer coefficients, $\mathbf{g}_{l,r}$ denotes an incoming liquid flow in the form of rain and T_{eq} denotes the equivalent temperature, which combines the temperature of the ambient air T_a, short wave solar radiation and long wave ground radiation. More details on the terms and coefficients of Eq. 1.27 are given below.

1.2.4.1 Surface transfer coefficients

Convective heat exchange between the surface and the atmosphere is described by the surface transfer coefficients α and β, which respectively denote the resistance of the air surface layer to heat and moisture transfer. α can be estimated from the dimensionless Nusselt number, usually calculated using correlation formula based on the air velocity [VDI 10]. Literature shows that the transfer coefficient can increase up to tenfold from an indoor surface exposed to natural convection [AWB 98] to an external surface exposed to wind [LOV 96]. Because of the similarity in the basic mechanisms of heat and mass exchange at a material boundary, it is also possible to relate it to the moisture transfer coefficient. The Chilton-Colburn analogy allows estimating one of the exchange coefficients from the other:

$$\frac{\beta}{\alpha}=\frac{D_{v,a}}{R_v T \lambda_a}\mathrm{Le}^{2/3}\approx 7.45\times 10^{-9} \tag{1.28}$$

where $D_{v,a}$ is the diffusivity [$\mathrm{m}^2.\mathrm{s}^{-1}$] of water vapour in air and Le is the non dimensional Lewis number, which represents the ratio of thermal to mass diffusivity.

1.2.4.2 Wind-driven rain

The contact of rain with the material occurs either in case of tilted surfaces (e.g. roofs) or of wind providing a horizontal component to raindrop trajectories. In case of important wind and precipitation, rainfall can be a significant source of moisture income on a facade. Because of the complexity of the phenomena at stake, it is difficult to precisely estimate the quantity of water impacting a given surface, depending on the building geometry, its position and environment, the wind speed and direction, the

horizontal rainfall and the distribution of raindrop sizes. The literature on the field of wind-driven rain (WDR) is therefore quite large, as reviewed by Blocken and Carmeliet [BLO 04].

A common way to inclure WDR into HAM simulations is the use of semi-empirical models relating the surface moisture source term $\mathbf{g}_{l,r}$ to the horizontal rainfall intensity R_h, the local wind speed U, and the angle of the facade to the wind direction θ:

$$\mathbf{g}_{l,r} = \alpha_{WDR} R_h U \cos\theta \tag{1.29}$$

The coefficient α_{WDR} represents the ratio of rain drops of given size distribution impacting the facade. This WDR coefficient can be expressed by semi-empirical models such as Straube and Burnett's [STR 00], as to fit previous measurements.

The ratio of WDR to horizontal rainfall, or catch ratio, can also be estimated by means of Computational fluid dynamics (CFD). Choi [CHO 93, CHO 94] introduced a methodology for determining it: first, the steady-state wind-flow pattern around the building is calculated, using Reynolds-averaged Navier-Stokes equations with a k-ϵ turbulence model. The raindrop trajectories are then calculated from this wind-flow pattern, and the amount of raindrops impacting a given facade allows estimating its catch ratio.

According to a recent comparison of these two modelling approaches [BLO 10], semi-empirical models, while coarser than CFD models, can provide appropriate results while having a much lower computational cost.

1.2.4.3 Radiative heat exchange

In addition to the convective heat exchange between a surface and the ambient air, radiative processes can be accounted for. These processes include direct and diffuse solar radiation, as well as long-wave radiative exchange between the surface and its environment. A simplified way to include these phenomena in calculations is the use of an equivalent boundary temperature, which is the surface temperature at which the heat transfer rate due to the temperature difference across the wall is the same as the rate due to the combined effects of convection, conduction and radiation.

$$\alpha\left(T_{eq} - T\right) = \alpha\left(T_a - T\right) + \kappa I_{sol} + \sigma\epsilon I_{LW} \tag{1.30}$$

where κ and ϵ are the solar absorption coefficient and long-wave emmissivity of the material, and σ is the Boltzmann constant. I_{sol} and I_{LW} respectively depict the short-wave and long-wave radiative exchange between the surface and its environment. Short-wave radiation consists pf direct and diffuse solar irradiance. Long-wave radiation is exchanged between the facade and the ground, nearby buildings and sky. The radiation balance in a given urban setting is however highly complex, as is shown by studies on the radiative exchange in urban canyons [HAR 04].

1.3 Hygrothermal behaviour of fractured porous media

Multiphase flow in cracked porous materials has long drawn interest in the fields of geology, petrology and aquifer study. In these lines of research, it is indeed crucial to dispose of reliable methods for the characterisation of fractures and fracture networks, and for flow and transport measuring and modelling, from small to large scales of cracking. A review on flow and transport in cracked geological media was given in 2002 by Berkowitz [BER 02]. However, little interest had been given to the case of fractured construction materials until the early 1990's [KER 91, SAM 92]. Subsequent studies on the subject were mostly motivated by the effects of water on the durability of concrete structures under tension [SAM 92, GER 96, ALD 99, LIM 00], as it accelerates deterioration processes.

The present section is an overview of the existing methods for heat and moisture flow modelling and monitoring in such aged structures. The first requirement in such studies is the gathering of fracture geometries, either by means of a predictive approach (fracture modelling) or by experimental characterisation.

1.3.1 Fracture and damage identification

1.3.1.1 Fracture mechanics of cementitious materials

Many construction materials, such as concrete and mortar, are quasi-brittle materials. In such a material subjected to stress, micro-cracks first form at the location of initial voids and defects. Under further loading, the deformations concentrate in a narrow zone of high local stress, and a macroscopic crack initiates and propagates through the material. The historical development of failure modelling separates continuous and discontinuous approaches, respectively for the description of diffusely damaged media and macroscopic fractures.

The prediction of macroscopic crack propagation in brittle and quasi-brittle materials originates in the theory of linear elastic fracture mechanics (LEFM) [IRW 57]. The numerical implementation of fracture mechanics theories is usually carried by means of the finite element method [HIL 76], or more recently the extended finite element method (XFEM), which allows incorporating discontinuities in displacement fields [MEL 96, BEL 01], predicting crack growth independently from the finite element mesh [MOE 99], and including interactions between two sides of a crack [DOL 00, WEL 01] in the calculations.

Continuum damage mechanics propose constitutive laws to include the loading history of a material to its stress-strain behaviour. Several formulations have been elaborated for the case of quasi-brittle building materials under different types of loading [BAZ 83, MAZ 89, MES 98, FIC 99, LEM 00]. Rather than explicitly modelling micro-cracks, these theories represent isotropic or anisotropic damage by a set of scalar or tensorial parameters.

1.3.1.2 Characterisation of fracture patterns

Alternatively to the prediction of damage and failure, cracks can be identified and quantified by a variety of experimental techniques. These techniques can be implemented either during mechanical tests, in which case they are referred to as damage monitoring, or afterwards, by means of destructive or non-destructive methods. The main asset of damage measurements over modelling approaches is the fact that they provide the exact geometries of crack patterns and do not require an extensive understanding of all factors generating them.

One of the earliest attempts at cracks observation in concrete was performed by Slate and Olsefski [SLA 63], who used X-rays to observe cracks caused by drying or compressive loading. X-ray radiography and tomography provide mappings of the absorptivity of a material, which is related to its atomic number and allows segregating cracks and voids from the solid skeleton. Examples of X-ray tomography implementations include microstructural observations for permeability calculations [QUE 98, BEN 00], three-dimensional fracture observation [LAN 03] or propagation monitoring [LAN 07]. The technique is however limited by a heavy computational cost, and only applies to relatively small samples. The detection of pre-existing cracks can be facilitated by impregnation techniques [HOR 96] allowing their automatic detection and quantification [AMM 00] by microscopic examinations.

Other non-destructive imaging techniques can be mentioned for two-dimensional damage monitoring: electronic speckle pattern interferometry [JIA 94, SHA 99] and digital image correlation [SUT 83] consist in measuring in-plane displacements on specimen surfaces. The latter has been used for the estimation of stress intensity factors near crack tips [RET 05, ROU 06] or the identification of elastic properties [HIL 06] or damage laws [LEP 10], among other uses. The technique has been shown suitable to the observation of local displacements of brittle building materials such as concrete [CHO 97, COR 07].

A third category of damage monitoring methods includes the recording of acoustic emissions (AE). In a material under loading, elastic waves are emitted as a consequence of crack initiation and propagation. Recording and analysis of acoustic activity is of great importance in the fields of seismology and civil engineering. Among others, it has been used for damage estimation of concrete [OHT 01, COL 03, SUZ 04], identification of damage mechanisms [PHI 98, GOD 04, ELA 07, OHN 10], estimation of fracture energy [MUR 10, VID 11] or failure prediction [SHI 94].

Among these damage monitoring techniques, AE is the most suitable for *in situ* applications at the building scale. However, it suffers from an important drawback in comparison to optical or radiography techniques, as soundwaves do not directly translate into the geometric parameters of the cracks. An attempt at overcoming this issue was made in this study, and is presented in Chap. 3.

1.3.2 Permeability measurements of fractured porous media

Fractures are known to accelerate moisture ingress in porous materials, because of capillary suction phenomena, and because they reduce the overall tortuosity of the porous network. The main motivation behind the first quantitative studies of the transport properties of concrete under mechanical loading was the fact that moisture ingress directly impacts its durability and structural integrity. Authors of these studies proceeded by applying compressive loading on concrete disks and recording their permeability during loading or after unloading. A review was written by Hoseini *et al.* [HOS 09] on this matter: the effect of parameters such as temperature [CHO 07], mix composition [KER 91], presence of fibres [RAP 02] or size of the aggregates [SAM 92] was studied.

Two phases are generally noticed during the loading process. In the pre-peak phase, variations of transport propertries are moderate: Choinska *et al.* [CHO 07] noticed a slight decrease of permeability under low compressive stress values, followed by a higher increase of up to fivefold as the peak stress is approached [SUG 96, LIM 00]. While an initial drop can be caused by the consolidation of the porous network under compressive loading, the permeability increase, starting aroung 80% of the peak stress has also been seen by bending or tensile tests [LAW 02, RAP 02]. When the loading is carried beyond the peak stress and a macroscopic fracture of crack-opening displacement (COD) over 50 μm is formed, the transport properties of the specimen increase drastically. The increase of permeability as a function of the COD was measured by [GER 96, WAN 97, ALD 99], and can span over several orders of magnitude.

1.3.3 Hydromechanical coupling phenomena

While cracking has a notorious effect on the permeability of building materials, their moisture content also affects their mechanical properties. There is therefore a strong coupling between hydraulic and mechanical phenomena, particularly in rock-like and cement-based materials. The mechanics of saturated porous media were first studied by Biot [BIO 41, BIO 55], and later extended to non-saturated materials. The basis for the interaction between fluid and solid lies in the theory of poromechanics [COU 04], accounting for the effects of the pore pressure on the effective stress applied in a continuum.

This theory is now commonly used to improve estimates for the lifetime of concrete structures by accounting for the hydraulic contribution in its degratation. For instance, Bary *et al.* [BAR 00] studied the effect of hydrostatic pressure on the fracture mechanics of concrete. They showed the coupled effects of crack formation, accelerating the imbibition of concrete by fluid which therefore increasingly acts on the matrix. Meschke and Grasberger [MES 03, GRA 04] simulated the opening of microcracks in a concrete wall undergoing drying, and its rewetting including the influence of cracks on moisture transport. Benboudjema *et al.* [BEN 05] proposed a fully coupled hydromechanical model accounting for the creep mechanisms of drying concrete. These

examples demonstrate the possibility of a strongly coupled numerical methodology for the service life prediction of building materials: models for damage evolution and fracture mechanics can be associated with models for flow and transport in porous networks and fractures, while coupling terms such as the Biot coefficient ensure the mutual dependence of both phenomena.

1.3.4 Models for flow and transport in fractured porous media

While it is clear that the evolution of the transport properties of damaged porous materials depends on numerous factors (composition, type of loading, temperature...), a common observation is generally shared: as fracture mechanics separate diffuse damage from localised cracks, the hygrothermal behaviour of a material under stress is highly dependent of matters of scales. Flow and transport modelling therefore must follow different approaches for the cases of diffusely damaged media and fractured ones. This matter is schematically shown on Fig. 1.2.

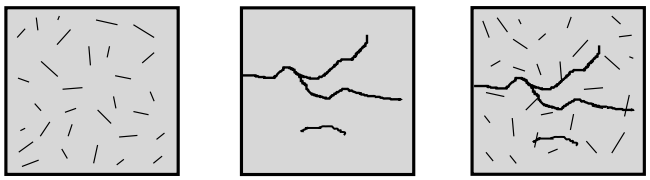

Figure 1.2: (a) Diffusely damaged medium, (b) discrete fracture network, (c) mixed medium

In order to deal with such variety of possible crack geometries and dimensions, models for fluid flow in saturated or non-saturated, isotropic or anisotropic, damaged or fractured porous media, can generally be separated into two main categories.

Continuum models consist in prescribing equivalent macroscopic transport properties. Fissures are not explicitely modelled, but their effect on the flow is accounted for at a higher scale. This approach is appropriate if a REV can be defined at a scale smaller than that of the problem of interest, such as in the case of a dense network of small cracks. The equivalent permeability of a diffusely damaged porous medium, illustrated on Fig. 1.2 (a), can also be approximated by semi-empirical models, which consist in the approximation of experimental measurements by an analytic formula. Several authors [BAR 00, PIC 01, PIJ 09] suggested power laws or exponential regressions for the expression of the increase in gas permeability with the damage value, which held for strain values below yield strain, i.e. for non-localised damage.

Discrete fracture networks, Fig. 1.2 (b), are sets of cracks of which dimensions are not significantly lower than that of the scale of observation. The volume-averaging method no longer holds, and the influence of each crack on flow and transport needs to be explicitly accounted for. These models allow a higher level of detail in the consideration of longiudinal and transverse flow in fractures. However, computational limita-

tions may arise for flow modelling at larger scales. Also, their implementation requires an extensive knowledge of the crack network geometry.

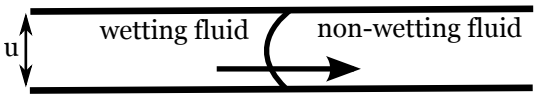

Figure 1.3: Illustration of water infiltration in a fracture

The most simple representation of a fracture for the derivation of its hydraulic and thermal properties, consists of two parallel plates of given aperture u (see Fig. 1.3). The saturated water permeability of this configuration is found using the Poiseuille equation [SNO 69].

$$K_{fs} = \frac{\rho_l u^2}{12\eta_l} \tag{1.31}$$

where η_l is the viscosity of water. Two methodologies can be followed in order to include cracks in simulations of moisture uptake.

The first method is a fully coupled approach, in which the same finite-element mesh is used for flow and transport modelling in both the fracture and the porous network. For this type of approach, the FE mesh must be adapted to the geometry of the cracks [REI 06], and strategies have been proposed for its automated refinement with crack propagation [SCH 06]. Segura and Carol [SEG 04] assigned a type of double-nodded, zero-thickness elements to the crack, allowing an explicit formulation of longitudinal and transverse flows, and of exchange terms between the matrix and the fracture. They later used this formulation for the expression of a fully coupled hydro-mechanical model [SEG 08a] for the prediction of flow in fracturing geomaterials.

The second method is a staggered approach, in which the transport equations for flow and transport are iteratively solved in the porous matrix and in the fracture. Between each iteration, the capillary pressure corresponding to the calculated pressure field in the crack is imposed as boundary condition at the matrix-fracture interface. This approach was followed by Roels *et al.* [ROE 03b, ROE 06b], who followed the progress of the moisture front in a fracture by combining a quasi-static pressure equation and a Darcian flux equation. An important asset of the staggered approach is the fact that it allows emancipating the FE mesh from the crack geometry: the extended (or generalised) finite element method (XFEM), based on the partition of unity method [MEL 96], allows including discontinuities in the problem field by adding degrees of freedom to a set of nodes surrounding the cracks [DOL 00, WEL 01]. This method allows accounting for crack propagation without modification of the mesh [MOE 99]. It was applied in recent studies for the modelling of hygrothermal damage processes [MOO 09], moisture uptake [ALF 10] and heat transfer [MOO 11] in fractured porous media.

Both monolithic and staggered approaches allow accounting for moving fractures and including all coupled hydromechanical effects at the interfaces between fractures

and matrix. Some authors argue that the staggered approach is more effective in terms of computational costs [ROE 03b, MOO 09, ALF 10], although Segura and Carol found the monolithic approach more appropriate in case of strong coupling or non-linear discontinuity behaviour [SEG 08b].

1.4 Outcome

It emerges from the above literature survey that coupled heat and mass transfer modelling in porous building materials, based on principles of mechanics and thermodynamics of porous media, is now a widespread tried and tested practice. This practice has been supported by numerous contributions for the experimental characterisation of hygrothermal transport and storage properties of materials, models for the expression of flow and transport, and numerical implementation of the transport equations. Moreover, theories developed in the course of the last few decades have expressed the coupled effects of material degradation and hygrothermal processes, allowing for the service life prediction of construction materials.

However, limitations remain in the numerical simulations of the hygromechanical degradation of building materials. In the current state of research, long-term simulations of building components do not include the effects of material ageing. Inversely, current applications of full hygro-thermo-mechanical modelling often lie on the manual input of fractures in the problem field [ROE 03b, REI 06, RET 07, SEG 08b, ALF 10, MOO 11], which does not reflect the complexity of real crack patterns. Indeed, a numerical simulation of the ageing of a building component over years of service life, including coupled hydromechanical effects and progressive damage modelling, would require an extensive knowledge of all environmental factors which may influence material degradation. The above mentioned cases are suitable for the service life prediction of construction materials. A complementary approach is required for the hygrothermal performance estimation of existing, already damaged building components.

An alternative methodology is proposed in the present study, in order to achieve a first step towards the integration of damage effects in heat and moisture transfer simulations at the building scale. A mixed approach is followed to this aim, using experimental measurements of crack patterns as an input for a numerical model for coupled heat and moisture flow. The structure of the manuscript follows the four successive steps of the reasoning behind this aim:

- First, we need to determine whether a continuum model is suited for the description of damage in hygrothermal models. A methodology was established to quantify the evolution of water vapour permeability in diffusely damaged materials, by applying inverse methods on profiles of mass uptake.

- Having identified the need for quantitative description of crack patterns, we tested and implemented non-destructive techniques for their characterisation

during mechanical loading of samples. The target was to assess the capacity of optical methods to provide detail measurements of crack patterns, and to lay the foundations for the interpretation of the acoustic activity of building materials.

- Then, we developed a numerical model, which can integrate experimental measurements of fractures as input for heat and moisture transfer modelling. An experimental procedure was conducted for the validation is such a model: digital image correlation was performed during the fracturing of concrete samples, in which moisture uptake was then monitored using X-ray radiography.

- Finally, we used validated model in order to determine whether cracks may have an impact on the thermal performance of a building. Test cases were conducted, modelling intact or damaged multi-layer building facades during several months of simulation including climatic data.

Each of these four steps is the subject of one chapter of the present manuscript. The organisation of the study is summarised on Fig. 1.4. The work was aimed at constituting a whole. All chapters are complementary, but since they concern entirely different concepts, they can be read separately without major issues of comprehension.

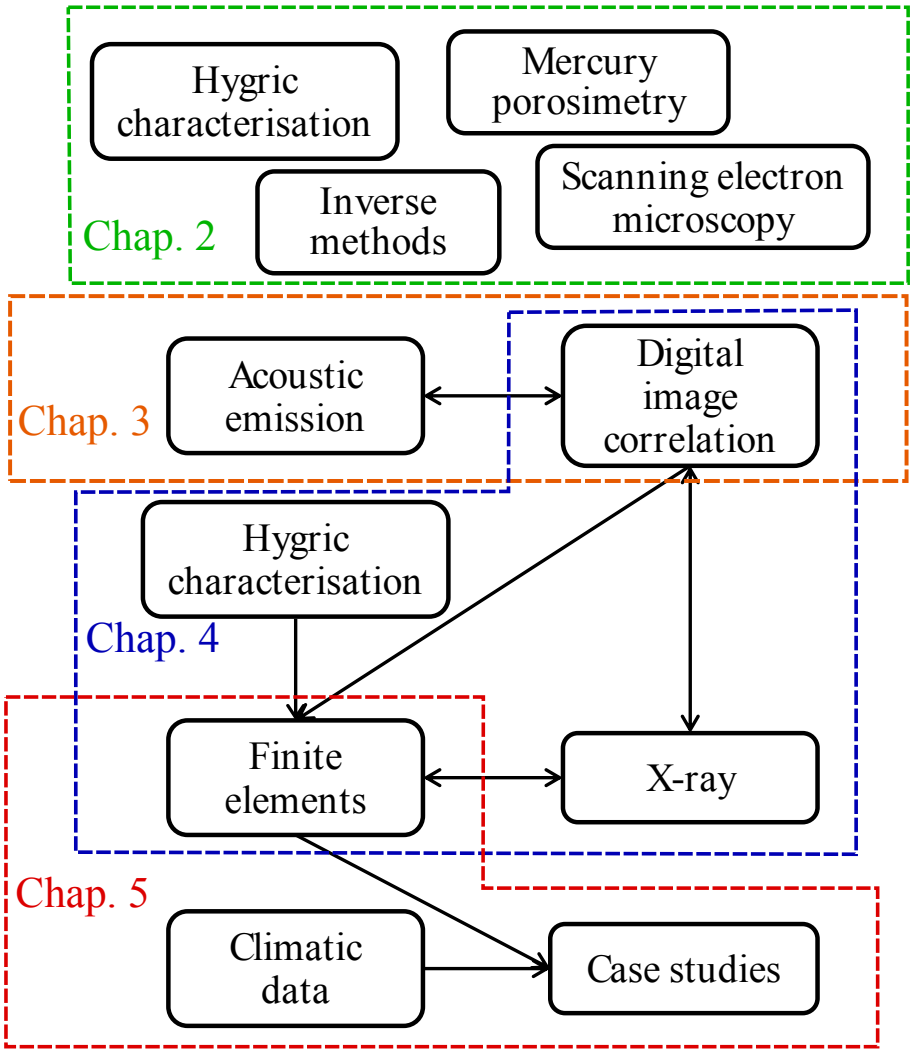

Figure 1.4: Organisation of the study

Chapter 2

Influence of diffuse damage on the water vapour permeability

The first part of the work aimed at completing the knowledge on transfer in diffusely damaged media, by measuring their water vapour permeability. An experimental procedure was developed for this purpose, and completed by two new methods for transient hygric characterisation. This leads to the conclusion that microcracks may significantly increase moisture content fluctuations of building components. It is also established that further crack characterisation will be required in the rest of the work.

Contents

As previously described, two stages of cracking occur in quasi-brittle construction materials such as mortar and concrete: diffuse damage develops in a relatively large area before the initiation and propagation of a macroscopic fracture. The general methodology for including the effects of degradation on the moisture permeability of such a material is twofold: an equivalent permeability is assigned to diffusely damaged areas, while larger fractures, of much higher permeability, are explicitely represented in the calculations. The present first step of the work is a preliminary study, of which target is the following: we need to identify whether an accurate prediction of heat and moisture flow in damaged and fractured building components can be obtained by using continuum models (assigning equivalent values of permeability), or if it requires accounting for discrete fracture networks.

Equivalent continuum models can be suited for damaged building components with a high number of well-distributed microcracks. Recent studies have shown the consequences of diffuse micro-cracking on the intrinsic permeability of concrete during mechanical loading or after unloading. The liquid and gaseous conductivity of cementitious materials can be significantly increased before the formation of a macroscopic fracture. However, moisture transport in building materials is not only caused by the displacement of a continuous liquid phase which can appear in case of rain, but is also caused by water vapour gradients and sorption processes in the hygroscopic range. The complete understanding of the influence of damage on these processes requires experimental characterisation to support numerical modelling.

A complete experimental setup, starting from material elaboration up to mechanical loading and hygric characterisation, has been developed. Coupled with appropriate numerical tools, this methodology allowed estimating the effects of damage on the water vapour transfer properties of a glass fibre-reinforced mortar. The present chapter starts with the outline of the methodology. Two methods are then described and for the estimation of hygric transport properties based on transient measurements of mass uptake in the mortar samples. The results are then displayed and discussed. The methodology and main findings of this chapter were presented in [ROU 12a].

2.1 Experimental methodology

2.1.1 Material

The material used for all tests is a commercial formulation (Lafarge, MAITE monocomposant) used for external thermal insulation composite systems. It is a Portland cement mortar including dry redispersable polymer systems with a water to dry material weight ratio of 0.16 and reinforced with 1% weight of glass fibres. This material belongs to the category of engineered cementitious composites [LI 03]. The addition of polymers in mortar and concrete-like materials has been extended during the last decade, and an increasing number of studies are being focused on their impact on the microstructure and physical properties of such composites [JEN 05, JEN 06, SIL 06,

WET 12].

While cement particles are dissolved and hydrated, polymers are dispersed in the liquid phase, and form a continuous solid network with the formed hydrates and the unreacted cement or fillers. Earlier studies [CHA 10a] proved that during tensile loading, the material shows a non-brittle behaviour, developing progressive diffuse cracking before the formation of a main macroscopic fracture. The sand and cement were mixed with water for a minute before incorporation of the glass fibres and two more minutes of mixing. The paste was then moulded into prismatic samples of 500 g and approximately 300×100×10 mm, and kept two days at a 90% relative humidity to prevent excessive water loss of the cement paste. The samples were then unmoulded and kept for 21 days of maturation at 50%RH: the mechanical behaviour of fibre-reinforced mortar resulting from this maturation procedure are known [CHA 10b].

After maturation, and prior to its mechanical and hygric characterisation, the porous structure of the material was observed by mercury intrusion porosimetry (MIP) and scanning electron microscopy (SEM). The material has an open porosity of approximately 40% and an average density of 1450 kg.m^{-3}.

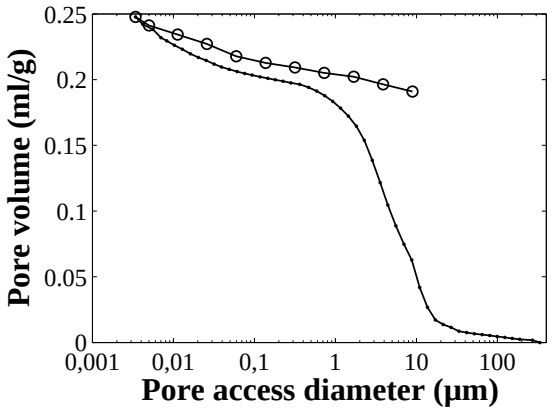

Figure 2.1: Pore intrusion (dots) and extrusion (circles) diameter distributions measured by mercury intrusion porosimetry.

Fig. 2.1 shows the mercury intrusion profile (below), measured by applying a pressure of up to 400 MPa, and accessing pore diameters of down to 3 nm. The upper curve is the extrusion profile from this point. As exhibited by the intrusion profile, the percolation threshold of this pore network is located around 4 μm. This means than most cavities are larger than this threshold, and are connected by channels of 1 to 10 μm diameter. An important part of the pore volume is also present at smaller scales, as the slope of the intrusion profile is still important near the limit of mercury porosimetry. The extrusion profile presents an important hysteresis behaviour caused by the ink bottle effect: mercury can only leave large cavities by flowing through smaller channels. This observation confirms the fact that the material includes several superimposed scales of pores.

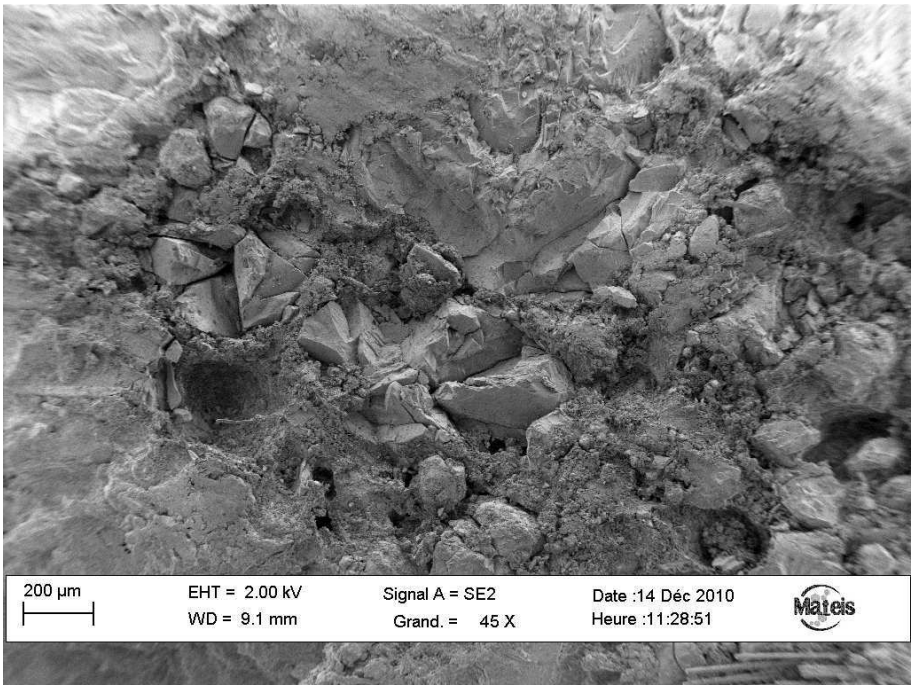

Figure 2.2: SEM overview of the material

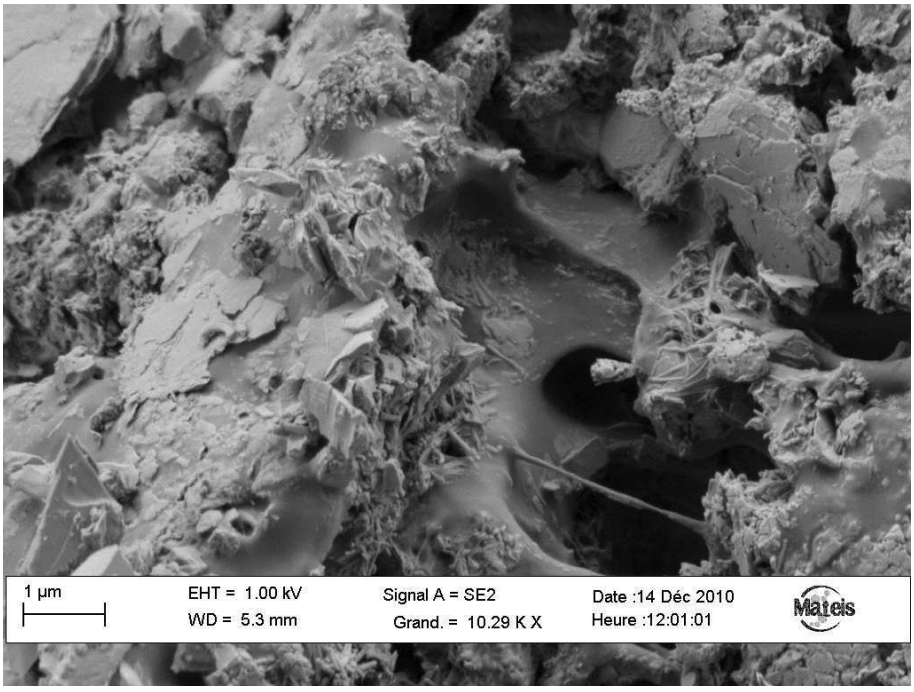

Figure 2.3: SEM observation of the material including dispersed polymers

SEM observations can confirm this multiscale nature: Fig. 2.2 and 2.3 display images captured with two levels of magnification. The first image illustrates the heterogeneity of the material including aggregates, cement paste and large circular pores. Smaller pores are visible with a higher magnification (Fig. 2.3), along with dispersed polymer systems.

All results presented in Sect. 2.3 concern three series of 16 samples. Since the conditions of sample manufacturing, ambient humidity and temperature in the laboratory can differ from one day to another, all comparisons of samples, in terms of hygric or mechanical properties, were made between samples of the same production series. This was to make sure that the measured differences in permeability were not due to outside factors.

2.1.2 Mechanical characterisation

After maturation, the prismatic samples were damaged by tensile loading beyond their limit of elasticity, using a 5 kN force cell imposing a constant displacement speed of 1 mm/min. An optical extensometer was used for monitoring the deformation rate ϵ in the direction of loading.

As a first step, the full tensile response of the mortar was observed with a full mechanical loading for the estimation of the peak strain (see left side of Fig. 2.4). Repeated observations, earlier confirmed by stereocorrelation [CHA 10a] showed that a macroscopic fracture initiates during the strain-softening phase subsequent to the peak strain ϵ_{peak}.

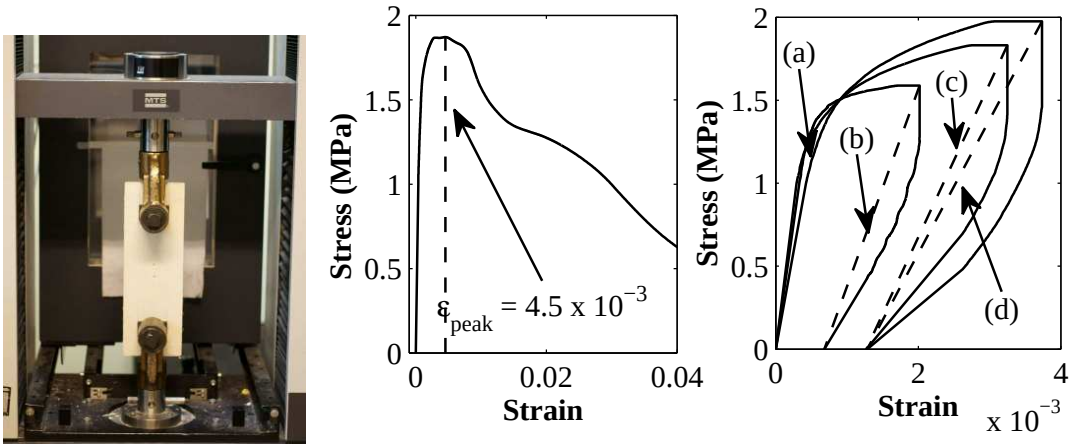

Figure 2.4: Stress-strain profiles on a full tensile loading (left) and on three tests interrupted before peak strain (right): (a) E_0 = 2750 MPa, (b) E_e = 1170 MPa, (c) E_e = 859 MPa, (d) E_e = 782 MPa

In order to apply diffuse microscopic damage on the samples before hygric characterisation, tensile loading on the tested samples was manually interrupted before the peak strain, as shown on the right side of Fig. 2.4. The diffuse damage induced by this

mechanical loading was characterised by a single scalar value D, defined as the relative change in their Young modulus [MAZ 89]:

$$D = 1 - \frac{E_e}{E_0} \tag{2.1}$$

where E_0 is the initial elastic modulus of a sample and E_e is its effective modulus after unloading, as shown with dotted lines on Fig. 2.4. D spans from 0 for undamaged materials to 1 for fully fractured samples, although this value is not reached within the frame of this study.

Among the tested series of samples, the value of the scalar damage reached with tensile loading spans from 0 (samples kept intact) to 0.7 (before peak stress). Higher damage is difficult to reach without causing a macroscopic crack initiation, i.e. the appearance of a localised crack of over 50 μm aperture, in which case an equivalent permeability cannot be defined over the surface of the sample. After unloading, the central part of each plate was used for hygric characterisation in a climatic chamber.

2.1.3 Hygric characterisation

Samples of dimensions 100×100×10 mm were extracted from the plates after unloading, and covered with aluminium tape on all faces but one, as to insulate them from moisture. Only the upper face was left unsealed, so that mass transfer could be considered unidimensional in all tests. The samples were then placed on up to eight weighing systems inside a climatic chamber, continually recording their mass without the need to take them out of the chamber, thus avoiding disturbances in the ambient humidity level. The systems can measure mass with a precision of 10^{-3}g, and were set to provide averaged values of 20 consecutive weighings every 10 seconds to reduce noise effects in the results. This procedure was developed as part of the *Humibat* project [DOU 08].

The inside of the chamber is ventilated by a fan in order to ensure a homogeneous distribution of RH and temperature. This homogeneity was confirmed prior to the test by a series of distributed probes. The ability of the chamber to recreate a stepwise change in relative humidity in isothermal conditions was assessed as well. The average recorded time for the relative humidity to stabilise after a change in the set point was 14 min. The maximal deviation of temperature from its expected value was 0.4 K. The experimental setup is schematically summarised on Fig. 2.5.

The hygric characterisation of the fibre-reinforced mortar was conducted inside the climatic chamber according to two different pre-programmed variations of relative humidity as shown on Fig. 2.6. Each of these programs served as basis for the estimation of the water vapour permeability of the material, as explained in the following section. In both cases, a constant humidity of 50% is imposed during the first 48 h, in order to reduce the mass uptake rate before the start of the stepwise variations. Although equilibrium is not strictly reached, the mass variations at the end of these 48 h are negligible in comparison to the uptake rate after a sudden change in hygric boundary conditions.

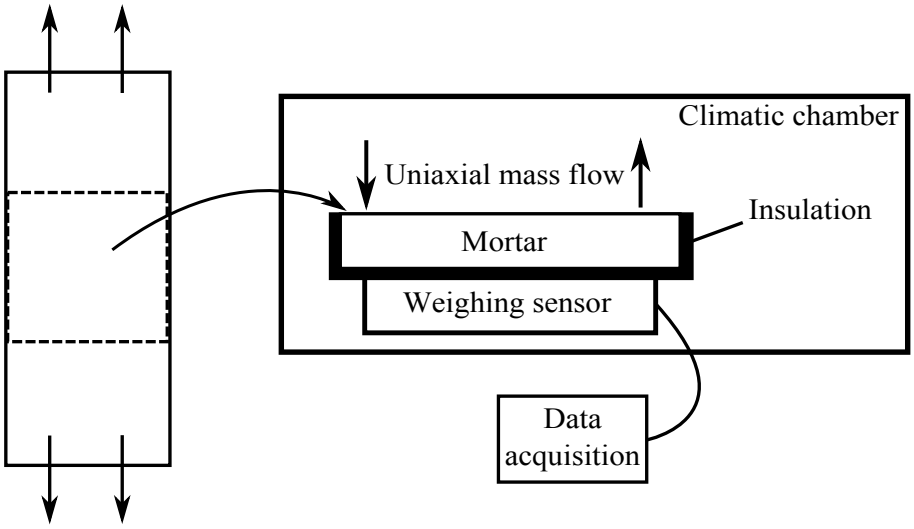

Figure 2.5: Sketch of the sample extraction from the loaded plates and *Hydrodyn* experimental setup developed in MATEIS

The first program followed the Nordtest protocol [ROD 03], which was originally proposed for the definition and experimental characterisation of the moisture buffering capacity of building materials. The purpose was to produce successions of high and low humidity phases, similar to either outdoor or indoor conditions in buildings, and to observe the rate and amplitude of the variations of moisture content in the materials. In this case, the chamber imposed cycles consisting of a high humidity step (8 h at 75% relative humidity) and a longer low humidity step (16 h at 33% RH) at a constant temperature of 23°C (see Fig. 2.6). These 24 h sequences were repeated over up to 5 days, until two successive days of measurement presented the same variations of moisture content. The recorded mass uptake in a mortar sample during steps of higher humidity was used as basis for the estimation of its permeability, as described in Sect. 2.2.2.1. This approach also gave a direct outline of the behaviour of the material in ambient humidity conditions approaching in situ building conditions.

The second program shown on Fig. 2.6 was a single step from 50 to 75% relative humidity. The recorded mass uptake as a response to this step was interpreted following Sect. 2.2.2.2. This program allows estimating the permeability, and moreover gave a theoretical value of the equilibrium water content and the surface transfer coefficient, as explained below.

Both methods are based on the assumption that the equilibrium moisture content of the material was not affected by damage. In order to confirm this hypothesis, the total mass uptake from 50% to 75%RH was measured in intact and damaged samples, in addition to the measurements of water vapour permeability. Hysteresis effects between the sorption and desorption profiles were not considered, since all permeability estimations were based on sorption measurements.

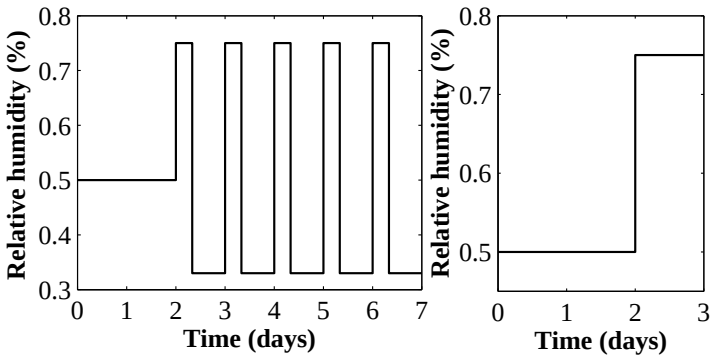

Figure 2.6: Relative humidity programs inside the climatic chamber, respectively method 1 (left) and 2 (right)

2.2 Water vapour permeability characterisation

2.2.1 Principle and notations

The mass conservation equation for water was formulated earlier (see Eq. 1.9). The term of hygric characterisation refers to the use of experimental techniques for the estimation of the moisture transport and storage properties of a material, which are required for the implementation of this equation:

- The moisture capacity $\partial w/\partial p_c$ is the slope of the moisture retention curve $w\left(p_c\right)$, which indicates the equilibrium concentration of water in the pore network for each value of capillary pressure or relative humidity.

- The transfer properties are the liquid permeability K_l (see Darcy's law, Eq. 1.11), and the vapour permeability δ_p (see Fick's law, Eq. 1.10). Alternatively, the term of moisture diffusivity D_w can be chosen, integrating transfer in both phases (see Eq. 1.15).

This target of this step of the work is to observe the effects of damage on the water vapour permeability of variously damaged mortar samples. Experimental conditions were thus set so as to simplify the estimation of δ_p:

- moisture transfer is one-dimensional,

- measurements occur in isothermal conditions, without air transfer in the material,

- no continuous liquid phase forms in the pore network,

- a narrow range of relative humidity is observed, in which hygric properties are constant.

Under these assumptions, the moisture conservation equation can be significantly simplified:

$$\frac{\xi}{p_s}\frac{\partial p_v}{\partial t} = \nabla \cdot \left(\delta_p \nabla p_v\right) \tag{2.2}$$

where $\xi = \partial w/\partial \phi$ is the slope of the sorption isotherm, or moisture capacity (ϕ being the relative humidity). The vapour exchange at the surface of a sample is described by the convective mass transfer coefficient β :

$$\delta_p \left(\nabla p_v \cdot \mathbf{n}\right) = \beta \left(p_{v,a} - p_v\right) \tag{2.3}$$

where $p_{v,a}$ is the ambient water vapour pressure and $\mathbf{n}$ the normal vector of the surface. The convective coefficient β characterises the boundary layer at the surface of the sample and is a function of multiple parameters such as the moisture concentration, the air velocity or the presence of turbulence.

The standardised methodology for vapour permeability characterisation is to measure the one-dimensional water vapour flow rate across a specimen of given thickness, by setting different values of water vapour pressure on both its sides [ISOb]. The "cup method" consists in a cylindrical material sample put on top of a cup, in which the relative humidity is set by a saturated saline solution. The cup is placed inside a climatic chamber keeping a constant RH on the other side of the sample, and successive weighings of the system give the moisture flow rate across the sample, from which the permeability is derived. An extended description of the equipment is given by [KWI 09]. This method can provide the permeability independently from the sorption isotherm and is relatively simple to implement. It is however hardly flexible as it only allows measurements in certain pre-set values of RH given by the available saline solutions. Furthermore, measurements can take several weeks or months, since moisture equilibrium must be reached at each point.

This drawback can be overcome by transient techniques, that do not require reaching equilibrium. These methods are based on analyses of the mass uptake rate of a specimen shortly after a stepwise change in ambient relative humidity. The $\sqrt{t}$-type methods [CRA 75, GAR 06, AND 08] are based on the assumption that changes in mass in the initial phase of the adsorption or desorption, are proportional to the square root of time. Other methods rely on the analytical resolution of the transport equation, under certain assumptions concerning the boundary and initial conditions [GAR 06, GAR 10]. Anderberg and Wadsö [AND 08] also propose extrapolating uptake profiles as to estimate the equilibrium moisture content at the end of the step.

Two methods were implemented here, adapted from these existing techniques as to appropriately cope with the experimental procedure described above. The first method is of the $\sqrt{t}$-type and allows measuring the permeability without knowledge of the sorption isotherm. The second method is based on an analytical resolution of the simplified moisture transport equation and allows measuring not only the permeability, but the equilibrium moisture content and convective transfer coefficient as well. The results provided by both methods, along with the equations they are based on, is summarised in Tab. 2.1.

	Method 1	Method 2
Type	$\sqrt{t}$	Analytical resolution
Results	permeability (no absolute value)	permeability equilibrium moisture content surface transfer coefficient
Equation	2.7	2.10

Table 2.1: Description of the hygric characterisation methods

2.2.2 Transient methods implementation

2.2.2.1 Method 1: square root of time

The notion of moisture buffer value (MBV) of a building material was introduced as part of the Nordtest project [ROD 03] which aimed at finding an appropriate measure for the adsorption and release of moisture by hygroscopic materials subjected to daily environmental fluctuations. The MBV is connected to the moisture effusivity b_m, which is an indicator of the rate of moisture intrusion after a sudden change of boundary conditions:

$$b_m = \sqrt{\delta_p \frac{\partial w}{\partial p_v}} = \sqrt{\frac{\delta_p \xi}{p_s}} \tag{2.4}$$

Shortly after a stepwise change in ambient relative humidity, a fairly accurate approximation is to consider the instantaneous mass uptake rate in a specimen g_m as proportional to the ratio of effusivity to the square root of time [ROD 03]:

$$g_m \propto \frac{b_m}{\sqrt{t}} \tag{2.5}$$

where t is the elapsed time since the change in the moisture boundary condition. Eq. 2.5 holds as long as the moisture penetration depth does not exceed the sample thickness. In the present study, time steps of 8 h are performed and this assumption is considered valid in regards to the expected value of the permeability and the sample thickness.

Eq. 2.5 is made possible under the assumption that relatively small humidity steps are considered, and that the moisture resistance caused by the boundary layer at the surface of the material is small in comparison to the water vapour resistance of the material itself. Under these hypotheses, it is possible to find a relation of proportionality between the measured mass uptake Δm of a sample during a humidity timestep after a time t and its permeability δ_p:

$$\frac{\Delta m}{S} = \int_0^t g_m \mathrm{d}\tau \propto \sqrt{\frac{\delta_p \xi}{p_s}} \sqrt{t} \tag{2.6}$$

where S is the exposed surface of the sample. This surface of contact with the environment is prevailing over the volume of the sample for the mass uptake rate, as long as the sample thickness exceeds the moisture penetration depth for the fluctuations at stake. Equation 2.6 states a relation of proportionality: absolute values of permeability cannot be estimated by this procedure but relative variations could be measured by comparing several samples. If we express the ratio of expression 2.6 for two material specimens represented by subscripts 1 and 2, the relation yields:

$$\frac{\delta_{p,1}}{\delta_{p,2}}\frac{\xi_1}{\xi_2} = \left(\frac{\Delta m_1}{\Delta m_2}\frac{S_2}{S_1}\right)^2 \tag{2.7}$$

It is therefore possible to estimate the relative evolution of the permeability with the development of damage compared to its value for the intact material, by supposing that the slope of the sorption isotherm ξ is not influenced by the presence of fractures. This is consistent with the usual observation that cracks do not participate in the moisture retention of a material, especially one with relatively high porosity as is the case in this study. In method 1, the permeability is computed using Eq. 2.7 after the mass uptake recorded during each period of high humidity of the Nordtest protocol (see Fig. 2.6), assuming that the moisture content distribution is close to homogeneous at the end of a low humidity step. This method however only allows estimating ratios between permeabilities of several samples, rather than their absolute values.

2.2.2.2 Method 2: analytic resolution of the transport equation

A second procedure is proposed for the derivation of δ_p from mass uptake measurements, which theoretically also allows for a simultaneous estimation of all three parameters needed for mass transfer simulations: permeability δ_p, moisture capacity ξ and convective mass transfer coefficient at the surface of the sample h_p. The method is based on an analytical resolution of the moisture transport equation under the following assumptions:

- the moisture transfer is one-dimensional
- the permeability and moisture capacity are constant in the observed humidity range
- coupling terms induced by air and heat transfer are neglected

The second hypothesis restricts the procedure to a limited interval of relative humidity, which must also not exceed a certain value above which the sorption isotherm becomes strongly non-linear. In the present case, this interval is 50%-75%. As a consequence of these simplifications, the Eq. 2.2 becomes:

$$\frac{\partial w}{\partial t} = \delta_p \frac{p_{sat}}{\xi}\frac{\partial^2 w}{\partial x^2} \tag{2.8}$$

Equation 2.8 is similar to one-dimensional heat transfer through solids and can be analytically solved [POL 05, GAR 10] for a sample of thickness L, exposed on one surface and insulated on the other, and initially placed at a uniform moisture content w_0 :

$$m = \int_0^L (w(x,t) - w_0)\,\mathrm{d}x \tag{2.9}$$

$$m = L\,\xi\,\Delta\phi\left[1 - \sum_{k=1}^{\infty} \frac{2\sin^2\delta_k}{\delta_k\,(\delta_k + \sin\delta_k\cos\delta_k)} \exp\left(-\delta_k^2 \frac{\delta_p}{\xi}\frac{p_{sat}\,t}{L^2}\right)\right] \tag{2.10}$$

where m is the mass increase by unit surface of the sample since the beginning of the humidity step $\Delta\phi$. This formulation is summed over a series of increasing numbers δ_k defined after the hygric Biot number Bi. This number is defined similarly to its thermal equivalent (see for instance [POL 05]) as a measure of the comparative influence of the surface transfer resistance to diffusion phenomena across the sample of width L:

$$\frac{\mathrm{Bi}}{\delta_k} = \tan\delta_k \tag{2.11}$$

$$\mathrm{Bi} = \frac{h_p L}{\delta_p} \tag{2.12}$$

The δ_k numbers are of decreasing influence on the result of the expression 2.10 and a sufficiently accurate result can be reached by considering only the first five terms of the series. The entire procedure for the derivation of Eq. 2.10 is shown on appendix A.2.

A Levenberg-Marquardt algorithm [MAR 63] is then applied for the estimation of the transport properties by correlating the non-linear Eq. 2.10 with mass uptake measurements by the least-squares method. This algorithm is based on the iterative resolution of the following system of equations:

$$\left[\mathbf{J}^t\mathbf{J}\right]_n \mathbf{u}_{n+1} = \mathbf{J}_n^t\left[m_{exp,i} - m(\mathbf{u}_n, t_i)\right] \tag{2.13}$$

where the subscript n indicates the iteration, $m_{exp,i}$ is a series of experimental measurements at the time coordinates t_i, $\mathbf{u}$ is the vector of the parameters (δ_p, ξ, h_p) and $\mathbf{J}$ is the matrix of the derivatives of m with respect to u:

$$\mathbf{J}_{i,j} = \frac{\partial m(\mathbf{u}, t_i)}{\partial u_j} \tag{2.14}$$

The expressions of $\partial m/\partial\delta_p$, $\partial m/\partial h_p$ and $\partial m/\partial\xi$ required in this expression can all be derived analytically from Eq. 2.10.

This procedure requires a sufficient input of mass measurements $m_{exp,i}$, preferably evenly spaced in time. It theoretically allows the calculation of all parameters influencing the water uptake rate of the specimen, but might lack of accuracy when attempting a simultaneous estimation of all three, due to the approximations. These matters will be addressed in Sec. 2.3.2.2.

2.3 Results and discussion

Each of the two methodologies presented in Sec. 2.2.2 was applied with its corresponding humidity program in order to simultaneously measure the permeability of sample series. The advantages of each method are compared and summed up as a conclusion.

2.3.1 Equilibrium moisture content

In order to confirm the assumption under which fractures have a negligible impact on the sorption isotherm of fibre-reinforced mortar, the equilibrium weight of intact and damaged specimen was measured at two humidity points (50 and 75%RH). The samples were first placed in a stable 50%RH environment until complete equilibrium was reached (defined as two identical consecutive weighings at 48 h time interval). The same measurements were then performed at 75%RH. The results are displayed in Table 2.2.

	$\overline{\Delta w}$ [kg.m^{-3}]	$\widetilde{\Delta w}$ [kg.m^{-3}]
$D = 0$ (8 samples)	6.27	0.63
$D > 0$ (6 samples)	6.12	0.47

Table 2.2: Average value $\overline{\Delta w}$ and standard deviation $\widetilde{\Delta w}$ of the equilibrium moisture content variation from 50%RH to 75%RH

These results do not form a full characterisation of the sorption isotherm, but confirm the original hypothesis, under which the moisture retention capacity of the material is not impacted by cracks. Indeed, the porosity of the studied material being relatively high, its specific area was globally not impacted by smeared cracks. These measurements also allow an other assumption: the total mass uptake under 75%RH is quite low and allowed assuming that no continuous liquid phase has appeared in the porous network, thus validating the present methodology for the estimation of the water vapour permeability.

2.3.2 Water vapour permeability

2.3.2.1 Method 1: square root of time

After a stepwise rise in ambient relative humidity, the permeability of the samples placed in the climatic chamber is proportional to the square of the slope of mass uptake versus square root of time. Such a mass uptake during one of the high humidity steps of the Nordtest protocol is shown for two samples in Fig. 2.7, along with the corresponding linear approximations.

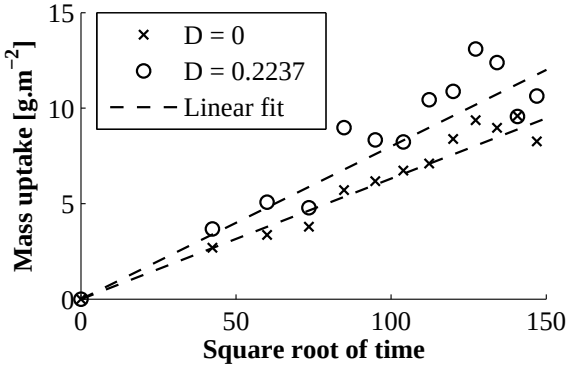

Figure 2.7: Profiles of mass uptake versus square root of time in two samples after a stepwise increase of humidity

Each time the humidity program was started, some of the scales in the chamber were occupied by non-damaged samples and the remaining scales by variously damaged samples. Each one is characterised by the ratio of its mass uptake rate to the mean mass uptake rate of the intact samples during high humidity phases of the Nordtest protocol. After 48 h at 50%RH, the protocol runs during 5 days. The value of the relative permeability is computed in all samples based on all high humidity steps of 75%RH. The result for each sample, displayed on Fig. 2.8, is the averaged permeability over these five consecutive mass uptake measurements.

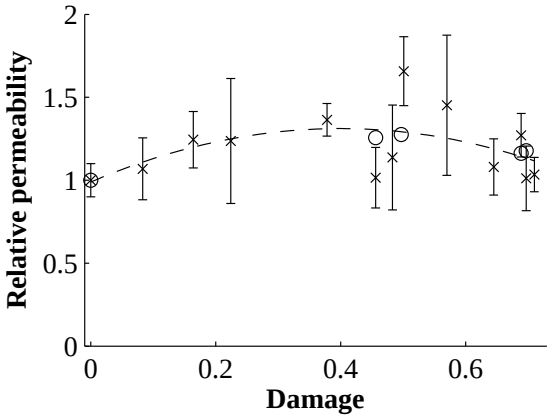

Figure 2.8: Average relative permeability calculated with method 1 (crosses) and method 2 (circles); the vertical lines show the standard deviation of method 1 over the series of measurements.

According to this definition, the value of the averaged relative permeability was set to 1 for $D = 0$. Each point of Fig. 2.8 represents one of the samples, and its relative permeability presented on the graph is the mean value for all the high humidity steps it has been subjected to. The progressive wetting and drying steps of a same series of

measurements may have an influence on the gap in mass uptake between intact and damaged samples, though such a trend was not captured here.

A trend can be observed, showing a potential permeability increase of up to 50% in the material before macroscopic fracture propagation. Although the uncertainties are quite high due to the high heterogeneity of the material and the characterisation of damage by a single value for the entire surface of the sample, measurements have shown an increase of permeability for the earlier stages of damage, followed by a decreasing trend for higher values of D. A possible explanation for this behaviour is a damage process occurring in two phases: at first, a smeared pattern of microscopic cracks, perpendicular to the exposed surface, extends through the porous network, increasing its connectivity and allowing a faster vapour adsorption in the intact parts of the material. At further loading stages, the exposed crack surface reaches a maximum value, thus no longer involving an increase in permeability. The observed subsequent decrease of permeability with increasing damage, though seemingly contradictory, can be explained by the propagation of a macroscopic fracture causing the closure of neighboring cracks, thus reversing the process of increasing pore network connectivity. The crack development in this material under compression has previously been analysed by [ELA 07] and showed similarities with such observations.

Since damage has induced an increase of up to 50% in water vapour permeability, finite volume simulations were run in order to find out whether such an increase could imply a significant change in the daily moisture content fluctuations of the material submitted to the Nordtest protocol, even when considering the sorption isotherm unchanged. The transport equation for moisture transfer was implemented into a simple algorithm using 1-D finite volume method with an implicit temporal discretisation. The setup of the simulations was the same as in the experiments (see Fig. 2.5). The humidity profile within the material was computed at each time step and summed over the domain, as to obtain the total water content per unit surface versus the time of the simulation. Results of these simulations are shown on Fig. 2.9 for a 24 h phase. Results are displayed as a mass uptake by unit surface.

The procedure is as follows: the mass profile of a raw sample ($D = 0$, crosses) is approximated by setting a value of δ_p by trial and error. The simulations are based on the previously measured value of ξ from 50 to 75%RH, and on an empirical value from 50 to 33%RH: this lower value of ξ was set so that the mass profile of the undamaged sample fitted the measurements. Therefore, eventual hysteresis effects are expected to be included by the setting of the lower value of ξ. Once a close fit was reached for the intact sample, the permeability was raised by 50% in order to simulate mass uptake in a damaged sample, which was compared to the measured mass profile in a sample of relative permeability of 1.5 ($D = 0.57$, circles).

Both simulations and experiments confirmed an increase of 50% in permeability, caused by microcracking, results in a 20% higher amplitude of the daily moisture fluctuations (denotes Δm on Fig. 2.9). It must be noted that such an increase in the amplitude of fluctuations was reached although the equilibrium moisture content was considered unchanged by any amount of damage imposed to the material.

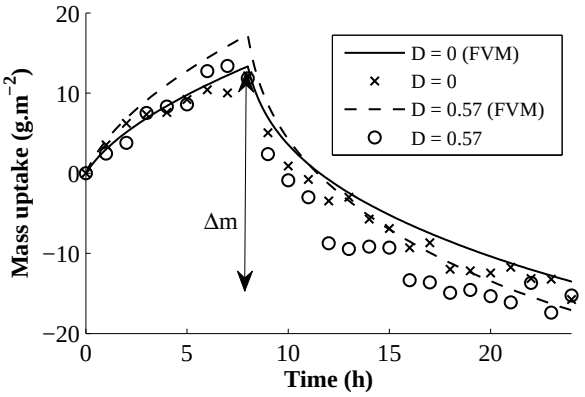

Figure 2.9: Mass measurements during one day of the Nordtest program and corresponding profiles computed by finite volume simulations

2.3.2.2 Method 2: analytic resolution of the transport equation

In addition to the study of adsorption during daily humidity cycles, the permeability was also estimated by attempting to coincide Eq. 2.10 with the measured mass uptake during a high humidity step. For this purpose, the climatic chamber program imposed a single 24 h stage of 75% relative humidity, following a supposed equilibrium state of 50%RH. These measurements are then used as an input for the Levenberg-Marquardt algorithm presented in Sect. 2.2.2.2 for an estimation attempt of (ξ, h_p, δ_p). Although the surface transfer coefficient h_p is not a material property, its value is unknown for the present experimental configuration (ventilated climatic chamber). For the sake of this methodology, the slope of the sorption isotherm ξ is considered constant in this humidity interval. This assumption is reasonable in regards to the relatively low measured value of the equilibrium moisture content at 75%RH. The procedure for calculating transfer properties consists in three steps:

1. The algorithm is first run considering all three parameters as unknown.

2. The slope of the sorption isotherm ξ is set to a known value, as it was previously measured in this humidity range, and the algorithm is then run considering the two remaining parameters as unknown.

3. The surface transfer coefficient is set to its average value calculated at step 2, and the algorithm was then finally run for the calculation of the permeability δ_p only.

The first step, simultaneous estimation of all parameters, resulted in estimates of the moisture capacity ξ far from their measured values. Such an estimation of the moisture equilibrium content based on only 24 h of measurements was found inaccurate. A similar method for simultaneous approximation of the sorption isotherm and permeability based on a stepwise change in relative humidity was recently presented by [AND 08]: the diffusion coefficient can be estimated within the first hours

of measurements from the slope of the mass uptake curve versus square root of time. The sorption isotherm however is obtained from extrapolation of the equilibrium mass before it is reached, and an early interruption of the measurements usually leads to an inaccurate estimation. Similar results are found in this study, as trying to calculate ξ from only 24 h of mass uptake measurements results in erroneous estimates of the sorption isotherm.

The second step corrects this fault by setting the value of ξ for all samples, that has been measured prior to the tests. The algorithm is then used for the estimation of the surface transfer coefficient and the moisture permeability. This simplification is made possible by the fact that the slope of the sorption isotherm is assumed to be undisturbed by the presence of cracks and therefore is not considered a function of D. Five samples were used for this step of the calculation. An increase in the water vapour permeability with increasing values of D could be noticed, although different values of β were also obtained for all samples.

The climatic chamber in which the samples are placed is well ventilated and it is likely that the surface transfer coefficient should have similar values on all samples, as it is not a material property. The recorded values of β have an average of 3.0×10^{-8} [kg.Pa^{-1}.m^{-2}.s^{-1}] and a standard deviation of 6.33×10^{-9} [kg.Pa^{-1}.m^{-2}.s^{-1}]. Therefore, it cannot be stated that the second step of the calculations results in an accurate estimation of the permeability.

The third step of the calculations is based on this average calculated value of β, and is run with δ_p as the only unknown variable. Results of this last step are shown on Table 2.3 and Fig. 2.10. They were also included in Fig. 2.8 for comparison with method 1.

D	0	0.401	0.497	0.689	0.697
δ_p ($\times 10^{-13}$ [kg.Pa^{-1}.m^{-1}.s^{-1}])	8.46	10.63	10.79	9.23	9.96

Table 2.3: Final computed values of the moisture permeability

These computations result in the same observations as in method 1: the water vapour permeability increases with moderate values of D and tends to decrease for higher values, but a clear trend cannot be observed.

2.4 Conclusion

Two methods were presented for the estimation of the influence of mechanical damage on the water vapour permeability of fibre-reinforced mortar. The main asset of these methods is to enable comparing multiple samples in which the adsorption rate is measured at the same time, without a prior knowledge of the equilibrium moisture content.

The first method, based on alternative low and high humidity steps, gave a direct estimate of the behaviour of the material placed in realistic climatic hygric conditions

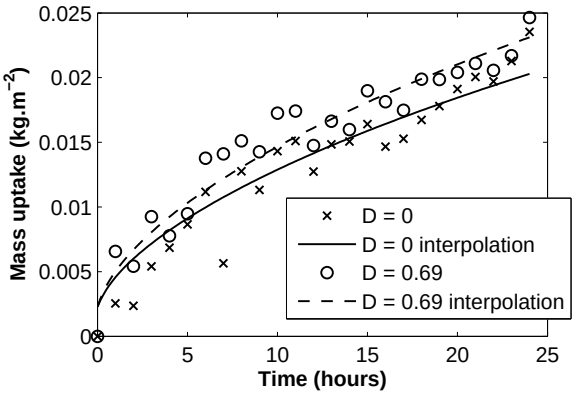

Figure 2.10: Mass uptake of damaged and undamaged samples during the first humidity step and fitting of the water vapour permeability

and allows to compare the permeability of several samples which sorption isotherm is not necessarily known. The second method is directly based on the resolution of the one-dimensional moisture transport equation and also allowed the estimation of the convective mass transfer coefficient in addition to the moisture diffusivities of the samples.

In both cases, a trend can be noticed in an increase in water vapour permeability for earlier stages of damage, followed by a plateau for medium values of D and a decrease at higher values. This can be explained by the fact that the first signs of damage occur quickly once the applied stress exceeds the elastic strength of the material, causing a drop in the global tortuosity of the porous network. Further loading then seemed to increase the width of these discontinuities rather than their number, which might explain a slower increase in permeability. At a further point in the loading process, the stress distribution within the material tends to concentrate on a single crack tip which, when propagating, will close neighboring microcracks. This caused previously opened paths for moisture to close and may explain the observed decreasing tendency for the vapour permeability at high values of damage. Loading stages beyond the peak strain have not been investigated here, but it is expected that the water vapour permeability is far less influenced by macroscopic fractures than the liquid conductivity, which can rise on several orders of magnitude between intact and cracked samples.

The increase rate of δ_p with the damage value is most likely to be influenced by the nature of the material itself, as the degradation of the elastic modulus can be caused by various forms of microstructural dislocations or, in the case of cementitious materials, of interfacial debondings. The particular formulation of mortar used in this study was specifically designed as to be less brittle as standard cement paste and to present an important diffuse damage before failure. The observable increase in water vapour permeability might therefore occur differently for other cementitious materials. Such results are also to be related to measurements of liquid permeability of fractured concrete, of which aim and conclusions are similar[CHO 07, HOS 09]: the effects of mi-

crocracking on transport coefficients, although not negligible, depend on the material and on the type of loading.

These results confirmed the prognosis formulated at the end of the bibliographic study: the use of a single macroscopic damage variable may only allow a coarse description of diffusely damaged media and their permeability. Such a simple description of damage cannot properly capture all geometrical properties of the cracks, that may influence moisture and heat flows. These properties become essential for the modelling of flow in macroscopic fracture networks that may develop in construction materials. To this aim, a reliable crack characterisation technique at the building scale must be found: this is the subject of the following part of the manuscript.

Chapter 3

Non-destructive damage monitoring

Digital image correlation (DIC) and acoustic emission (AE) monitoring were simultaneously performed during tensile loading tests of fibre reinforced mortar samples. The full-field displacement mappings obtained by DIC revealed all ranges of cracks, from microscopic to macroscopic, and an image processing procedure was conducted as to quantify their evolution in the course of the degradation of the samples. The comparison of these measurements with the acoustic activity of the material showed a fair match in terms of quantification and localisation of damage. It is shown that after such a calibration procedure, AE monitoring can be autonomously used for the characterisation of damage and fractures at larger scales.

Contents

The importance of fracture and damage observation techniques for the understanding and prediction of fluid flow has already been underlined. Establishing a procedure for reliable measurements of crack patterns is essential to the present work, as the upcoming transfer simulations will rely on experimental fracture data rather than on damage modelling and failure prediction. An important requirement of these measurements is to provide damage mappings as well as geometrical characteristics of macroscopic fractures, in order to allow implementation of either continuum or discrete models. In the following, we chose the terms of damage monitoring to describe measurements taking place during material degradation, and of crack detection if measurements are performed after degradation. As previously reviewed in Sec. 1.3.1.2, three main classes of methods can be considered: post-damage imaging, displacement mapping, and acoustic emission.

Imaging techniques for crack detection include X-ray radiography and tomography [SLA 63, TOD 04] for three-dimensional fracture observation [LAN 03] or propagation monitoring [LAN 07]. The detection of pre-existing cracks can be facilitated by impregnation techniques [HOR 96] allowing their automatic detection and quantification [AMM 00] by microscopic examinations. While these techniques may have a good resolution and precision, they are limited in terms of specimen size and thus not applicable at the building scale. Another possible method for such large scale applications is the recording of elastic wave velocities, which can for instance be applied to durability studies or to repair work assessments [SHI 09].

Displacement mapping techniques are applicable to damage monitoring, and consist in measuring local displacements of a sample during its deformation. Electronic speckle pattern interferometry [JIA 94, SHA 99] and digital image correlation (DIC) [SUT 83] are optical non-destructive techniques and can be used for the observation of the progressive crack development, or more generally of two-dimensional strain mapping. Optical methods have also been recently extended to three-dimensional displacement and strain fields [ORT 09, CHA 10a].

A third category of damage monitoring methods includes the recording of acoustic emissions (AE). In a material under loading, elastic waves are emitted as a consequence of crack initiation and propagation. Recording and analysis of acoustic activity is of great importance in the fields of seismology and civil engineering. Among others, it has been used for damage estimation of concrete [OHT 01, COL 03, SUZ 04], identification of damage mechanisms [PHI 98, GOD 04, GOD 06, ELA 07, OHN 10, MOM 12], estimation of the fracture energy [MUR 10] or failure prediction [SHI 94, MOM 10, MAI 12].

The present step of the study aims at investigating which technique may be applicable for *in situ* damage identification in building components. Acoustic emission and other wave propagation measurement techniques are the most preferable methods for large scale damage monitoring, but the interpretation of recorded waveforms requires preliminary studies. Digital image correlation and acoustic emission recording were simultaneously performed during tensile loading of fibre reinforced mortar samples. The methodology aims at correcting the downsides of two techniques by combining them: the applicability of optical techniques hardly extends to field studies, while the

interpretation of AE measurements is difficult without a view of the crack evolution. A methodology is presented, which allows interpreting acoustic signals on the basis of a previous characterisation. Mortar samples were loaded by uniaxial tension while the local displacements of their surface were monitored by a camera, and the acoustic activity was recorded by sensors placed around the damaged area. By correlating the data gathered by the two techniques during this lab experiment, it is possible to interpret field AE measurements with more clarity. The main target is therefore to calibrate the AE technique, so that it can be autonomously used for damage monitoring of building components [ROU 13].

3.1 Methodology

3.1.1 Experimental setup

The experimental setup is based on the same formulation of fibre reinforced mortar as in the preliminary study. Its elaboration process is described in Sec. 2.1.1. The prismatic samples were notched as to ensure stress concentration on a relatively small area during mechanical loading, on which the observation was focused. Tensile loading was applied along the vertical axis, using a 5 kN force cell imposing a constant displacement speed of 1 mm/min. The tests were carried out until complete failure of the specimen. The setup of the samples and of the observation equipment is displayed on Fig. 3.1.

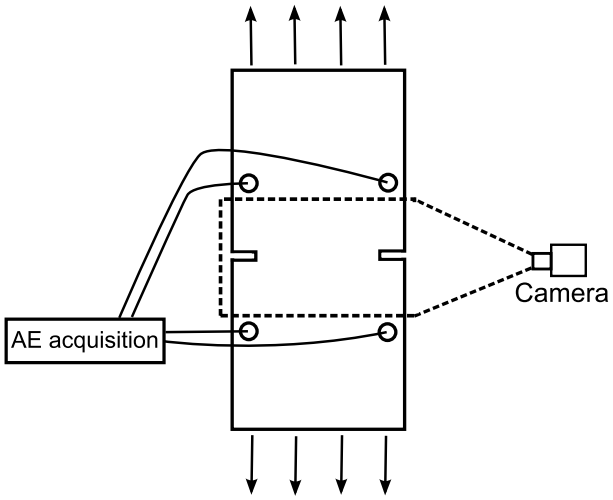

Figure 3.1: Experimental setup for tensile loading and damage monitoring

The experimental setup includes a CCD camera with a fixed 2.8 focal ratio, focused on the surroundings of the notch. Because of the shallow depth of field of the camera in this configuration, the focus is manually fixed as to prevent an automatic adjustment of the lens during the tests. The camera was positioned as to cover an observation

zone of 101×67 mm with a spatial resolution of 22 μm/pixel. A non-uniform speckle pattern was applied on the specimen surface with a black paint spray as to facilitate the procedure of the correlation algorithm: this ensures that the initial gray-scale level distribution is close to random. Pictures were taken at time intervals of 5 or 10 seconds in order to allow computation of the displacement mappings during successive stages of loading. The camera was used as an optical extensometer to monitor the macroscopic strain in the direction of loading. The material presents some ductility before the peak of loading [ROU 12a], followed by a strain-softening behaviour during which crack propagation is slowed by the presence of fibres. This behaviour enabled the progressive damage monitoring by acoustic and optical measurements.

In addition to the optical monitoring apparatus, four Micro-80 acoustic sensors were placed around the monitored area of the specimen, continuously recording the AE activity during damage and fracture propagation. The sensors form a 80 × 70 mm (height×width) area and are connected via pre-amplifiers to a MISTRAS data acquisition system. They have a diameter of 8 mm, and are characterised by the position of their center. The settings of the AE recording setup are detailed below.

The methodology has been applied on a series of samples, 6 of which showed suitable for data interpretation (i.e. stress concentration and fracture occured in the observation area). Results are presented in two parts: first, the ability of digital image correlation for the observation of fracture patterns is assessed (Sec. 3.2). Strain mappings are calculated by the DIC algorithm and a procedure is explained for observing the evolution of crack size distributions during tensile tests. In the second part (Sec. 3.3), these optical measurements serve as a basis for the interpretation of AE recordings. Measurements performed on all samples were used to establish the ability of AE to quantify, locate and identifty damage and fractures.

3.1.2 Digital image correlation

Optical techniques such as DIC are non-destructive and therefore do not disturb eventual further testing on the samples. DIC provides a full map of the deformations at the surface of a specimen and allows following the fracture development without restriction of number or size of the cracks. It also presents the advantage of being easily implemented into most experimental setups, requiring no strict operating conditions or time consuming preparation, nor does it require gauges in contact with the specimen which might interfere with the experiment. The technique enables full field measurements of the local displacements of a sample's surface. It has been used for the estimation of stress intensity factors near crack tips [RET 05, ROU 06] or the identification of elastic properties [HIL 06] or damage laws [LEP 10], among other uses. The technique has also been proven suitable for the observation of local displacements of brittle building materials such as concrete [CHO 97, COR 07, ROU 12b], and of cracking due to drying shrinkage in coating mortar [MAU 12]. The principle of DIC is briefly summed up below. For a more complete view of its theory and applications, one can refer to a recent book on the subject [SUT 09].

The principle of digital image correlation is the conservation of the optical flow between two pictures of a specimen, taken at different stages of its deformation [SUT 83]: it lies on the assumption that two consecutive images contain the same total amount of each gray-scale level, and are only distinguished by their spatial distributions. The planar displacement $\mathbf{u}(\mathbf{x})$ at each pixel of coordinates $\mathbf{x}$ of a surface is defined as:

$$g(\mathbf{x}+\mathbf{u}) = f(\mathbf{x}) \tag{3.1}$$

where f is the distribution of gray-scale level, or the texture, of a reference image, typically taken at the start of the mechanical loading, and g is that of a deformed image. Eq. 3.1 means that the gray-scale level of a pixel of coordinates $\mathbf{x}$ on the initial image f is equal to that of a pixel of coordinates $\mathbf{x}+\mathbf{u}$ on the final image g, i.e. that this pixel has been displaced by a vector $\mathbf{u}$. The exact displacement field $\mathbf{u}(\mathbf{x})$ can generally not be explicitely calculated without additional assumptions of regularity. In the prospects of the numerical resolution of Eq. 3.1, the functional ϕ, operating on displacement fields, is defined:

$$\phi(\mathbf{v}) = \iint \left(g(\mathbf{v}+\mathbf{x}) - f(\mathbf{x})\right)^2 \mathrm{d}\mathbf{x} \tag{3.2}$$

where $\mathbf{v}$ is an approximation of the solution $\mathbf{u}$, and is constructed as a linear combination of functions v_i:

$$\mathbf{v}(\mathbf{x}) = \sum N_i(\mathbf{x})\, v_i \tag{3.3}$$

where N_i are chosen basis functions (typically bilinear functions of $\mathbf{x}$). The target is to determine the best possible approximation by minimising the value of ϕ on all elements of the grid. Assuming a certain smoothness of the investigated displacement field, g is replaced by its first-order Taylor expansion in Eq. 3.2, resulting in:

$$\left[\iint \left(\nabla g(\mathbf{v}+\mathbf{x}) \otimes \nabla g(\mathbf{v}+\mathbf{x})\right) : \left(N_j \otimes N_i\right) \mathrm{d}x\right] v_i = \iint \left(f(\mathbf{x}) - g(\mathbf{x})\right) \nabla g(\mathbf{x})\, N_i(\mathbf{x})\, \mathrm{d}\mathbf{x} \tag{3.4}$$

Since f, g and $N_i(\mathbf{x})$ are known, Eq. 3.4 is a linear system of unknowns v_i, from which the approximate displacement field $\mathbf{v}$ can be obtained. Understandably, the choice of the basis functions $N_i(\mathbf{x})$ is important for a good approximation of the displacement field, and several options have been presented in the literature for different types of mechanical tests. In the present case, the computation of the displacements is achieved with the Icasoft software[1], which uses bilinear finite element shape functions. The displacement field is analysed by dividing the image into grid elements, each of which is assigned two displacement components in the decomposition of Eq. 3.3. The result of Eq. 3.4 is a rough estimate of the real solution, since it only computes an integer number of pixels for the displacement fields. Subpixel displacements can be determined by interpolating the displacement fields between elements of the grid with bilinear or spline functions [HIL 06].

The result of the algorithm is an approximation of the displacement field $\mathbf{u}$ of each point of the surface. While gradients of $\mathbf{u}$ define the strain fields, a local displacement

[1] Icasoft Digital Image Correlation Software - http://icasoft.insa-lyon.fr/

jump indicates a discontinuity that appeared after the reference image was taken: in quasi-brittle materials, it translates as a crack of measurable aperture.

3.1.3 Acoustic emission

3.1.3.1 Principle

In a material under loading, elastic waves are emitted as a consequence of microstructural dislocations or crack propagation suddenly releasing stored energy. An AE hit occurs as a signal captured by a sensor exceeds a pre-set threshold value of amplitude. The successive peaks of amplitude shape the waveform of the signal, as long as they occur within a small enough time frame. Three timing parameters (peak definition time, hit definition time and hit lockout time) are set for distinguishing signals from an uninterrupted AE stream. The result of the measurement procedure is a set of temporally separated AE hits being captured during the recording process. In the present study, the interpretation of these measurements is threefold: we investigated how AE signals can be used for damage quantification, localisation and identification.

Quantitative damage estimations consist in measuring the mechanical degradation state of a material sample on the basis of the number of recorded AE signals, or on their generation rate. Ohtsu and Watanabe [OHT 01] performed such a diagnostic procedure on concrete samples and established a relationship between the AE emission rate and damage evolution. Similar analyses were later carried out by Suzuki and Ohtsu [SUZ 04], among others.

It is also possible to locate the source of a signal by placing several sensors in contact of a specimen. When the propagation speed of AE waves in the given material is known, the different arrival times of a same hit at each sensor enables the localisation. The source can be located on a 1D axis with two sensors, on a plane with three and in 3D with four. Examples of 2D or 3D crack and damage localisation include [GRA 07, OHN 10] and generally employ more sensors than strictly necessary, for accuracy purposes. In the following, the term of AE event denotes a hit received by all sensors placed on the sample.

3.1.3.2 Settings

The propagation speed of acoustic waves in each material sample was measured prior to the tests with the lead breaking procedure: a repeatable AE wave is generated on the specimen surface by breaking pencil leads and measuring the difference in arrival times between sensors. This method also allows measuring the attenuation of the material, i.e. the amplitude decrease of a wave per unit length. The average measured values of the propagation speed and attenuation coefficient are shown on Tab. 3.1, along with the settings of the AE recording system.

During mechanical tests, four AE sensors were placed on the specimen as shown on Fig. 3.1, forming a 80×70 mm area. The acquisition system records the waveform

Preamplifier gain	40 dB
Threshold of detection	32 dB
Peak definition time	50 μs
Hit definition time	100 μs
Hit lockout time	1000 μs
Propagation speed	2313440 mm.s^{-1}
Attenuation	0.25 dB.mm^{-1}

Table 3.1: Settings of the AE acquisition system

of all AE hits received by all sensors. When a signal is captured by three or more sensors within a small enough time frame, a localisation algorithm is run as to calculate the 2-dimensional coordinates of its source. In case of a signal captured by four sensors, the calculation is repeated for all combinations of three, and the final result is the averaged value of all combinations. The following usual assumptions are made for simplifications purposes: the specimen thickness is neglected, AE propagation speed is uniform and constant (not influenced by damage). Because of these assumptions, and of the heterogeneity of the material, uncertainties are expected in the results of the localisation process.

3.1.3.3 2D signal localisation

Principle

The present paragraph describes the numerical procedure for the localisation of AE sources, based on the arrival time of the emitted waves at each sensor placed on a sample surface. Fig. 3.2 serves as a pictural support for the following explanations.

When a hit is detected by two sensors, the distance from the source M to each of these sensors, A and B, is related to the difference between the two arrival times of the wave t_A and t_B

$$\mathrm{MB} - \mathrm{MA} = (t_B - t_A)\ V \tag{3.5}$$

where V is the propagation speed of AE waves in the medium, and was measured prior to the tests. This is the equation of a hyperbola branch of parameters a, b, c and eccentricity e defined as such:

$$a = \frac{(t_B - t_A)\ V}{2}\,; \quad b = \sqrt{c^2 - a^2}\,; \quad c = \mathrm{AB}\,; \quad e = \frac{c}{a} \tag{3.6}$$

assuming the wave reaches A before B. If the AB segment forms an angle θ with the first coordinate axis and its midpoint is denoted I, as is pictured on Fig. 3.2(a), the

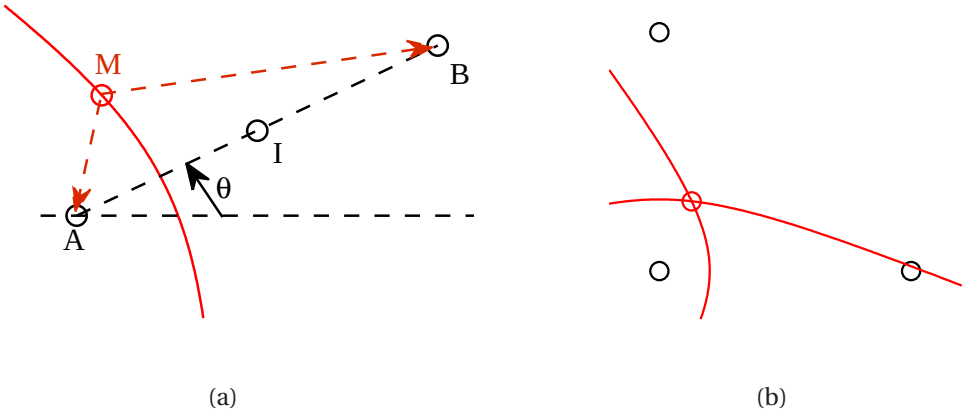

(a) (b)

Figure 3.2: Localisation of an AE source after a signal has been captured by 2 sensors (a) or 3 (b)

hyperbola branch can be described by means of the following parametric equations:

$$\begin{pmatrix} x \\ y \end{pmatrix} = \begin{pmatrix} x_I \\ y_I \end{pmatrix} + \begin{pmatrix} \cos\theta & -\sin\theta \\ \sin\theta & \cos\theta \end{pmatrix} \begin{pmatrix} -a\cosh t \\ b\sinh t \end{pmatrix} \tag{3.7}$$

Therefore, if an AE wave is detected by only two sensors, its source can not be precisely located, as it can range over an entire branch of the hyperbola (the minus sign in the last term of Eq. 3.7 indicates that it can only belong on the branch surrounding the first sensor). The spatial coordinates of the source (x, y) are expressed after one parameter t, that is only bounded by the size of the specimen. However, if the wave is captured by three sensors, Eq. 3.5 can be written twice, defining two hyperbola branches, of which intersection indicates the origin of the AE signal as shown on Fig. 3.2(b).

$$\begin{pmatrix} x_{I_1} \\ y_{I_1} \end{pmatrix} + \begin{pmatrix} \cos\theta_1 & -\sin\theta_1 \\ \sin\theta_1 & \cos\theta_1 \end{pmatrix} \begin{pmatrix} -a_1\cosh t_1 \\ b_1\sinh t_1 \end{pmatrix} = \begin{pmatrix} x_{I_2} \\ y_{I_2} \end{pmatrix} + \begin{pmatrix} \cos\theta_2 & -\sin\theta_2 \\ \sin\theta_2 & \cos\theta_2 \end{pmatrix} \begin{pmatrix} -a_2\cosh t_2 \\ b_2\sinh t_2 \end{pmatrix} \tag{3.8}$$

Accuracy assessment

An accuracy test of the signal localisation algorithm was performed prior to the mechanical loading tests. First, the isotropy of the material in regards to the propagation speed was confirmed. Then, sensors were placed on a specimen surface and pencil leads were broken on a set of test points. Five lead breaks were performed on each of the five test points. Pencil breaks have a high energy release and are easily distinguishable from background noise: weaker events were filtered out, and stronger ones were localised. The results are shown on Fig. 3.3.

The accuracy of the localisation algorithm is estimated by comparing the exact origins of the signals (the test points) with the computed ones: the overall precision of the

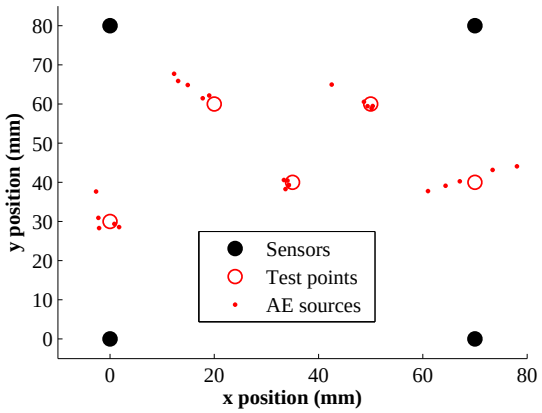

Figure 3.3: Accuracy testing of the localisation procedure

results is satisfactory but irregular. Acoustic waves generated in the center of the monitored area are the most accurately located. Inversely, signals originating from the sides of the monitored area are found with less precision. The material is indeed heterogeneous and the propagation speed may exhibit local variations due to variable pore and grain sizes [ROU 12a]. The accuracy of the algorithm is however considered sufficient for the purpose of the study.

3.2 Imaging results

All material samples were loaded as described above and pictures of their surfaces were taken at time intervals of 5 or 10 seconds during loading. For purposes of clarity, the procedure for extracting the crack size distributions from the optical measurements is illustrated with one of the samples (later labeled as sample 1). The results are then displayed for all samples on Fig. 3.7.

The correlation algorithm works by applying Eq. 3.4 to the reference image f (taken at the beginning of the loading process) and the deformed image g (taken during loading), in order to compute the displacement field over a grid on the specimen surface. Fig. 3.4 shows the image of the sample surface from the CCD camera shortly after crack initiation, before its input into the correlation algorithm. The calculation area of the DIC algorithm is delimited by the notches and shown by the red dotted line.

The influence of the grid size on the accuracy of the subpixel interpolation algorithm has been studied by many authors (see for instance [BES 06, HIL 06]). With the settings of the present work, i.e. a grid composed of 8×8 pixel elements, performance estimations show a possible accuracy of 10^{-1} to 10^{-2} pixel for the computation of the displacement fields: in the present case, the displacement uncertainty is under 1 μm. An example of strain mapping resulting from the correlation procedure is shown on Fig. 3.5, on which the gray scale levels indicate the local value of the longitudinal strain in the direction of loading.

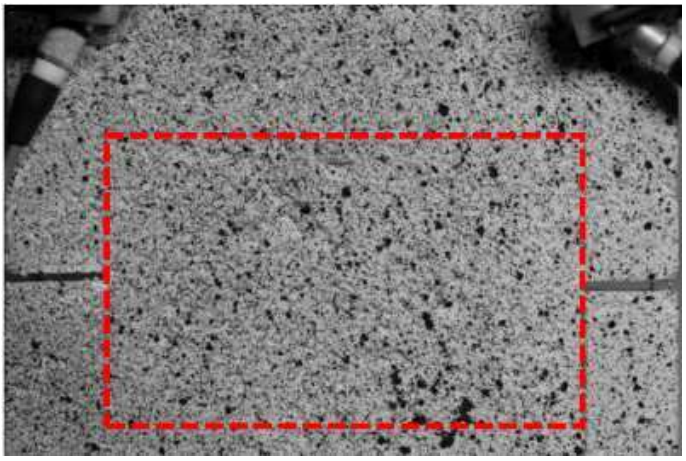

Figure 3.4: Original picture in 8-bit gray scale showing the input area of the DIC algorithm

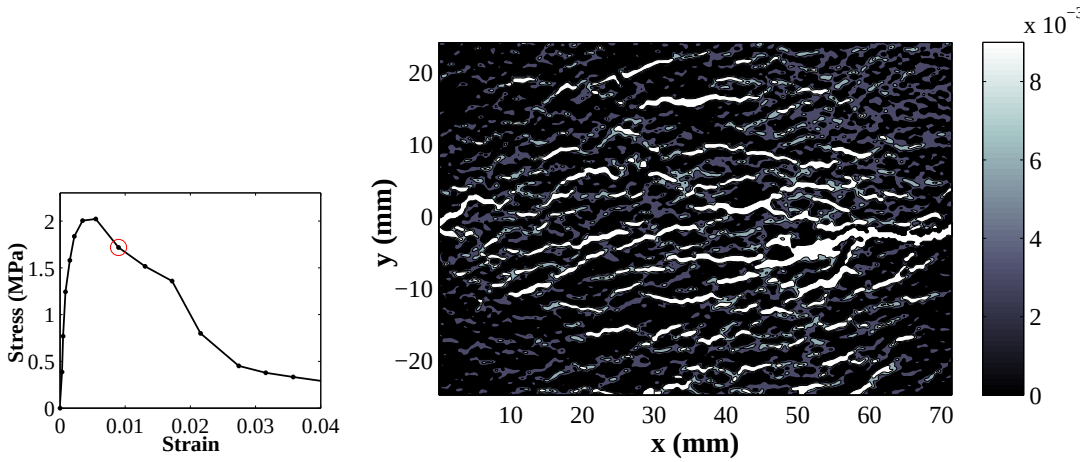

Figure 3.5: Example of a longitudinal strain mapping

This local strain value is the gradient of displacement between adjacent pixels. Since the material is quasi-brittle, locally high values indicate the presence of cracks. These cracks originate from the tips of the notches ($y = 0$ mm, $x = 0$ or 70 mm) and spread on a relatively large area of over 40 mm height. The present example shows the state of the sample surface shortly after the initiation of a macroscopic fracture (see Fig. 3.5(a)). The displayed strain mapping (Fig. 3.5(b)) therefore includes cracks of a wide range of apertures.

On the basis of these full field strain mappings, a methodology is proposed and implemented to measure the aperture and total length of all cracks appearing on the sample surface: successive thresholds were applied on each strain mapping, as to only display cracks exceeding certain values of aperture. Image processing of the resulting profiles allowed measuring the total developed crack length in each width interval. An

example of this procedure is shown on Fig. 3.6

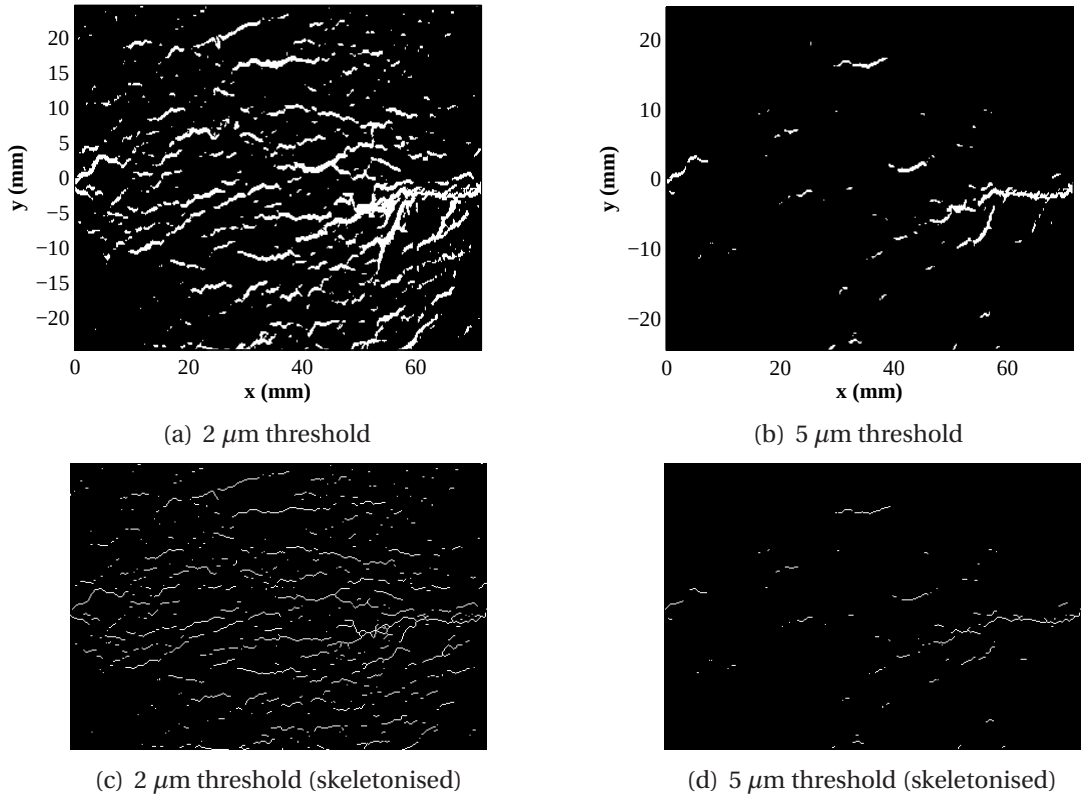

(a) 2 μm threshold

(b) 5 μm threshold

(c) 2 μm threshold (skeletonised)

(d) 5 μm threshold (skeletonised)

Figure 3.6: Image processing procedure for the measurement of crack size distributions: thresholds of 2 μm (left) and 5 μm (right)

Fig. 3.6(a) and 3.6(b) show the strain mapping 3.5 once it has been thresholded as to only display discontinuities of over 2 μm and 5 μm, respectively. The appearing patterns were processed by topological skeletonisation in order to reveal cracks as tortuous linear paths: the skeleton of a shape is a thin version that is equidistant to its boundaries, and preserves its main geometrical properties, such as its length, connectivity and direction. The ImageJ software was used for this process. As an example, its applicaton to the distributions showed on Fig. 3.6(a) and 3.6(b) are respectively on Fig. 3.6(c) and 3.6(d). The resulting paths are measurable, and the substraction of the total visible crack length of Fig. 3.6(c) by that of Fig. 3.6(d) gives the amount of cracks of which aperture w is in this interval. The procedure was performed on each successive strain mapping of each specimen, for a set of threshold values allowing separating microcracks from larger fractures: 3, 5, 10, and 50 μm. The results are shown on Fig. 3.7.

These results are displayed as total visible crack length in each aperture interval, per square meter of specimen surface, as a function of the progression of the mechanical loading process. This progression is quantified by ϵ/ϵ_{peak}, where ϵ_{peak} indicates the

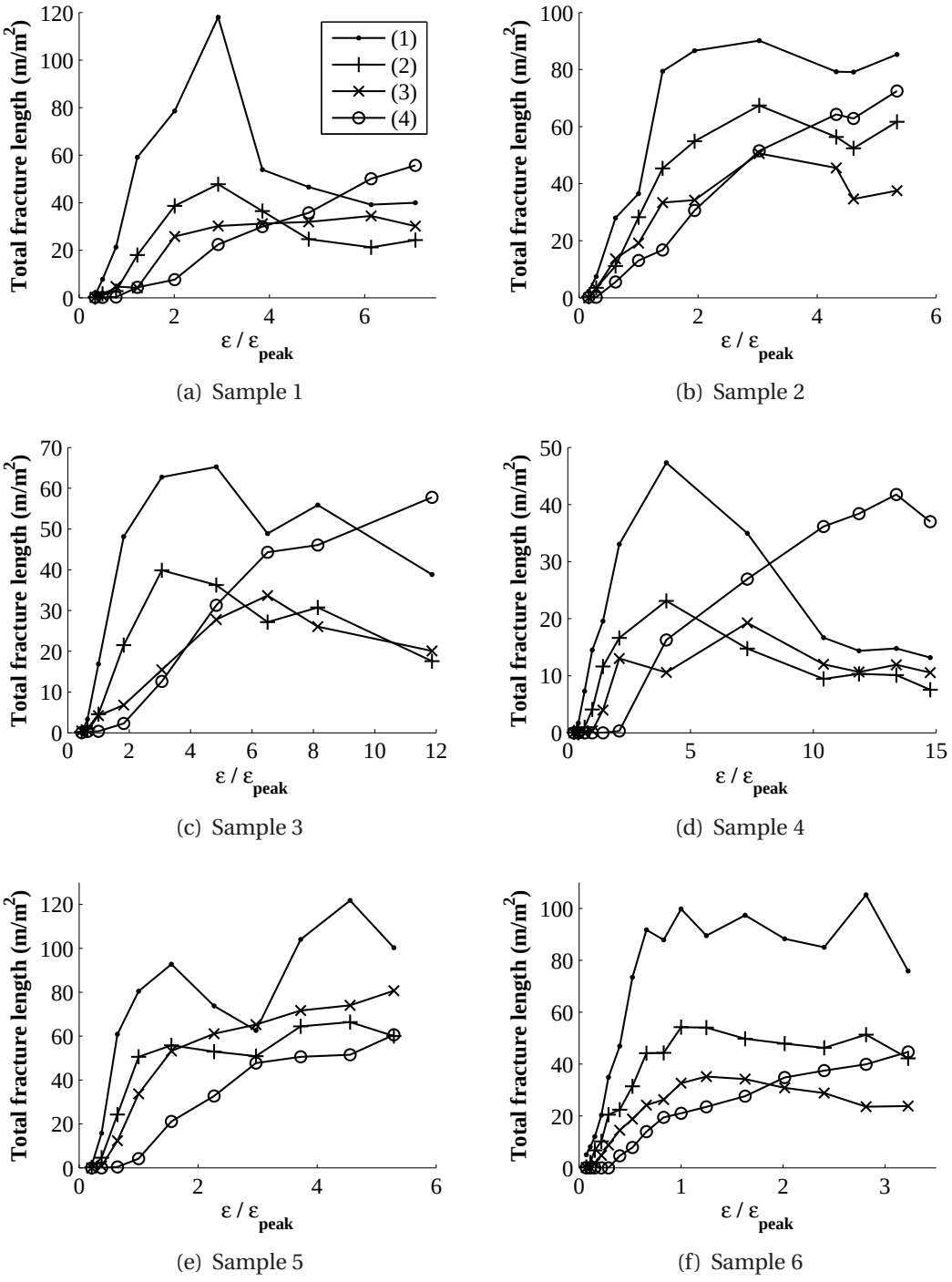

(a) Sample 1

(b) Sample 2

(c) Sample 3

(d) Sample 4

(e) Sample 5

(f) Sample 6

Figure 3.7: Visible fracture length per square meter of sample surface : (1) $3 \leq w < 5$ μm, (2) $5 \leq w < 10$ μm, (3) $10 \leq w < 50$ μm, (4) $w \geq 50$ μm

value of peak strain. The observation was limited to crack apertures exceeding 3 μm, as smaller strain values may be difficult to distinguish from the background noise of the mappings. Two observations can be made on the basis of these profiles:

- Smaller crack ranges always appear first during loading. The development of successive ranges of aperture follows the same order, from smaller to larger cracks. While this observation was to be expected, the clear visualisation of this succession indicates the validity of the methodology for quantifying cracks by ranges of size.
- In most samples, the smaller ranges of fissures reach a maximum around $\epsilon/\epsilon_{peak} = 3$ to 4, before decreasing. This phenomenon is caused by the presence of a macroscopic fracture, that initiates around $\epsilon = \epsilon_{peak}$. The opening of this fracture causes neighboring cracks to close, decreasing the total length of the smaller scales.

In addition to these results, a specific fracture area A_{frac} was defined as such:

$$A_{frac}(t) = \sum_i \overline{w}_i l_i(t) \tag{3.9}$$

where the subscript i ranges over the number of aperture subsystems measured by the image processing procedure. $\overline{w}_i$ is the mean crack width of the corresponding subsystem and l_i its specific length, i.e. the ordinate of Fig. 3.7. The specific fracture area is therefore a summation of the visible lengths of all intervals, weighted by their respective openings. For the purpose of this calculation, the amount of aperture subsystems is greater than that displayed on Fig. 3.7: ranges were defined between values of 2, 3, 5, 10, 50 and 100 μm. A_{frac} is non-dimensional and represents the ratio of visible sample surface occupied by cracks. The purpose of defining this quantity is the comparison of DIC and AE results, as explained below.

These measurements show that digital image correlation allows measuring all geometrical characteristics of cracks that may influence fluid flow in a construction material. With a relatively simple experimental setup, and the appropriate set of tools for image processing, the progressive opening and closing of discontinuities can be quantified without restriction of number or density. Although it is limited to 2-dimensional observations in the present case, the technique is therefore suitable to serve as a basis for the understanding of acoustic signals recordings. The following section shows how DIC can be used for the calibration of AE measurements, so that this technique can be autonomously used for damage monitoring of building components.

3.3 Interpretation of acoustic emission

3.3.1 Damage quantification

First, an attempt of global damage quantification was made on the basis of the total AE activity. This activity is represented by the number of localised AE events, i.e. signals

received by three or more sensors. Noise effects are therefore expected to be reduced, as low-energy, non-localisable AE hits are not accounted for. Fig. 3.8 depicts the cumulative number of AE events and the loading profile of each sample.

Acoustic signals start emitting before the peak of loading at a slow rate. The recorded acoustic energy in this interval is low, and few signals can be captured as the material's acoustic attenuation is relatively high (approximately 0.25 dB.mm^{-1}). These signals are emitted as a consequence of the previously observed microcracking. The profiles of cumulative AE events then increase significantly after peak strain: on all tests, high AE rates can be seen to occur simultaneously with sudden stress drops caused by crack propagation.

As a consequence of this observation, an attempt was made to correlate the total amount of visible fractures, previously observed by optical measurements, with the cumulated AE activity at each time of loading. For all available data points, the value of A_{frac} was compared with the cumulated AE activity at the corresponding time of the test. Fig. 3.9 shows this comparison over all strain mappings captured during loading of all samples, representing a total of 83 data points.

It has already been found [OHT 01, SUZ 04] that the AE rate can give a quantitative indication on the damage level of construction materials. This is confirmed in the present case: the profile of fracture specific surface A_{frac} versus cumulated AE events N can be roughly approximated by a power law (see Fig. 3.9), resulting in a correlation coefficient of $R^2 = 0.9236$ between the results of both techniques (DIC and AE). Such an agreement is quite satisfactory, considering that the two techniques rely on very different physical principles. A connection was established between the amount of cracks appearing on the surface of the specimen and the rate at which elastic waves are released in the medium under tension. This observation confirms that AE can be used for damage quantification of building components with fair accuracy, once it has been calibrated by a method such as digital image correlation.

3.3.2 Damage localisation

The previous section addressed the matter of global damage quantification, and showed a connection between the cumulated number of AE events and the total opening of fractures. The resulting empiric evolution law, however, does not separate or identify cracks of different sizes, nor does it allow their localisation. The present section addresses the latter question by applying the localisation procedure, of which accuracy was previously assessed. In addition to the set of variables describing its waveform, each AE signal is assigned one temporal and two spatial coordinates. All localised sources were then superimposed with the strain mappings computed by the DIC algorithm. Fig. 3.10 shows the example of five successive stages of a sample, indicated on its loading profile 3.10(a).

The first image (Fig. 3.10(b)) depicts the sample surface at the stress peak, at the time of initiation of a macroscopic crack. The red dots depict all AE sources that have been located from the beginning of the test. As can be seen on Fig. 3.8, the cumulative

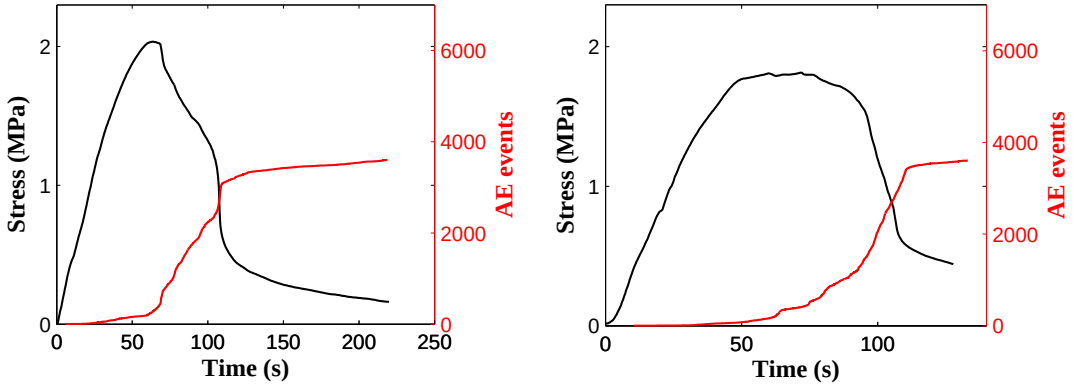

(a) Sample 1

(b) Sample 2

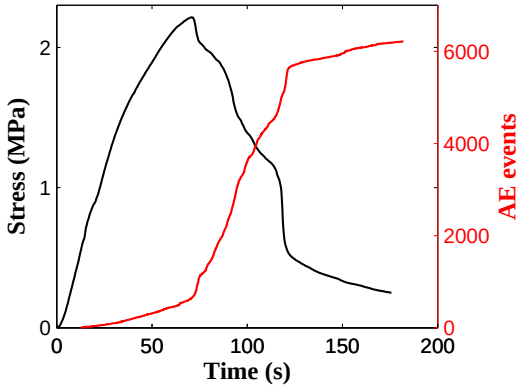

(c) Sample 3

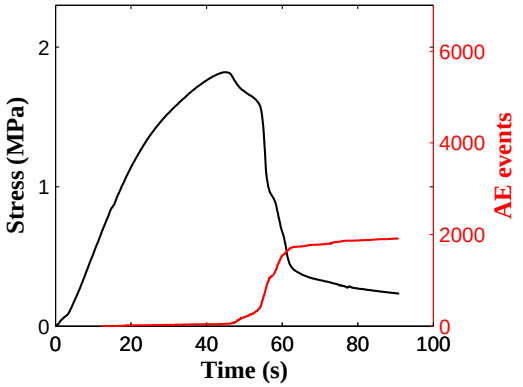

(d) Sample 4

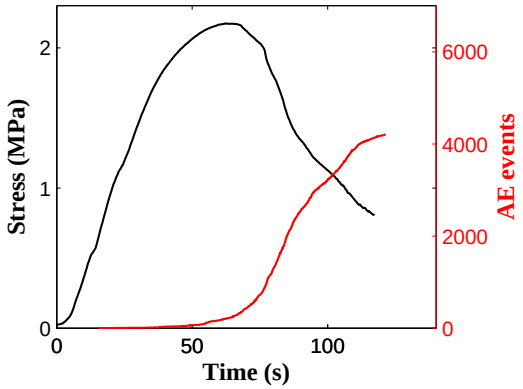

(e) Sample 5

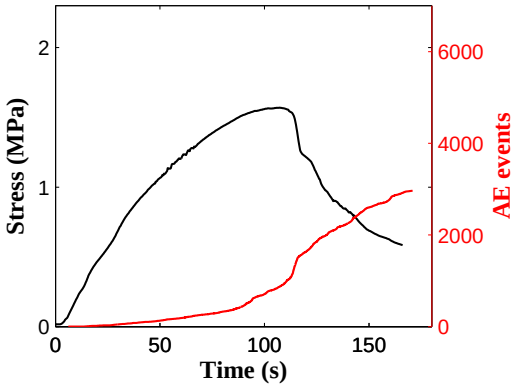

(f) Sample 6

Figure 3.8: Stress-strain profiles and cumulative AE signal distributions

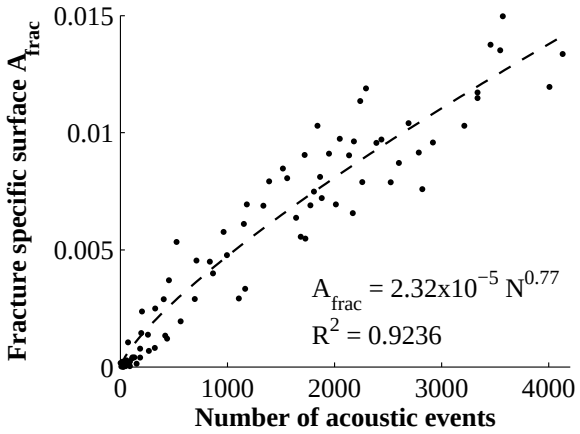

Figure 3.9: Fracture specific surface versus number of recorded acoustic events, and power law approximation

number of AE events is still low at this point. A moderate concentration of signals originates from a relatively large area around the fracture process zone, and occurs mostly ahead of the crack tip. After this point of the loading process, a higher emission rate is recorded during macroscopic crack expansion. Fig. 3.10(c) to 3.10(f) show the state of the sample surface during its propagation. This propagation generates significantly higher concentrations of AE signals, that follow the crack trajectory.

The spatial correlation of both techniques is quite satisfying : most AE sources were located in areas of high strain, and their progress through the width of the sample is coordinated with the optically recorded crack propagation. The localisation procedure is however not flawless, as showed in the previous paragraph. This can explain the imperfect match between spots of high AE concentration and crack patterns. An other possibility is the fact that DIC only captures discontinuities that appear on the specimen surface, while AE sources originate from the entire volume. This matter is however minimised by the small thickness of the sample.

These measurements were carried out on all tested samples, and led to similar results. An important outcome of this procedure is the observation that AE signals seem to occur in two phases during the entire damage and fracture process. First, a moderate number of spatially scattered waves can be recorded as the material undergoes microcracking, distributed over a relatively large area. Then, during the propagation of a macroscopic crack, AE signals are captured at a much higher rate. Although the signal concentration is higher, their spatial distribution is still scattered, possibly because of the local variation of the AE wave propagation speed, which were not accounted for. Distributed signals continue to be emitted ahead of the crack tip. It must be recalled that most crack patterns appearing on the optical measurements have an aperture in the order of a few micrometers: AE monitoring allows the observation of crack far below the visible range.

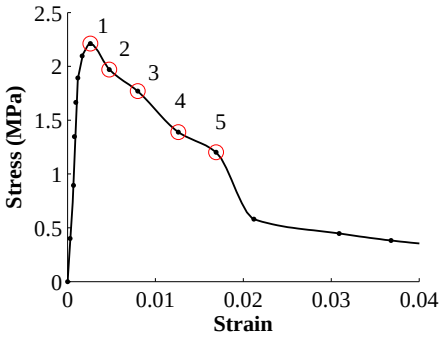

(a) Position of the images on the loading profile

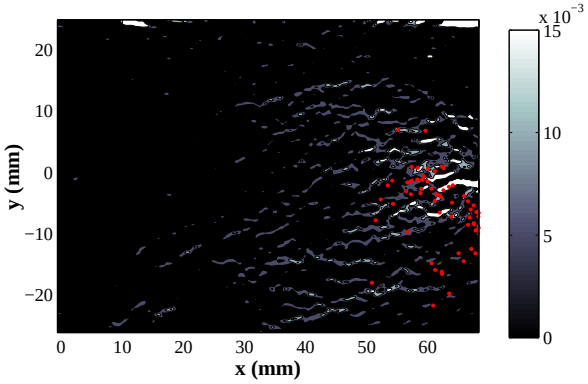

(b) Point 1

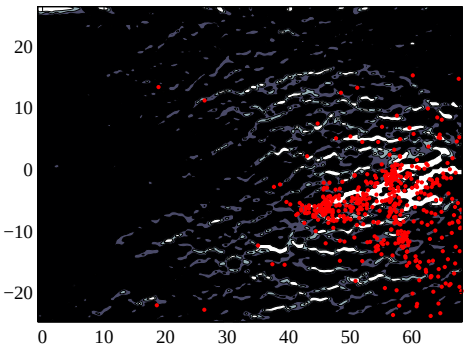

(c) Point 2

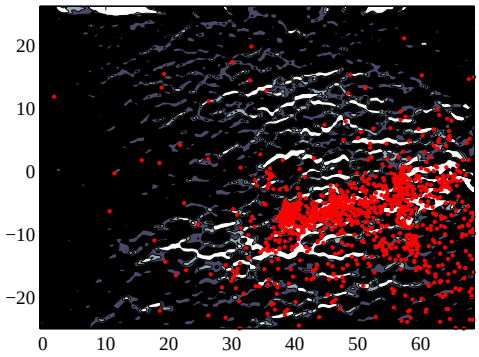

(d) Point 3

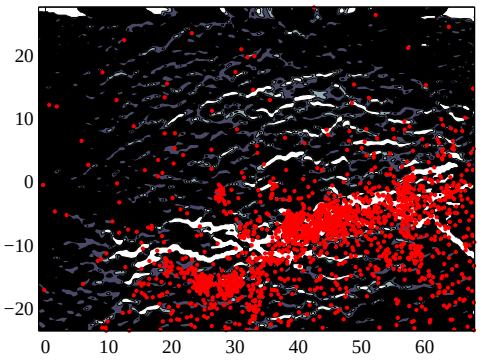

(e) Point 4

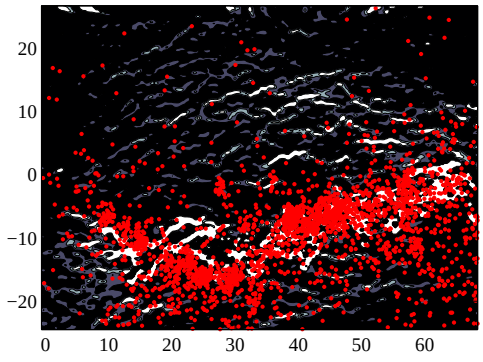

(f) Point 5

Figure 3.10: AE sources localisation (dots) and strain mapping (black and white patterns)

3.3.3 Damage identification

Signal localisation has added geometrical informations to the quantitative estimation of damage. In addition to informing on the global degradation state of the material, it has been shown that the AE technique may indicate where damage occurs, and give an estimate of the trajectory of the main cracks. However, it does not provide a complete understanding of damage mechanisms so far. The separation between microcracks and larger fractures has been graphically showed and translates into different concentrations of signals, but these observations do not allow their systematic separation.

For this purpose, the waveforms of the recorded AE events were studied in an attempt at identifying damage mechanisms. The waveform of a signal is the recording of the amplitude fluctuations of the sensor picking it up. A schematic example of one is shown on Fig. 3.11.

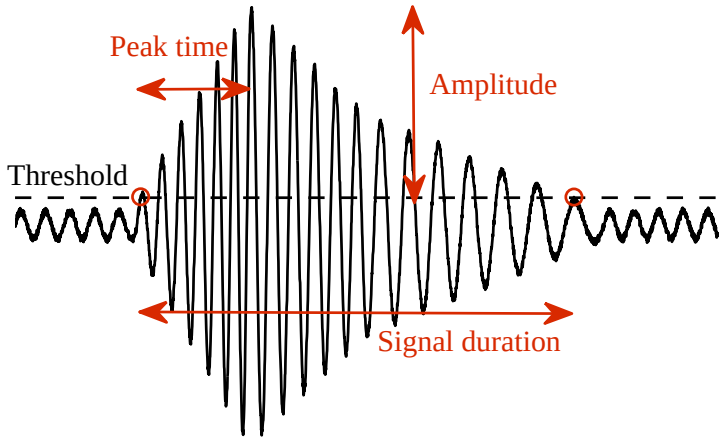

Figure 3.11: Scheme of an AE waveform

A signal is defined between the first and the last points at which the amplitude exceeds the threshold of detection (shown by red circles), for as long as the time interval between successive hits does not exceed the hit definition time (of 100μs in the present case). The signal generally shows a steep increase in amplitude, followed by a longer decay. Theresulting waveform can be described by means of several variables, or descriptors, such as its average frequency, peak time, amplitude, duration, number of counts... Different crack mechanisms are expected to generate different types of waveforms: attempting to identify these mechanisms on the basis of the descriptors is the target of signal classification.

Two methods were followed for identifying the damage mechanisms from the waveforms of the signals. First, we show how the evolution of signal amplitude distributions allow crack scale scattering and specimen failure time prediction. A more thorough classification was then conducted, sampling groups of signals exhibiting similar

waveforms, in order to observe their spatial distribution in the material.

3.3.3.1 Ib analysis

AE amplitude is associated with the magnitude of the fracture, since the emitted energy depends on the crack opening displacement. Microcracks that develop before stress concentration and material failure are therefore expected to generate AE waves of smaller amplitude than larger fractures. This assumption can be made to study the development of the fracture process of concrete and rock-like materials.

In the field of seismology, the b-value serves as a predictive tool for material failure and is defined as the ratio of AE events of small to large amplitude:

$$\log_{10} N = a - bA \tag{3.10}$$

where N is the number of signals, among a number of recently detected AE waves, exceeding a given amplitude A. At any time during the development of damage, the parameters a and b are defined by linear approximation of the current N versus A profile. High b-values therefore indicate a prevalence of microcracks, while lower values indicate their coalescence into macrocracks. An improved value of this indicator, or Ib-value, was proposed by [SHI 94] and applied by [COL 03, AGG 11], among others, to study the fracture behaviour of concrete:

$$Ib = \frac{\log_{10} N\left(\mu - \alpha_1 \sigma\right) - \log_{10} N\left(\mu + \alpha_2 \sigma\right)}{\left(\alpha_1 + \alpha_2\right)\sigma} \tag{3.11}$$

where μ and σ are the averaged value and standard deviation of the AE amplitude among the group of recent hits, α_1 and α_2 are filtering parameters (both were set to 0.5 in the present study). At any given time, $N\left(\mu - \alpha_1 \sigma\right)$ indicates the number of recent events, of which amplitude exceeds $\mu - \alpha_1 \sigma$ (similarly, $N\left(\mu + \alpha_2 \sigma\right)$ indicates the number of recent events of which amplitude exceeds $\mu + \alpha_2 \sigma$). The definition of the Ib-value is similar to that of the b-value, with an additional filtering of non-representative signals of very high or low amplitude that might disturb the results.

At all times of a test, the Ib-value is calculated from the amplitude distribution of the 200 latest consecutive signals. In order not to filter out waves of smaller amplitude, the procedure was applied on the basis of all recorded AE hits rather than of the localised events. Fig. 3.12 shows the Ib profiles superimposed with the loading curves of the fibre reinforced mortar samples.

As already mentioned, and seen by other authors [SHI 94, SHI 01], the evolution Ib is strongly related to the type of fracture. A common observation [COL 03, AGG 11] is that it starts at higher values as the first signs of damage are in the form of diffuse microcracking, generating mostly AE waves of low amplitude. Shortly before the initiation of a macroscopic fracture, these cracks aggregate: the energy release increases, decreasing the slope of the amplitude distribution. This results in a sudden drop of the Ib-value shortly before the maximum stress, that acts as a warning for the specimen failure. Such a drop can be seen on most samples of which the Ib profiles are shown on

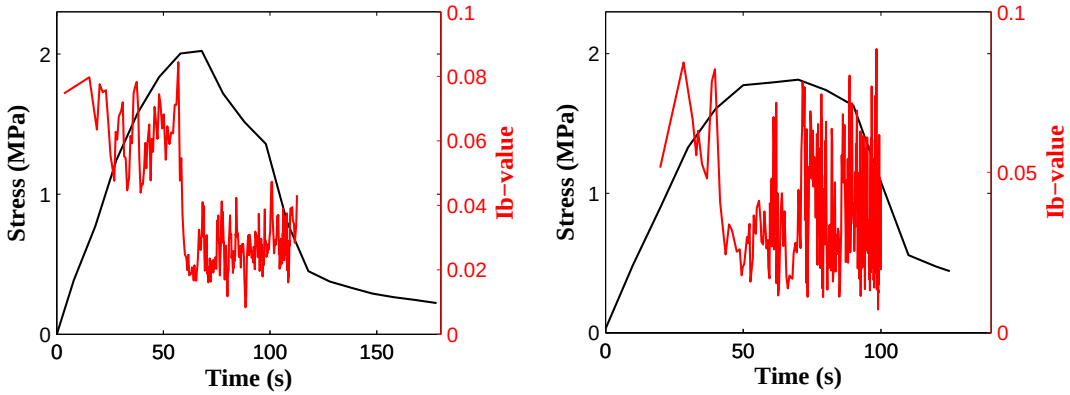

(a) Sample 1

(b) Sample 2

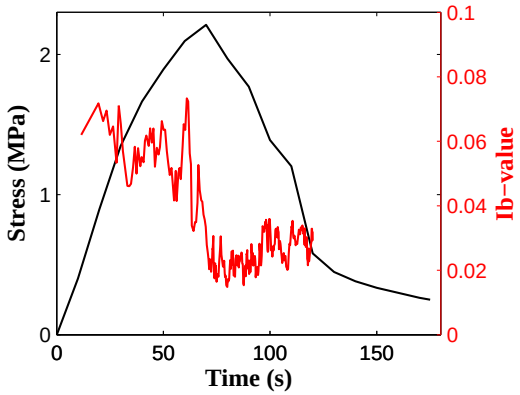

(c) Sample 3

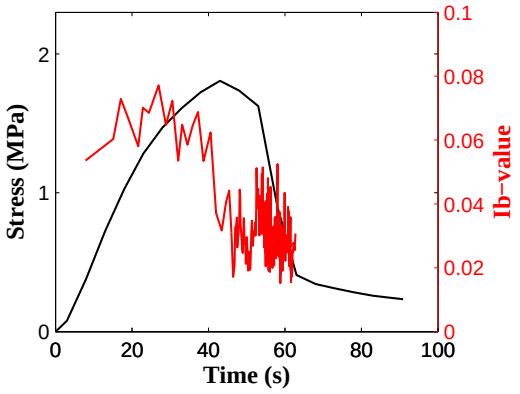

(d) Sample 4

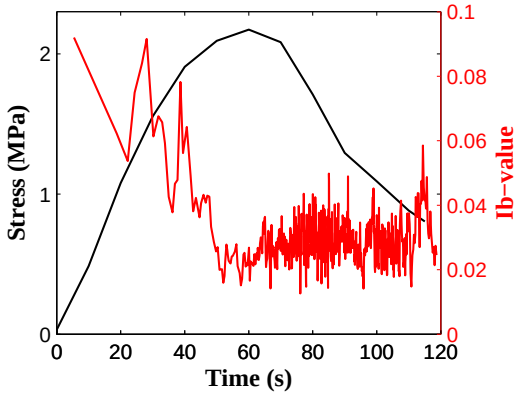

(e) Sample 5

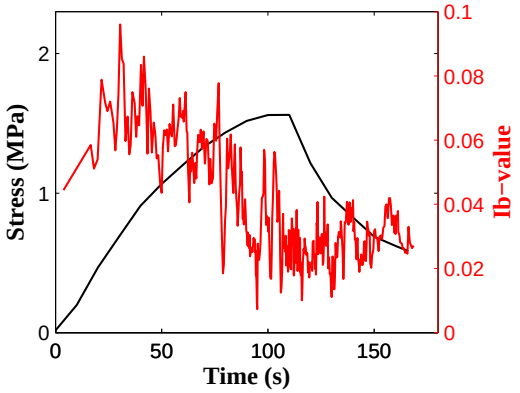

(f) Sample 6

Figure 3.12: Loading and *Ib*-value profiles of fibre reinforced mortar

Fig. 3.12. In the case of the present material, a decrease of the value under 0.03 to 0.04 is a fair indicator for crack initiation. This trend is however not always clear: indeed, the material has a high acoustic attenuation and the number of low-energy signals, detected before macro-fracturing, may be low.

As can be seen on Fig. 3.10, the time of drop of the Ib indicator corresponds to the time at which AE sources start concentrating in a narrow band close to the point of macro-crack initiation. This observation indicates that, in addition to a quantitative estimation of damage, AE allows the separation of fissures according to their size, as well as the time and position of failure.

3.3.3.2 Signal classification

In addition to the peak amplitude, an AE waveforms exhibit a number of parameters that can be used for their classification. Indeed, as the energy release depends on the type of crack, grouping AE events in classes of similar patterns may allow identifying different damage mechanisms.

Two parameters are generally used for crack classification in concrete and rock-like materials : the rise angle RA, or ratio of peak amplitude to rise time, and the average frequency AF, or the ratio of number of counts to duration. Crack modes of concrete can be identified on the basis of these two criterions: tensile cracks have a low RA and high AF, while shear cracks have higher RA and lower AF. [IWA 97, SHI 01, OHN 10]. Crack classification in composite systems however requires a more systematic approach. The material under study includes Portland cement reinforced with dispersed polymer systems and glass fibres. As samples undergo tensile loading, AE waves may not only originate from tensile or shear cracking of the cement matrix, but also from fibre debonding or the yielding of polymer bridges. A more complete classification methodology was conducted in an attempt at separating potential classes of damage mechanisms. This approach aims at being generalisable to new reinforced building materials such as engineered cementitious composites [LI 03], which are increasingly used in construction.

The classification procedure follows the unsupervised clustering methodology described by Moevus *et al.* [MOE 08]. The waveform of each AE event is described by 18 parameters, or descriptors. The correlation matrix of these features was calculated in order to only select a representative set of descriptors and removing redundant ones. Five descriptors were kept: average frequency, number of counts to the peak, rise frequency, signal energy, and rise angle. A principal component analysis [JOH 02] was performed in order to define uncorrelated features by linear combinations of the selected descriptors [MOE 08]. A k-means algorithm [MAC 67, LIK 03] was then applied: coordinates of cluster centers are first randomly initialised, then each pattern is assigned to the nearest cluster. For this purpose, an Euclidean distance is defined in the space of the features found by principal component analysis. The new cluster centers are then computed and the calculation is iterated as such until convergence.

The k-means algorithm is not a reproductible procedure and was conducted several times for each number of clusters until an optimal solution was found. The qual-

ity of a classification is estimated by means of the Davies-Bouldin index [DAV 79]. The procedure was performed on all samples, and the results shown on Fig. 3.13 and discussed below concern the sample 1.

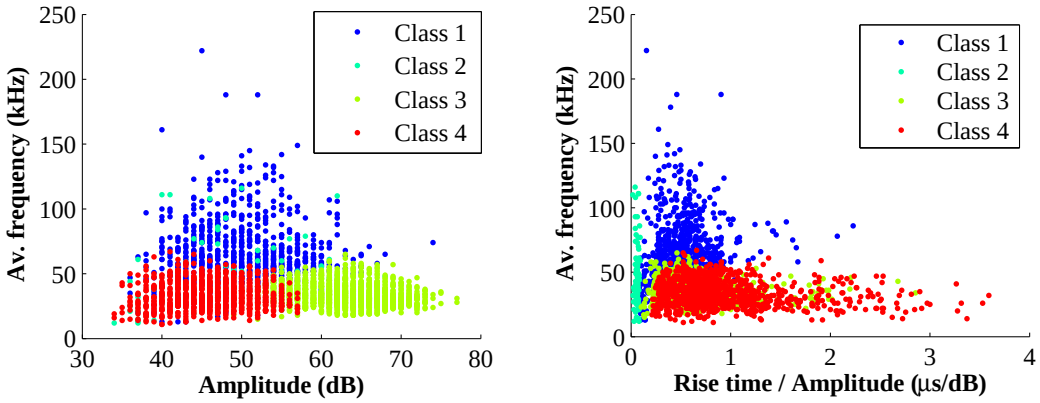

(a) (b)

Figure 3.13: AE classification results

The optimal clustering was achieved with 4 classes, resulting in a Davies-Bouldin index of 0.39. From these calculations, it cannot be confirmed that the identified classes match with either tensile or shear cracks, or with other possible degradation mechanisms. The understanding of all damage processes in the composite material would require a more extensive study. As a consequence, the distinction between clusters is not clear and does not allow a thorough interpretation of the results.

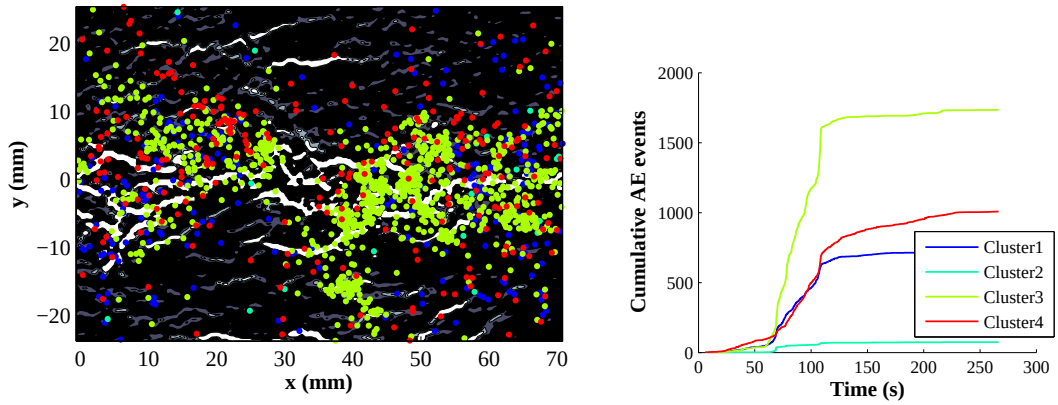

(a) (b)

Figure 3.14: 3.14(a) Spatial distribution and 3.14(b) cumulative number of AE events by cluster

Some observations are however possible: the clusters labeled 3 and 4 include a large majority of the signals, and mainly differ in terms of amplitude distributions, as

shown on Fig. 3.13(a). It is possible, yet not ensured, that they respectively depict micro and macro-cracks. This assumption is confirmed by the spatial distributions of the signals: class 3 signals, of lower energy, are scattered in a relatively large area, while higher energy class 4 signals are concentrated along the trajectory of the macro-crack (see Fig. 3.14(a)). Moreover, the emission of class 3 signals starts before initiation of the macroscopic fracture (see Fig. 3.14(b)), and continues during the entire degradation process, while class 4 signals are nearly exclusively emitted during macro-crack propagation.

This procedure, and the corresponding results, are an introduction to the possibilities of AE clustering. Although the nature of the material (highly porous composite of high acoustic attenuation) renders the interpretation of the measurements difficult, it is possible, with such a methodology, to identify the damage mechanisms. This has already been done on ceramic composites [MOE 08] and concrete [OHN 10] with promising results.

3.4 Conclusion

In the purpose of extending the use of non destructive damage observation applied to building materials, the present study consisted in the simultaneous use of digital image correlation and acoustic emission for the monitoring of progressive damage development in a formulation of fibre reinforced mortar under tensile loading. The aim was to assess the ability of AE to provide quantitative measurements of the crack networks, and to calibrate it with the support of an optical technique. In the course of the presented methodology, the following results were obtained:

- Digital image correlation, associated with an automated image processing procedure, allowed a precise two-dimensional mapping of damage patterns, from micro-cracks to macroscopic fractures.

- The cumulative number of captured AE signals is a fair quantitative indicator of the total developed crack area.

- Before propagation of a macroscopic fracture, a moderate number of AE signals are emitted in a large area ahead of the crack tip. High concentrations of AE signals are then emitted along the crack trajectory, in fair accordance with damage mappings performed by digital image correlation.

- The time and position of initiation of a macro-crack can be anticipated by means of a simple indicator. The waveforms of the AE signals can be interpreted for separating different scales of degradation.

The methodology can however be improved: a better localisation can be reached by accounting for the variations of the AE propagation speed in the damaged material. This

is partially possible with preliminary measurements performed in a diffusely damaged medium, but may be more challenging after fracture initiation and a highly non-uniform distribution of cracks. Furthermore, a more thorough interpretation of the AE waveforms may provide a better interpretation of the signals and a better understanding of the degradation mechanisms of the material.

Chapter 4

Moisture uptake monitoring and modelling in a discrete fracture network

After having established reliable methods for experimental measurements of crack patterns, the next step of the study is the development of a simulation code that can account for these measurements into simulations of coupled heat and moisture transfer. An experimental study was conducted in order to validate such a model: digital image correlation was performed during the fracturing of concrete samples, in which moisture uptake was then monitored using X-ray radiography. Moreover, a full hygric characterisation of the material was conducted. A simulation code was then developed, integrating fracture geometries into a finite-element mesh. A good accordance was then found between experimental and numerical results in terms of 2-dimensional moisture concentration distributions.

Contents

It has been established in Chap. 2 that a continuous description of damage cannot reach a satisfying accuracy in case of advanced degradation of a material, and that fractures must be explicitely accounted for. Then, Chap. 3 aimed at investigating the potential non destructive techniques for damage monitoring and detection at the building scale. A methodology was proposed for enabling acoustic emissions to provide crack measurements for use in flow simulations. The next logical step is the central piece of the work: a simulation code was developed and validated, that integrates damage and fracture measurements as an input for heat and moisture flow modelling.

The requirements of the simulation code were twofold:

- Fractures measured by one of the tested characterisation techniques must be automatically read and included in a FE mesh, refined according to their geometries. This includes non-trivial tortuous patterns, possibly with intersections and multiple junctions.

- The model must allow long-term simulations of coupled heat and mass transfer in a multi-layered wall.

The use of the model supposes that it has been validated in regards to both these points. The second requirement is addressed in Chap. 5. The first one is the subject of the present chapter: a set of experimental measurements must be gathered, that ensures the validity of moisture flow simulations in a porous medium including fractures of any number, sizes and connectivity.

To this aim, a complete experimental and numerical setup was developed. A standard formulation of concrete, reinforced with steel fibres, was used. Concrete is a composite material made of porous, permeable cement paste binding aggregates of various sizes with very low permeability. Therefore, in such a material, fractures caused by mechanical loading have a tortuous shape and variable aperture due to the presence of aggregates or initially distributed shrinkage cracks. Digital image correlation was performed during the fracturing of the concrete specimen, in which moisture uptake was then monitored by X-ray radiography. In addition the sorption isotherm of the material was measured by dessiccators and extractors. This experimental setup provided a complete characterisation and validation data set, that was used for the development of the simulation code.

The present chapter is organised as follows: Sec. 4.1 describes the recording of a complete data set for the validation of a simulation code for isothermal moisture flow modelling in fracture networks. This data set is made of two types of measurements: crack geometries, which are to be integrated in the simulated porous medium, and moisture content distributions, that allow comparing the predicted and real fluid infiltration in the aforementioned crack patterns. Then, Sec. 4.2 summarises the experimental procedure for the complete hygric characterisation of the observed formulation of concrete, and shows its results. These measurements are essential for operating the model. Finally, the development of the code is described in Sec. 4.3. The model has

been used to recreate the conditions of the experimental setup: these numerical results have then been confronted to the X-ray radiography measurements. Finally, a short mesh-sensitivity analysis has been conducted: simulations have been run with several densities of fracture discretisation. The quality of the flow prediction is estimated on the basis of the total quantity of capillary adsorbed water, as to propose guidelines for this discretisation.

The experimental work herein described, as well as a large part of the numerical procedure, were performed at the Department of Civil Engineering of the Technical University of Denmark (DTU Byg). The methodology and main findings were presented in [ROU 12b].

4.1 Observation of moisture uptake in cracked concrete

4.1.1 Experimental methodology

A formulation of steel fibre reinforced concrete was prepared, based on the proportions shown in table 4.1, using Aalborg portland cement with a water to cement ratio of 0.5. It followed the proportions from previous studies [PEA 10] performed at the Technical University of Denmark. The steel fibres have a length of 12.5 mm and a diameter of 0.4 mm. Their purpose was to allow the interruption of the mechanical loading before complete failure of the specimen, and to ensure their post-crack cohesion in order to use them for subsequent moisture uptake tests.

Water/cement ratio	0.5
Cement	3.465 kg
Sand 0-4 mm	8.043 kg
Aggregates 4-8 mm	11.580 kg
Steel fibres	0.2 kg

Table 4.1: Concrete proportions

The mixture was cast in prismatic forms of dimensions 350×100×100 mm, and first wrapped in plastic sheets during 48h after casting as to initially maintain a high relative humidity (RH), then stored during 28 days in a stable environment of 50% RH. After maturation, the edges of the beams were removed since their cement/aggregate ratio is not representative of the average volumetric distributions of the material. Smaller samples of dimensions 140×50×15 mm were cut out from the beams and notched in their middle as depicted in Fig. 4.1. The purpose of the notch is to ensure stress concentration and fracture initiation in a concentrated area on which the observation could be focused.

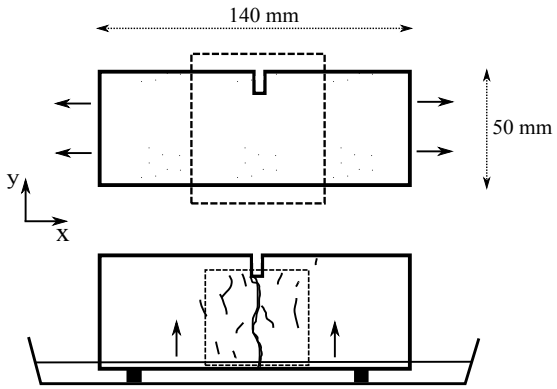

Figure 4.1: Setup of the samples during mechanical loading (above) and capillary uptake experiments (below). The arrows respectively show the directions of the tensile loading and moisture uptake, the dotted lines respectively show the DIC and X-ray observation zones

The specimen were loaded by uniaxial tension with a 10 kN force cell imposing a constant longitudinal displacement speed of 0.5 mm/min in the direction shown in Fig. 4.1. A reference picture of the surface was taken with the camera before loading. The tests were then manually interrupted after initiation of a macroscopic fracture. A total of 15 samples was tested and 6 were kept for the moisture uptake measurements.

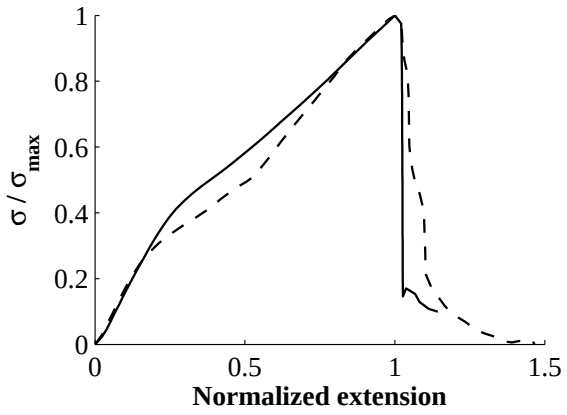

Figure 4.2: Complete (dotted line) and interrupted (continuous line) tensile loading profile of steel fibre reinforced concrete

Fig. 4.2 shows the response to tensile loading of two specimen of steel fibre reinforced concrete, one of which was fully fractured whereas the other was interrupted before complete failure. The profiles are normalised over their maximal stress and peak displacement. The material shows a quasi-brittle behaviour until its tensile strength is reached. After an important drop in the stress profile indicating fracture initiation, co-

hesive forces still apply between both sides of the main crack where its aperture is still low [HIL 76]. In order to dispose of partially fractured specimen, the tests were interrupted during this stage of the loading, and a second picture of the sample surface was taken with the camera after unloading. The DIC algorithm was then run by comparing this deformed image with the reference image, revealing the local displacements on the sample surface after loading, and thus the crack patterns (see Sec. 3.1.2 for an introduction to the technique).

The fractured specimen were then kept in a 45°C oven until their water content stabilised at a nearly entirely dry state. Prior to a water uptake test, the sides of each sample were insulated with impermeable tape in order to avoid 3-dimensional hygric effects such as evaporation. Their lower side was put in contact with a water surface as shown on Fig. 4.1 and the upper side was left open as to avoid entrapping of the air initially contained by the porous network as the water front rises inside the sample. The water content distribution was monitored during the uptake by 2-dimensional X-ray radiography applied on an observation zone centered on the main fracture originating from the notch. These measurements, superimposed with DIC displacement mappings, form a complete validation set for moisture uptake in a material including a non-trivial fracture network. The applied procedures for obtaining this data set are detailed below.

4.1.2 Fracture observation

The camera was used with similar settings as in the previous part of the study (see Sec. 3.1). Pictures of the sample surface were however not taken during the entire course of loading: only the final state of the specimen was observed.

Unlike the previous display of damage in fibre-reinforced mortar (see Fig. 3.5), the results are shown here as contour lines of the displacement field in the direction of the loading: this representation was found more appropriate in case of a single predominant macroscopic fracture. Each line of Fig. 4.3(b) represents a difference of 5 μm of the displacement field in the x (horizontal) direction. A local concentration of the contour lines indicates a steep local difference in the displacement, and therefore locates a fracture.

The mechanical loading of the sample was interrupted before its entire failure. The main fracture can be seen on Fig. 4.3(a) originating from the notch in the middle of the upper boundary, and propagating downwards. This crack exhibits a tortuous shape and secondary discontinuities can be seen propagating from it, mostly along the cement/aggregate interfaces. The horizontal contour lines on both sides of the main crack do not indicate the presence of fractures, but are caused by the notch on the upper side of the sample: as the crack expands, both sides of the sample tend to slightly rotate around the third axis in opposite directions, causing a gradient of horizontal displacement along the vertical coordinate. With further loading, the main fracture (shown by the higher concentration of contour lines) expands and tends to cause the surrounding cracks to close. It can therefore be expected that the moisture content

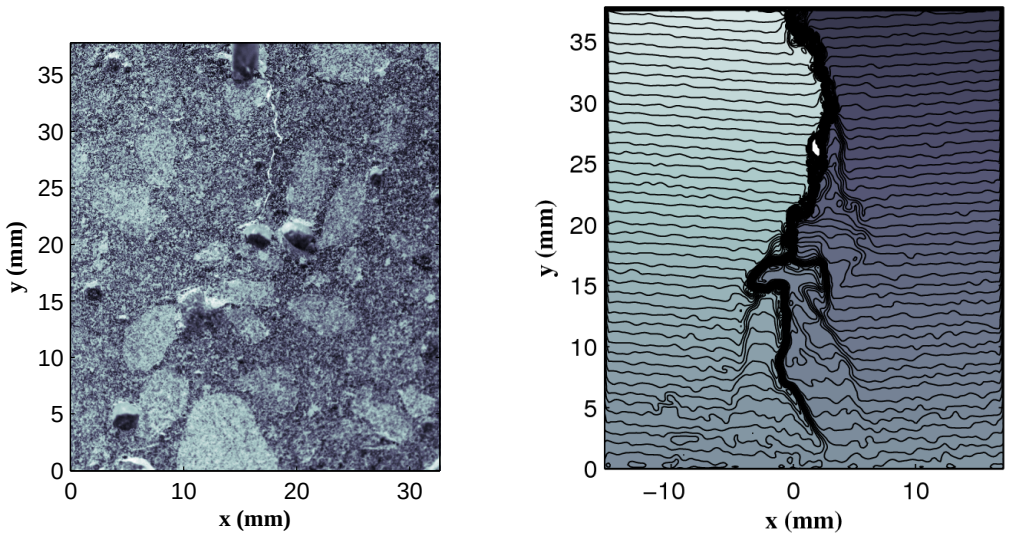

Figure 4.3: (a) Picture of a specimen surface after mechanical loading, (b) surface displacement mapping of a concrete sample from Digital Image Correlation (5 μm/line)

distributions observed during water uptake tests will be influenced by the state of the sample when mechanical loading is interrupted.

The performance of DIC leads to the same observations as earlier. Cracks of under 10 μm aperture can be detected on a relatively large area of observation. In terms of spatial resolution, other techniques such as electronic speckle pattern interferometry or micro-tomography have been found to detect cracks of under 1 μm opening [SHA 99]. The spatial resolution of DIC is mostly a matter of the physical pixel size, i.e. of the settings of the camera (spatial position, focal length). A compromise must be found between searching for smaller crack apertures and covering a large enough observation area. The technique also provides the shape and tortuosity of all fractures, as well as the local variations of their aperture. All of these parameters are likely to have an influence on the moisture flow inside the fractures [VAN 03] and in the surrounding porous material. DIC therefore has the potential to be a significant improvement to the moisture flow prediction in comparison to an arbitrary choice of the fracture geometry.

4.1.3 X-ray radiography

The observation of the two-dimensional moisture concentration distributions in porous building materials is now a common procedure in the characterisation of their hygric properties. This can be done using gravimetric methods [DRC 03] or techniques such as nuclear magnetic resonance, γ-ray attenuation, capacitance method or X-ray projection [CER 02]. Several purposes can be served by these methods: extrapolation of the liquid conductivity from transient one-dimensional moisture uptake tests [CAR 04], observation of local variations of the flow speed due to fractures [ROE 06a] or of the infiltration of chemicals, studies of reinforcement corrosion in con-

crete [PEA 10]... In the recent years, these techniques have been increasingly used in material sciences, and new operating methods were presented for their optimisation and for a more efficient interpretation of their results.

4.1.3.1 Principle

The principle of X-ray radiography is summed up on Fig. 4.4. A photon beam is generated on one side of a specimen, and a camera placed on its other side detects the amount of transmitted photons. In the case of building materials, this allows measuring the concentration of water or other chemicals.

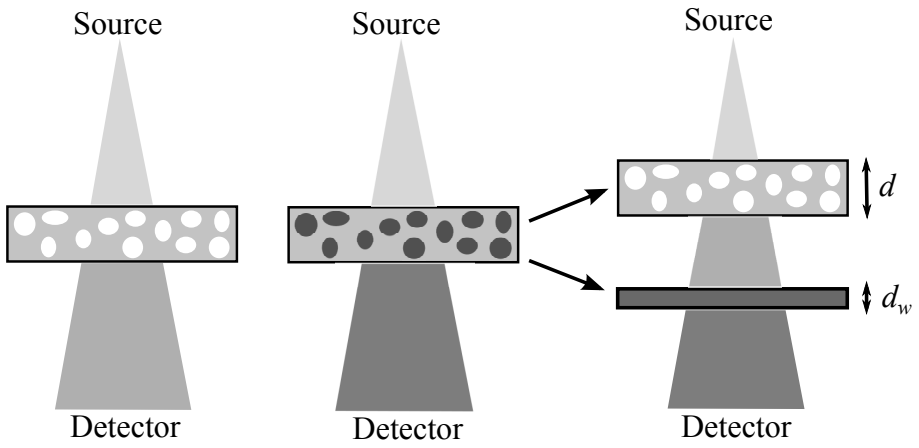

Figure 4.4: Measurement procedure of the moisture concentration by X-ray radiography

If the intensity of the source is denoted I_0, the intensity I transmitted by a sample of thickness d is expressed by Beer's law:

$$I = I_0 \exp\left(-\mu d\right) \tag{4.1}$$

where μ is the attenuation coefficient of the material. This coefficient indicates the probability of a photon to interact with the material (and to not reach the camera) per unit length. It is a function of the photon energy, the density and effective atomic number of the material. In case of a moisture uptake experiment, the local water concentration inside a specimen can be considered as an additional layer of thickness d_w and attenuation coefficient μ_w. The measured intensity across a wet sample I_{wet} can then be expressed as separately attenuated by the dry material and this water layer.

$$I_{wet} = I_{dry} \exp\left(-\mu_w d_w\right) = I_0 \exp\left(-\mu d - \mu_w d_w\right) \tag{4.2}$$

The moisture content w is related to this fictitious moisture thickness by:

$$w = \frac{\rho_w d_w}{d} \tag{4.3}$$

The water concentration inside the porous medium can therefore be derived from the intensities measured through the material before and after its contact with water:

$$\Delta w = -\frac{\rho_w}{\mu_w d} \ln\left(\frac{I_{wet}}{I_{dry}}\right) \tag{4.4}$$

where Δw is the increase in water content from the initial state, which is not necessarily entirely dry. The linear attenuation coefficient of water is considered unknown at first and will be determined by coinciding the X-ray intensity transmitted by a water-saturated concrete sample with the measured capillary moisture content.

The procedure of the experiment is as follows: the sample is initially placed in a container and a first image is taken to measure the dry intensity I_{dry}. Water is then poured into the container as to be in contact with the bottom surface of the sample. Measurements of intensity transmitted by the wet material I_{wet} follow regularly as the moisture front rises inside the material.

According to Eq. 4.4, the result w shown at one location of the 2-dimensional plane of observation is the average of the water mass per volume over the thickness of the sample. If the material is considered homogeneous in comparison with its dimensions and the size of the observation zone, w will reach a homogeneous distribution at saturation. However, concrete is a highly heterogeneous material, and the specimen of the study have a thickness of only a few times the size of the largest aggregates. The assumption of homogeneity can therefore not be made here. Aggregates have a much lower equilibrium moisture content than cement paste, and the observation of the local water concentration does not depict the actual wetting state of a specimen correctly. This is corrected for by considering the non-dimensional water content s, or saturation degree of the liquid phase:

$$s = \frac{\ln\left(I_{wet}/I_{dry}\right)}{\ln\left(I_{sat}/I_{dry}\right)} \tag{4.5}$$

where I_{sat} is the recorded intensity transmitted by a capillary saturated sample. This definition implies that a series of measurements must be carried on until saturation of the specimen in order to normalise the water content between an initial and a final state.

4.1.3.2 Settings

The moisture profile tests were performed with the GNI X-Ray system at DTU Byg. The following parameters must be set before running moisture concentration measurements in concrete samples:

- The position and motion of the camera during measurements
- The X-ray intensity and energy of the source
- The number of recorded images at each location and integration time

- The warm-up and stabilisation time of the X-ray source

The intensities are recorded by the camera as 16-bit images showing up to 65535 greyscale levels. The size of each image is 252×256 pixels covering an area of 12×12 mm, i.e. with a pixel size of 50 μm. The X-ray source and the camera can be displaced following a pre-programmed path, which allows the user to visualise larger areas by assembling images taken at several adjacent locations. The entire observation zone for each series of measurements covers a square area of 3×3 images, centered on the main fracture of the specimen, as schematically shown on Fig. 4.5. This setup allows including the entire height of the sample between the water front and the notch, and covering a large enough area as to capture the evolution of the water front within several hours of measurements. Attempting to cover larger observation areas may imply longer acquisition times, and a possibility for the moisture front to evolve while it is recorded.

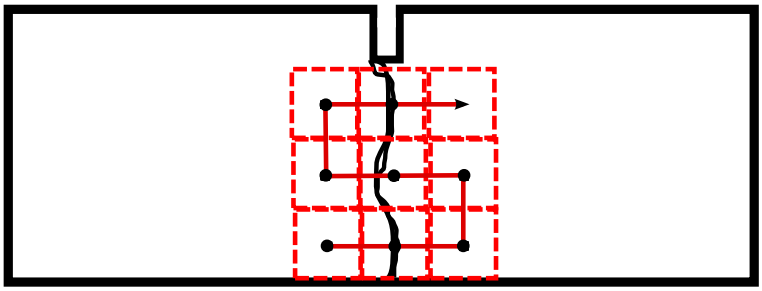

Figure 4.5: Observation area of the X-ray apparatus and course of the camera

The energy of the X-ray source is set as to ensure a good resolution of the water content profiles. According to [ROE 06a], the resolution of moisture content R_w is defined as one greyscale step of an image and is mainly a function of the sample thickness for each type of material.

$$R_w = -\frac{\rho_w}{\mu_w d} \ln\left(\frac{I_{dry}-1}{I_{dry}}\right) \tag{4.6}$$

The drawback of a high energy is a possible instability of the source which as a consequence would make longer integration times necessary. A fair compromise was found at $E = 85$ keV, which coincides with the energy suggested by [ROE 06a] for ceramic brick samples of similar thickness and density. This results in an average resolution of $R_w < 0.5$ kg·m^{-3}. The intensity I_0 was set to 70 μA. The X-ray tube was set to warm-up for 200 seconds and stabilise for 600 seconds to minimise variations in this incident intensity.

Since non-negligible fluctuations in the intensity of the X-ray source are expected during the measurements, each image of the assembling is the averaged intensity measured over a series of images of the same location, each of which taken with a given camera integration time. The number of picture must be set as a compromise to maximise precision and keep the measurement time low. The integration time must be set

as to maximise the standard deviation of the greyscale levels and avert saturation on either side of the spectrum. The system was set as to record 40 images on each part of the grid with and integration time of 1500 ms. The entire acquisition of the observation area, including the time of displacement of the camera and source between the locations, therefore lasts around 10 minutes. Such a time interval between the first and the last images of a series is not problematic here because of the low permeability of concrete, and all images can be considered taken at the same time.

The X-ray receptor exhibits a constant response, or dark current, during periods when it is not actively being exposed to the photon beam. As a consequence, images recorded by the camera while no X-rays are being produced by the tube, must be substracted from the measurements, in order to remove the influence of the dark current. This operation is illustrated on Fig. 4.6. Dark current measurements must be carried in the course of the entire monitoring procedure, as its amplitude may vary in the course of the day. This means that the X-ray source must be switched on and off repeatedly between measurements.

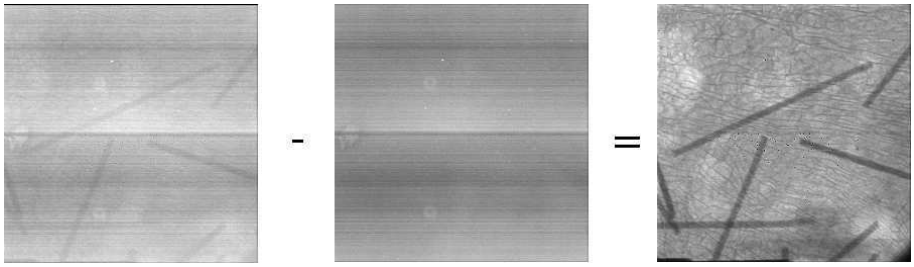

Figure 4.6: Elimination of the dark current from X-ray measurements

Following this procedure, each X-ray image of a concrete sample is the result of the averaging, assembling and analysing of 360 original images, and 360 dark current images, processed by a batch code written in the ImageJ software. Additional information on the principle and operating procedure of the GNI X-ray system at DTU-Byg can be found in a previous thesis written at the department [PEA 10].

4.1.3.3 Results

Moisture content distributions

The moisture infiltration was recorded in all fractured concrete specimen. The procedure for one of the samples is as follows: first, the sample was placed inside a container in the X-ray system, so that its position in respect to the camera was known. A reference image was then taken, as well as dark current recordings, covering the observation area of the dry specimen. Water was then poured into the container as to slightly exceed the bottom sample surface. Measurements of transmitted X-ray intensities were then performed during 24 hours, alternated with dark current recordings. A final measurement was performed once the observation area reached saturation, in

order to dispose of the saturated intensity profile I_{sat} required for the use of Eq 4.5. Once processed, the measured intensities resulted in successive moisture content distributions over the observation area. These distributions are shown on Fig. 4.7 for one of the treated samples.

Fig. 4.7(a), 4.7(c) and 4.7(e) show successive moisture content distributions calculated using Eq. 4.4. The intensity I_{dry} is given by the reference image of the dry sample, while the mappings of I_{wet} are given by the recordings of the wet sample. The X-ray attenuation coefficient of water was set to $\mu_w = 12.17\ \mathrm{m}^{-1}$. Justification for this value is given in Sec. 4.2.2, as it has been determined in the process of hygric characterisation. The origin of the horizontal axis on the figures was set at the position of the notch on the upper side of the sample, from which the crack can be seen originating.

The displayed sample exhibits a single macroscopic crack, originating from the notch and propagating downwards. The crack filled with water within a few seconds after wetting. Moisture then spreaded from both the fracture and the bottom water surface into the surrounding porous material. However, as earlier mentioned, concrete is a highly heterogeneous material: its components (aggregates, cement paste, steel fibres…) have different physical properties, particularly resulting in local variations of the X-ray attenuation coefficient μ. Moreover, the moisture permeability of the cement paste is significantly higher than that of the aggregates, resulting in highly heterogeneous moisture concentration distributions. The thickness of the samples is not large enough to be considered representative of the heterogeneous medium. This matter is solved by applying Eq. 4.5 to calculate non-dimensional saturation distributions, respectively shown on Fig. 4.7(b), 4.7(d) and 4.7(f). This results in a better view of both moisture fronts (originating from the crack and from the bottom), although some irregularities remain.

DIC and X-ray superposition

In order to ensure that the present data set is suitable for the validation of the transfer model, we must ensure the spatial correlation between the fracture positions located by digital image correlation and the moisture distributions monitored by X-ray radiography. This target is addressed by Fig. 4.8.

Similarly to Fig. 4.3(b), the displacement fields, computed over a grid at the surface of the specimen, are shown by contour lines, each of which indicates a difference of 5 μm of the displacement field in the x (horizontal) direction. Each image of Fig. 4.8 shows the first moisture concentration mapping obtained on each of the tested concrete samples. Most samples exhibit a fair accordance between the early moisture concentration patterns and the shape of the main macroscopic crack. In some cases, moisture can be seen to have taken additional paths which do not coincide with the displacement gradients measured by DIC. Indeed, this optical technique is based on the observation of the sample surface and cannot capture the 3-dimensional shape of the cracks, while the local water content measured by X-ray is averaged over the sample thickness. These observations underline the applicability of DIC as a mean to predict

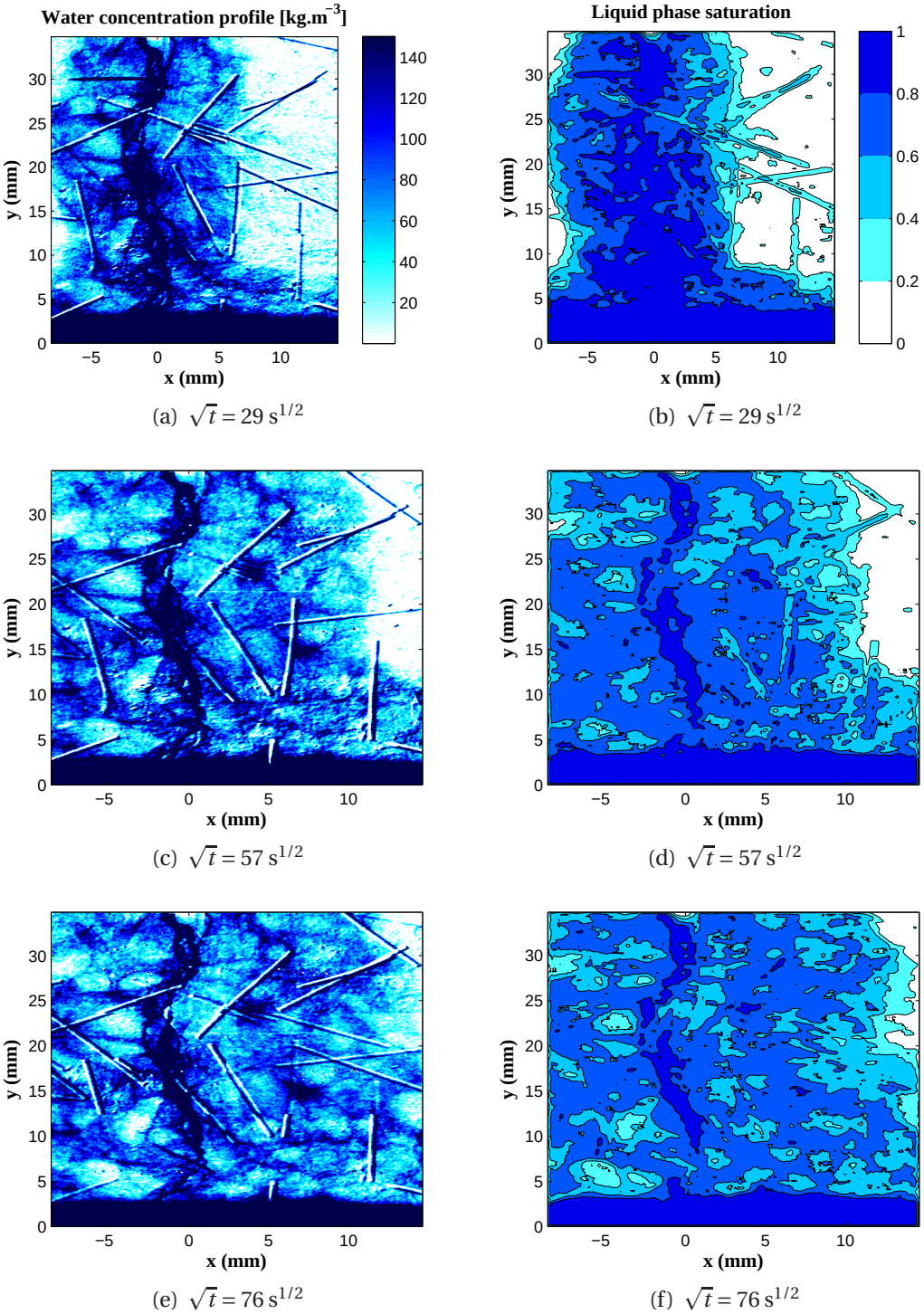

(a) $\sqrt{t} = 29\ \mathrm{s}^{1/2}$ (b) $\sqrt{t} = 29\ \mathrm{s}^{1/2}$

(c) $\sqrt{t} = 57\ \mathrm{s}^{1/2}$ (d) $\sqrt{t} = 57\ \mathrm{s}^{1/2}$

(e) $\sqrt{t} = 76\ \mathrm{s}^{1/2}$ (f) $\sqrt{t} = 76\ \mathrm{s}^{1/2}$

Figure 4.7: Successive X-ray mappings of the moisture concentration (left) and saturation (right) distributions

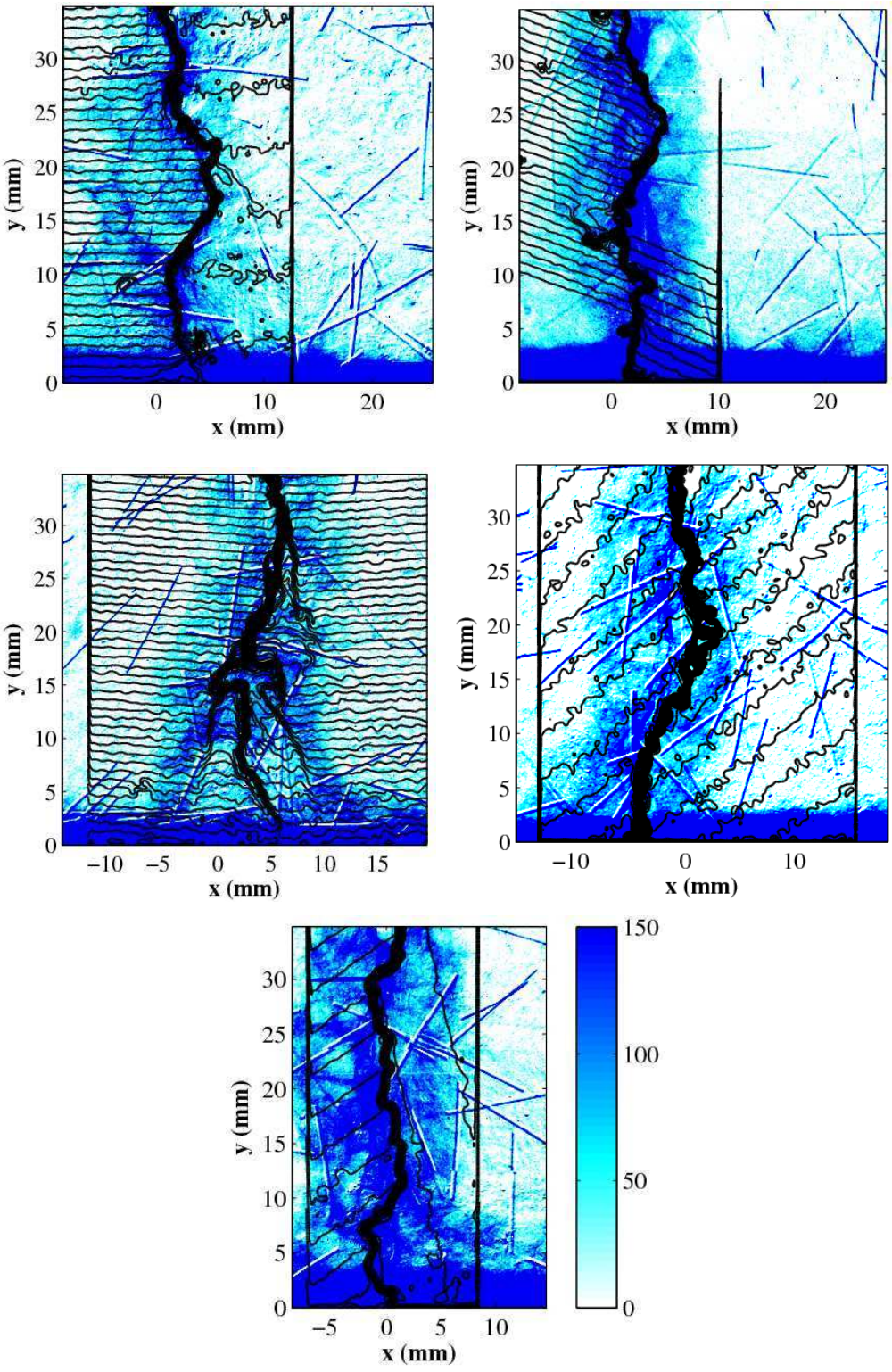

Figure 4.8: Superposition of DIC displacement mappings (contour lines) and moisture content distributions on 5 cracked concrete samples

preferential moisture paths, but also show its limitations. Some of these limitations can be overcome by the use of 3-dimensional crack observation techniques.

The crack geometries are to be implemented into the finite element code, of which accuracy is to be assessed by comparison with the X-ray moisture content mappings. In addition to this procedure, the moisture transport and storage properties of undamaged concrete must be measured in order to supply the code with the necessary information for flow prediction. The methodology and results of these measurements are presented in the following section.

4.2 Hygric characterisation of concrete

The assumptions on which the balance equations for heat and moisture in porous media have been based, were formulated in Sec. 1.2. One of these hypotheses is the thermal non-dependency of the moisture storage and transport properties of the material. These properties were therefore measured on the entire humidity range for one value of the temperature. The conservation equation for isothermal moisture transfer in building materials was written in Eq. 1.9 and is recalled here as to show the quantities of interest of the characterisation procedure:

$$\frac{\partial w}{\partial p_c}\frac{\partial p_c}{\partial t} = \nabla \cdot \left(K_w \nabla p_c\right) \tag{4.7}$$

This equation is written as to include water vapour and liquid moisture transfer into a single term, driven by a gradient of capillary pressure and a total moisture permeability K_w:

$$K_w = K_l + \delta_p \frac{p_v}{\rho_l R_v T} \tag{4.8}$$

The full hygric characterisation of porous building materials includes measurements of the retention curve $\partial w/\partial p_c$ and of the permeability K_w, in both hygroscopic and over-hygroscopic ranges. In the hygroscopic range, moisture transfer mostly occurs through diffusion or advection phenomena of water in the gaseous phase. The over-hygroscopic range represents higher concentrations of water in the material, where transfer in the liquid phase prevails. The modelling work is aimed at covering both cases.

The transport and equilibrium properties of concrete are to be measured during wetting, as opposed to previous studies concerning the drying of several formulations of concretes and cement pastes [BAR 99]. The procedures for experimental characterisation of storage and transport properties are explained below: the moisture retention curve was characterised by weighing samples placed in stable humidity conditions. The permeability was measured following the Boltzmann technique [CAR 04], which requires the monitoring of moisture concentration distributions in the material during capillary uptake.

4.2.1 Sorption isotherm

4.2.1.1 Equipment and procedure

The complete profile of moisture content w versus capillary pressure p_c was measured using two separate methods in order to cover the entire humidity range: desiccators and pressure plates. A common hypothesis, already assumed in the preliminary study, is the fact that fractures have little contribution to the storage capacity of a porous material. Under this assumption, the sorption isotherm was measured on a series of non-cracked samples, and considered valid for all states of damage.

Desiccators

The sorption isotherm of concrete was measured in the hygroscopic range between 11% and 97% relative humidity using the desiccator method presented in the ISO-12571 standard [ISOa]. The procedure, summed up on Fig. 4.9, consists in placing small material samples in constant conditions of relative humidity and recording their equilibrium mass compared to that of their dry state.

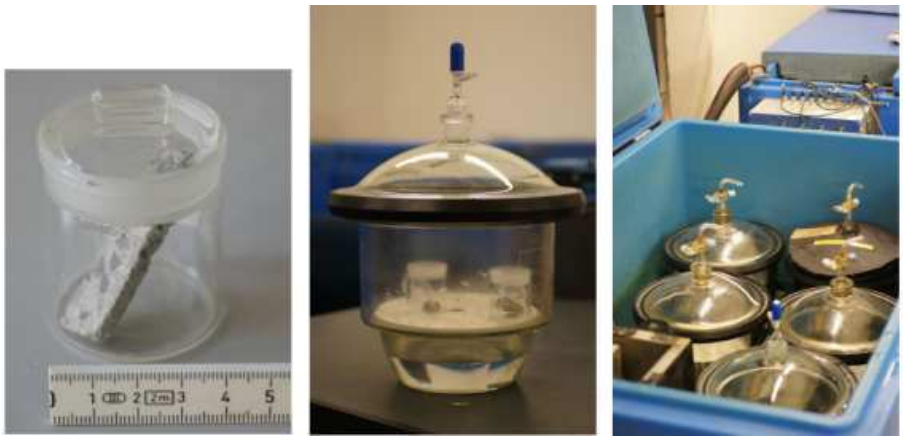

Figure 4.9: Experimental setup for sorption isotherm measurements in desiccators

A total of 12 initially oven-dried samples of 40×10×2 mm were placed in weighing cups distributed inside 7 desiccators. The bottom of each desiccator was filled with saturated aqueous solutions listed in Tab. 4.2, in order to recreate pre-set values of relative humidity. Once the cups were placed and their lids were removed, the air pressure inside the desiccators was lowered as to accelerate the sorption process. Successive weighings were then performed, opening the desiccators and covering the cups with lids as to insulate the samples during their exposure to ambient air. Equilibrium is considered reached when the same results are obtained from two consecutive weighing performed at an interval of 48 hours.

N°	Product	Relative humidity (%)
1	LiCl	11
2	$MgCl_2.6H_2O$	33
3	NaBr	53
4	NaCl	75
5	KCl	86
6	KNO_3	93
7	K_2SO_4	97

Table 4.2: Values of relative humidity in the desiccators

Container 1		Container 2	
Pressure (bar)	RH (%)	Pressure (bar)	RH (%)
0.665	99.95	4	99.70
1.38	99.90	5.6	99.59
2.05	99.85	8	99.41
2.7	99.80	10	99.26
3.4	99.75	12	99.12

Table 4.3: Values of capillary pressure in the pressure plates

Pressure plates

Neither climatic chambers nor the acqueous solutions used in desiccators allow generating stable humidity conditions in the over-hygroscopic range (RH > 97%, $p_c < 4 \times 10^6$ Pa). A suction technique based on the use of pressure plates was therefore used for complementary measurements of the retention curve near the saturation state of the concrete samples. The principle of this suction technique is as follows: water-saturated samples are placed in a container. Moisture is forced out by an applied pressure through a porous ceramic plate and collected outside the container. When equilibrium is reached, i.e. no more water is extracted, the samples are taken out of the containers and weighed. The equilibrium moisture content, related to the applied (capillary) pressure, is calculated from the difference with the mass of the saturated specimen. The procedure is then repeated with increasing values of the pressure. A more thorough description of the pressure plate apparatus can be found in [KRU 96].

A total of six samples, of average dimensions 75×50×10 mm, was placed in two separate containers. Each of the containers was successively prescribed increasing values

of pressure as to cover the near-saturation humidity range. These values are summed up in Tab. 4.3.

4.2.1.2 Results

The samples used for the dessiccator method are initially oven-dried, whereas the pressure plate method proceeds by extracting water from initially vacuum-saturated samples. Therefore, the former method provides the sorption curve for the hygroscopic range, while the latter provides the desorption curve for the over-hygroscopic range. This was corrected for by subtracting the recorded difference between capillary and vacuum saturation contents to the desorption (extractors) measurements. This difference being relatively low, the assumption could be made that the result is a full sorption curve.

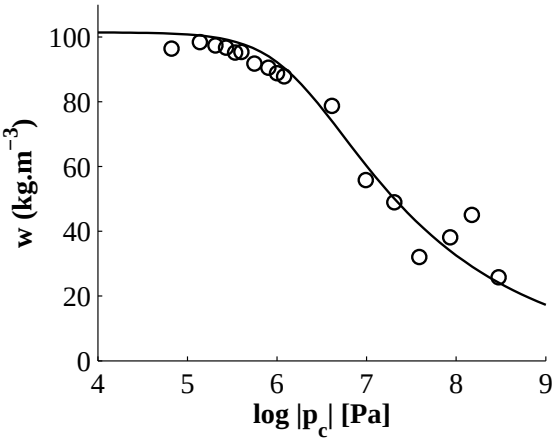

Figure 4.10: Moisture retention curve of concrete: measurements and approximation by van Genuchten's model

The results of the two procedures explained above is a set of 17 measurement points on the w versus p_c profile, each of which is the averaged value of the moisture content recorded on several samples. This profile is shown on Fig. 4.10. A Levenberg-Marquardt algorithm (see Sec. 2.2.2.2) was then used in order to approach these measurements with a van Genuchten model [GEN 80]. The multimodal expression of this model was given earlier (see Eq. 1.20) and was used here in its monomodal form:

$$w = w_{sat}\left[1 + \left(\alpha|p_c|\right)^n\right]^{-m} \tag{4.9}$$

where the saturation moisture content and the parameters m, n and α are given in Tab. 4.4.

Since the hysteresis effects are not considered in the present study, these parameters form a complete characterisation of the sorption isotherm of concrete, covering the hygroscopic range and the near-saturated state. The sorption profile can be seen

m	n	α (Pa^{-1})	w_{sat} (kg.m^{-3})
0.2191	1.2566	6.165×10^{-7}	101.44

Table 4.4: Coefficients of the sorption isotherm approximation for concrete

to be relatively high at low values of relative humidity, confirming the fact that the material presents an important proportion of small pores. The derivative of the profile, $\partial w/\partial p_c$, is the moisture capacity of Eq. 4.7, and is required for the following characterisation of the unsaturated permeability profile.

4.2.2 Moisture permeability

4.2.2.1 Procedure

After determination of the moisture storage properties, the study now focuses on the transport coefficients. For this purpose, the recording of moisture content distributions is required. The full unsaturated permeability profile is estimated using the Boltzmann transformation method. Any technique capable of determining moisture content profiles is suitable for this methodology [ROE 04]. In the present case, the X-ray projection equipment was used. The method, more extensively described by [CAR 04], is briefly summed up here.

The method is based on an alternative expression of the one-dimensional moisture conservation equation. If water infiltration is assumed to occur in the x direction, the Boltzmann variable λ is defined as

$$\lambda = \frac{x}{\sqrt{t}} \tag{4.10}$$

which reduces Eq. 1.14 to an ordinary (non-partial) differential equation:

$$-\frac{\lambda}{2}\frac{\mathrm{d}x}{\mathrm{d}\lambda} = \frac{\mathrm{d}}{\mathrm{d}\lambda}\left(D_w\frac{\mathrm{d}w}{\mathrm{d}\lambda}\right) \tag{4.11}$$

with the initial and boundary conditions

$$\begin{aligned} t = 0 \quad &\Rightarrow \quad \lambda \to \infty \qquad \text{and} \quad w = w_0 \\ x = 0 \quad &\Rightarrow \quad \lambda = 0 \qquad\ \ \text{and} \quad w = w_B \end{aligned} \tag{4.12}$$

These conditions describe the operating conditions of the experiment: a material sample of initial moisture content w_0 is placed at the time $t = 0$ in contact with a water surface on its side described by $x = 0$. This surface moisture content is denoted w_B. The X-ray system records successive w-λ profiles, from which the moisture diffusivity can be derived after integration of Eq. 4.11 using the conditions 4.12:

$$D_w = -\frac{1}{2}\frac{\int_0^w \lambda\,\mathrm{d}w}{\partial w/\partial\lambda} \tag{4.13}$$

4.2.2.2 Results

Moisture uptake in a non-damaged concrete sample was monitored by X-ray projection following the same procedure as described above (see Sec. 4.1.3). Six successive intensity mappings were recorded after contact of the sample with water. Because of the high heterogeneity of concree, the observation area for this series of measurements is slightly wider than that of cracked specimen (i.e. 5 cm width), in order to capture a representative section of the medium.

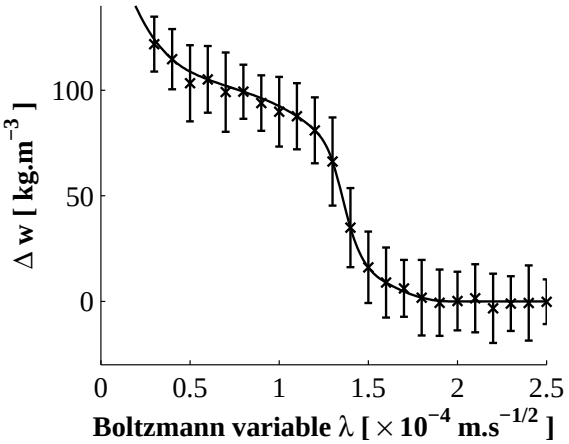

Figure 4.11: Superposition of successive moisture content profiles (error bars) and spline interpolation

These distributions were averaged over the width of the observation area and the thickness of the sample. After application of the Boltzmann transformation, the resulting w-λ profiles were superimposed and displayed on Fig. 4.2.2.2. This graph shows the average value of all profiles at a discrete set of values of λ, as well as the corresponding error bars. It can be seen that despite a non-negligible scatter due to the heterogeneity of the material, the profiles coincide appropriately. All profiles were then assembled as one average distribution, which was then smoothed and approached by a cubic spline interpolation. After this operation, it is possible to apply Eq. 4.13 in order to obtain the evolution of the moisture diffusivity D_w versus the concentration w, shown on Fig. 4.12(a).

As stated by [CAR 04], a boundary moisture content w_B must be assigned at the inflow surface in order to satisfy the Boltzmann boundary conditions. This value allows defining a boundary layer located at low values of λ in which the moisture content may exceed capillary saturation. In the present case, it was set to the value of w at which the maximal moisture diffusivity is reached (showed by the red dotted line on Fig. 4.12(a)). The moisture diffusivity was first computed based on one-dimensional concentration profiles resulting from an arbitrary value of the photon attenuation coefficient of water μ_w. This coefficient was then arranged so that w_B matched the known value of the

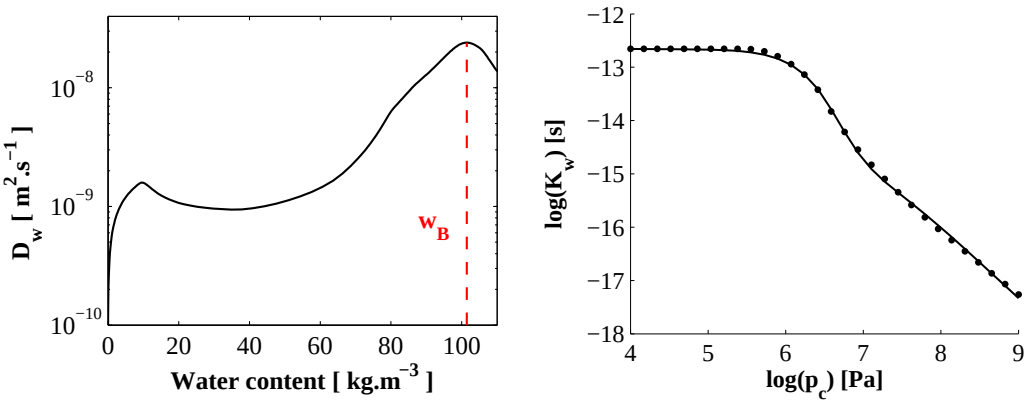

(a) (b)

Figure 4.12: (a) Moisture diffusivity and (b) permeability profiles, including Durner model interpolation

capillary saturation content w_{sat}, resulting in a value of $\mu_w = 17.12\,\mathrm{m}^{-1}$. This has been accounted for in the aforementioned graphs.

The computed diffusivity profile was finally translated into the moisture permeability through the previously measured sorption isotherm:

$$K_w = D_w \frac{\partial w}{\partial p_c} \tag{4.14}$$

which was then interpolated by means of a multimodal Durner model [PRI 06]:

$$K_w = K_{l,sat}\, s^{\tau} \left[\frac{\sum_i l_i \alpha_i \left(1 - \left(1 - s_i^{1/m_i}\right)^{m_i}\right)}{\sum_i l_i \alpha_i} \right]^2 \tag{4.15}$$

$$s_i = \frac{w_i}{w_{sat}} = l_i \left[1 + \left(\alpha_i |p_c|\right)^{n_i}\right]^{-m_i} \tag{4.16}$$

The parameters of this model applied to concrete are given in Tab. 4.5 and the resulting unsaturated moisture permeability profile is displayed on Fig. 4.12(b)

m	n	α (Pa^{-1})	l	K_{sat} (s)	τ
0.6148	2.5963	5.5383×10^{-7}	0.5062	2.2182×10^{-13}	-4.6975
0.1913	1.2366	2.2493×10^{-8}	0.4938		

Table 4.5: Coefficients of the multi-modal approximation of the moisture retention profile

Measurements of the transport and storage properties of non-damaged concrete have been performed, covering the entire range of relative humidity, and thus allowing modelling all transport phenomena of water in this material. These measurements have been interpolated by analytical expressions that may be implemented into a simulation code. All experimental data are therefore gathered for attempting the prediction of flow in fractured samples of concrete and validating these simulations in a two-dimensional frame.

4.3 Moisture flow modelling

The application of numerical simulation codes for coupled heat and moisture flow modelling is now a standard procedure in the study of porous construction materials and in their integration into the building envelope. Starting from originally simple calculation tools, methods of increasing complexity have been developed as to include effects of moisture buffering, mould growth, ageing... The last decade has seen the standardisation of the general expression of the heat and moisture conservation equations, and of the corresponding transport and storage coefficients [HAG 04, JAN 07]. The general framework of such models is the finite-element method (FEM). It is privileged for its applicability to a wide variety of problems, and its capacity to be extended as to allow their complexification.

A review on methods for fluid flow in porous media including discrete fracture networks was given in Sec. 1.3.4, identifying two separate approaches: fully coupled, and staggered. The coupled approach uses the same finite-element mesh for flow and transport modelling in the fractures and in the porous network, and the transport equations for both media are simultaneously solved. In the staggered approach, the transport equations for flow and transport are iteratively solved in the porous matrix and in the fracture, and boundary conditions are imposed at the interface, accounting for the variations of the pressure fields. One of the advantages of the staggered approach is that the FE mesh can be defined independently from the fractures by using the extended finite-element method, allowing including crack expansion without remeshing.

The specificities of the present work allowed developing a relatively simple numerical model while fully integrating the complexity of fracture networks. Simulations are run in already damaged media for the evaluation of their hygrothermal properties after ageing. Fracture positions and geometries are set prior to the simulations, which removes the need to include hydromechanical effects or fracture models, as well as the possibility of crack expansion. As a consequence, the following methodology is preferred: a finite-element frame is developed, integrating the conservation equations for coupled heat and moisture transfer in anisotropic porous media. A methodology for the automated processing of optical recordings of fracture geometries was then undertaken, that gives crack networks in the form of a set of segments. These segments are integrated into the finite-element mesh, which is automatically refined accordingly.

Specific transport properties are then attributed at the nodes located on fracture segments. This is a fully coupled approach, that allows including the description of longitudinal and transverse transport properties of cracks.

4.3.1 Model description

4.3.1.1 Finite-element frame

The FEM simulation code is based on the previously mentioned heat and moisture balance equations (see Sec. 1.2.2), which can be expressed as follows [JAN 07] :

$$c_{mm}\frac{\partial p_c}{\partial t} + c_{mh}\frac{\partial T}{\partial t} - \nabla \cdot \left(k_{mm}\nabla p_c + k_{mh}\nabla T\right) = 0 \tag{4.17}$$

$$c_{hh}\frac{\partial T}{\partial t} + c_{hm}\frac{\partial p_c}{\partial t} - \nabla \cdot \left(k_{hh}\nabla T + k_{hm}\nabla p_c\right) = 0 \tag{4.18}$$

where c_{xx} are the terms of hygric or thermal capacity, and k_{xx} are the terms of permeability or conductivity. This notation encompasses the effects of one field on the other by explicitely expressing the coupling terms. Here is a summary of all coefficients:

$$\begin{aligned}
c_{mm} &= \frac{\partial w}{\partial p_c} \\
c_{mh} &= 0 \\
c_{hh} &= c_m \rho_m + c_l w \\
c_{hm} &= c_l T \frac{\partial w}{\partial p_c} \\
k_{mm} &= K_l + \delta_p G_P \\
k_{mh} &= \delta_p G_T \\
k_{hh} &= \lambda + (c_v T + L_{lv})\,\delta_p G_T \\
k_{hm} &= c_l T K_l + (c_v T + L_{lv})\,\delta_p G_P
\end{aligned} \tag{4.19}$$

where the terms G_P and G_T originate from the translation of the vapour pressure gradient into capillary pressure and temperature gradients, previously explicited in Eq. 1.12:

$$\nabla p_v = G_P \nabla p_c + G_T \nabla T \quad \Rightarrow \begin{cases} G_P = \dfrac{p_v}{\rho_l R_v T} \\ G_T = \dfrac{p_v}{\rho_l R_v T^2}\left[\rho_l L_{lv} + p_c\left(\dfrac{T}{\sigma}\dfrac{\partial \sigma}{\partial T} - 1\right)\right] \end{cases} \tag{4.20}$$

The numerical implementation of Eq. 4.17 and 4.18 was performed by the finite-element method, following [JAN 07]. The Galerkin weighted-residual method was used for the spatial discretisation over a triangular mesh of Lagrange-type quadratic elements. The temporal discretisation follows the implicit scheme. As the storage and

transport coefficients of the equations are functions of the field variables p_c and T, the discretised system is strongly non-linear: the solution of each time step is approached iteratively, and a Newton-Raphson iterative scheme was used as to accelerate the convergence. Finally, a dynamic time stepping was implemented, adapting the size of each time step according to the number of iterations of the previous step. A more thorough explanation of this procedure for the numerical implementation of the model is given in appendix B.

4.3.1.2 Integration of fracture networks

The present section describes the undertaken methodology for simulating flow in the measured fracture networks with the finite-element model. The first step into this procedure is the integration of crack geometries into the FE grid, and is illustrated on Fig. 4.13 with the example of one of the tested concrete samples.

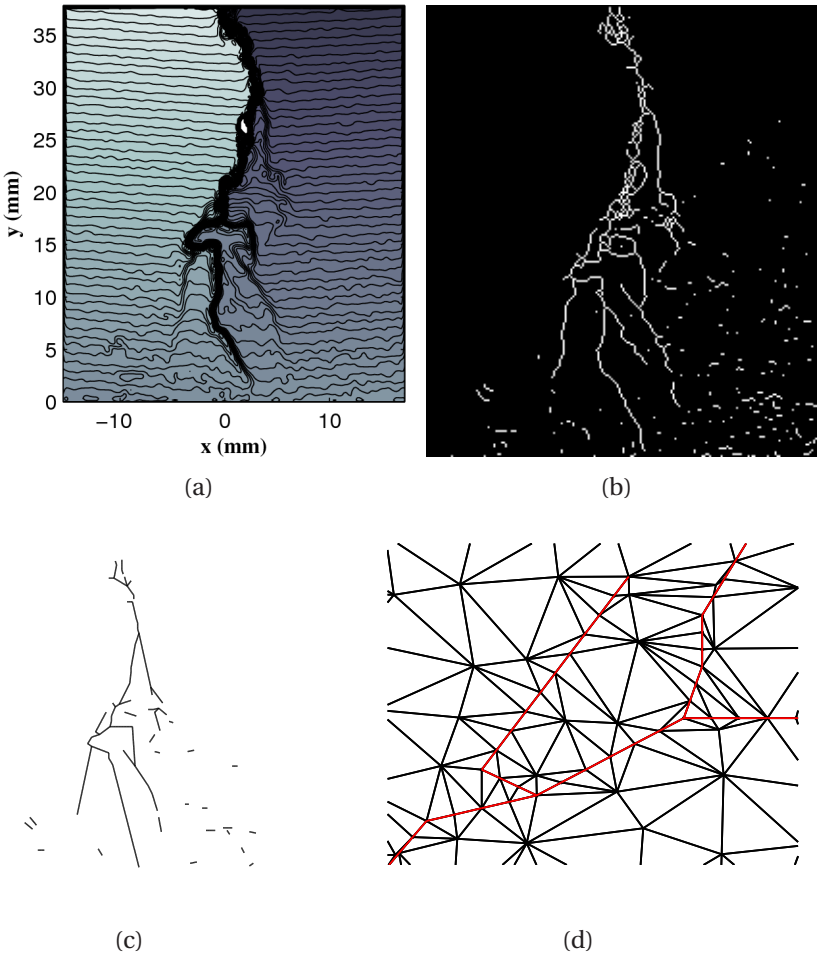

Figure 4.13: (a) DIC displacement mapping, (b) skeletonised and (c) discretised fracture network, (d) close-up of an adapted finite-element mesh

The crack integration procedure consists of four steps:

1. The displacement mapping at the surface of the specimen is computed with the DIC algorithm, by comparing the reference image of the initial state of the sample with the image taken after mechanical loading and unloading. This reveals displacement gradients in the form of contour lines (see Fig. 4.13(a)) indicating the presence of fractures and their local aperture.

2. A threshold is applied on strain mappings as to reveal the cracked surface in the form of a binary image. This step in similar to the procedure of Sec. 3.2. The resulting patterns are treated by topological skeletonisation, revealing crack networks as shown on Fig. 4.13(b).

3. These networks are discretised as a set of segments of given position, length and aperture (see Fig. 4.13(c)).

4. The finite-element mesh is generated over the observation area (see Fig. 4.13(d)). Nodes are added along the fracture segments, discretising each one into smaller elements. The mesh is then readjusted so that these segments match the edges of the surrounding elements.

The present model therefore belongs to the category of mesh-adapting models. Cracks are explicitly modelled in the primary FE mesh, as opposed to staggered approaches [ROE 06b, RET 07, ALF 10, MOO 11] in which transport equations are solved separately in the fractures and in the porous medium. For such a fully coupled analysis, fracture elements can be double-nodded for a full account of transverse diffusion mechanisms through the interfaces [SEG 04]. A less comprehensive formulation is however privileged here for simplification purposes. Another potential of improvement of the current methodology is the fact that the current mesh is not optimised near the discontinuities, resulting in possible stretched element shapes (see Fig. 4.13(d)). This can be improved by envisaging more advanced refinement strategies [SEC 03, SCH 06].

4.3.1.3 Fracture flow

Once integrated into the FE mesh, specific transport properties are attributed to fracture nodes. This matter is illustrated on Fig. 4.14. The expression of the liquid water permeability K_l of these nodes is replaced by a permeabiliy tensor $\mathbf{k}_f$ such as:

$$\mathbf{k}_f = \mathbf{R}^T \begin{pmatrix} k_{f,l} & 0 \\ 0 & k_{f,t} \end{pmatrix} \mathbf{R} \tag{4.21}$$

in which $k_{f,l}$ and $k_{f,t}$ are the respective values of the longitudinal and transverse fracture permeability, and $\mathbf{R}$ is the rotation matrix for directing the permeability tensor in the direction of the crack:

$$\mathbf{R} = \begin{pmatrix} \cos\theta & \sin\theta \\ -\sin\theta & \cos\theta \end{pmatrix} \tag{4.22}$$

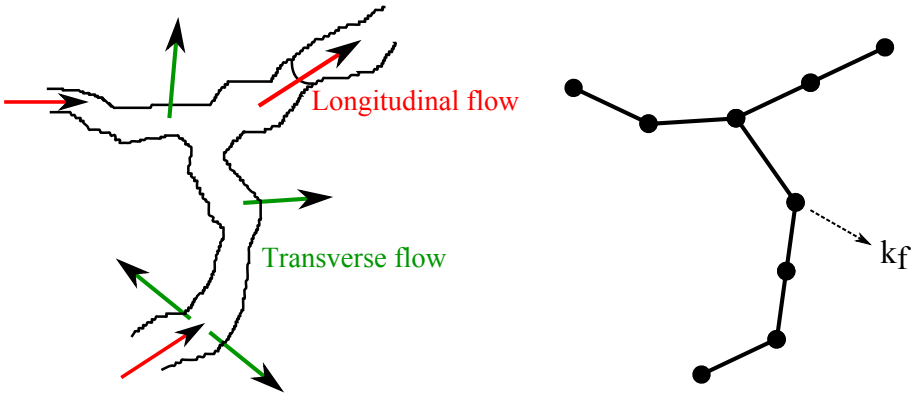

Figure 4.14: Fracture discretisation and expression of the longitudinal and transverse flow

where θ is the angle of the crack segment with the coordinate system, or the average value of the angle in case of a node located at the intersection between several segments. The expression of the longitudinal permeability in a water-saturated crack of aperture u results from the analytical solution of the Navier-Stokes equations for flow between two parallel plates:

$$k_{f,l} = \begin{cases} \dfrac{\rho_l}{\eta_l}\dfrac{u^2}{12} & \text{if} \quad |p_c| \leq \dfrac{2\sigma}{u} \\ k^*_{f,l} & \text{if} \quad |p_c| > \dfrac{2\sigma}{u} \end{cases} \tag{4.23}$$

A critical capillary pressure is defined according to the occupancy criterion [VAN 03], derivated from the Young-Laplace equation (Eq. 1.2). This value separates fracture segments filled with water, of which permeability is set to $k^{sat}_{f,l} = \rho_l u^2/12\eta_l$, from non-saturated segments of permeability $k^*_{f,l}$. This non-saturated longitudinal fracture permeability was simplified to a logarithmic interpolation as to reach a computational value of zero (namely 10^{-17} s) at dry conditions. The profile of $k_{f,l}$ is shown on Fig. 4.15 with the example of a crack of aperture $u = 2 \times 10^{-6}$ m.

In the formulation of the occupancy criterion (Eq. 4.23), the influence of the water/air contact angle is neglected. Some authors however argue that its value may differ between the cases of water suction and drainage [VAN 03]. This formulation of the longitudinal fracture permeability $k_{f,l}$ directly impacts the transport coefficients k_{mm} and k_{hm} of Eq. 4.17 and 4.18. Transverse flow in the cracks, as well as effects of the resistance of the crack/matrix interfaces to moisture flow, were neglected: this involves that the transverse permeability $k_{f,t}$ written in the $\mathbf{k}_f$ tensor was set to the same value as in the surrounding porous medium.

This formulation has been chosen for its relatively simple implementation into the developed finite-element frame. It suffers however from an important drawback, caused by the fact that values of permeability are added onto the primary mesh. When calculating the element permeability matrices of the triangular elements surrounding

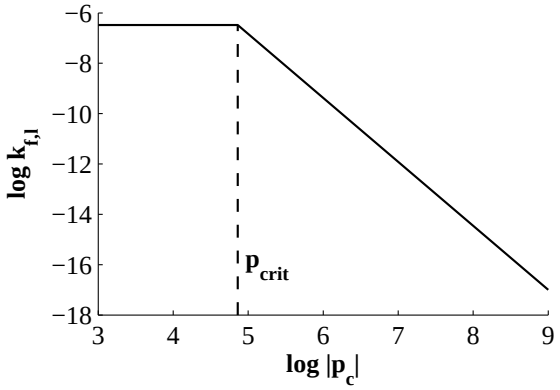

Figure 4.15: Fracture discretisation and expression of the longitudinal and transverse flow

a crack (Eq. B.15), the permeability of the primary nodes are interpolated to the Gauss integration points (Eq. B.33). This results in a mesh-dependent smoothing of the value of permeability around cracks. As a consequence, the calculated capillary pressure distributions are expected to slightly deviate from the real solutions during the filling and draining of fracture segments. The importance of this mesh-dependency is to be estimated in a sensitivity analysis, shown in Sec. 4.3.2.2.

The above described procedure, although it does not encompass an extensive description of flow mechanisms at the smaller scales, is considered satisfactory for its accurate description of the real fracture geometries and its relatively simple implementation. Moreover, the concept can be extended as to include the effects of the longitudinal and transverse thermal conductivities of fractures. Further possibilities for the improvement of the code include:

- a more comprehensive description of the unsaturated permeability and storage capacity of fractures segments as function of their aperture and rugosity [VAN 03],
- the optimisation of the mesh refinement strategy near the integrated fractures [SCH 06],
- the integration of the transverse fracture flow [SEG 04].

These simplifications are expected to have little impact on the simulation results, but may influence the overall performance of the code. This will be discussed after the display of the results.

4.3.2 Results and discussion

Simulations were set to recreate the operating conditions of the moisture uptake experiments performed in the X-ray system (Sec. 4.1.3).

- initial conditions of a dry sample: $p_c = -5 \times 10^8$ Pa, $T = 20°$ C
- isothermal transfer
- constant capillary pressure ($p_c = -10^3$ Pa) prescribed on the bottom boundary, and upper boundary open to air: RH = 50%, $T = 20°$ C, $\alpha = 7$ W.m^{-2}, $\alpha = 3 \times 10^{-8}$ s.m^{-1}

Results are displayed in the present section concerning one of the tested samples, of which crack pattern is shown on Fig. 4.13 and moisture infiltration on Fig. 4.8(c). This example was chosen as to show the correct prediction of flow in a non-trivial set of crack branches resulting in a non-rectilinear moisture front. A triangular mesh of 70×70 nodes was generated on the observation area of 4 cm side. The size of the element edges is therefore of roughly 0.6 mm per element, although this size varies due to the non-structured nature of the mesh. After generation of this primary mesh, the measured fracture geometries were superimposed, and fracture segments were discretised with a 0.3 mm distance between nodes.

4.3.2.1 Moisture content distributions

A qualitative overview of moisture content distributions computed by the simulation code is first provided. These results are shown in two parts: first (Fig. 4.16), the early water infiltration is shown in the crack network. Then (Fig. 4.17), the predicted uptake is compared to the X-ray mappings of moisture content as to validate the model.

Fig. 4.16 shows the non-dimensional saturation level of the two-dimensional concrete specimen, as well as the discretised fracture segments (red lines), during the first minute after initiation of the wetting phase. The suction of water by the crack segment reaching the bottom surface, and all interconnected segments, can be seen to occur promptly. The code therefore takes good account of the anisotropy of the material, and handles all fracture geometries well, including intersections and isolated cracks. After this first phase of wetting, the moisture front expands in the surrounding porous medium at a slower pace, as is displayed on Fig. 4.17.

The comparative results of the moisture concentration monitoring and modelling are shown as two consecutive measurements of the saturation distributions for the same sample. The displacement field at the surface of the sample is shown as contour lines on the upper left image. The simulations show a fair accuracy in the shape and evolution of the moisture fronts from the bottom water surface and from the fractures. At earlier stages of wetting, it is visible on both simulations and experiments that the shape and tortuosity of the cracks has a noticeable impact on the shape of the moisture fronts (Fig. 4.17(a) and 4.17(b)). The crack width shows no noticeable impact on the moisture flow in the neighbouring porous material: because concrete has a low permeability, the flow inside the fracture occurs at a much smaller time scale than through the porous network. Therefore, the moisture saturation of a water-filled crack does not appear affected by the migration of moisture through its walls to the porous network.

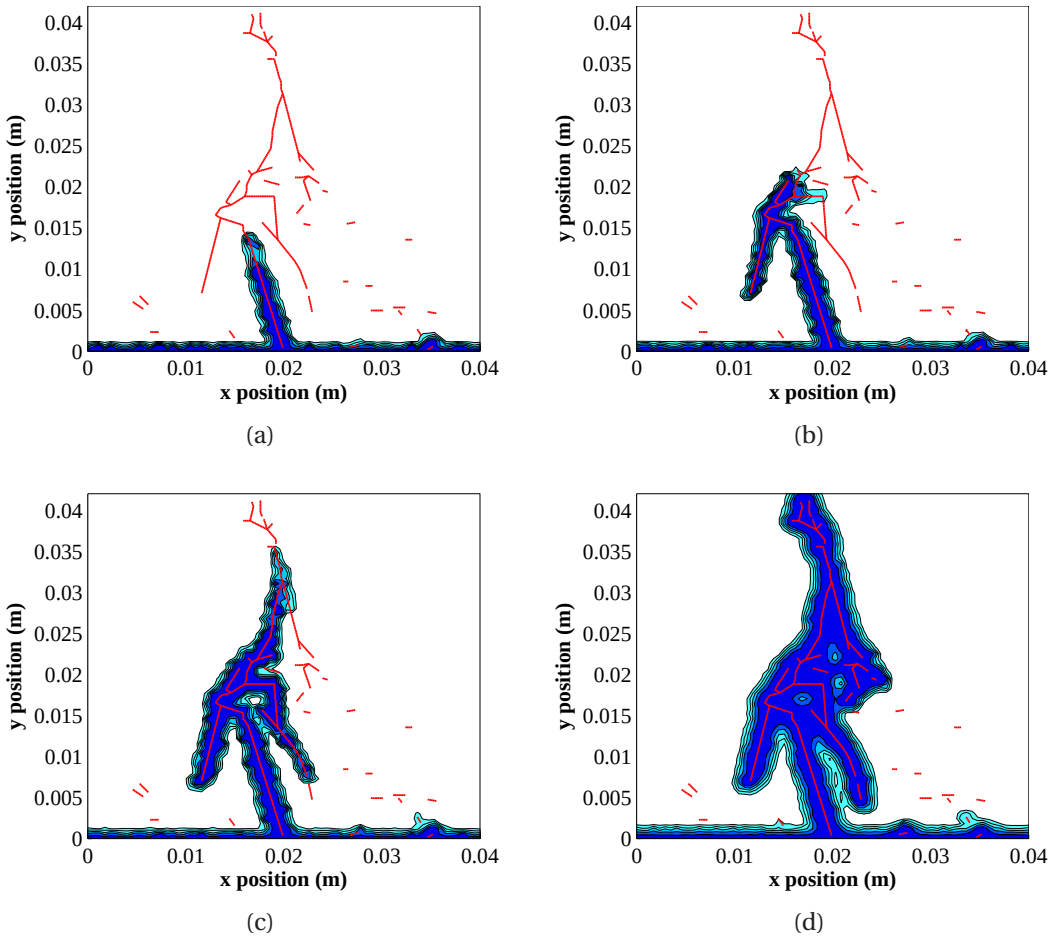

Figure 4.16: Non-dimensional moisture content distributions after (a) 10, (b) 15, (c) 20 and (d) 60 seconds of wetting

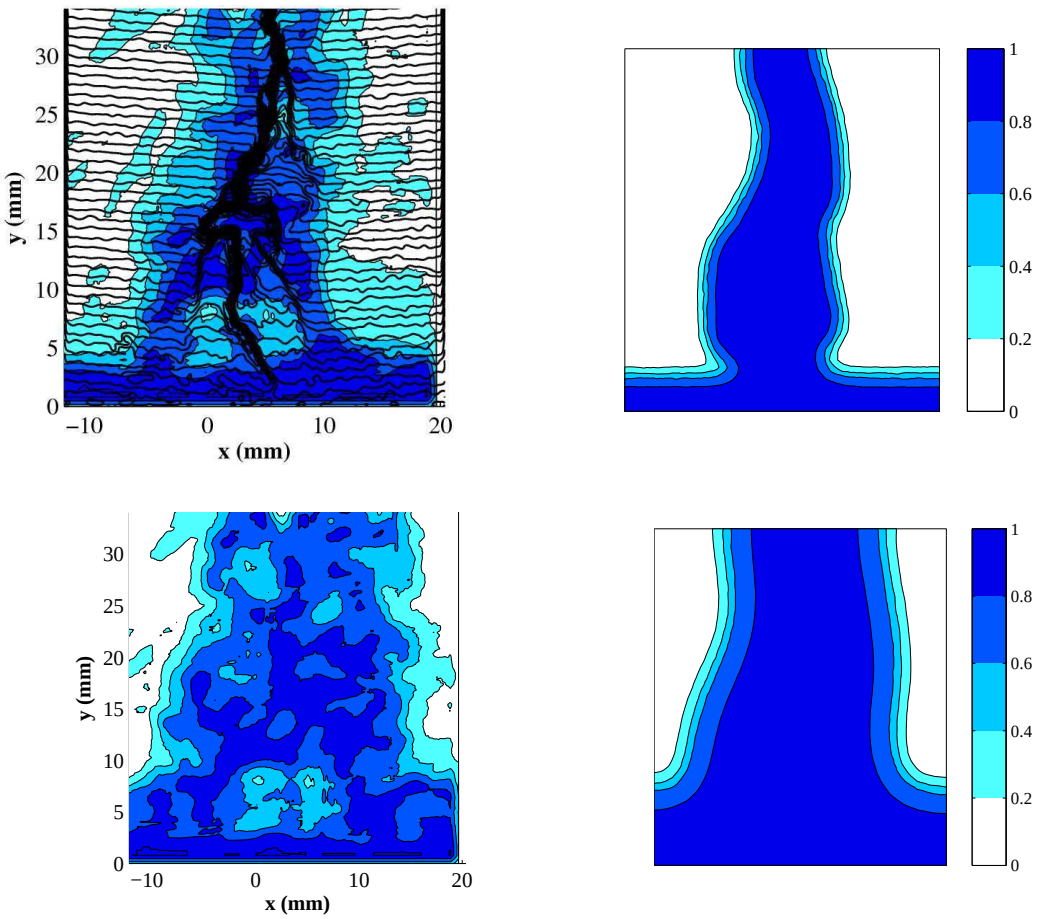

Figure 4.17: Measured (left) and simulated (right) distributions of the saturation degree s after 10 minutes (above) and 40 minutes (below) of wetting

4.3.2.2 Mesh sensitivity and validation

The model has been shown to properly account for the presence of fractures in the finite-element mesh. This qualitative overview of the results is now completed by quantitative information. More specifically, simulations are confronted with the measurements in terms of the total amount of water adsorbed by the material sample. This criteria is applied for assessing the importance of the discretisation density of the fracture segments: a basic mesh sensitivity analysis is performed.

Because of the very high moisture permeability of cracks in comparison to that of the surrounding porous material, it is clear that the density of the discretisation has an impact on the quality of the simulations. As described earlier, nodes are distributed along fracture segments with a given density, herein referred to as the density of crack discretisation, or fracture refinement. The distance between these nodes must be smaller than that between nodes of the primary FE mesh, as illustrated on Fig. 4.18.

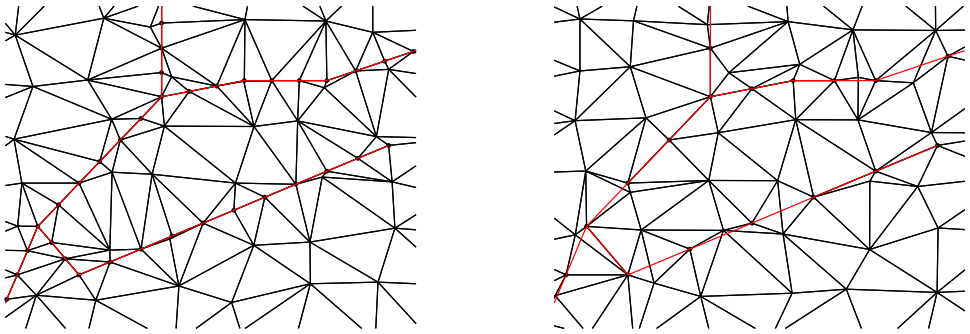

(a) (b)

Figure 4.18: Close-up of the mesh resulting from a crack discretisation of (a) 3×10^{-4} m and (b) 7×10^{-4} m

Given a set of node coordinates, the edges of the elements are generated by Delaunay triangulation. If the distance between fracture nodes is small enough, these points are necessarily each other's natural neighbor, and an element edge is systematically generated along each crack segment. This is shown on Fig. 4.18(a), in which the fracture refinement was set to 0.3 mm while the average distance between primary nodes is 0.6 mm. If however the fracture refinement is coarser than that of the initial mesh, parts of the cracks will not be located along element edges, as shown by Fig. 4.18(b). This has important consequences on the calculations: in these cases, the interpolation of the moisture permeability to the Gauss-Legendre integration points (see Eq. B.31) will not account for the presence of the fracture.

The influence of the density of crack discretisation on the solution is studied. Starting from a same density of the initial mesh, a series of simulations were run, each one with a different value of the distance between fracture nodes: 0.1, 0.3, 0.5 and 0.7 mm.

The total amount of absorbed water in the observation area of all simulations is showed versus the square root of time on Fig. 4.19.

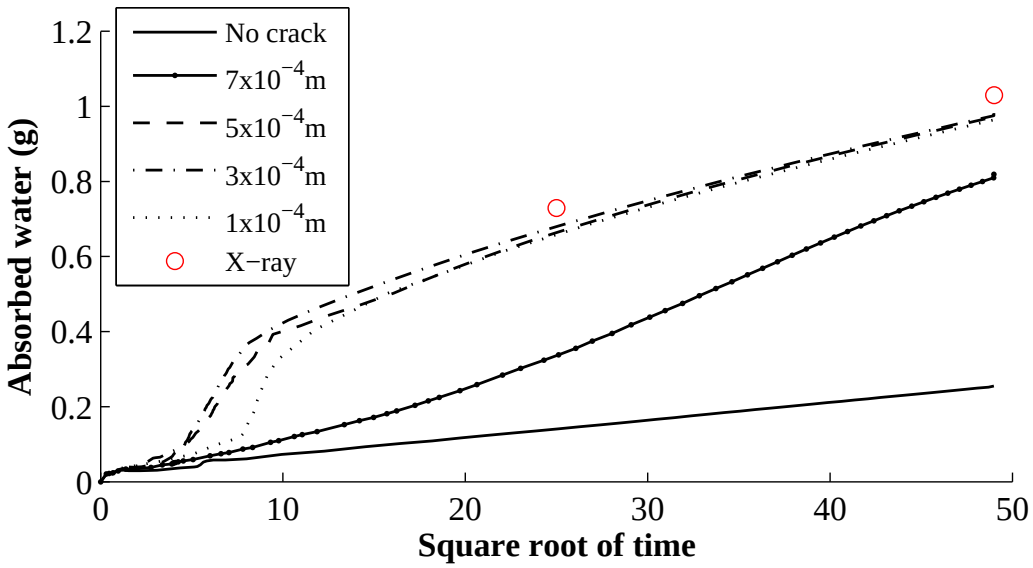

Figure 4.19: Quantity of absorbed water by capillary uptake versus square root of time for several densities of crack discretisation

The continuous line shows the results of a reference calculation of capillary uptake in the non-damaged porous medium. The evolution of mass uptake versus square root of time is nearly linear, as is expected from one-dimensional free moisture uptake. The absorption rate of water is higher in the presence of cracks (dotted lines), but seems to be influenced by the mesh density.

- If the crack discretisation density is finer than that of the original FE mesh (1×10^{-4}, 3×10^{-4} and 5×10^{-4} m per segment), a steep increase of moisture content occurs at small simulation times ($0 \leq \sqrt{t} \leq 10\ \mathrm{s}^{1/2}$), during water migration in the main fracture (see Fig. 4.16). Once this fracture is filled, moisture diffusion continues at a nearly linear rate. The slope is higher than in the non-damaged simulation, as the moisture front extends not only from the bottom water surface, but also from the sides of the crack (see Fig. 4.17(b) and 4.17(d)).

- If the fracture refinement is coarser than the original mesh (7×10^{-4} m per segment) the main crack is not fully integrated in the mesh (see Fig. 4.18(b)): the moisture uptake rate is decreased, although it remains higher than in the non-fractured case.

The current procedure for crack integration in a FE mesh therefore implies the existence of a threshold value for the distance between fracture nodes. The automated Delaunay triangulation as it is applied does not allow explicitely setting the edges of

the elements, and this threshold must be respected for a full integration of cracks in the final mesh.

The simulations performed with finer discretisation densities however do not fully coincide. The phase of water suction in the fractures, i.e. the time interval of highest uptake rate, seems to always initiate with a delay, which is not reproducible. Moreover, this delay increased by simulating capillary uptake with a high fracture refinement of 1×10^{-4} m. This behaviour seems counterintuitive and could be explained by the distorsion of the triangular elements near the fracture, occuring when the crack refinement is high in compaison to the density of the surrounding mesh (see Fig. 4.20).

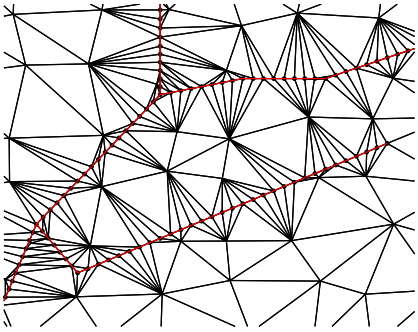

Figure 4.20: Close-up of the mesh resulting from a crack discretisation of 1×10^{-4} m

The interpretation of the simulation results yields an additional observation. On Fig. 4.19, the red circles show the total experimentally measured moisture content, which have been recorded by X-ray radiography as shown on Fig. 4.17(a) and 4.17(c). Although this moisture content is slightly underestimated by the simulations (likely because of the underestimation of the fracture suction rate), the slope between the two measurement points is very well captured by the calculations. This means that moisture diffusion in the porous medium is accurately predicted once the cracks are filled with water.

4.3.2.3 Calculation time

During water suction by a fracture, the moisture content distributions undergo very fast local variations. As a result, convergence may only be reached in case of very small time steps, in the order of 0.1 s. The highest computational cost therefore originates from this first phase of wetting: with the current settings, using a standard desktop computer, the first minute of simulation time (during the fracture flow) requires around four hours of calculations. Once the main fracture is filled, the variations of moisture content are slower because of the relatively low permeability of concrete: the time step automatically increases as a smaller number of iterations is necessary to reach convergence. The computational cost is then significantly reduced.

The fracture discretisation density has little impact on the computational cost of the problem. Indeed, the number of additional nodes, even in case of high refinement, is low in comparison to that of the primary mesh.

4.3.2.4 Discussion

This set of simulation results, compared to moisture content distribution measurements by the X-ray radiography technique, leads to a twofold conclusion concerning the proposed methodology. First, the numerical integration of fracture anisotropy was successfull, and crack geometries were properly accounted for in the geometry of the problem. Moreover, the prediction of moisture ingress in the porous medium once the fractures are filled with water are accurate in terms of shape of the moisture content distributions, as well as in terms of quantitative estimation of the total moisture content. However, as earlier mentioned, the addition of an extra permeability to the integration points yields mesh-sensitive results: unaccuracies remain in the prediction of fracture flow and of moisture diffusion towards the porous medium. The validation of the simulation code in regards to isothermal moisture flow in fractured porous materials is therefore incomplete, but problems are restricted to the short-term part of moisture uptake simulations. Moreover, the calculation of the flow inside the fractures leads to computational difficulties because of their very high liquid permeability, which can locally rise by up to six orders of magnitude between adjacent elements of the mesh.

Another possibility for calculating the progress of the moisture front in a fracture is the moving front technique [HVI 98] that separates a 1D discrete model for flow inside the fracture with the model for the porous matrix, and solves the equations iteratively. This method was found to improve convergence but was only applied to a simplified crack geometry [ROE 03b]. The methodology chosen in the present work was aimed at being directly applicable to any given network of interconnected fractures of all sizes and orientations. Moreover, it allows an unambiguous implementation of the non-saturated permeability of fractures, as well as their contribution in the drying of specimen. It is expected that the convergence problems may be partially solved by applying more advanced mesh refinement strategies [SCH 06], which may also reduce computational costs.

4.4 Conclusion

The target of the work presented in this chapter was the development and the validation of a simulation code for coupled heat and moisture transfer, which enables the user to integrate measured fracture geometries, and predicts the resulting flow. Cracked samples of concrete have been submitted to moisture uptake measurements by X-ray radiography, after their fracture patterns were observed by digital image correlation. Moisture uptake was monitored as to confirm the ability of computer vision

to predict the moisture uptake paths in the earlier stages of wetting. The water infiltration from the fractures to the surrounding porous material was then observed. These moisture content profiles were then approached by finite-element moisture uptake modelling based on the measurements of deformation fields at the surface of the samples. The moisture characterisation of concrete was performed, in order to supply the model with the necessary parameters for moisture transfer prediction. The experimental methodology was carried on a series of samples and provided a complete data set for the validation of the simulation code. A good agreement was found between measurements and modelling results in terms of 2D moisture content distributions, and of total quantity of absorbed water.

Several possibilities can be considered for the improvement and the extension of this procedure. First, in order to be applicable to the case of fracture observations performed at larger scales, a new method must be implemented for the input of crack geometries obtained from other measurement techniques. The previous chapter investigated how Acoustic Emission can be used to this aim. Since this technique allows a 3-dimensional localisation of sources of damage, the model can be extended for 3D modelling of flow in fractures. For the validation of such a model, 3D monitoring of water uptake by X-ray tomography can be considered. Further possible improvements of the simulation code include the refinement of the FE mesh and the account of transverse flow in fractures.

Chapter 5

Application of the simulation code

The last step of the study is the application of the previous results to the estimation of the long-term consequences of cracking at the scale of building components. Measurements of a fracture network were integrated into simulations of multi-layered facades, subjected to realistic climatic conditions. The impact of cracks on the hygrothermal performance of these facades was estimated by comparing these results with the behaviour of non-damaged walls. Moisture infiltration and accumulation is visualised, allowing durability assessments.

Contents

Long-term simulations of the hygrothermal performance of building components are now a common practice for the assessment of moisture related damage and the identification of potential durability issues. These considerations can moreover be integrated into the larger frame of building-scale simulations [CRA 00, KAL 07] in order to account for the all environmental factors impacting damage on a given facade. The effects of ageing on the transport and storage properties of materials, as well as the presence of discontinuities such as fractures, is however not accounted for in such numerical studies: this is the motivation of the present work, as was announced in the beginning of the manuscript. Simulations of flow in materials undergoing damage or crack propagation have been already conducted by several authors as to recreate lab measurements [ROE 03b, MOO 09, ALF 10]. They were however not applied to large time intervals or confronted with the hygric and thermal boundary conditions of an existing building. To the author's knowledge, no existing code conciliates a precise knowledge of fracture geometries with long-term hygrothermal performance assessments.

The target of the last step of the work is to show how the presented methodology can lead to hygrothermal performance and durability assessments of any type of fractured building component. It is the logical conclusion of the two previous steps, respectively the investigation of experimental methods for damage quantification, and the development of the simulation code enabling the user to integrate such measurements into a finite-element frame.

First, Sec. 5.1 shows how the developed model has been validated in regards to coupled heat and mass transfer in multi-layered walls, under severe climatic loads. Then, in Sec. 5.2, the conditions of a series of simulations are laid, which have been defined in order to illustrate the potential impact of cracks of the moisture infiltration and heat loss of simple wall geometries. Finally, the results of these simulations are presented in Sec. 5.3.

5.1 Non-isothermal validation

In the previous chapter, we mentioned two specifications required from the simulation code. The first requirement is the possibility of including fracture measurements into simulations of moisture flow, and is the main subject of the previous chapter. The second specification of the model is allowing long-term simulations of coupled heat and mass transfer in a multi-layered wall. For complexity reasons, acquiring a complete set of experimental measurements for the validation of a model in regards to coupled heat and mass transfer under climatic loads, and during long simulation time spans, was not undertaken. Instead, the capacity of the model to handle these conditions, without the presence of fractures, was assessed by comparison with results of other simulation codes.

The Hamstad project was initiated by the European Union to develop a platform for the assessment of computational HAM modelling in building physics. The first

package of the project [ROE 03a] addressed material characterisation, while the second package [HAG 02b] established a standard methodology of HAM modelling, in order to provide an alternative to the Glaser method for calculation, prediction and evaluation of the moisture performance of the building enveloppe. As part of this work package, a series of benchmarks were proposed [HAG 02a] in order to cover various combinations of climatic loads and of materials, and to deal with resulting phenomena: internal condensation, moisture movement caused by thermal gradients, effect of water on the thermal conductivity...

The project served as a set of guidelines for the development of the simulation code. These guidelines can be summed up by the following requirements: it must enable heat and mass transfer simulations of multi-layered walls, including materials covering wide ranges of hygric and thermal properties, under possibly severe climatic loads. The model was tested and validated with four of the five benchmarks of the project. The exception is the third benchmark, dealing with air transfer, which the model was not set to handle. The following paragraphs illustrates this validation with the example of the fourth benchmark, which is the most demanding part of the work package.

5.1.1 Benchmark description

The considered benchmark (response analysis) deals with the one-dimensional moisture movement inside a wall with a hygroscopic finish. The simulation time is 5 days, during which highly changing climatic conditions are imposed, successively generating moisture condensation, redistribution and evaporation [HAG 04]. The boundary conditions are prescribed in the form of heat and moisture flows, given in Eq. 1.27. Hourly values of the external and internal air temperature and vapour pressure are given, as well as an equivalent external temperature including the influence of solar radiation (see Eq. 1.30), and the liquid inflow caused by rain (see Eq. 1.29). The case is complicated by capillary active materials of very high moisture permeability. The thermal conductivity and hygric parameters of such materials can be strongly influenced by the moisture content.

Moisture transfer is a strongly non-linear phenomenon and the resolution of Eq. 4.17 and 4.18 involves important mathematical difficulties. The considered benchmark case being particularly demanding, the numerical results obtained by the participants may differ, although the simulation codes apply the same transport equations. A statistical approach is used for the evaluation of the solution, based on the analogy with a t-distribution. A band of acceptance is defined as the range within which results are considered acceptable:

$$\overline{x} - t_p \frac{\sigma_x}{\sqrt{n}} \leq \mu \leq \overline{x} + t_p \frac{\sigma_x}{\sqrt{n}} \tag{5.1}$$

where $\overline{x}$ and σ_x are the main value and standard deviation of the sample set, n is the number of observations and t_p is a function of n and the confidence grade p, defined as the risk the band of acceptance does not contain the true numerical solution. For

a given value of p, an increase of the number of participants reduces t_p and narrows the band of acceptance, as the probability of knowing the real solution of the problem increases. In the following display of the results, the confidence interval was set to $p = 1\%$, i.e. a 99% chance that the band contains the correct solution, resulting in a value of $t_p = 3.71$.

Although the simulation case is one-dimensional, the HAM simulation code was only developed for 2D cases: a quasi-1D mesh was therefore generated with a narrow rectangular geometry and two insulation boundary conditions. The density of the mesh is an important parameter of the simulations: indeed, very important gradients of capillary pressure can be present at the moisture front in case of nearly water-saturated areas generated by rain, and due to moisture redistribution across the interface between the two layers. The mesh was made of quadratic triangular elements of roughly 1 mm edges. Moreover, the high moisture permeability of both materials involves a fast advance of the moisture front: the adaptative time stepping method finds its use by decreasing the time step to the order of seconds at the beginning of rain showers, or at sudden changes of the external equivalent temperature.

5.1.2 Results

The benchmark exercise was undertaken by 6 participants [HAG 02a]: Chalmers University of Technology, University of Leuven, Technical University of Dresden, Technion Institute of Technology, National Research Council of Canada, and Fraunhofer Institute of Building Physics. The results obtained in these institutes were compared in terms of temporal evolution of the field variables at given locations in the wall, and of spatial distributions at given times of simulation. The results of the presented model are shown on Fig. 5.1 to 5.4, respectively depicting the evolution of the moisture content and of the temperature, at the inner and outer surfaces of the facade, during the five days of simulation.

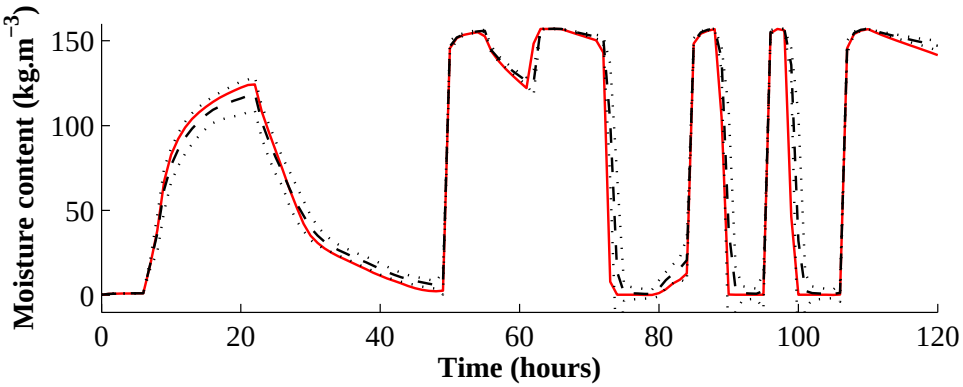

Figure 5.1: Moisture content at the outer surface

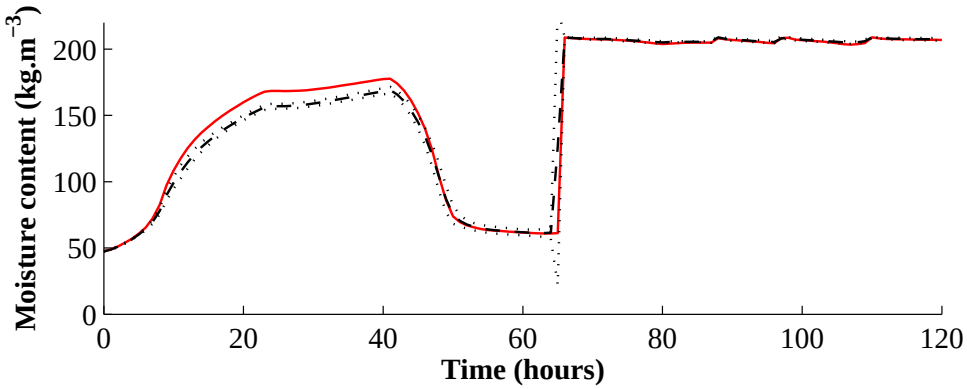

Figure 5.2: Moisture content at the inner surface

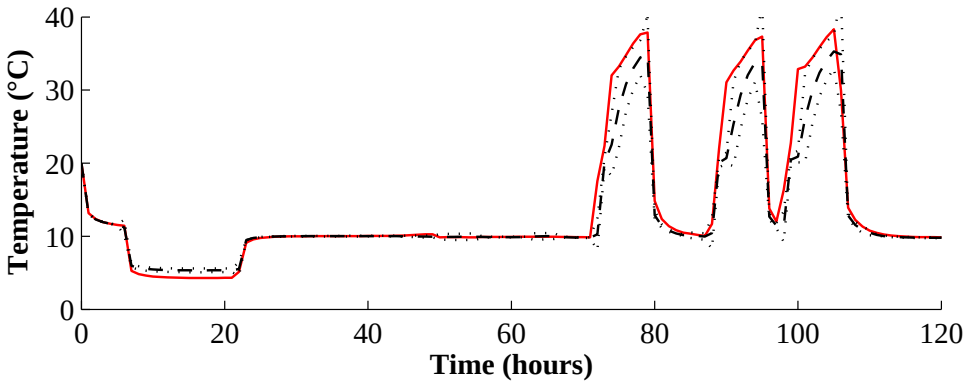

Figure 5.3: Temperature at the outer surface

On each graph, the red continuous line shows the distribution obtained by the current model, while the dotted lines show the average distribution of the other six participants, as well as the limits of the 99% confidence interval. During the entire time of simulation, the external air temperature and vapour pressure, and the internal equivalent temperature, are constant. The variations of the other boundary conditions roughly occur in three main successive stages.

- The first phase lasts from 0 to 49 hours of simulations: a drop of the equivalent external temperature to -2°C generates condensation on the external wall surface, and the moisture content of the internal layer rises due to an increase of internal vapour pressure.

- The second phase lasts from 50 to 66 hours: all temperatures are constant, and two closely successive rain showers occur. The first rain shower generates a sudden rise of the external surface moisture content to the state of saturation. After the rain stops, this concentration decreases as the material dries, and because of moisture redistribution. Shortly after the second rain shower, the moisture front

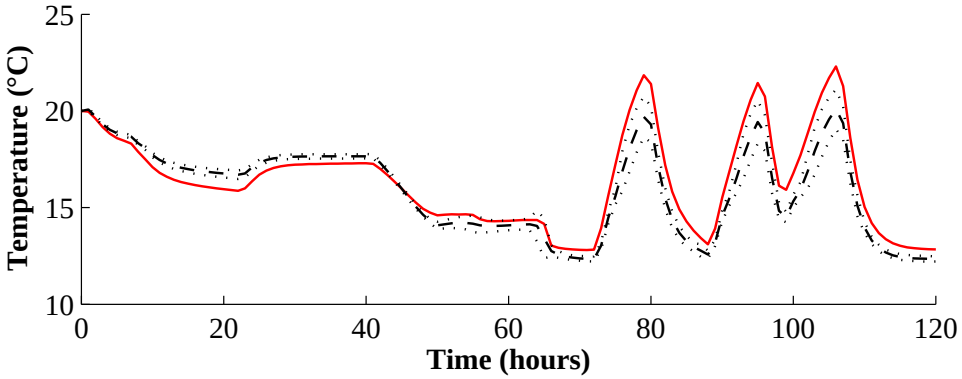

Figure 5.4: Temperature at the inner surface

reaches the second material layer (hygroscopic finish) and the moisture content of the internal surface rises as well.

- The third phase lasts from 67 to 120 hours. Square-wave fluctuations of the external equivalent temperature between 10 and 50°C occur alternating with rain showers. Because of the high mositure diffusivity of the load bearing material, these rain showers prevent the internal layer from drying. Temperature variations quickly affect the external surface temperature, and affects the internal surface temperature with some delay.

The performance of the proposed model during these solicitations offers a fair accordance with the statistical analysis based on the previous results of the other participants. The calculated moisture content distributions mostly stay within the band of acceptance. However, the evolution of the external and internal surface temperature diverges slightly from the expected values when the ambient thermal load is important. This implies a light overestimation of the moisture condensation at the internal layer during the first phase of the simulation protocol. This stage of the simulation is particularly sensitive to the expression of the coupling between heat and moisture transfer, particularly to the value of the latent heat of evaporation L_{lv}, of which influence appears on Eq. 1.6, 1.12, 1.19 and 1.27.

The simulation code can therefore be considered appropriately able to predict coupled heat and moisture transfer in multi-layered facades, under heavy climatic loads, during longer times of simulation. Along with the validation of water infiltration in fractures, presented in the previous chapter, the conditions are met for the application of the model to a set of simulation cases. This is the subject of the next part of the study: the simulation cases are described in Sec. 5.2, and the results of the calculations are displayed in Sec. 5.3.

5.2 Definition of the simulation cases

The last step of the study is the application of the validated model to the evaluation of the hygrothermal performance of building components integrating fractured material layers. For this purpose, a series of simulations has been performed, so that the comparison of their results gives an estimate of how fractures may influence phenomena such as moisture accumulation and heat loss. The present section is the description of these simulation cases: first, the building components and materials are presented in Sec. 5.2.1.1. Then, Sec. 5.2.2 describes the choice of boundary conditions and climatic data, and further settings of the model are detailed in Sec. 5.2.3.

These simulation cases have been defined in order to answer a threefold questioning:

- to estimate the consequences of fractures on the moisture accumulation and heat loss of a standard wall,
- to find whether these consequences are aggravated by the infiltration of moisture towards insulation materials,
- to illustrate how outer insulation including hygrophobic materials can correct the flaws generated by fractures.

5.2.1 Geometry

5.2.1.1 Components and materials

The setup of the simulated walls is shown on Fig. 5.5 and the corresponding materials are listed in Tab. 5.1 along with the reference for their properties.

Three facades have been defined: a simple non-insulated wall with an internal finishing layer (case 1), a similar wall including inner insulation (case 2) and one including outer insulation (case 3). In all cases, the load-bearing material is a layer of concrete of 20 cm, and a gypsum board of 1.25 cm thickness is added at the internal surface. Case 2 includes a 10 cm layer of interior insulation (fibreboard), and case 3 includes an outer insulation made of 1 cm hygrophobic coating (fibre-reinforced mortar) and 10 cm insulation (mineral wool). The moisture transport and storage properties of concrete and mortar have been previously characterised. Their thermal properties, as well as all transport and storage properties of the other materials, were taken from databases or from the literature: [HAG 02a, KUM 02] for the gypsum board and fibre board, [JIR 06, PAV 09] for the mineral wool. To each case is assigned an equivalent wall, in which the concrete layer integrates a network of fractures, as shown on the bottom of Fig. 5.5. This network is the same as that of Sec. 4.3.2, except the dimensions of the cracks have been increased in proportion to the thickness of the material layer.

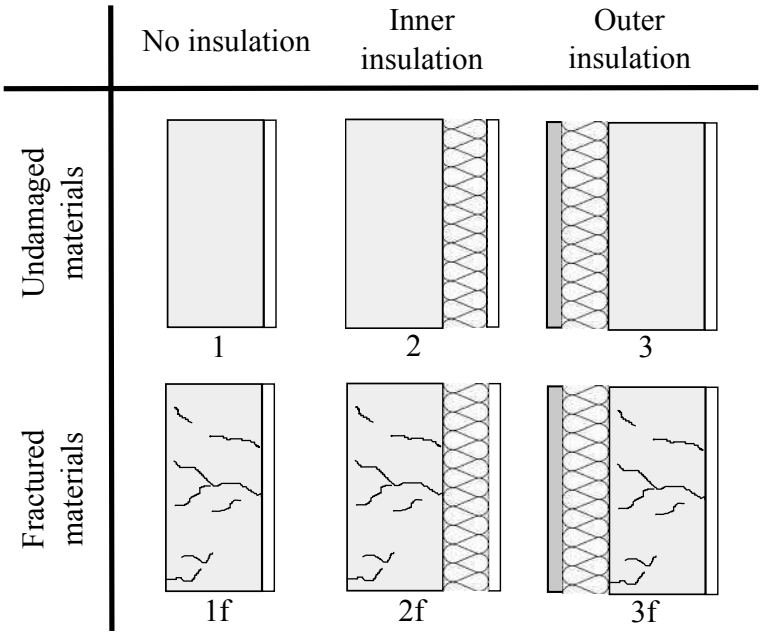

Figure 5.5: Definition of the simulation cases

Case	Material	Thickness	Properties
1	Concrete	20 cm	Sec. 4.2
	Gypsum board	1.25 cm	[HAG 02a, KUM 02]
2	Concrete	20 cm	Sec. 4.2
	Fibre board	10 cm	[HAG 02a]
	Gypsum board	1.25 cm	[HAG 02a, KUM 02]
3	Mortar	1 cm	2.3
	Mineral wool	10 cm	[JIR 06, PAV 09]
	Concrete	20 cm	Sec. 4.2
	Gypsum board	1.25 cm	[HAG 02a, KUM 02]

Table 5.1: Materials used in each simulation case

5.2.1.2 Mesh

The most mathematically challenging phenomenon occuring in the presented simulations is moisture transfer in the liquid phase, which generates steep gradients of capillary pressure and of the related transport and storage coefficients. Therefore, the main factor for the determination of the mesh density of a component is its liquid permeability. More specifically, the abruptness of the permeability profile, and of the retention curve, is key: the mesh density of a material must be high enough to ensure a sufficient smoothness of their local variations. A multi-layered wall therefore consists of several concatenated mesh densities. The fracture segments have the highest saturated moisture permeability, and are discretised with intervals of 3×10^{-4} m. A non-structured triangular mesh is applied on the surrounding porous medium, integrating the crack geometry as described in Sec. 4.3.1.2. The distance between nodes is the set according the each material's moisture permeability, and ranges from 1 mm for gypsum board to 3 mm for concrete. In simulating the undamaged walls (case 1, 2 and 3), a quasi-1D mesh was generated with a narrow rectangular geometry and two insulation boundary conditions. The walls including a fractured concrete layer (case 1f, 2f and 3f) were modelled in 2D with a height of 20 cm. As an illustration, the mesh used for the simulation case 1f is displayed on Fig. 5.6.

Although the current settings of the meshing procedure allow including any fracture geometry into the finite-element mesh and predicting flow accordingly, some improvements remain to be made for its optimisation. For instance, the current algorithm does not allow a progressive increase of the mesh density near fractures: the mesh is therefore fully refined in the entire material layer that includes fracture segments. This involves high mesh densities in locations where they are not required, and consequently increases the computational time. The current code also does not allow simultaneously using triangular and square-shaped finite-elements: a triangular non-structured mesh is applied on the non-fractured material layers as well.

5.2.2 Boundary conditions

The exterior boundary conditions of the problem are implemented after climatic data files measured in Lyon (France) during the year 2011. The following quantities are available as instantaneous measurements recorded with time steps of one minute: altitude and azimuth of the sun, diffuse and direct horizontal irradiance, wind speed and direction, relative humidity, horizontal rainfall intensity and dry bulb temperature. The relative humidity and air temperature can be directly used in the expression of the boundary heat and moisture flows (see Eq. 1.27), and the other measurements were used to calculate further necessary parameters: convective transfer coefficients, equivalent temperature and wind-driven rain. As the effect of the facade orientation in these calculations is significant, four one-year climate files with time steps of 10 minutes were generated, each one corresponding to a different orientation (north, east, south and west).

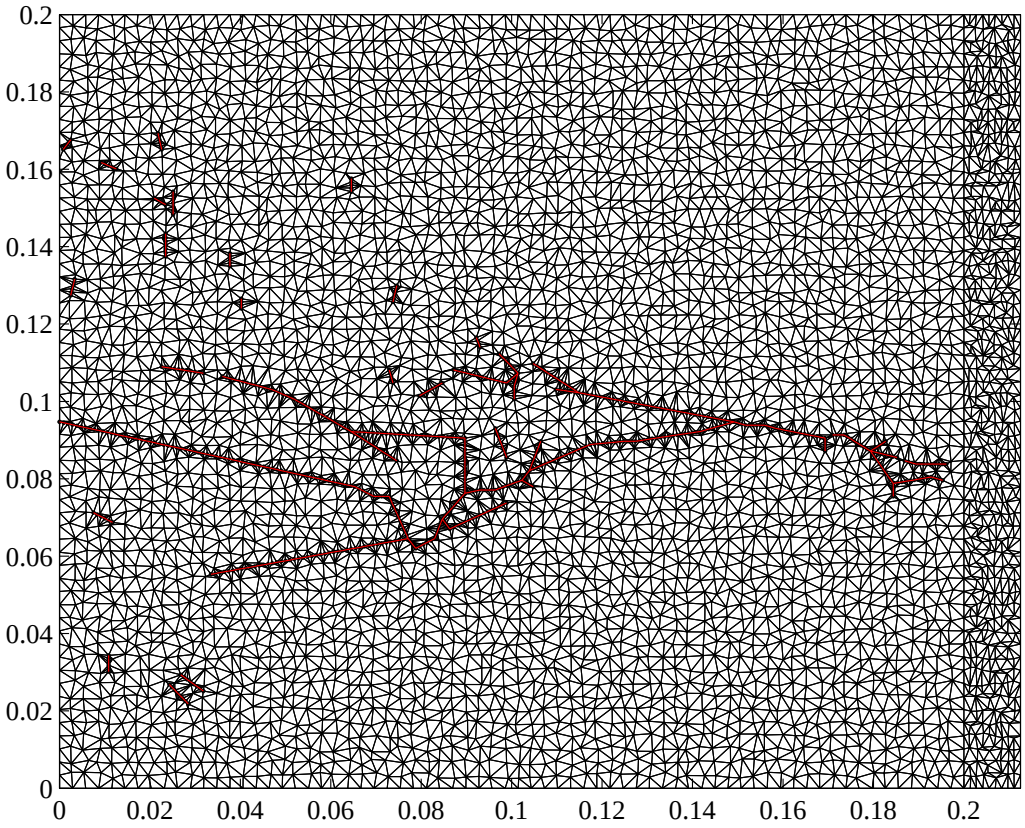

Figure 5.6: Generated mesh for the simulation case 1f

For simplification purposes, the interior boundary conditions of all simulation cases are constant: RH = 75%, $T = 20°C$, $\alpha = 7$ W.m^{-2}.K^{-1}, $\beta = 3 \times 10^{-8}$ s.m^{-1}. Although a large part of the moisture income towards building materials originates from the indoor humidity level, influenced by the occupants, this matter has been simplified here.

5.2.2.1 Convective transfer coefficients

The heat and moisture transfer rate between the ambient air and a porous medium is governed by the gradient of temperature and humidity, as well as by the local air velocity, the roughness of the material surface and its moisture content [WOR 04]. The accurate expression of the α and β coefficients denoting convective transfer can therefore be problematic, as their values correspond to specific cases. The convective heat transfer coefficient can be simplified by empirical formula, obtained from large scale measurements of convective heat transfer at building surfaces [SHA 84, LOV 96]:

$$\alpha = 1.7\, V_{loc} + 5 \tag{5.2}$$

where the local air velocity V_{loc} is a function of the building geometry and the wind speed and direction, and can also be quantified by empirical models based on CFD simulations:

$$V_{loc} = \begin{cases} 1.8\,U + 0.2 & \text{if} \quad \cos(\theta_{wind} - \theta_{wall}) \geq 0 \\ 0.4\,U + 1.7 & \text{if} \quad \cos(\theta_{wind} - \theta_{wall}) < 0 \end{cases} \tag{5.3}$$

where U and θ_{wind} are the wind speed and direction, and θ_{wall} denotes the facade orientation: $\theta_{wall} = 0$ for a wall facing north, $\theta_{wall} = \pi/2$ for a wall facing east, etc. The moisture convective transfer coefficient can be expressed by the previously mentioned Chilton-Colburn analogy 1.28:

$$\frac{\beta}{\alpha} = \frac{D_{v,a}}{R_v T \lambda_a} \mathrm{Le}^{2/3} \tag{5.4}$$

It can be seen that the effects of the environment topography and building geometry have been considerably simplified. The use of empirical models for the expression of the surface transfer coefficients is however common practice [JAN 07]: a possible alternative for a better expression of the boundary transfer is the coupling of the model with CFD simulations accounting for the environment of the building. Although it is possible that wind may have an impact on air infiltration in fractures and resulting advection phenomena, this effect was not specifically studied here and the empirical approach was considered suitable for answering the previously mentioned goals of the simulations.

5.2.2.2 Equivalent temperature

As previously explained, the effects of solar radiation are integrated in the expression of an equivalent temperature at which the heat transfer rate due to the temperature across the wall is the same as the rate due to the combined effects of convection, conduction and radiation. This temperature was introduced in Eq. 1.27 and Eq. 1.30, recalled here:

$$\alpha\left(T_{eq} - T\right) = \alpha\,(T_a - T) + \kappa I_{sol} + \sigma\epsilon I_{LW} \tag{5.5}$$

The long-wave term I_{LW} is the radiative heat exchange between surface, atmosphere, ground and surrounding buildings, and was neglected in the present study. The absorbed short-wave radiation I_{sol} consists of the direct irradiance I_{dir} and the diffuse irradiance I_{dif}. The latter is given in climatic tables and is applicable to all surface orientations. The direct absorbed radiation on each building facade was calculated from the direct horizontal irradiance as shown on Fig. 5.7. The value of the absorptivity was set to that of concrete and mortar $\kappa = 0.6$, as these materials form the external layers of the simulated walls.

The left part of Fig. 5.7 shows how the horizontal solar radiation I_{hor} is related to the radiation incoming to a vertical surface I_{ver} through the altitude angle of the sun θ_{alt}:

$$\frac{I_{ver}}{I_{hor}} = \frac{1}{\tan\theta_{alt}} \tag{5.6}$$

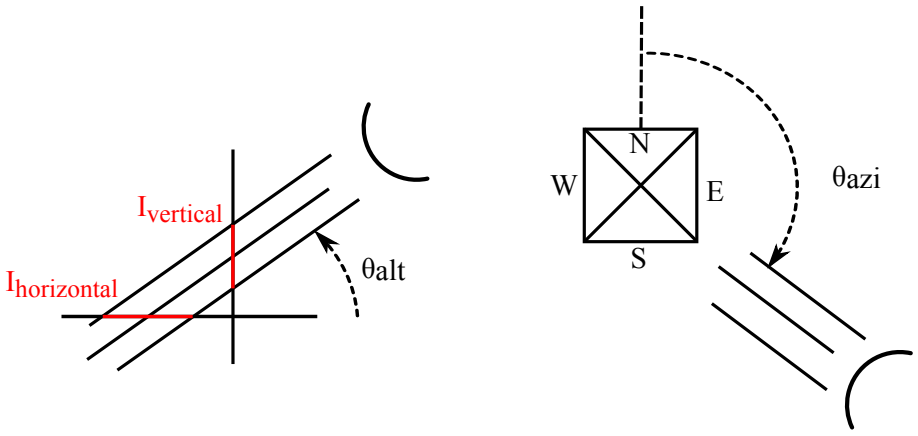

Figure 5.7: Calculation procedure of the direct solar radiation

and the right part shows the effect of the facade orientation θ_{wall} and of the azimuth of the sun θ_{azi}. The resulting expression of the direct radiation on a facade, as a function of the parameters given by the climatic tables, is therefore summed up as:

$$I_{dir} = I_{hor} \frac{\max\left[\cos\left(\theta_{azi} - \theta_{wall}\right), 0\right]}{\tan\theta_{alt}} \tag{5.7}$$

As it was the case for the expression of the surface transfer coefficients, the effects of the environment was not taken into account: for instance, the simulated wall is not influenced by eventual trees or other buildings that may protect it from direct sunlight at certain times of the day. This may cause an overestimation of the incoming heat flow and of drying phenomena, but was not considered relevant for the current questioning.

5.2.2.3 Wind-driven rain

In the simulated building components, wind-driven rain is the main cause for water infiltration in fractures and for subsequent moisture accumulation. It is therefore important to include it in the calculations. It was already mentioned in Sec. 1.2.4.2 that empirical models can be used for the expression of $\mathbf{g}_{l,r}$. Such models sum up results of CFD simulations into wind-driven rain coefficient α_{WDR}, which translates the rain drop size and velocity into an amount of water captured by a building facade. In the present case, this coefficient was set to a constant value of 0.222 [BLO 04], simplifying Eq. 1.29 into a function of the horizontal rainfall R_h, and of the wind speed and direction:

$$\mathbf{g}_{l,r} = 0.222\, R_h^{8/9} U \max\left[\cos\left(\theta_{wind} - \theta_{wall}\right), 0\right] \tag{5.8}$$

where the value of the horizontal rainfall, originally given in [mm.min^{-1}], is transposed into [kg.m^{-2}.s^{-1}] for the integration into the simulation code:

$$R_h\left[\text{kg.m}^{-2}.\text{s}^{-1}\right] = \frac{\rho_l}{1000 \times 60} R_h\left[\text{mm.min}^{-1}\right] \tag{5.9}$$

This expression does not explicitely account for the raindrop size distribution, nor does it include the impact of the building height and of the wind speed, but its description of the rain loads is nevertheless considered appropriate for the current study. In addition to the convective vapour transfer at the surface of the porous medium, the total boundary moisture flow reads:

$$\mathbf{g}_m = \beta \left[\underbrace{\left(p_{v,a} + \frac{\mathbf{g}_{l,r}}{\beta} \right)}_{p_{eq}} - p_v \right] \tag{5.10}$$

where an equivalent ambient pressure p_{eq} is defined, including moisture exchange in both liquid and gaseous phases. In order to prevent computational difficulties arising from heavy climatic loads caused by strong rain showers, a maximal theoretical value of this equivalent pressure was set:

$$\begin{cases} p_{eq} \leq 2\, p_s & \Rightarrow \quad \text{Neumann} \\ p_{eq} > 2\, p_s & \Rightarrow \quad \text{Dirichlet} \end{cases} \tag{5.11}$$

When the equivalent pressure exceeds a value defined by the saturation vapour pressure p_s, the moisture load is switched to a Dirichlet-type boundary condition indicating moisture saturation at the surface of the material: $p_c = 10^{-3}$ Pa. The mass exchange is otherwise expressed by a Neumann-type condition (convective transfer $\mathbf{g}_m$). This procedure allows for a better convergence in case of important moisture income. The temperature of the rain is chosen equal to that of air.

5.2.3 Further settings

5.2.3.1 Time resolution

The presented methodology consists of long-term simulations including highly variable boundary conditions such as sudden rain showers. A compromise must be found concerning the magnitude of the time step, in order to account for all variations of the climatic data while avoiding tremendous calculation times. Previous questionings on the required time resolution for the wind and rain input data in order to obtain accurate calculation results show that time steps of up to 10 min yielded a good agreement with experimental data [BLO 04]. Hourly or daily time resolutions based on an arithmetic averaging of the climatic data can however imply important errors: these errors may be reduced by using a weighted averaging technique [BLO 08].

The climatic tables, available as 1 min input data, were arithmetically averaged to a time resolution of 10 min. The algorithm includes an adaptative time stepping procedure, adapting the size of each time step Δt according to the number of iterations of the previous step m [JAN 07]:

$$\Delta t^{i+1} = \min \left[\Delta t^i \ \min \left(\frac{m_{max}}{2m}, 2 \right), \Delta t_{max} \right] \tag{5.12}$$

where $m_{max} = 12$ is the maximal authorised number of iterations. Should convergence not be reached at the end of this series of iterations, a new attempt is made with half the size of the time step. Such a reduction for instance occurs at the beginning of rain showers, decreasing the time step to the order of seconds. The step then increases when climatic conditions allow a faster convergence, and is bounded by a maximal value of $t_{max} = 10$ min as to not exceed the climatic input frequency. A full description of the calculation algorithm is given in Sec. B.2 along with the description of the implementation of the dynamic time stepping procedure.

5.2.3.2 Output

The setup of the simulations, summarising the notations, wall geometry and boundary conditions, is shown on Fig. 5.8.

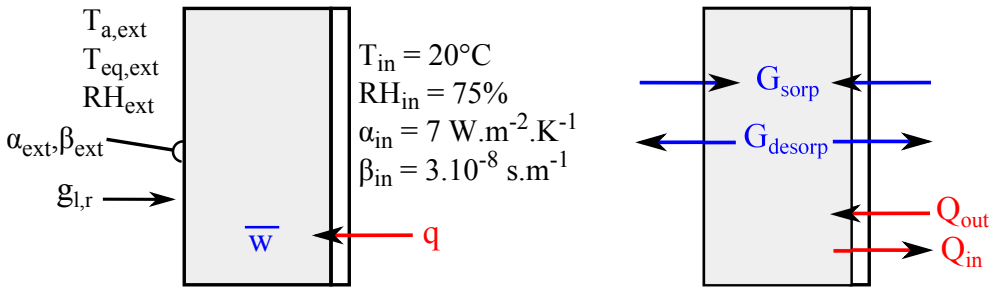

Figure 5.8: Simulation setup (left) and definition of the balance quantities (right)

The results presented in the following section are twofold. First, temporal distributions are used for a qualitative illustration of the differences between several simulation cases. They are graphs showing the evolution, during a month or a year of simulation, of an instantaneous value. These values, illustrated on Fig. 5.8, are the heat flux towards the inner surface $\mathbf{q}$ [W.m^{-2}], and the average moisture content of the wall $\overline{w}$ [kg.m^{-3}]:

$$w_{total} = \frac{\sum_m \overline{w}_m x_m}{\sum_m x_m} \tag{5.13}$$

which is the averaged value of the moisture content of each material layer $\overline{w}_m$, weighted by their thickness x_m. The convention for quantifying the heat flow was chosen in order for $\mathbf{q}$ to be representative of the heat loss or gain of the inner environment.

The second class of variables used for the display of the results are integrated values used for quantitative comparisons, shown on the right side of Fig. 5.8. Q_{out} [J.m^{-2}] and Q_{in} respectively denote the raw total outwards and inwards heat flow, calculated by integrating the positive or the negative part of $\mathbf{q}$ over the inner surface S_{int} during a month or a year of simulations:

$$Q_{out} = \int_t \left[\int_{S_{int}} \max(\mathbf{q}, 0)\, \mathrm{d}S \right] \mathrm{d}t \tag{5.14}$$

$$Q_{in} = -\int_t \left[\int_{S_{int}} \min\left(\mathbf{q}, 0\right) \, \mathrm{d}S \right] \mathrm{d}t \tag{5.15}$$

Q_{out} has been defined as to be a measure for the total heat loss of a wall per unit facade during a given amount of time. Though it does not directly translate into heating needs for keeping the inner conditions constant, it can be used as a comparative indicator of the thermal performance of several facade configurations. Similarly, Q_{in} is the total heat flow from the wall towards the inner environment.

The moisture balance quantities G_{sorp} and G_{desorp} [kg.m^{-2}] are respectively defined as the total raw intake and release of water between the wall and both inner and outer environments. They are calculated by integrating the positive or negative part of g on both the external S_{ext} and the internal surfaces:

$$G_{sorp} = \int_t \left[\int_{S_{int}+S_{ext}} \max\left(\mathbf{g}, 0\right) \, \mathrm{d}S \right] \mathrm{d}t \tag{5.16}$$

$$G_{desorp} = -\int_t \left[\int_{S_{int}+S_{ext}} \min\left(\mathbf{g}, 0\right) \, \mathrm{d}S \right] \mathrm{d}t \tag{5.17}$$

High values of both these quantities denote important moisture content fluctuations, while an high difference between them denotes an accumulation of moisture in the wall during the considered period. As both phenomena influence the material degradation, G_{sorp} and G_{desorp} can be used as indicators of the durability of a building component.

5.3 Results

The previous section describes many possibilities for calculations by combining all six walls geometries with all four facade orientations, each one during a year of simulation. While such a long simulation time is possible for the undamaged walls (case 1, 2 and 3), geometries including fractured material layers have a much higher number of FE nodes and therefore involve much longer computational times. In order to answer the questioning presented in the introduction of Sec. 5.2 within a reasonable term, the conditions of the simulations must be chosen as to be representative of the potential effects of fractures while avoiding redundancy of the results.

5.3.1 Undamaged materials

5.3.1.1 Facade orientation

As previously mentioned, four separate climatic data files were generated, since the expression of the external boundary conditions depends on the facade orientation. However, simulating the behaviour of all combinations of simulation cases and facade orientations was not considered necessary. Instead, a sensibility study of the output to the orientation was performed: the wall n° 1 was simulated during one year using each

climatic data file. The results of these four calculations were then compared in order to select one facade orientation, which was then no longer modified for all subsequent simulations. The dynamic behaviour of all facades is partially shown on Fig. 5.9, showing the temporal evolution of the outwards heat flux $\mathbf{q}$ and of the wall moisture content $\overline{w}$. For purposes of clarity, the former distribution is shown during one month, while the latter is shown during the entire year.

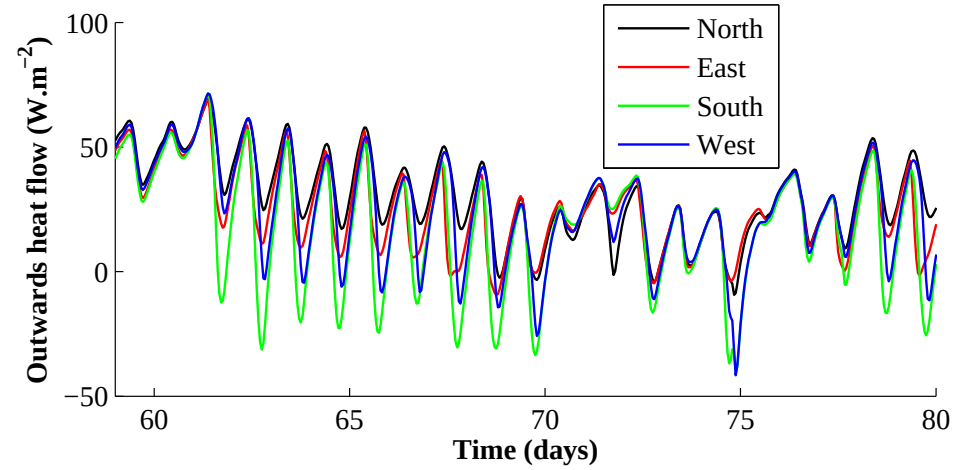

(a)

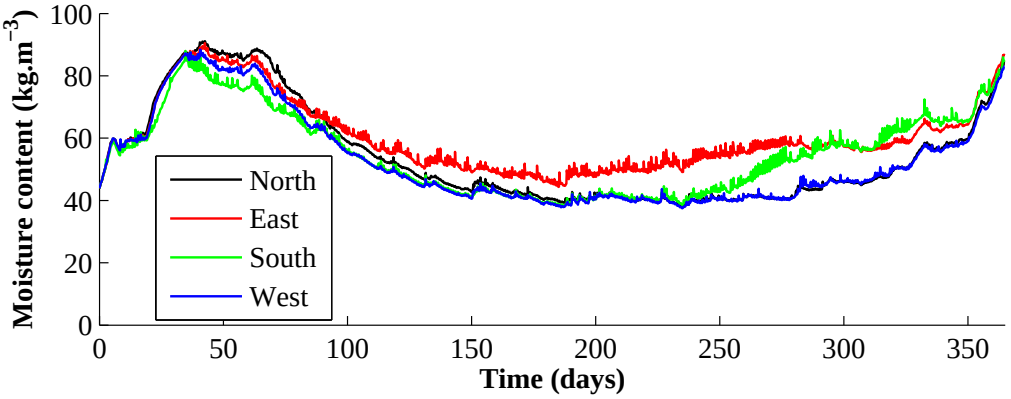

(b)

Figure 5.9: Effect of the facade type on the (a) outwards heat flow and (b) moisture content

The temporal resolution of Fig. 5.9(a) is 10 min, and that of Fig. 5.9(b) is 4 h. The observed behaviour matches the expectations on the response of each facade according to the climatic solicitations: daily cycles are clearly visible in all cases in the form of fluctuations of the outwards heat flux (Fig. 5.9(a). These fluctuations have a higher amplitude on the southern facade due to the direct sunlight, and a lower amplitude on the northern facade. The averaged moisture content of the wall (Fig. 5.9(b)) exhibits a general trend of high humidity in the winter period and lower values in summer. In ad-

dition to this trend, faster variations of low amplitude are visible on the profiles, due to daily fluctuations of the relative humidity, drying and wetting due to the temperature variations, and rain.

The general observation that can be made from these distributions is the fact that the eastern and western facades globally have an intermediate response to the thermal solicitations, and are more representative of an average behaviour than the northern and the southern facades. In order to confirm this observation, Fig. 5.10 shows the balance quantities defined in Eq. 5.14 to 5.17.

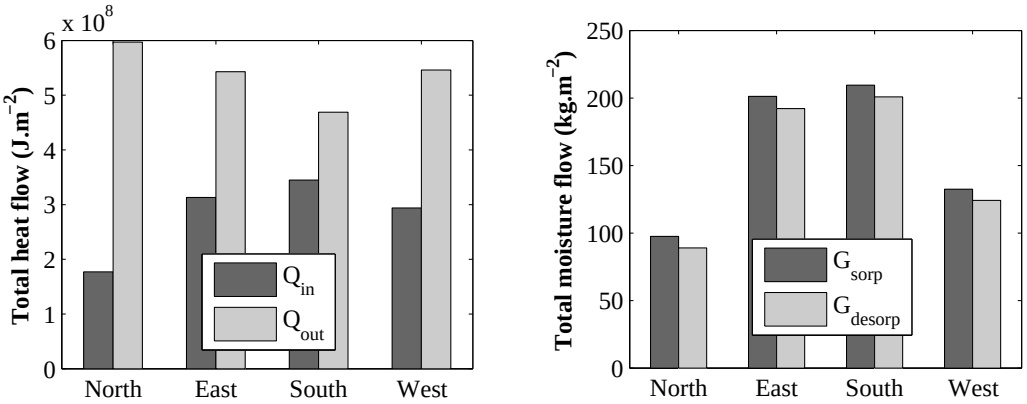

Figure 5.10: (a) Total heat flow and (b) moisture sorption and desorption, during a year of simulation, as a function of the facade orientation

Fig 5.10(a) shows the comparative values of Q_{out} and Q_{in} resulting from the same simulation case, exposed to each of the climatic files. Fig. 5.10(b) similarly shows the values of G_{sorp} and G_{desorp}. The following observations can be drawn:

- As could be anticipated, the northern facade exhibits the highest heat loss Q_{out} and the lowest heat gain Q_{in}. The southern facade shows the opposite result, and the eastern and western facades have intermediate responses.
- The sorption/desorption cycles, translated by the quantities G_{sorp} and G_{desorp}, are higher in the eastern and southern facades.
- The orientation has little influence on moisture accumulation in the wall i.e. the substraction $G_{sorp} - G_{desorp}$.

The outcome of this series of simulations is the response of the same multi-layered wall to different climatic inputs. In order to avoid running all calculations four times, and to show the effects of cracking in average and representative climatic conditions, all following simulations took place using the climatic file of the western facade orientation. Indeed, the main purpose of this choice was to observe the average response of the wall, rather than its behaviour in extreme cases.

5.3.1.2 Effects of thermal insulation

The last step of the study before simulations of fractured building components is to ensure the consistency of the effect of thermal insulation on the hygrothermal performance of the wall. The selected climatic data file was implemented into year-long simulations of the cases 1, 2 and 3 (undamaged components). The results were then compared as to estimate whether the expectations of the insulating components are met. The presentation of the results is the same as in the previous paragraph: first, Fig. 5.11 shows the dynamic behaviour of the walls on the basis of the temporal evolution of $\mathbf{q}$ and $\overline{w}$.

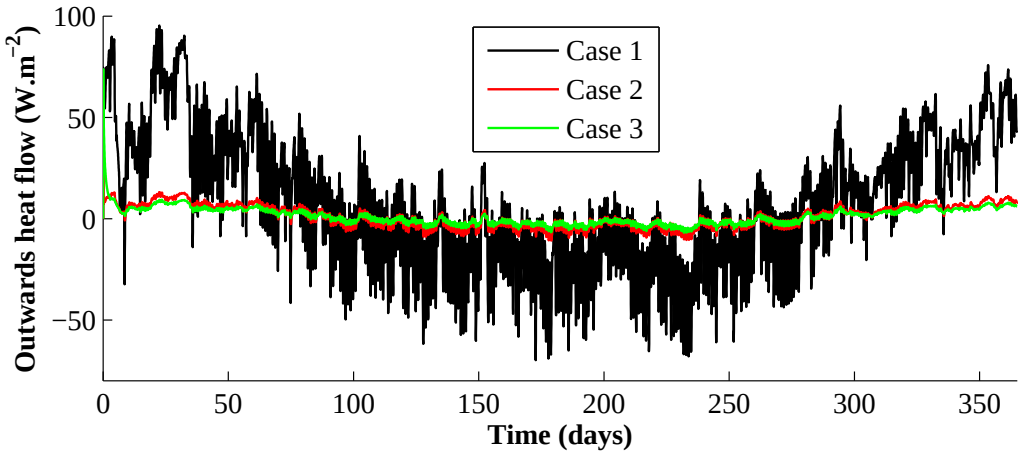

(a)

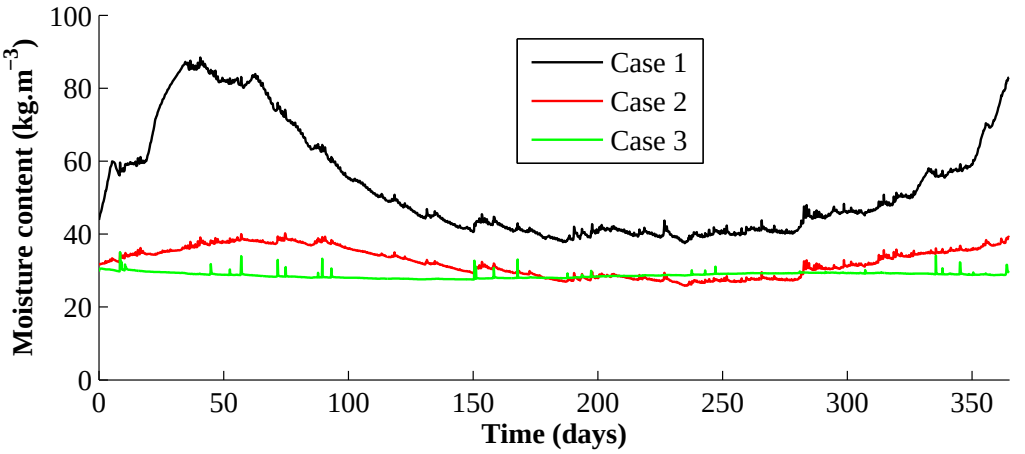

(b)

Figure 5.11: Effect of the facade orientation on the (a) outwards heat flow and (b) moisture content during a year of simulations

The non-insulated wall (case 1) can be seen to show significantly higher values of

heat flow, in both winter and summer periods (Fig. 5.11(a)). Its thermal inertia is much smaller, as can be seen by high daily fluctuations of **q**. In this regard, the performances of the inner and outer thermal insulation modules are quite similar. In terms of variations of the moisture content (Fig. 5.11(b)), the case 2 exhibits yearly fluctuations, coordinated with those of the case 1. The simulation case 3 offers a steadier profile. Indeed, the principal source of moisture income to the wall is the exterior environment, from which this composite is insulated by a layer of hygrophobic coating. These observations are confirmed by the comparison of the balance quantities, shown on Fig. 5.12.

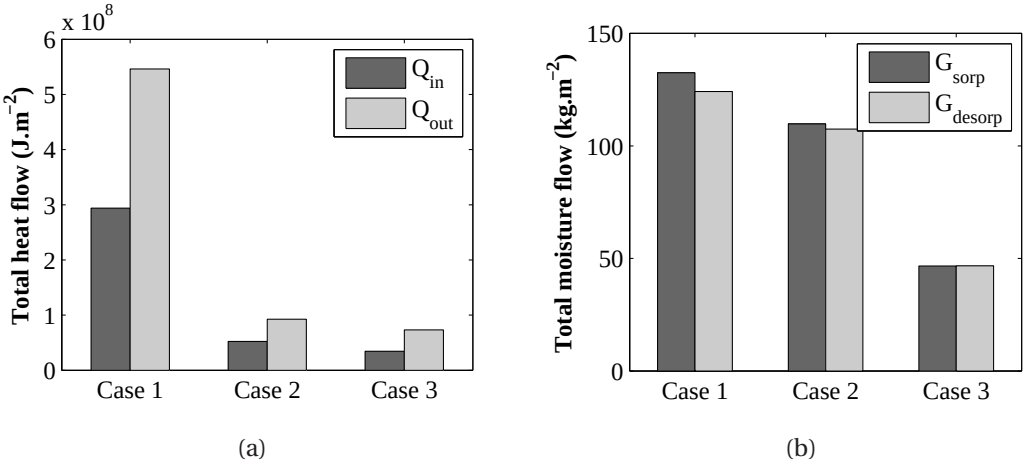

Figure 5.12: (a) Total heat flow and (b) moisture sorption and desorption, during a year of simulation, as a function of the facade type

- Case 1 exhibits a very high value of both Q_{out} and Q_{in} (Fig. 5.12(a)), as well as of the general amplitude of the moisture content fluctuations, shown by G_{sorp} and G_{desorp} (Fig. 5.12(b))
- Case 2 shows that the addition of an inside insulation layer considerably decreases the heat loss and gain through the wall. However, it only has a small impact on the amplitude of sorption/desorption cycles, particularly concerning the concrete layer exposed to the exterior climatic conditions.
- The thermal response of case 3 is very close to that of case 2. However, this outside insulation composite includes a hygrophobic coating layer making the wall practically impermeable to external liquid moisture income: the cycles of successive moisture intake and release are considerably reduced. As these cycles are one of the main causes for material degradation, such an insulation module is expected to have a positive impact on the durability of the component.

Although most of these observations are not new, they allow ensuring that the results given by the finite-element model are consistent with the definition of the simulation cases.

5.3.2 Fractured materials

The last part of the work consists of simulating the behaviour of building components including fractured materials, i.e. the simulation cases 1f, 2f and 3f. The geometries of these components is identical to the previously considered undamaged cases, except that the load-bearing material layer (concrete) includes a fracture network, which was taken from previous measurements performed in Chap. 3. The questioning of this numerical study was laid in the form of three targets, the first one of which is to estimate the consequences of fractures on the moisture accumulation and heat loss of a standard wall. This is done by comparing the values of the balance quantities (Q_{out}, Q_{in}, G_{sorp} and G_{desorp}) resulting cases 1 and 1f. The second question is to find whether these consequences are aggravated by the infiltration of moisture towards insulation materials: this is done by comparing these two cases with cases 2 and 2f. The last target is to illustrate how outer insulation may correct the flaws generated by fissures: it is the purpose of the cases 3 and 3f.

The previous section has set the frame for this last step of the numerical work. On the basis of year-long simulations of undamaged building components, a climate file was selected as to be representative of the standard solicitations occuring on a building facade. This allowed reducing the number of calculations required to answer the questioning. Furthermore, the hygrothermal behaviour of the walls was only observed during two separate months of simulations instead of an entire year: a winter month (february) and a summer month (july). Indeed, a full simulation year of fractured components would imply long computational times with the current settings of the model, and the two selected months are representative of the conditions to which the walls may be subjected.

5.3.2.1 Dynamic behaviour

First, the dynamic behaviour of the walls is displayed. Each of the following graphs shows the temporal evolution of $\overline{w}$ and $\mathbf{q}$ for both undamaged and damaged versions of a wall geometry, during one month of simulation. Fig. 5.13 and 5.14 show the behaviour of the non-insulated wall (cases 1 and 1f), while Fig. 5.15 and 5.16 show the behaviour of the inner insulated wall (cases 2 and 2f), respectively during the winter and the summer month. The initial conditions of the winter simulations are $T = 10°C$ and RH = 75%, and those of the summer simulations are $T = 20°C$ and RH = 75%.

On each graph, the hygric and thermal behaviour of the undamaged component is shown by the black lines, while the blue and red lines respectively indicate the evolution of the moisture content $\overline{w}$ of the damaged wall and of the thermal flow through its inner surface $\mathbf{q}$.

The interpretation of Fig. 5.13 leads to the following observations: first, the evolution of the moisture content, and of the heat loss, during the first period of the simulations, is almost identical whether the concrete layer is fractured or not. This period is characterised by moderate conditions of humidity and occasional small quantities of wind-driven rain impacting the building facade: with the present settings of the frac-

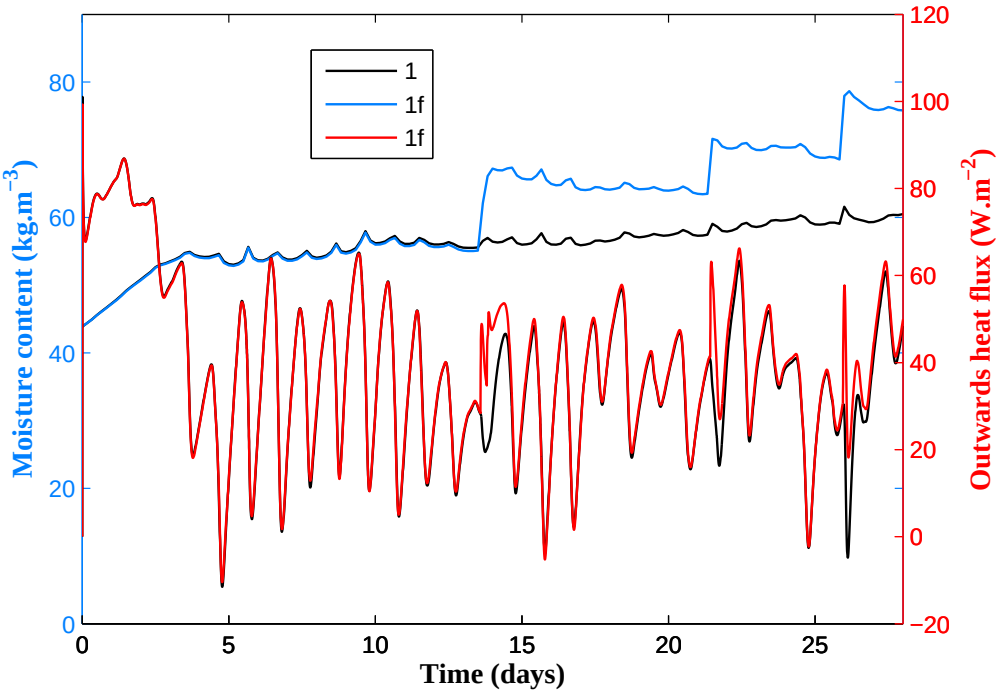

Figure 5.13: Non-insulated wall (february)

ture moisture permeability (see Eq. 4.23 and Fig. 4.15), the presence of cracks do not significantly accelerate moisture ingress in the vapour phase. A rain shower then occurs (around $t = 14$ days), causing an abrupt rise in the moisture content of the fractured wall due to water suction in the main fracture. The amount of water captured by the concrete layer after this rain shower then decreases slowly: although the fracture contributes to the drying process, an important accumulation of moisture remains in this material of low permeability. In the present case, this accumulation is aggravated by frequent rain showers preventing the drying of the wall. The thermal behaviour of the damaged facade is displayed on Fig. 5.13 as well. The first disparity between cases 1 and 1f in this regard is caused by the sudden moisture content rise which increases the thermal conductivity of concrete. The profiles of outwards heat flow then coincide again as the amount of water captured by the case 1f diffuses in a larger area, and have a smaller impact on the conductivity. Although cracking seems to have little direct consequence on the thermal performance of the wall, the accumulation of moisture over time may result in larger gaps between the initial and the fractured building components. The simulation of the same walls during the summer month (Fig. 5.14) leads to similar observations. The drying rate of the fractured wall after a rain shower is however higher because of higher air temperatures.

Fig. 5.15 and 5.16 show the moisture content and heat flow profiles of both inner insulated walls. The general shape of the hygric behaviour is very close to that of the

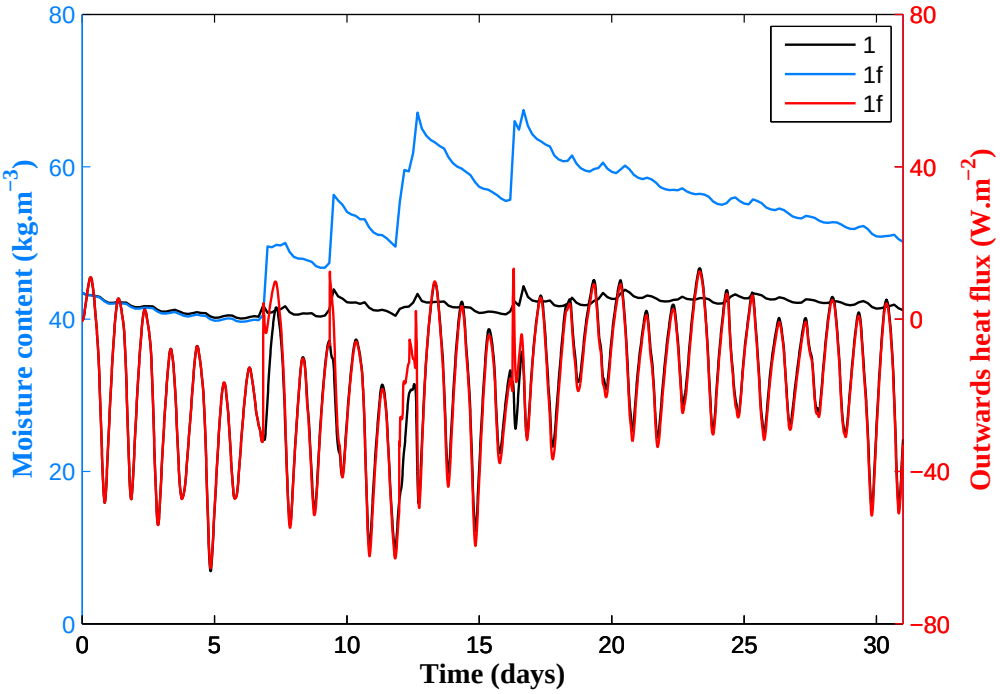

Figure 5.14: Non-insulated wall (july)

non-insulated facade. The accumulation of water in the fractured case however seems aggravated. The crack geometry included in the concrete layer indeed nearly reaches the insulation material, causing possible moisture accumulation inside the wall. The consequences of cracking on the thermal behaviour therefore seem more important than in the non-insulated case: first, this configuration has a higher initial thermal resistance, and the impact of moisture on the thermal conductivity of the materials is proportionally higher. Second, this impact is lasting because of the slow rate at which moisture leaves the wall. Alhough the short-term effects of fractures on the heat loss are limited, it can be expected that longer simulation times result in an aggravation of moisture accumulation in the insulation layer of this wall configuration, and thus durably affect its thermal conductivity.

5.3.2.2 Heat and moisture balance

The results of the monthly simulations are summarised by showing the value of the balance quantities defined in Eq. 5.14 to 5.17. Fig. 5.17 displays the total amount of adsorbed and released moisture, per unit exposed surface of each wall, during a month of simulation.

Two main quantities can be related to a durability assessment of a building component. First, the values of G_{sorp} and G_{desorp} illustrate the amplitude of the average sorption/desorption cycles. Secondly, the quantity $\Delta m = G_{sorp} - G_{desorp}$ (see Fig. 5.17(a)), il-

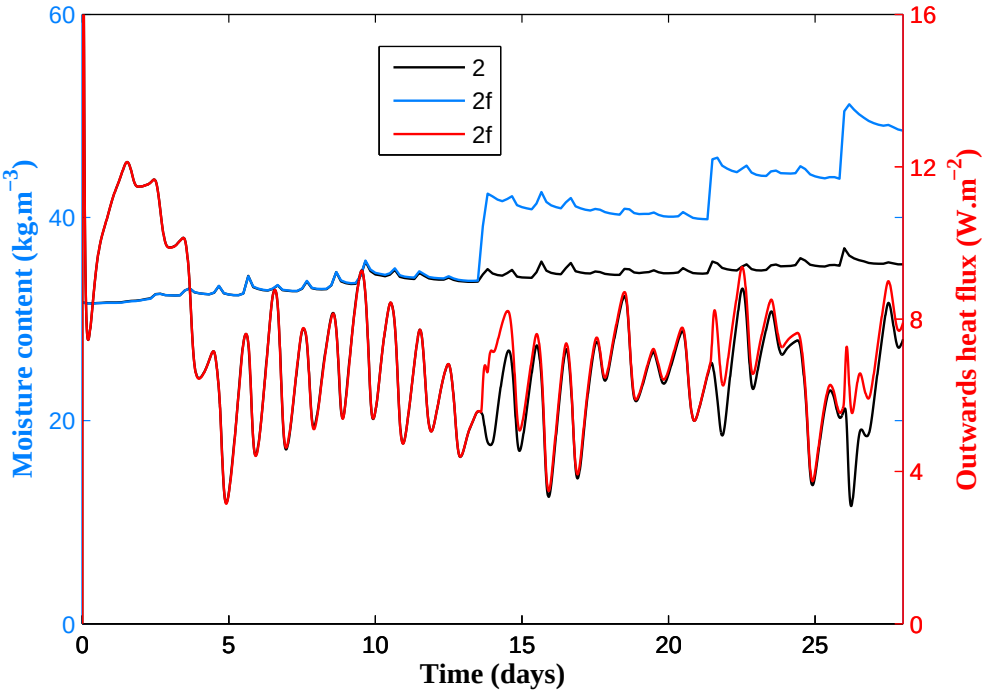

Figure 5.15: Wall with inner insulation (february)

lustrates moisture accumulation in the component. Both phenomena are known to accelerate degradation mechanisms: the amplitude of drying/wetting cycles accelerates the chemically induced degradation suffered by concrete [AND 99] (alkali-silica reaction, steel reinforcement corrosion, carbonation) and accumulated water may cause frost damage in case of low temperatures, or diffuse towards the entire envelope and generate mould growth [CLA 99]. In regards to both these parameters (moisture accumulation and wetting/drying cycles), it is clear that the presence of cracks inevitably accelerates degradation processes. While this observation could be expected, the presented model allows quantifying these phenomena, allowing more advanced durability assessments. The interpretation of Fig. 5.17 furthermore yields the following observations:

- The aggravation of moisture accumulation due to cracking concerns both non-insulated and inner-insulated walls equally. In the second case, the infiltration of water may also reach the insulation material, should cracks form a continuous path towards this layer. This has important potential repercussions, considering such materials often do not tolerate moisture accumulation.

- During the summer month, the final moisture balance is negative in the non-damaged walls 1 and 2 ($G_{desorp} > G_{sorp}$), and positive in the walls including fractured components 1f and 2f.

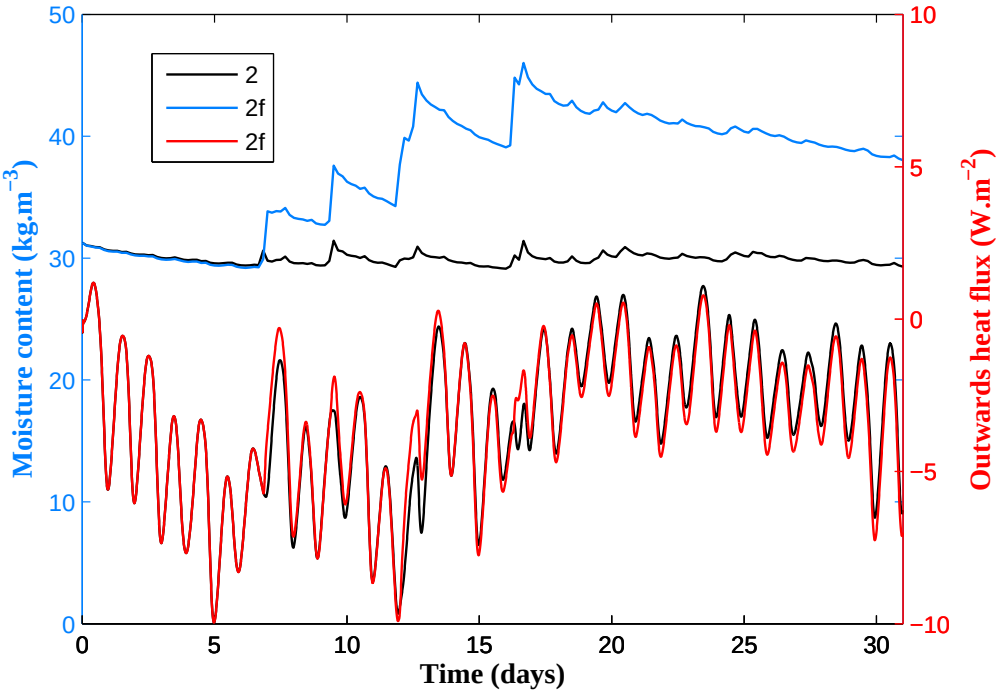

Figure 5.16: Wall with inner insulation (july)

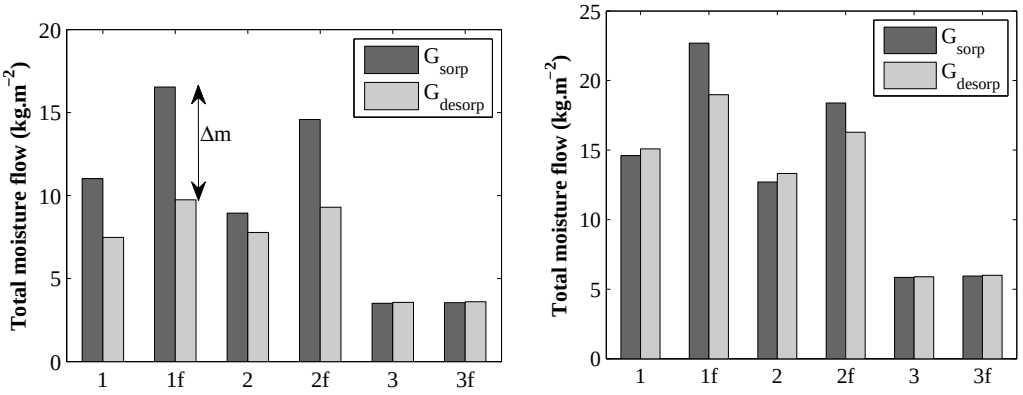

Figure 5.17: Total moisture sorption and desorption in all simulation cases, during (a) the winter month and (b) the summer month

- Cracking has very little impact on the hygric performance of the outer-insulated wall (simulation cases 3 and 3f). This observation shows that the addition of a protective hygrophobic coating may correct the flaws generated by ageing, and consequently improve the durability of the structure.

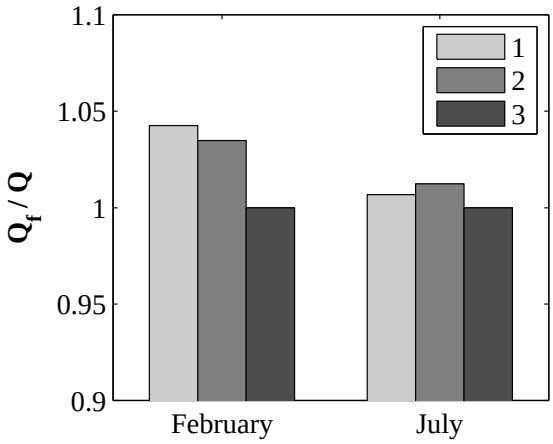

Figure 5.18: Consequences of cracking on the thermal performance

The thermal balance of the simulations is showed on Fig. 5.18. Each value presented on this graph is the ratio of the total heat transfer across a damaged facade Q_f to that across the initial wall Q, for each facade type, during a month of simulation.

$$\frac{Q_f}{Q} = \begin{cases} \dfrac{Q_{out,f}}{Q_{out}} & \text{(february)} \\ \dfrac{Q_{in,f}}{Q_{in}} & \text{(july)} \end{cases} \tag{5.18}$$

As was previously noted, due to the moisture-dependency of the thermal conductivity of construction materials, cracking may affect heat transfer across the facade. The direct consequences on the general heat balance at the building scale are however limited, as shown by the low values of Q_f/Q exhibited by Fig. 5.18.

It must be noted that the observations resulting from this series of simulations are given by specific cases, which have been defined in order to illustrate the potential effects of cracking on the hygrothermal performance of building components. These results are therefore to be analysed with caution. Furthermore, the procedure is based on a number of simplifying hypotheses and flaws: simplification of the climatic load, imperfect meshing strategy, restriction to 2-dimensional observation... However, they illustrate the impact cracks may have on hygrothermal performances, and justify the need for the procedure which has been developed in the frame of this work.

5.3.2.3 Calculation time

It was mentioned in Sec. 4.3.2 that very small time steps, under 0.1 s, are required for convergence during the phase of water suction by a fracture. The initial time step of the calculations is of 10 min. At the start of a rain shower, convergence cannot be reached within the prescribed maximum number of iterations: the adaptative time stepping

procedure automatically reduces the time step until the calculation can proceed. This implies an important increase of the computational costs.

The geometry of the non-damaged walls is close to one-dimensional: due to a relatively small number of nodes, and to the absence of fracture flow, a year-long simulation can be conducted in less than 24 hours using a standard desktop computer, with time steps oscillating between 0.87 s and 10 min. The walls including fractured concrete are however much more demanding in terms of computational time. With the presented spatial discretisation settings, the simulation cases 1f and 2f respectively include 13722 and 16628 nodes. As an example, the simulation of the case 1f during the winter month involves a total of 4389 time steps, between 0.0014 s and 10 min, for a total of 9801 iterations. The average time of one iteration is 31 s, and the total calculation time is approximately 4 days.

Such computational costs make long simulations quite cumbersome: this justifies the restriction of the simulation cases to a single facade orientation, during only two months. A potential improvement of the procedure can however be easily identified: the current mesh generation algorithm does not allow a progressive increase of the mesh density near fractures. This involves the presence of an unnecessarily high number of nodes, visible on Fig. 5.6. The optimisation of this meshing procedure may therefore significantly reduce the time of calculation.

5.4 Conclusion

This chapter is centered on the application of the previously developed finite-element model for heat and moisture flow simulations in fractured porous media.

- The model was validated in regards to coupled transfer on the basis of international benchmarks. It was shown suitable for predicting the behaviour of multi-layered building components under heavy climatic loads.

- A series of simulation cases was defined in order to estimate the consequences of concrete cracking on the hygrothermal performance of non-insulated and insulated building facades. A climatic file, representative of average conditions in Lyon, was assigned to the simulations.

- The accumulation of moisture in the wall, as well as the amplitude of the sorption/desorption cycles, can be directly visualised. This allows comparing the performance and the durability of a given wall geometry, after integrating measurements of fracture networks.

- Long-term consequences of cracking on the hygrothermal performance of components can be estimated.

- Fractures observed in one of the material layers may influence the properties and the durability of the other layers of the facade, because of moisture infiltra-

tion. Simulations of inner-insulated walls were performed as an example of this phenomenon.

- The case of an outer insulation including hygrophobic coating is suggested as a means to correct the negative impact of cracking and prevent an acceleration of ageing.

The main advantage of the undertaken procedure is its applicability to a wide range of facade types. Crack geometries, integrated in the calculations, originate from experimental measurements and have no restrictions of number and sizes. Because the mechanical behaviour of the materials is not calculated, the methodology does not require the superposition of sub-systems in a staggered resolution scheme: the time-stepping procedure is simplified in comparison to fully predictive approaches. Furthermore, long-term simulations can be performed within reasonable computational time.

Conclusion

Summary and outcome

The objective of the work was to propose a methodology for including the effects of material ageing in simulations of coupled heat and mass transfer at the scale of building components, in the prospects of identifying their need for renovation. It ensued from a literature survey (Chap. 1) that the modelling of the hygrothermal behaviour of building components is now a standardised technique, and that important advances were recently achieved for modelling the mechanical behaviour of construction materials undergoing hygric and mechanical solicitations. However, such predictive approaches, while applicable to life-cycle analyses and studies performed ahead of the building design, suppose that all causes for degradation are quantified during the entire simulation time. In order to allow assessing the hygrothermal behaviour of materials of which damage patterns are unknown, a combined experimental and numerical procedure was developed. This procedure consisted in implementing non-destructive techniques for characterising damage and fracture geometries in construction materials, in order to integrate these measurements into a newly developed simulation code for coupled heat and moisture transfer modelling in cracked porous media.

Preliminary study

The work started with a preliminary experimental study, which aimed at identifying further experimental and numerical requirements (Chap. 2). The main questioning of this first step was to establish whether a continuous description of damaged building materials with equivalent macroscopic transport properties is suitable for allowing an accurate prediction of flow. To this aim, an experimental methodology was carried: diffuse damage patterns were generated in samples of a new formulation of fibre reinforced mortar, which were then placed inside a climatic chamber recreating fluctuations of relative humidity. The water vapour permeability of all samples was then calculated by applying inverse methods to the mass uptake profiles.

As a result to this procedure, a trend was observed, showing a slight increase of the water vapour permeability with damage. The reproducibility of these measurements was however not satisfactory, as large deviations of permeability were exhibited. It was therefore stated that the description of damage on the basis of a single macroscopic

variable in order to characterise moisture transport properties may not allow an accurate prediction of flow. This observation led to the following conclusion: an adequate prediction of coupled heat and moisture flow, accounting for the influence of all scales of damage and fractures, must be based on a finer knowledge of crack network geometries.

Non-destructive testing

A new experimental methodology was then carried, implementing non-destructive techniques for damage and fracture characterisation during the mechanical loading of mortar samples (Chap. 3). The surface displacements of these samples were measured by digital image correlation, while acoustic sensors were distributed as to monitor the emission activity of the material during the development of damage. The procedure had two main objectives: first, to establish a reliable method for providing measurements of crack networks to the model for heat and moisture transfer simulations. Then, to propose a methodology for monitoring and characterising the degradation state of aged materials at the scale of building components.

The first objective was met on the basis of the imaging results. Digital image correlation, associated with an image processing procedure, allowed visualising the evolution of all ranges of cracks, from microscopic to macroscopic, during the entire mechanical loading process. All geometrical characteristics of these cracks can be quantified through a simple experimental and numerical method. The second objective lies on the simultaneous use of optical measurements and acoustic emission monitoring: acoustic measurements are to be calibrated and interpreted on the basis of damage mappings resulting from digital image correlation, in order to allow their extension to larger scales of observation. A good match was found between both techniques in terms of damage quantification and localisation. Furthermore, acoustic emission allows anticipating the initiation of macroscopic cracks.

Model development and validation

The next step of the work was the development of a numerical frame, which allows a user to include fracture measurements into simulations of heat and moisture transfer in a porous medium (Chap. 4). First, an experimental procedure was carried, in order to provide a data set for the validation of the model. Concrete samples were fractured and observed by a camera for digital image correlation, then placed in an X-ray ragiography apparatus for monitoring the resulting capillary moisture uptake. A finite-element model was then developed as to integrate DIC measurements, explicitely expressing the moisture transport properties of fractures in a fully coupled scheme.

A satisfactory match was found between moisture content distributions observed by X-ray radiography, and those predicted by the finite-element model on the basis of the crack geometry. The mesh density was found to be an important parameter of the calculations, and guidelines were proposed for a reliable integration of discontinuities

in the finite-element mesh. These results are a validation of the general methodology of the work: this mixed experimental and numerical procedure enables the user to recreate complex mechanisms of moisture flow in non-trivial fracture networks.

Model application

After establishing a reliable methodology for gathering experimental data on damage and fracture geometries, and developing the numerical frame which integrates these geometries for the prediction of the flow, the procedure was applied to a set of case studies (Chap. 5). First, benchmark studies were used in order to validate the model in regards to coupled heat and moisture transfer in multi-layered walls under severe climatic loads. Then, a series of examples was defined, in order to illustrate how the developed methodology can be used for assessing the consequences of material degradation on the hygrothermal performance of building components.

The outcome of these calculations is the possibility to quantify heat and moisture transfer in multi-layered building components including one or more fractured material layers, during long simulation times. Processes related to material degradation, such as moisture accumulation or sorption/desorption cycles, could be visualised. This allows assessing the performance and the durability of a given wall geometry, once its damage and fracture patterns are known. Furthermore, the consequence of fractures observed in one material layer on the surrounding components can be visualised. This procedure is expected to yield reliable results allowing the identification of the renovation needs of existing building components.

Recommendations for further research

Multi-scale modelling

As it was noted in the literature survey (see Sec. 1.3.4), models for fluid flow in saturated or non-saturated, damaged or fractured porous media, can be separated into two main categories: continuum models prescribing equivalent macroscopic transport properties, and discrete models explicitely accounting for the presence of discontinuities. The present work started with the first scale of observation, by measuring the equivalent water vapour permeability of diffuse damage networks (Chap. 2). The remainder of the study then focused on the integration of discrete fracture networks into finite-element calculations. However, real materials tend to exhibit a superposition of several scales of fissures, from diffuse to localised damage distributions [PIJ 09, MOO 09]. The present work however did not attempt to superpose multiple scales of cracking. This could be considered by chosing to explicitely include cracks exceeding a certain aperture into the finite-element mesh, and assigning equivalent (possibly anisotropic) transport properties to the surrounding, diffusely damaged, porous medium according to the local value of a damage variable. This supposes a good resolution of the observation technique used for the quantification of fissures.

Damage monitoring

One of the announced purposes of the experimental study conducted in Chap. 3 was to investigate the possibility of applying damage monitoring to field measurements, in order to gather data that can be related to the moisture permeability. The implementation of acoustic emission was suggested, and a method was proposed as to calibrate this technique on the basis of optical measurements in the prospects of its autonomous use at the building scale.

However, important advances remain necessary, should this prospect gain interest. Damage quantification was related to the cumulative number of AE events (or to the AE generation rate according to other authors [OHT 01]), but not to the evolution of the material's transport properties. This can for instance be the subject of experimental studies, measuring the moisture uptake rate related to given numbers of AE events. Since signals can be located and separated according to their waveform in order to separate microscopic fissures from macroscopic fractures, this could result in three-dimensional permeability mappings including the effects of all ranges of cracks. Furthermore, newly developed signal classification techniques [MOE 08, OHN 10, MOM 12] may allow a better understanding of degradation mechanisms.

Three-dimensional extension

The entire work presented here focused on two-dimensional measurements and simulations. This was considered sufficient for developing the experimental and numerical methodology, and for assessing possible consequences of cracking on the durability and hygrothermal performance of building components. However, fractures generally have a three-dimensional shape, and are likely to impact flow in all directions. In order to include these considerations, the developed procedure may be extended to 3D simulations by adapting the numerical code. In the prospects of its validation, X-ray tomography can be used to provide three-dimensional measurements of crack patterns and of moisture infiltration. Furthermore, the acoustic emission technique is directly applicable to volumetric damage observations. This would however involve a larger complexity of the numerical system and longer computational times: a more advanced meshing strategy than the one presented in Sec. 5.2 would be necessary for the extension of the procedure to the 3D case.

Durability assessment

The last part of the study has shown how the developed procedure can lead to quantitative estimations of the moisture accumulation in walls, aggravated by the presence of cracks. A possible continuation is to relate these results with an estimation of their effects on the durability of the building components. Indeed, the numerical study leads to a complete knowledge of the moisture transport and storage in the simulated ma-

terials. As a consequence, one can consider quantifying the causes for degradation in these materials: environmentally induced deterioration [BAN 03], infiltration of chemicals (chloride ions, carbon dioxide), mould development [CLA 99], freeze-thaw damage... The methodology of the present work is therefore a potentially important contribution to the detection of renovation needs and to the improvement of the overall building performance.

Bibliography

[AGG 11] AGGELIS D., SOULIOTI D., SAPOURIDIS N., BARKOULA N., PAIPETIS A., MATIKAS T.
Acoustic emission characterization of the fracture process in fibre reinforced concrete. *Construction and Building Materials*, vol. 25, n° 11, 2011, p. 4126-4131.

[ALD 99] ALDEA C.-M., SHAH S., KARR A.
Permeability of cracked concrete. *Materials and Structures*, vol. 32, 1999, p. 370-376.

[ALF 10] ALFAIATE J., MOONEN P., SLUYS L., CARMELIET J.
On the use of strong discontinuity formulations for the modeling of preferential moisture uptake in fractured porous media. *Computational Methods Applied Mechanical Engineering*, vol. 199, 2010, p. 2828-2839.

[AMM 00] AMMOUCHE A., BREYSSE D., HORNAIN H., DIDRY O., MARCHAND J.
A new image analysis technique for the quantitative assessment of microcracks in cement-based materials. *Cement and Concrete Research*, vol. 30, n° 1, 2000, p. 25-35.

[AND 99] ANDRADE C., SARRÍA J., ALONSO C.
Relative humidity in the interior of concrete exposed to natural and artificial weathering. *Cement and Concrete Research*, vol. 29, n° 8, 1999, p. 1249-1259.

[AND 08] ANDERBERG A., WADSÖ L.
Method for simultaneous determination of sorption isotherms and diffusivity of cement-based materials. *Cement and Concrete Research*, vol. 38, n° 1, 2008, p. 89-94.

[ARF 00] ARFVIDSSON J., CUNNINGHAM M.
A transient technique for determining diffusion coefficients in hygroscopic materials. *Building and Environment*, vol. 35, n° 3, 2000, p. 239-249.

[AWB 98] AWBI H. B.
Calculation of convective heat transfer coefficients of room surfaces for natural convection. *Energy and Buildings*, vol. 28, n° 2, 1998, p. 219-227.

[BAN 03] BANGERT F., GRASBERGER S., KUHL D., MESCHKE G.
Environmentally induced deterioration of concrete: physical motivation and numerical modeling. *Engineering Fracture Mechanics*, vol. 70, n° 7-8, 2003, p. 891-910.

[BAR 99] BAROGHEL-BOUNY V., MAINGUY M., LASSABATERE T., COUSSY O.
Characterization and identification of equilibrium and transfer moisture properties for ordinary and high-performance cementitious materials. *Cement and Concrete Research*, vol. 29, n° 8, 1999, p. 1225-1238.

[BAR 00] BARY B., BOURNAZEL J.-P., BOURDAROT E.
Poro-damage approach applied to hydro-fracture analysis of concrete. *Journal of Engineering Mechanics*, vol. 126, n° 9, 2000, p. 937-943, ASCE.

[BAZ 82] BAZANT Z., RAFTSHOL W.
Effect of cracking in drying and shrinkage specimens. *Cement and Concrete Research*, vol. 12, 1982, p. 209-226.

[BAZ 83] BAZANT Z., OH B.
Crack band theory for fracture of concrete. *Materials and Structures*, vol. 16, 1983, p. 155-177.

[BEL 01] BELYTSCHKO T., MOES N., USUI S., PARIMI C.
Arbitrary discontinuities in finite elements. *International Journal for Numerical Methods in Engineering*, vol. 50, 2001, p. 993-1013.

[BEN 00] BENTZ D., QUENARD D., KUNEL H., BARUCHEL J., PEYRIN F., MARTYS N., GARBOCZI E.
Microstructure and transport properties of porous building materials II: three-dimensional X-ray tomographic studies. *Materials and Structures*, vol. 33, 2000, p. 147-153.

[BEN 05] BENBOUDJEMA F., MEFTAH F., TORRENTI J.
Interaction between drying, shrinkage, creep and cracking phenomena in concrete. *Engineering Structures*, vol. 27, n° 2, 2005, p. 239-250.

[BER 02] BERKOWITZ B.
Characterizing flow and transport in fractured geological media: a review. *Advances in Water Resources*, vol. 25, n° 8-12, 2002, p. 861-884.

[BES 06] BESNARD G., HILD F., ROUX S.
"Finite-Element" displacement fields analysis from digital images: application to Portevin-Le Châtelier bands. *Experimental Mechanics*, vol. 46, 2006, p. 789-803.

[BIO 41] BIOT M.
General theory of three-dimensional consolidation. *Journal of Applied Physics*, vol. 12, 1941, p. 155-164.

[BIO 55] BIOT M.
Theory of elasticity and consolidation for a porous anisotropic solid. *Journal of Applied Physics*, vol. 26, 1955, p. 182-185.

[BLO 04] BLOCKEN B., CARMELIET J.
A review of wind-driven rain research in building science. *Journal of Wind Engineering and Industrial Aerodynamics*, vol. 92, n° 13, 2004, p. 1079-1130.

[BLO 08] BLOCKEN B., CARMELIET J.
Guidelines for the required time resolution of meteorological input data for wind-driven rain calculations on buildings. *Journal of Wind Engineering and Industrial Aerodynamics*, vol. 96, n° 5, 2008, p. 621-639.

[BLO 10] BLOCKEN B., CARMELIET J.
Overview of three state-of-the-art wind-driven rain assessment models and comparison based on model theory. *Building and Environment*, vol. 45, 2010, p. 691-703.

[BUR 53] BURDINE N.
Relative permeability calculations from pore-size distribution data. *Trans. AIME*, vol. 198, 1953, p. 71-78.

[CAR 99] CARMELIET J., DESCAMPS F., HOUVENAGHEL G.
A multiscale network model for simulating moisture transfer properties of porous media. *Transport in Porous Media*, vol. 35, 1999, p. 67-88.

[CAR 01] CARMELIET J., ROELS S.
Determination of the isothermal moisture transport properties of porous building materials. *Journal of Thermal Envelope and Building Science*, vol. 24, 2001, p. 183-210.

[CAR 02] CARMELIET J., ROELS S.
Determination of the moisture capacity of porous building materials. *Journal of Thermal Envelope and Building Science*, vol. 25, 2002, p. 209-237.

[CAR 04] CARMELIET J., ABEELE K. V. D.
Poromechanical approach describing the moisture influence on the non-linear quasi-static and dynamic behaviour of porous building materials. *Materials and Structures*, vol. 37, n° 268, 2004, p. 271-280.

[CAR 05a] CARMELIET J., DE WIT M., JANSSEN H.
Hysteresis and moisture buffering of wood. *7th Nordic Symposium on Building Physics*, 2005.

[CAR 05b] CARSON J. K., LOVATT S. J., TANNER D. J., CLELAND A. C.
Thermal conductivity bounds for isotropic, porous materials. *International Journal of Heat and Mass Transfer*, vol. 48, n° 11, 2005, p. 2150-2158.

[CEL 90] CELIA M., BOULOUTAS E., ZARBA R.
A general mass-conservative numerical solution for the unsaturated flow equation. *Water Resources Research*, vol. 26, 1990, p. 1483-1496.

[CER 02] CERNÝ R., ROVNANÍKOVÁ P.
Transport processes in concrete. London: Spon Press, 2002.

[CHA 10a] CHALENCON F.
Etude des intéractions rhéologie, fissuration et microstructure pour le développement d'un outil de formulation : application aux mortiers poreux minces fibrés dédiés à l'ITE. Thèse de doctorat, INSA Lyon, 2010.

[CHA 10b] CHALENCON F., ORGÉAS L., DUMONT P., FORAY G., CAVAILLÉ J.-Y., MAIRE E., DU ROSCOAT S. R.
Lubricated compression and X-ray microtomography to analyse the rheology of a fibre-reinforced mortar. *Rheologica Acta*, vol. 49, 2010, p. 221-235.

[CHO 93] CHOI E.
Simulation of wind-driven rain around a building. *Journal of Wind Engineering and Industrial Aerodynamics*, vol. 46, 1993, p. 721-729.

[CHO 94] CHOI E.
Determination of wind-driven rain intensity on building faces. *Journal of Wind Engineering and Industrial Aerodynamics,* vol. 51, 1994, p. 55-69.

[CHO 97] CHOI S., SHAH S.
Measurement of deformations on concrete subjected to compression using image correlation. *Experimental Mechanics*, vol. 37, 1997, p. 307-313.

[CHO 07] CHOINSKA M., KHELIDJ A., CHATZIGEORGIOU G., PIJAUDIER-CABOT G.
Effects and interactions of temperature and stress-level related damage on permeability of concrete. *Cement and Concrete Research*, vol. 37, n° 1, 2007, p. 79-88.

[CLA 99] CLARKE J., JOHNSTONE C., KELLY N., MCLEAN R., ANDERSON J., ROWAN N., SMITH J.
A technique for the prediction of the conditions leading to mould growth in buildings. *Building and Environment*, vol. 34, n° 4, 1999, p. 515-521.

[COL 03] COLOMBO S., MAIN I. G., FORDE M. C.
Assessing damage of reinforced concrete beam using "b-value" analysis of acoustic emission signals. *Journal of Materials in Civil Engineering*, vol. 15, 2003, p. 280-286.

[COR 07] CORR D., ACCARDI M., GRAHAM-BRADY L., SHAH S.
Digital image correlation analysis of interfacial debonding properties and fracture behavior in concrete. *Engineering Fracture Mechanics*, vol. 74, n° 1-2, 2007, p. 109-121.

[COU 04] COUSSY O.
Poromechanics. New York, John Wiley & Sons, 2004.

[CRA 75] CRANK J.
The mathematics of diffusion. Oxford Science Publications, New York, 1975.

[CRA 00] CRAWLEY D., LAWRIE L., PEDERSEN C., WINKELMANN F.
EnergyPlus: Energy simulation program. *ASHRAE Journal*, vol. 42, 2000, p. 49-56.

[DAV 79] DAVIES D., BOULDIN D.
A cluster separation measure. *IEEE Transactions on Pattern Analysis and Machine Intelligence*, vol. PAMI-1, 1979, p. 224-227.

[DER 07] DERLUYN H., JANSSEN H., DIEPENS J., DEROME D., CARMELIET J.
Hygroscopic behavior of paper and books. *Journal of Building Physics*, vol. 31, 2007, p. 9-34.

[DOL 00] DOLBOW J., MOËS N., BELYTSCHKO T.
Discontinuous enrichment in finite elements with a partition of unity method. *Finite Elements in Analysis and Design*, vol. 36, n° 3-4, 2000, p. 235-260.

[DOU 08] DOUAT T., FORAY G., WOLOSZYN M.
Mise au point d'un système dédié de mesures de sorption dynamique par matériaux du bâtiment. Master's thesis, INSA Lyon, 2008.

[DRC 03] DRCHALOVÁ J., ČERNÝ R.
A simple gravimetric method for determining the moisture diffusivity of building materials. *Construction and Building Materials*, vol. 17, n° 3, 2003, p. 223-228.

[DUN 85] DUNAVANT D.
High degree efficient symmetrical Gaussian quadrature rules for the triangle. *International Journal for Numerical Methods in Engineering*, vol. 21, 1985, p. 1129-1148.

[DUR 94] DURNER W.
Hydraulic conductivity estimation for soils with heterogeneous pore structure. *Water Resources Research*, vol. 30, 1994, p. 211-223.

[ELA 07] ELAQRA H., GODIN N., PEIX G., R'MILI M., FANTOZZI G.
Damage evolution analysis in mortar, during compressive loading using acoustic emission and X-ray tomography: effects of the sand/cement ratio. *Cement and Concrete Research*, vol. 37, n° 5, 2007, p. 703-713.

[FAT 56] FATT I.
The network model of porous media. *Petroleum Transactions, AIME*, vol. 207, 1956, p. 144-177.

[FIC 99] FICHANT S., BORDERIE C. L., PIJAUDIER-CABOT G.
Isotropic and anisotropic descriptions of damage in concrete structures. *Mechanics of Cohesive-Frictional Materials*, vol. 4, 1999, p. 339-359.

[GAR 06] GARBALINSKA H.
Application of sqrt-t-type, logarithmic and half-time methods in desorptive measurements of diffusivity in narrow humidity ranges. *Cement and Concrete Research*, vol. 36, n° 7, 2006, p. 1294-1303.

[GAR 10] GARBALINSKA H., KOWALSKI S. J., STASZAK M.
Linear and non-linear analysis of desorption processes in cement mortar. *Cement and Concrete Research*, vol. 40, n° 5, 2010, p. 752-762.

[GEN 80] VAN GENUCHTEN M.
A closed-form equation for predicting the hydraulic conductivity of unsaturated soils. *Soil Sci. Soc. Am.*, vol. 44, 1980, p. 892-898.

[GER 96] GERARD B., BREYSSE D., AMMOUCHE A., HOUDUSSE O., DIDRY O.
Cracking and permeability of concrete under tension. *Materials and Structures*, vol. 29, 1996, p. 141-151.

[GOD 04] GODIN N., HUGUET S., GAERTNER R., SALMON L.
Clustering of acoustic emission signals collected during tensile tests on unidirectional glass/polyester composite using supervised and unsupervised classifiers. *NDT&E international*, vol. 37, 2004, p. 253-264.

[GOD 06] GODIN N., HUGUET S., GAERTNER R.
Influence of hydrolytic ageing on the acoustic emission signatures of damage mechanisms occuring during tensile tests on unidirectionnal glass/polyester composites: application of a Kohonen's map. *Composite Structures*, vol. 72, 2006, p. 79-85.

[GRA 04] GRASBERGER S., MESCHKE G.
Thermo-hygro-mechanical degradation of concrete : from coupled 3D material modelling to durability-oriented multifield structural analysis. *Materials and Structures*, vol. 37, 2004, p. 244-256.

[GRA 07] GRANGER S., LOUKILI A., PIJAUDIER-CABOT G., CHANVILLARD G.
Experimental characterization of the self-healing of cracks in an ultra high performance cementitious material: Mechanical tests and acoustic emission analysis. *Cement and Concrete Research*, vol. 37, n° 4, 2007, p. 519-527.

[GUM 80] GUMMERSON R., HALL C., HOFF W.
Water movement in porous building materials–II. Hydraulic suction and sorptivity of brick and other masonry materials. *Building and Environment*, vol. 15, n° 2, 1980, p. 101-108.

[HAG 02a] HAGENTOFT C.
HAMSTAD WP2 - Benchmark package. rapport, 2002, Dept. of Building Physics - Chalmers University of Technology.

[HAG 02b] HAGENTOFT C.
HAMSTAD WP2 - Reference document basic modelling physics. rapport, 2002, Dept. of Building Physics - Chalmers University of Technology.

[HAG 04] HAGENTOFT C.-E., KALAGASIDIS A., ADL-ZARRABI B., ROELS S., CARMELIET J., HENS H., GRUNEWALD J., FUNK M., BECKER R., SHAMIR D., ADAN O., BROCKEN H., KUMARAN K., DJEBBAR R.
Assessment method of numerical prediction models for combined heat, air and moisture transfer in building components. Benchmarks for one-dimensional cases. *Journal of Thermal Envelope and Building Science*, vol. 27, 2004, p. 327-352.

[HAR 04] HARMAN I., BEST M., BELCHER S.
Radiative exchange in an urban street canyon. *Boundary-Layer Meteorology*, vol. 110, 2004, p. 301-316.

[HAS 79a] HASSANIZADEH M., GRAY W.
General conservation equations for multi-phase systems: 1. Averaging procedure. *Advances in Water Resources*, vol. 2, 1979, p. 131-144.

[HAS 79b] HASSANIZADEH M., GRAY W.
General conservation equations for multi-phase systems: 2. Mass, momenta, energy, and entropy equations. *Advances in Water Resources*, vol. 2, 1979, p. 191-203.

[HAS 86a] HASSANIZADEH S.
Derivation of basic equations of mass transport in porous media, part 1. Macroscopic balance laws. *Advances in Water Resources*, vol. 9, 1986, p. 196-296.

[HAS 86b] HASSANIZADEH S.
Derivation of basic equations of mass transport in porous media, part 2. Generalized Darcy's and Fick's laws. *Advances in Water Resources*, vol. 9, 1986, p. 207-222.

[HAS 93] HASSANIZADEH S., GRAY W.
Thermodynamic basis of capillary pressure in porous media. *Water Resources Research*, vol. 29, 1993, p. 3389-3405.

[HIL 76] HILLERBORG A., MODEER M., PETERSSON P.
Analysis of crack formation and crack growth in concrete by means of fracture mechanics and finite elements. *Cement and Concrete Research*, vol. 6, 1976, p. 773-782.

[HIL 06] HILD F., ROUX S.
Digital image correlation: from displacement measurement to identification of elastic properties - a review. *Strain*, vol. 42, 2006, p. 69-80.

[HOR 96] HORNAIN H., MARCHAND J., AMMOUCHE A., COMMÈNE J., MORANVILLE M.
Microscopic observation of cracks in concrete - a new sample preparation technique using dye impregnation. *Cement and Concrete Research*, vol. 26, 1996, p. 573-583.

[HOS 09] HOSEINI M., BINDIGANAVILE V., BANTHIA N.
The effect of mechanical stress on permeability of concrete: a review. *Cement and Concrete Composites*, vol. 31, 2009, p. 213-220.

[HVI 98] HVISTENDAHL-KARLSEN K., LIE K., RISEBRO N., FROYEN J.
A front-tracking approach to a two-phase fluid flow model with capillary forces. *In Situ*, vol. 22, 1998, p. 59-89.

[IRW 57] IRWIN G.
Analysis of stresses and strains near the end of a crack traversing a plate. *Journal of Applied Mechanics*, vol. 24, 1957, p. 361-364.

[ISOa] « EN ISO 12571. Hygrothermal performance of building materials and products - Determination of hygroscopic sorption properties ».

[ISOb] « EN ISO 12572. Hygrothermal performance of building materials and products - Determination of water vapour transmission properties ».

[IWA 97] IWANAMI M., KAMADA T., NAGATAKI S.
Application of AE technique for crack monitoring in RC beams. *JCA Proceedings of Cement and Concrete*, vol. 51, 1997, p. 192-197.

[JAN 07] JANSSEN H., BLOCKEN B., CARMELIET J.
Conservative modelling of the moisture and heat transfer in building components under atmospheric excitation. *International Journal of Heat and Mass Transfer*, vol. 50, n^o 5-6, 2007, p. 1128-1140.

[JEN 05] JENNI A., HOLZER L., ZURBRIGGEN R., HERWEGH M.
Influence of polymers on microstructure and adhesive strength of cementitious tile adhesive mortars. *Cement and Concrete Research*, vol. 35, 2005, p. 35-50.

[JEN 06] JENNI A., ZURBRIGGEN R., HOLZER L., HERWEGH M.
Changes in microstructures and physical properties of polymer-modified mortars during wet storage. *Cement and Concrete Research*, vol. 36, 2006, p. 79-90.

[JIA 94] JIA Z., SHAH S.
Two-dimensional electronic speckle pattern interferometry and concrete fracture processes. *Experimental Mechanics*, vol. 34, 1994, p. 262-270.

[JIR 06] JIRIČKOVÁ M., ČERNÝ R.
Effect of hydrophilic admixtures on moisture and heat transport and storage parameters of mineral wool. *Construction and Building Materials*, vol. 20, 2006, p. 425-434.

[JOH 02] JOHNSON M.
Waveform based clustering and classification of AE transients in composite laminates using principal component analysis. *NDT & E International*, vol. 35, n° 6, 2002, p. 367-376.

[KAL 07] KALAGASIDIS A., WEITZMANN P., NIELSEN T., PEUHKURI R., HAGENTOFT C.-E., RODE C.
The International Building Physics Toolbox in Simulink. *Energy and Buildings*, vol. 39, n° 6, 2007, p. 665-674.

[KER 91] KERMANI A.
Permeability of stressed concrete. *Building Research and Information*, vol. 19, 1991, p. 360-366.

[KRU 96] KRUS M.
Moisture transport and storage coefficients of porous mineral building materials: Theoretical principles and new test methods. Fraunhofer IRB Verlag, Stuttgart, 1996.

[KUM 02] KUMARAN M., LACKEY J., NORMANDIN N., TARIKU F., VAN REENEN D.
A thermal and moisture transport property database for common building and insulating materials. rapport, 2002, ASHRAE research project 1018-RP.

[KWI 09] KWIATKOWSKI J.
Moisture in buildings, air-envelope interaction. Thèse de doctorat, Institut National des Sciences Appliquées de Lyon, 2009.

[LAN 03] LANDIS E., NAGY E., KEANE D.
Microstructure and fracture in three dimensions. *Engineering Fracture Mechanics*, vol. 70, 2003, p. 911-925.

[LAN 07] LANDIS E., ZHANG T., NAGY E., NAGY G., FRANKLIN W.
Cracking, damage and fracture in four dimensions. *Materials and Structures*, vol. 40, 2007, p. 357-364.

[LAW 02] LAWLER J., ZAMPINI D., SHAH S.
Permeability of cracked hybrid fiber-reinforced mortar under load. *ACI Materials Journal*, vol. 99, 2002, p. 379-385.

[LEM 00] LEMAITRE J., DESMORAT R., SAUZAY M.
Anisotropic damage law of evolution. *European Journal of Mechanics - A/Solids*, vol. 19, n° 2, 2000, p. 187 - 208.

[LEP 10] LEPLAY P., RÉTHORÉ J., MEILLE S., BAIETTO M.-C.
Damage law identification of a quasi brittle ceramic from a bending test using Digital Image Correlation. *Journal of the European Ceramic Society*, vol. 30, n° 13, 2010, p. 2715 - 2725.

[LEV 81] LEVY F.
A modified Maxwell-Eucken equation for calculating the thermal conductivity of two-component solutions or mixtures. *International Journal of Refrigeration*, vol. 4, n° 4, 1981, p. 223 - 225.

[LEW 87] LEWIS R., SCHREFLER B.
The finite element method in the deformation and consolidation of porous media. John Wiley and Sons Inc.,New York, NY, 1987.

[LI 03] LI V.
On engineered cementitious composites (ECC) - a review of the material and its application. *Journal of Advanced Concrete Technology*, vol. 1, 2003, p. 215-230.

[LIK 03] LIKAS A., VLASSIS N., VERBEEK J.
The global k-means clustering algorithm. *Pattern Recognition*, vol. 366, 2003, p. 451-461.

[LIM 00] LIM C. C., GOWRIPALAN N., SIRIVIVATNANON V.
Microcracking and chloride permeability of concrete under uniaxial compression. *Cement and Concrete Composites*, vol. 22, n° 5, 2000, p. 353 - 360.

[LOV 96] LOVEDAY D. L., TAKI A. H.
Convective heat transfer coefficients at a plane surface on a full-scale building facade. *International Journal of Heat and Mass Transfer*, vol. 39, n° 8, 1996, p. 1729 - 1742.

[LUC 89] LUCKNER L., VAN GENUCHTEN M., NIELSEN D.
A consistent set of parametric models for the two-phase-flow of immiscible fluids in the subsurface. *Water Resources Research*, vol. 25, 1989, p. 2187-2193.

[MAC 67] MACQUEEN J.
Some methods for classification and analysis of multivariate observations. *Proceedings of the 5th Berkeley symposium on mathematical statistics and probability*, 1967.

[MAI 12] MAILLET E., GODIN N., R'MILI M., REYNAUD P., LAMON J., FANTOZZI G.
Analysis of acoustic emission energy release during static fatigue tests at intermediate temperatures on ceramic matrix composites: towards rupture time prediction. *Composites Science and Technology*, vol. 72, 2012, p. 1001-1007.

[MAR 63] MARQUARDT D.
An algorithm for least-squares estimation of nonlinear parameters. *SIAM Journal of Applied Mathematics*, vol. 11, 1963, p. 431 - 441.

[MAU 12] MAUROUX T., BENBOUDJEMA F., TURCRY P., AÏT-MOKHTAR A., DEVES O.
Study of cracking due to drying in coating mortars by digital image correlation. *Cement and Concrete Research*, vol. 42, n° 7, 2012, p. 1014-1023.

[MAZ 89] MAZARS J., PIJAUDIER-CABOT G.
Continuum damage theory - application to concrete. *Journal of Engineering Mechanics*, vol. 115, 1989, p. 345-365.

[MEL 96] MELENK J. M., BABUSKA I.
The partition of unity finite element method: Basic theory and applications. *Computer Methods in Applied Mechanics and Engineering*, vol. 139, n° 1-4, 1996, p. 289-314.

[MES 98] MESCHKE G., LACKNER R., MANG H.
An anisotropic elastoplastic-damage model for plain concrete. *International Journal for Numerical Methods in Engineering*, vol. 42, 1998, p. 703-727.

[MES 03] MESCHKE G., GRASBERGER S.
Numerical Modeling of Coupled Hygromechanical Degradation of Cementitious Materials. *Journal of Engineering Mechanics*, vol. 129, n° 4, 2003, p. 383-392, ASCE.

[MNA 06] MNAHONČÁKOVÁ E., JIŘIČKOVÁ M., PAVLÍK Z., FIALA L., ROVNANÍKOVÁ P., BAYER P., ČERNÝ R.
Effect of moisture on the thermal conductivity of a cementitious composite. *International Journal of Thermophysics*, vol. 27, n° 4, 2006, p. 1228 - 1240.

[MOE 99] MOES N., DOLBOW J., BELYTSCHKO T.
A finite element method for crack growth without remeshing. *International Journal for Numerical Methods in Engineering*, vol. 46, 1999, p. 131-150.

[MOE 08] MOEVUS M., GODIN N., R'MILI M., ROUBY D., REYNAUD P., FANTOZZI G., FARIZY G.
Analysis of damage mechanisms and associated acoustic emission in two SiC/[Si-B-C] composites exhibiting different tensile behaviours. Part II: Unsupervised acoustic emission data clustering. *Composites Science and Technology*, vol. 68, n° 6, 2008, p. 1258-1265.

[MOM 10] MOMON S., MOEVUS M., GODIN N., R'MILI M., REYNAUD P., FANTOZZI G., FAYOLLE G.
Acoustic emission and lifetime prediction during static fatigue tests on ceramic-matrix composite at high temperature under air. *Composites Part A: Applied Science and Manufacturing*, vol. 41, 2010, p. 913-918.

[MOM 12] MOMON S., GODIN N., REYNAUD P., R'MILI M., FANTOZZI G.
Unsupervised and supervised classification of AE data collected during fatigue test on CMC at high temperature. *Composites Part A: Applied Science and Manufacturing*, vol. 43, 2012, p. 254-260.

[MOO 09] MOONEN P.
Continuous-discontinuous modelling of hygrothermal damage processes in porous media. Thèse de doctorat, Katholieke Universiteit Leuven, 2009.

[MOO 11] MOONEN P., SLUYS L., CARMELIET J.
A continuous-discontinuous approach to simulate heat transfer in fractured media. *Transport in Porous Media*, vol. 89, 2011, p. 399-419.

[MUA 74] MUALEM Y.
A conceptual model of hysteresis. *Water Resources Research*, vol. 3, 1974, p. 514-520.

[MUA 76a] MUALEM Y.
Hysteretical models for prediction of the hydraulic conductivity of unsaturated porous media. *Water Resources Research*, vol. 12, 1976, p. 1248-1254.

[MUA 76b] MUALEM Y.
A new model for predicting the hydraulic conductivity of unsaturated porous media. *Water Resources Research*, vol. 12, 1976, p. 513-522.

[MUR 10] MURALIDHARA S., PRASAD B. R., ESKANDARI H., KARIHALOO B.
Fracture process zone size and true fracture energy of concrete using acoustic emission. *Construction and Building Materials*, vol. 24, n° 4, 2010, p. 479-486.

[OHN 10] OHNO K., OHTSU M.
Crack classification in concrete based on acoustic emission. *Construction and Building Materials*, vol. 24, n° 12, 2010, p. 2339-2346.

[OHT 01] OHTSU M., WATANABE H.
Quantitative damage estimation of concrete by acoustic emission. *Construction and Building Materials*, vol. 15, n° 5-6, 2001, p. 217-224.

[ORT 09] ORTEU J.-J.
3-D computer vision in experimental mechanics. *Optics and Lasers in Engineering*, vol. 47, n° 3–4, 2009, p. 282-291.

[PAV 09] PAVLÍK Z., ČERNÝ R.
Hygrothermal performance study of an innovative interior thermal insulation system. *Applied Thermal Engineering*, vol. 29, n° 10, 2009, p. 1941-1946.

[PEA 10] PEASE B.
Influence of concrete cracking on ingress and reinforcement corrosion. Thèse de doctorat, Department of Civil Engineering, Technical University of Denmark, 2010.

[PHI 98] PHILIPPIDIS T., NIKOLAIDIS V., ANASTASSOPOULOS A.
Damage characterization of carbon/carbon laminates using neural network techniques on AE signals. *NDT&E International*, vol. 31, n° 5, 1998, p. 329-340.

[PIC 01] PICANDET V., KHELIDJ A., BASTIAN G.
Effect of axial compressive damage on gas permeability of ordinary and high-performance concrete. *Cement and Concrete Research*, vol. 31, n° 11, 2001, p. 1525-1532.

[PIJ 09] PIJAUDIER-CABOT G., DUFOUR F., CHOINSKA M.
Permeability due to the increase of damage in concrete: from diffuse to localized damage distributions. *Journal of Engineering Mechanics*, vol. 135, 2009, p. 1022-1028.

[POL 05] POLIFKE W., KOPITZ J.
Wärmeübertragung. Pearson Studium, 2005.

[PRI 06] PRIESACK E., DURNER W.
Closed-form expression for the multi-modal unsaturated conductivity function. *Vadose Zone Journal*, vol. 5, 2006, p. 121-124.

[PRO 76] PROGELHOF R., THRONE J., RUETSCH R.
Methods for predicting the thermal conductivity of composite systems: A review. *Polymer Engineering and Science*, vol. 16, 1976, p. 615-625.

[QIN 09] QIN M., BELARBI R., AÏT-MOKHTAR A., ALLARD F.
Simulation of coupled heat and moisture transfer in air-conditioned buildings. *Automation in Construction*, vol. 18, 2009, p. 624-631.

[QIN 12] QIN M., WALTON G., BELARBI R., ALLARD F.
Simulation of whole building coupled hygrothermal-airflow in different climates. *Energy Conversion and Management*, vol. 52, 2012, p. 1470-1478.

[QUE 98] QUENARD D. A., XU K., KÜNZEL H. M., BENTZ D. P., MARTYS N. S.
Microstructure and transport properties of porous building materials. *Materials and Structures*, vol. 31, 1998, p. 317-324.

[RAP 02] RAPOPORT J., ALDEA C.-M., SHAH S., ANKENMAN B., KARR A.
Permeability of cracked steel fier-reinforced concrete. *ASCE Journal of Materials and Civil Engineering*, vol. 14, 2002, p. 355-358.

[REI 06] REICHENBERGER V., JAKOBS H., BASTIAN P., HELMIG R.
A mixed-dimensional finite volume method for two-phase flow in fractured porous media. *Advances in Water Resources*, vol. 29, n^o 7, 2006, p. 1020-1036.

[RET 05] RETHORÉ J., GRAVOUIL A., MORESTIN F., COMBESCURE A.
Estimation of mixed-mode stress intensity factors using digital image correlation and an interaction integral. *International Journal of Fracture*, vol. 132, 2005, p. 65-79.

[RET 07] RETHORÉ J., DE BORST R., ABELLAN M.-A.
A two-scale approach for fluid flow in fractured porous media. *International Journal for Numerical Methods in Engineering*, vol. 71, 2007, p. 780-800.

[ROD 03] RODE C.
Workshop on Moisture Buffer Capacity - Summary Report. rapport, 2003, Department of Civil Engineering, Technical University of Denmark.

[ROE 01] ROELS S., ELSEN J., CARMELIET J., HENS H.
Characterisation of pore structure by combining mercury porosimetry and micrography. *Materials and Structures*, vol. 34, 2001, p. 76-82.

[ROE 03a] ROELS S., CARMELIET J., HENS H.
HAMSTAD WP1 - Moisture transfer properties and materials characterization. rapport, 2003, K.U.Leuven - Laboratory of Building Physics.

[ROE 03b] ROELS S., VANDERSTEEN K., CARMELIET J.
Measuring and simulating moisture uptake in a fractured porous medium. *Advances in Water Resources*, vol. 26, n^o 3, 2003, p. 237-246.

[ROE 04] ROELS S., CARMELIET J., HENS H., ADAN O., BROCKEN H., CERNY R., PAVLIK A., ELLIS A., HALL C., KUMARAN K., PEL L., PLAGGE R.
A comparison of different techniques to quantify moisture content profiles in porous building materials. *Journal of Thermal Envelope and Building Science*, vol. 27, 2004, p. 261-276.

[ROE 06a] ROELS S., CARMELIET J.
Analysis of moisture flow in porous materials using microfocus X-ray radiography. *International Journal of Heat and Mass Transfer*, vol. 49, 2006, p. 4762-4772.

[ROE 06b] ROELS S., MOONEN P., PROFT K. D., CARMELIET J.
A coupled discrete-continuum approach to simulate moisture effects on damage processes in porous materials. *Computer Methods in Applied Mechanics and Engineering*, vol. 195, n^o 52, 2006, p. 7139-7153.

[ROU 06] ROUX S., HILD F.
Stress intensity factor measurements from digital image correlation: post-processing and integrated approaches. *International Journal of Fracture*, vol. 140, n^o 1, 2006, p. 141-157.

[ROU 12a] ROUCHIER S., FORAY G., WOLOSZYN M., ROUX J.-J.
Influence of diffuse damage on the water vapour permeability of fibre-reinforced mortar. *Transport in Porous Media*, vol. 93, 2012, p. 543-559.

[ROU 12b] ROUCHIER S., JANSSEN H., RODE C., WOLOSZYN M., FORAY G., ROUX J.-J.
Characterization of fracture patterns and hygric properties for moisture flow modelling in cracked concrete. *Construction and Building Materials*, vol. 34, 2012, p. 54-62.

[ROU 13] ROUCHIER S., FORAY G., GODIN N., WOLOSZYN M., ROUX J.-J.
Damage monitoring in fibre reinforced mortar by combined digital image correlation and acoustic emission. *Construction and Building Materials*, vol. 38, 2013, p. 371-380.

[SAM 92] SAMAHA H. R., HOVER K. C.
Influence of microcracking on the mass transport properties of concrete. *ACI Materials Journal*, vol. 89, n° 4, 1992, p. 416-424.

[SCH 06] SCHREFLER B. A., SECCHI S., SIMONI L.
On adaptive refinement techniques in multi-field problems including cohesive fracture. *Computer Methods in Applied Mechanics and Engineering*, vol. 195, 2006, p. 444-461.

[SCH 10] SCHEFFLER G. A., PLAGGE R.
A whole range hygric material model: Modelling liquid and vapour transport properties in porous media. *International Journal of Heat and Mass Transfer*, vol. 53, n° 1-3, 2010, p. 286-296.

[SEC 03] SECCHI S., SIMONI L.
An improved procedure for 2D unstructured Delaunay mesh generation. *Advances in Engineering Software*, vol. 34, n° 4, 2003, p. 217-234.

[SEG 04] SEGURA J., CAROL I.
On zero-thickness interface elements for diffusion problems. *International Journal for Numerical and Analytical Methods in Geomechanics*, vol. 28, 2004, p. 947-962.

[SEG 08a] SEGURA J., CAROL I.
Coupled HM analysis using zero-thickness interface elements with double nodes. Part I: theoretical model. *International Journal for Numerical and Analytical Methods in Geomechanics*, vol. 32, 2008, p. 2083-2101.

[SEG 08b] SEGURA J., CAROL I.
Coupled HM analysis using zero-thickness interface elements with double nodes. Part II: verification and application. *International Journal for Numerical and Analytical Methods in Geomechanics*, vol. 32, 2008, p. 2103-2123.

[SHA 84] SHARPLES S.
Full scale measurements of convective energy losses from exterior building surfaces. *Building and Environment*, vol. 19, 1984, p. 31-39.

[SHA 99] SHAH S., CHOI S.
Nondestructive techniques for studying fracture processes in concrete. *International Journal of Fracture*, vol. 98, 1999, p. 351-359.

[SHI 94] SHIOTANI T., FUJII K., AOKI T., AMOU K.
Evaluation of progressive failure using AE sources and improved B-value on slope model tests. *Prog Acoust Emiss*, vol. 7, 1994, p. 509-514.

[SHI 01] SHIOTANI T., OHTSU M., IKEDA K.
Detection and evaluation of AE waves due to rock deformation. *Construction and Building Materials*, vol. 15, 2001, p. 235-246.

[SHI 09] SHIOTANI T., MOMOKI S., CHAI H., AGGELIS D.
Elastic wave validation of large concrete structures repaired by means of cement grouting. *Construction and Building Materials*, vol. 23, n° 7, 2009, p. 2647-2652.

[SIL 06] SILVA D., MONTEIRO P.
The influence of polymers on the hydration of portland cement phases analyzed by soft X-ray transmission microscopy. *Cement and Concrete Research*, vol. 36, 2006, p. 1501-1507.

[SLA 63] SLATE F., OLSEFSKI S.
X-rays for study of internal structure and microcracking of concrete. *Journal of the American Concrete Institute*, vol. 60, 1963, p. 575-588.

[SNO 69] SNOW D.
Anisotropic permeability of fractured media. *Water Resources Research*, vol. 5, 1969, p. 1273-1289.

[STE 10] STEEMAN M., JANSSENS A., STEEMAN H., BELLEGHEM M. V., PAEPE M. D.
On coupling 1D non-isothermal heat and mass transfer in porous materials with a multizone building energy simulation model. *Building and Environment*, vol. 47, 2010, p. 865-877.

[STR 00] STRAUBE J., BURNETT E.
Simplified prediction of driving rain on buildings. *Proc. of the International Building Physics Conference, Eindhoven, The Netherlands*, 2000.

[SUG 96] SUGIYAMA T., BREMNER T., HOLM T.
Effect of stress on gas permeability in concrete. *ACI Materials Journal*, vol. 93, 1996, p. 443-450.

[SUT 83] SUTTON M., WOLTERS W., PETERS W., RANSON W., MCNEILL S.
Determination of displacements using an improved digital correlation method. *Image and Vision Computing*, vol. 1, 1983, p. 133-139.

[SUT 09] SUTTON M., ORTEU J.-J., SCHREIER H.
Image correlation for shape, motion and deformation measurements: basic concepts, theory and applications. Springer, 2009.

[SUZ 04] SUZUKI T., OHTSU M.
Quantitative damage evaluation of structural concrete by a compression test based on AE rate process analysis. *Construction and Building Materials*, vol. 18, 2004, p. 197-202.

[TOD 04] TODA H., SINCLAIR I., BUFFIÈRE J.-Y., MAIRE E., KHOR K., GREGSON P., KOBAYASHI T.
A 3D measurement procedure for internal local crack driving forces via synchrotron X-ray microtomography. *Acta Materialia*, vol. 52, n° 5, 2004, p. 1305-1317.

[VAN 03] VANDERSTEEN K., CARMELIET J., FEYEN J.
A network modeling approach to derive unsaturated hydraulic properties of a rough-walled structure. *Transport in Porous Media*, vol. 50, 2003, p. 197-221.

[VDI 10] VDI
VDI Heat Atlas. Springer, 2010.

[VEJ 09] VEJMELKOVÁ E., PAVLIKOVÁ M., JERMAN M., ČERNÝ R.
Free water intake as means of material characterization. *J Build Phys*, vol. 33, 2009, p. 29-44.

[VID 11] VIDYASAGAR R., RAGHUPRASAD B.
An experimental study on acoustic emission energy as a quantitative measure of size independent specific fracture energy of concrete beams. *Construction and Building Materials*, vol. 25, n° 5, 2011, p. 2349-2357.

[WAN 97] WANG K., JANSEN D., SHAH S., KARR A.
Permeability study of cracked concrete. *Cement and Concrete Research*, vol. 27, 1997, p. 381-393.

[WAN 06] WANG J., CARSON J. K., NORTH M. F., CLELAND D. J.
A new approach to modelling the effective thermal conductivity of heterogeneous materials. *International Journal of Heat and Mass Transfer*, vol. 49, n° 17-18, 2006, p. 3075-3083.

[WEL 01] WELLS G., SLUYS L.
A new method for modelling cohesive cracks using finite elements. *International Journal of Numerical Methods in Engineering*, vol. 50, 2001, p. 2667-2682.

[WET 12] WETZEL A., HERWEGH M., ZURBRIGGEN R., WINNEFELD F.
Influence of shrinkage and water transport mechanisms on microstructure and crack formation of tile adhesive mortars. *Cement and Concrete Research*, vol. 42, 2012, p. 39-50.

[WHI 69] WHITAKER S.
Advances in the theory of fluid motion in porous media. *Industrial and Engineering Chemistry*, vol. 12, 1969, p. 14-28.

[WOR 04] WORCH A.
The behaviour of vapour transfer on building material surfaces: the vapour transfer resistance. *Journal of Thermal Envelope and Building Science*, vol. 28, 2004, p. 187-199.

[XU 97a] XU K., DAIAN J.-F., QUENARD D.
Multiscale structures to describe porous media - Part 1 : theoretical background and invasion by fluids. *Transport in Porous Media*, vol. 26, 1997, p. 51-73.

[XU 97b] XU K., DAIAN J.-F., QUENARD D.
Multiscale structures to describe porous media - Part 2 : transport properties and application to test materials. *Transport in Porous Media*, vol. 26, 1997, p. 319-338.

Appendix A

Derivations

A.1 Equivalence between pressure gradients

It was stated in section 1.2.2 that it is preferable to only use one pressure variable as a driving potential for moisture transfer. In order to guarantee the applicability of Eq. 1.9, the equivalence between ∇p_v and ∇p_c must be established. The derivation of this equivalence is not trivial, as explained here.

If we wish to only keep the capillary pressure p_c and the temperature T as the main variables of the calculations, the gradient of vapour partial pressure can be expressed as such:

$$\nabla p_v = \underbrace{\frac{\partial p_v}{\partial p_c}}_{\text{(a)}} \nabla p_c + \underbrace{\frac{\partial p_v}{\partial T}}_{\text{(b)}} \nabla T \tag{A.1}$$

The basis for the derivation of this equation lies on Kelvin's law:

$$p_v = p_s \exp\left(\frac{p_c}{\rho_l R_v T}\right) \tag{A.2}$$

which leads to the following expression of the first derivative (a):

$$\frac{\partial p_v}{\partial p_c} = \frac{p_s}{\rho_l R_v T} \exp\left(\frac{p_c}{\rho_l R_v T}\right) \tag{A.3}$$

$$\frac{\partial p_v}{\partial p_c} = \frac{p_v}{\rho_l R_v T} \tag{A.4}$$

and to the following expression of the second derivative (b):

$$\frac{\partial p_v}{\partial T} = \frac{\partial p_s}{\partial T} \exp\left(\frac{p_c}{\rho_l R_v T}\right) + p_s \left[\frac{1}{\rho_l R_v T} \frac{\partial p_c}{\partial T} - \frac{p_c}{\rho_l R_v T^2}\right] \exp\left(\frac{p_c}{\rho_l R_v T}\right) \tag{A.5}$$

The first term on the right side follows directly from Clausius-Clapeyron's law:

$$\frac{\partial p_s}{\partial T} = \frac{L_{lv}}{R_v T^2} p_s \tag{A.6}$$

while the other thermal derivative follows from Young-Laplace's law, expressing the capillary pressure in a cylindrical tube of radius r:

$$p_c = -\frac{2\sigma\cos\theta}{r} \tag{A.7}$$

$$\frac{\partial p_c}{\partial T} = \frac{1}{\sigma}\frac{\partial \sigma}{\partial T} p_c \tag{A.8}$$

This leads to the following expression for the derivative of the partial pressure to the temperature:

$$\frac{\partial p_v}{\partial T}\frac{p_v}{\rho_l R_v T^2}\left[\rho_l L_{lv} + p_c\left(\frac{T}{\sigma}\frac{\partial \sigma}{\partial T} - 1\right)\right] \tag{A.9}$$

which, added to Eq. A.4, allows removing the gradient of partial pressure from the conservation equations, by replacing it with its equivalent

$$\nabla p_v = \frac{p_v}{\rho_l R_v T}\nabla p_c + \frac{p_v}{\rho_l R_v T^2}\left[\rho_l L_{lv} + p_c\left(\frac{T}{\sigma}\frac{\partial \sigma}{\partial T} - 1\right)\right]\nabla T \tag{A.10}$$

A.2 Analytic resolution of the moisture transport equation

A.2.1 Description of the problem

The present section describes how the moisture transport equation (Eq. 2.10) can be solved as to give an analytical expression for the mass uptake of a specimen, under appropriate assumptions and boundary conditions. These assumptions are:

- one-dimensional transfer,
- isothermal conditions,
- constant transport properties in the considered humidity interval,
- transfer only occurs in the gaseous phase.

The resulting transport equation, written with either the vapour pressure p or moisture content w as driving potential, reads:

$$\frac{\partial p}{\partial t} = a\frac{\partial^2 p}{\partial x^2} \tag{A.11}$$

where the diffusivity $a = \delta_p p_s/\xi$ is considered constant. This equation comes along with the following initial and boundary conditions:

$$\begin{aligned} p\big|_{t=0} &= p_1 \\ \left.\frac{\partial p}{\partial x}\right|_{x=0} &= 0 \\ \delta_p \left.\frac{\partial p}{\partial x}\right|_{x=L} &= \beta\left(p_2 - p_{x=L}\right) \end{aligned} \tag{A.12}$$

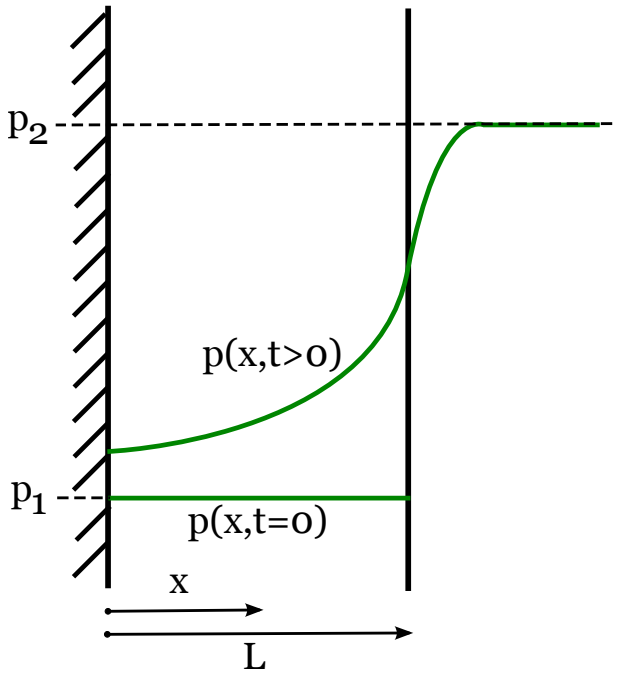

Figure A.1: One-dimensional moisture transfer in a plate

A layout of the problem is shown on Fig. A.1. The initial vapour pressure in the material is p_1 and a boundary pressure p_2 is imposed starting from $t = 0$. The pressure field p is a function of the spatial and temporal coordinates x and t, the thickness L, the initial and boundary pressures p_1 and p_2, the diffusivity a, the surface transfer coefficient β and the permeability δ_p.

A.2.2 Resolution of the transport equation

The methodology for the resolution of Eq. A.11 follows that of [POL 05], and starts with a change of variable in the aim of a non-dimensional formulation:

$$\theta = \frac{p_2 - p}{p_2 - p_1}; \quad u = \frac{x}{L}; \quad \mathrm{Fo} = \frac{at}{L^2}; \quad \mathrm{Bi} = \frac{\beta L}{\delta_p} \tag{A.13}$$

where Fo and Bi are the Fourier and Biot numbers, respectively. This results in the following conservation equation for the non-dimensional pressure θ as a function of Fo and the position u:

$$\frac{\partial \theta}{\partial \mathrm{Fo}} = \frac{\partial^2 \theta}{\partial u^2} \tag{A.14}$$

with the following boundary conditions:

$$\begin{aligned} \theta|_{\mathrm{Fo}=0} &= 1 \\ \left.\frac{\partial\theta}{\partial u}\right|_{u=0} &= 0 \\ \left.\frac{\partial\theta}{\partial u}\right|_{u=1} &= -\mathrm{Bi}\,\theta_{u=1} \end{aligned} \tag{A.15}$$

A method for the resolution of Eq. A.14 was proposed by Bernoulli, considering θ can be written as the product of functions of each variable Fo and u:

$$\theta\,(\mathrm{Fo}, u) = \Phi\,(\mathrm{Fo})\,\Psi\,(u) \tag{A.16}$$

The insertion of Eq. A.16 into Eq. A.14 gives:

$$\frac{\Phi'\,(\mathrm{Fo})}{\Phi\,(\mathrm{Fo})} = \frac{\Psi''\,(u)}{\Psi\,(u)} \tag{A.17}$$

where the $'$ sign respectively denotes the derivative of Φ and Ψ with respect to Fo and u. Since each term of this equation only depends on one of these independent variables, they are both necessarily valid for all values of the parameters, and therefore constant:

$$\frac{\Phi'\,(\mathrm{Fo})}{\Phi\,(\mathrm{Fo})} = \frac{\Psi''\,(u)}{\Psi\,(u)} = \pm\delta^2 \tag{A.18}$$

where the constant coefficient δ is unknown at first. From Eq. A.18, we obtain two separate differential equations of one variable each, for the functions Φ and Ψ. Their solutions are well-known:

$$\begin{aligned} \Phi\,(\mathrm{Fo}) &= \tilde{A}\exp\left(\pm\delta^2\,\mathrm{Fo}\right) \\ \Psi\,(u) &= \tilde{B}\sin\left(\delta\,u\right) + \tilde{C}\cos\left(\delta\,u\right) \end{aligned} \tag{A.19}$$

The expression of Φ only makes sense if the exponential function applies to a negative value. Indeed, a positive sign in front of δ^2 would cause a divergence of Φ, and therefore of p, with increasing time. The general form of the solution thus reads:

$$\theta\,(\mathrm{Fo}, u) = \left[B\sin\left(\delta\,u\right) + C\cos\left(\delta\,u\right)\right]\exp\left(-\delta^2\mathrm{Fo}\right) \tag{A.20}$$

The boundary condition on the insulated side of the plate specimen involves $B = 0$. The second boundary condition then translates into:

$$\left.\frac{\partial\theta}{\partial u}\right|_{u=1} = -\mathrm{Bi}\,\theta_{u=1} \quad \Rightarrow \quad \begin{cases} -C\,\delta\,\sin\left(\delta\right) = -\mathrm{Bi}\,C\,\cos\left(\delta\right) \\ \dfrac{\mathrm{Bi}}{\delta} = \tan\delta \end{cases} \tag{A.21}$$

This relation involves the non-unicity of the solution δ. As shown on Fig. A.2, estimating δ is equivalent to finding the intersection between the functions Bi/δ and $\tan\delta$,

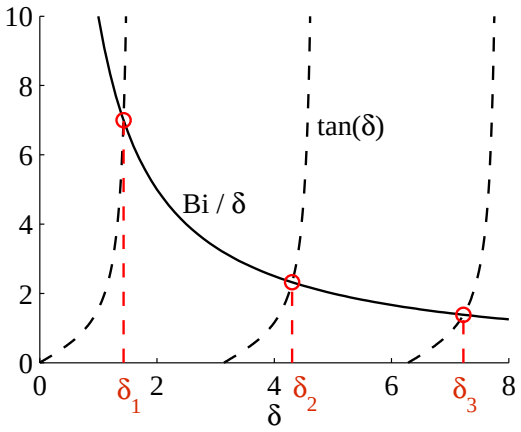

Figure A.2: Determination of the eigenvalues δ_k (example with Bi = 10)

which results in a series of values δ_k. Each of these values is calculated iteratively, and implies an eigenfunction θ_k:

$$\theta_k(\mathrm{Fo}, u, \mathrm{Bi}) = \cos(\delta_k u)\exp\left(-\delta_k^2 \mathrm{Fo}\right) \tag{A.22}$$

Each of the θ_k functions satisfies the partial differential equation A.14 and the boundary conditions of the problem (Eq. A.16). However, they do not satisfy the initial condition ($\theta_{k,\mathrm{Fo}=0} = 1$). The general solution of the problem is a series of these functions, weighted by additionnal coefficients C_k:

$$\theta(\mathrm{Fo}, u, \mathrm{Bi}) = \sum_{k=1}^{\infty} C_k \cos(\delta_k u)\exp\left(-\delta_k^2 \mathrm{Fo}\right) \tag{A.23}$$

This series satisfies the same differential equation and boundary conditions as the individual functions. The weighing coefficients C_k must be set so that the summation also satisfies the initial condition of the problem. Their expression is not trivially derived, and is given here without further details:

$$C_k = \frac{2\sin\delta_k}{\delta_k + \sin\delta_k \cos\delta_k} \tag{A.24}$$

It can be graphically guessed from Fig. A.2 that the values of the δ_k coefficients get closer to multiples of π as the index k increases, meaning that the C_k coefficients gradually decrease: an accurate solution of Eq. A.23 can be reached by restricting the summation to its first five terms.

Switching back from the results of this derivation to the initial dimensional notations, we obtain the solution of the moisture conservation equation (Eq. A.11) under the aforementioned hypotheses:

$$p(x,t) = p_1 + (p_2 - p_1)\left[1 - \sum_{k=1}^{\infty} C_k \cos\left(\delta_k \frac{x}{L}\right)\exp\left(-\delta_k^2 \frac{\delta_p p_s}{\xi L} t\right)\right] \tag{A.25}$$

The total mass uptake m of a specimen of exposed surface S can be calculated by integrating Eq. A.25 over the spatial coordinate x, for a given value of the temporal coordinate t:

$$m(t) = S\left(\int_{x=0}^{L} w(x,t)\,\mathrm{d}x - L\,w_1\right) \tag{A.26}$$

Because we assumed constant hygric properties, the sorption isotherm is considered linear in the observed humidity range. This simplification allows writing the following relation for any value of the moisture content w or of the relative humidity ϕ:

$$\frac{w-w_1}{\phi-\phi_1} = \frac{w_2-w_1}{\phi_2-\phi_1} = \xi \tag{A.27}$$

from which the integration of Eq. A.26 can be performed, resulting in the final expression for the mass uptake of a specimen:

$$m = V\,\xi\,\Delta\phi\left[1 - \sum_{k=1}^{\infty}\frac{2\sin^2\delta_k}{\delta_k\left(\delta_k+\sin\delta_k\cos\delta_k\right)}\exp\left(-\delta_k^2\frac{\delta_p}{\xi}\frac{p_{sat}\,t}{L^2}\right)\right] \tag{A.28}$$

where V is the sample's volume and $\Delta\phi$ is the initially imposed humidity step at the exposed boundary.

Appendix B

Finite-element modelling

The present appendix describes the method for the solving of the balance equations for heat and moisture in porous media (Eq. 4.17 and 4.18). Unless very restricting hypotheses, these equations have no analytical solution and a numerical procedure is required. The finite-element method was used for the discretisation of the transport equations into a linear system. Special care must be taken as to prevent possible computational difficulties arising from the strongly non-linear nature of the problem. The following derivations mostly follow the procedure presented by [JAN 07], and use the same notations.

B.1 Numerical implementation

B.1.1 Weak form

First, the spatial discretisation of the transport equations is presented. For purposes of clarity, let us describe the first step of the procedure with the example of the isothermal moisture transport equation:

$$\frac{\partial w}{\partial t} = -\nabla \mathbf{g} \tag{B.1}$$

Following the Galerkin approach, the weak form of this equation is given by:

$$\int_\Omega \eta \left[\frac{\partial w}{\partial t} + \nabla \mathbf{g} \right] \mathrm{d}\Omega = 0 \tag{B.2}$$

which must hold for all admissible variations η of the moisture content over the domain Ω. An integration by parts is applied on the second term of this equation:

$$\int \eta \, \nabla \mathbf{g} \, \mathrm{d}\Omega = \int \left[-\nabla \eta \cdot \mathbf{g} + \nabla \cdot \eta \mathbf{g} \right] \mathrm{d}\Omega \tag{B.3}$$

And the Green-Gauss theorem, over a domain Ω closed by a boundary Γ of outgoing normal vector $\mathbf{n}$, reads:

$$\int_\Omega \nabla \cdot \eta \mathbf{g} \, \mathrm{d}\Omega = \oint_\Gamma \eta \, \mathbf{g} \cdot \mathbf{n} \mathrm{d}\Gamma \tag{B.4}$$

Eq. B.4 is applied on the last term of Eq. B.3, which is then introduced into Eq. B.2. This results in a new formulation of the weak form of the conservation equation:

$$\int_\Omega \left[\eta \frac{\partial w}{\partial t} - \nabla\eta \cdot \mathbf{g} \right] \mathrm{d}\Omega = \oint_\Gamma -\eta\, \mathbf{g} \cdot \mathbf{n} \mathrm{d}\Gamma \tag{B.5}$$

The same manipulations, applied to the non-isothermal moisture transport equation (Eq. 4.17), result in:

$$\begin{aligned} \int_\Omega \left[\eta \left(c_{mm} \frac{\partial p_c}{\partial t} + c_{mh} \frac{\partial T}{\partial t} \right) + \nabla\eta \left(k_{mm} \nabla p_c + k_{mh} \nabla T \right) \right] \mathrm{d}\Omega \\ = \oint_\Gamma \eta \left(k_{mm} \nabla p_c + k_{mh} \nabla T \right) \cdot \mathbf{n} \mathrm{d}\Gamma \end{aligned} \tag{B.6}$$

B.1.2 Linearisation and discretisation

B.1.2.1 Spatial discretisation

According the to basic principle of the finite-element method, the computational domain Ω is subdivided into smaller element Ω^e. In two dimensions, these elements generally have a triangular or quadrilateral shape, each of which includes a certain number of nodes. In each element, the unknown continuous fields p_c and T are approximated by:

$$p_c = \mathbf{N}\mathbf{p}_c^e \tag{B.7}$$

$$T = \mathbf{N}\mathbf{T}^e \tag{B.8}$$

where the vector $\mathbf{N}$ contains the interpolation fonctions, or shape functions. $\mathbf{p}_c^e$ and $\mathbf{T}^e$ are vectors containing the nodal values of p_c and T at the nodes of the element. The temporal and spatial derivatives of the discretised expression of the capillary pressure respectively read:

$$\frac{\partial p_c}{\partial t} = \mathbf{N} \frac{\partial \mathbf{p}_c^e}{\partial t} \tag{B.9}$$

$$\nabla p_c = \mathbf{B}\mathbf{p}_c^e \tag{B.10}$$

where $\mathbf{B}$ is a $d \times N$ matrix, d being the number of dimensions of the problem, and N the number of nodal unknowns of the elements:

$$B_{ij} = \frac{\partial N_j}{\partial x_i} \tag{B.11}$$

where x_i denotes the d spatial coordinates. The present work uses six-nodded quadratic triangular elements. The expression of the shape fonctions of a reference element are shown in Tab. B.1.

Following the Galerkin finite-element method, the variational field η and its gradient $\nabla\eta$ undergo an identical discretisation. As a consequence, the introduction of

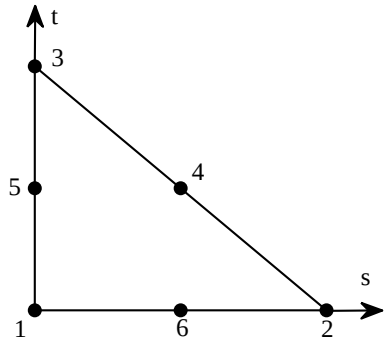

Point	Coordinates (s_i, t_i)	Shape function N_i
1	$(0;0)$	$L_1(2L_1-1)$
2	$(1;0)$	$L_2(2L_2-1)$
3	$(0;1)$	$L_3(2L_3-1)$
4	$(0.5;0.5)$	$4L_2L_3$
5	$(0;0.5)$	$4L_3L_1$
6	$(0.5;0)$	$4L_1L_2$
$L_1 = 1-s-t$	$L_2 = s$	$L_3 = t$

Table B.1: Node coordinates and shape functions of a quadratic triangular element

the discretised fields into the weak form of the conservation equations gives the set of equations for each element:

$$\mathbf{C}^e_{mm}\frac{\partial \mathbf{p}^e_c}{\partial t} + \mathbf{C}^e_{mh}\frac{\partial \mathbf{T}^e}{\partial t} + \mathbf{K}^e_{mm}\mathbf{p}^e_c + \mathbf{K}^e_{mh}\mathbf{T}^e = \mathbf{F}^e_m \tag{B.12}$$

$$\mathbf{C}^e_{hh}\frac{\partial \mathbf{T}^e}{\partial t} + \mathbf{C}^e_{hm}\frac{\partial \mathbf{p}^e_c}{\partial t} + \mathbf{K}^e_{hh}\mathbf{T}^e + \mathbf{K}^e_{hm}\mathbf{p}^e_c = \mathbf{F}^e_h \tag{B.13}$$

where $\mathbf{C}^e_{xy}$, $\mathbf{K}^e_{xy}$ are the element capacity and permeability matrices, calculated by integrating the capacity and permeability coefficients of Eq. 4.17 and 4.18, weighted by the shape functions of the element:

$$\mathbf{C}^e_{xy} = \int_{\Omega^e} \mathbf{N}^T c_{xy}\mathbf{N}\mathrm{d}\Omega^e \tag{B.14}$$

$$\mathbf{K}^e_{xy} = \int_{\Omega^e} \mathbf{B}^T \mathbf{k}_{xy}\mathbf{B}\mathrm{d}\Omega^e \tag{B.15}$$

It must be noted that the matrix multiplication of Eq. B.15 is valid whether $\mathbf{k}_{xy}$ is a scalar or a second order tensor. In order to account for the anisotropy of the material, one or several permeability terms (especially $\mathbf{k}_{mm}$, see Sec. 4.3.1.2) can be written as a tensor in this formulation.

In Eq. B.12 and B.13, $\mathbf{F}_m$ and $\mathbf{F}_h$ denote the element external load vectors:

$$\mathbf{F}^e_m = \int_{\Gamma^e} \mathbf{N}\left(\mathbf{g}\cdot\mathbf{n}\right)\mathrm{d}\Gamma^e \quad ; \quad \mathbf{F}^e_h = \int_{\Gamma^e} \mathbf{N}\left(\mathbf{q}\cdot\mathbf{n}\right)\mathrm{d}\Gamma^e \tag{B.16}$$

where $\mathbf{q}\cdot\mathbf{n}$ and $\mathbf{g}\cdot\mathbf{n}$ are the external heat and mass income to the element, formulated in Eq. 1.27.

The element matrices are calculated by numerical integration over triangular domains. This is done by means of the two-dimensional Gauss-Legendre quadrature, of which principle and numerical implementation are detailed below (see Sec. B.1.3).

B.1.2.2 Temporal discretisation

The temporal derivatives terms of the transport equation are approximated with a fully implicit finite difference scheme:

$$\frac{\partial \mathbf{p}_c^e}{\partial t} = \frac{1}{\Delta t}\left(\mathbf{p}_c^e - \mathbf{p}_c^e\big|^t\right) \tag{B.17}$$

where $\mathbf{p}_c^e\big|^t$ is the value of $\mathbf{p}_c^e$ at the previous converged time step, and Δt is the current time step. However, several authors have reported mass conservation errors arising from the fact that the temporal discretisation does not capture the non-linearity of the problem. A solution for averting this problem was proposed by [CEL 90] and implemented by [JAN 07] into a finite difference temporal discretisation. A mixed form of the moisture transport equation is written, based on both the moisture content w and the capillary pressure p_c. A better mass conservation is reached iteratively by replacing the expression of the mass storage in the following Eq. B.18 by the expression of Eq. B.19:

$$\frac{\partial w}{\partial t} = \left.\frac{\partial w}{\partial p_c}\right|_m^{t+\Delta t} \frac{\mathbf{p}_c^e\big|_{m+1}^{t+\Delta t} - \mathbf{p}_c^e\big|^t}{\Delta t} \tag{B.18}$$

$$\frac{\partial w}{\partial t} = \left.\frac{\partial w}{\partial p_c}\right|_m^{t+\Delta t} \frac{\mathbf{p}_c^e\big|_{m+1}^{t+\Delta t} - \mathbf{p}_c^e\big|_m^{t+\Delta t}}{\Delta t} + \frac{w|_m^{t+\Delta t} - w|^t}{\Delta t} \tag{B.19}$$

where the subscripts m and $m+1$ denote two consecutive iterations within the same time step, and the superscript t indicates a value at the previous converged time step. Integrating these two equations over an element yields:

$$\int_{\Omega^e} \mathbf{N}\frac{\partial w}{\partial t}\mathrm{d}\Omega = \frac{1}{\Delta t}\mathbf{C}_{mm}\left(\mathbf{p}_c\big|_{m+1}^{t+1} - \mathbf{p}_c\big|^t\right) \tag{B.20}$$

$$\int_{\Omega^e} \mathbf{N}\frac{\partial w}{\partial t}\mathrm{d}\Omega = \frac{1}{\Delta t}\mathbf{C}_{mm}\left(\mathbf{p}_c\big|_{m+1}^{t+\Delta t} - \mathbf{p}_c\big|_m^{t+\Delta t}\right) + \frac{1}{\Delta t}\int_{\Omega^e}\mathbf{N}\left(w|_m^{t+\Delta t} - w|^t\right)\mathrm{d}\Omega \tag{B.21}$$

Accounting for the mass conservation is done by replacing Eq. B.20 by Eq. B.21 in the set of spatially discretised equations (Eq. B.12 and B.13). Along with the choice of implicit temporal discretisation (Eq. B.17), this results in the following system of equations for each element:

$$\begin{aligned}&\begin{bmatrix}\mathbf{C}_{mm}^e + \Delta t\mathbf{K}_{mm}^e & \mathbf{C}_{mh}^e + \Delta t\mathbf{K}_{mh}^e\\ \mathbf{C}_{hm}^e + \Delta t\mathbf{K}_{hm}^e & \mathbf{C}_{hh}^e + \Delta t\mathbf{K}_{hh}^e\end{bmatrix}_m^{t+\Delta t}\begin{pmatrix}\mathbf{p}_c^e\\ \mathbf{T}^e\end{pmatrix}^{t+\Delta t}_{m+1}\\ &= \Delta t\begin{pmatrix}\mathbf{F}_m^e\\ \mathbf{F}_h^e\end{pmatrix}_m^{t+\Delta t} + \begin{bmatrix}\mathbf{C}_{mm}^e & \mathbf{C}_{mh}^e\\ \mathbf{C}_{hm}^e & \mathbf{C}_{hh}^e\end{bmatrix}_m^{t+\Delta t}\begin{pmatrix}\mathbf{p}_c^e\\ \mathbf{T}^e\end{pmatrix}_m^{t+\Delta t} - \begin{pmatrix}\mathbf{S}_m^e\\ \mathbf{S}_h^e\end{pmatrix}_m^{t+\Delta t} + \begin{pmatrix}\mathbf{S}_m^e\\ \mathbf{S}_h^e\end{pmatrix}^t\end{aligned} \tag{B.22}$$

where $\mathbf{S}_m^e$ and $\mathbf{S}_m^e$ are given by [JAN 07]:

$$\mathbf{S}_m^e = \int_{\Omega^e} w\mathbf{N}\mathrm{d}\Omega^e \tag{B.23}$$

$$\mathbf{S}_h^e = \int_{\Omega^e} T\left(c_m \rho_m + c_l w\right) \mathbf{N} \mathrm{d}\Omega^e \tag{B.24}$$

The element matrices of the system B.22 are calculated in all finite elements, and assembled into a single system of $2n$ equations, n being the total number of nodes of the problem:

$$\left(\mathbf{C}|_m^{t+\Delta t} + \Delta t\, \mathbf{K}|_m^{t+\Delta t}\right) \mathbf{U}|_{m+1}^{t+\Delta t} = \Delta t\, \mathbf{F}|_m^{t+\Delta t} + \mathbf{C}|_m^{t+\Delta t}\, \mathbf{U}|_m^{t+\Delta t} - \left(\mathbf{S}|_m^{t+\Delta t} - \mathbf{S}|^t\right) \tag{B.25}$$

where **C** and **K** are the total capacity and permeability matrices of the system, and **F** and **S** are the external load and mass conservation vectors. **U** is the vector of the unknown nodal values of both the capillary pressure and the temperature.

If the initial and boundary conditions of the problem are known, the solution of each time step can be found by iteratively solving Eq. B.25. The coefficients are updated at every iteration and the unknown vector $\mathbf{U}|_{m+1}^{t+\Delta t}$ is computed by solving the linear system of equations. Convergence is reached when the following criteria are met:

$$\begin{cases} \dfrac{\sum_i \left(p_c^i|_{m+1} - p_c^i|_m\right)^2}{\sum_i p_c^i|_m^2} \leq \epsilon_p \\ \dfrac{\sum_i \left(T^i|_{m+1} - T^i|_m\right)^2}{\sum_i T^i|_m^2} \leq \epsilon_T \end{cases} \tag{B.26}$$

meaning that the solution does not change significantly between two consecutive iterations. In the present work, the convergence criteria ϵ_p and ϵ_t are set to 10^{-5} for the simulation of non-fractured materials, and to 10^{-4} for fractured materials, in order to reduce the computational time.

B.1.2.3 Convergence scheme

Although Eq. B.25 is a simple method for solving the problem, it has been argued [JAN 07] that convergence problems may arise from the non-linearity of the boundary conditions: indeed, the external load vector **F** depends on the unknown **U**. This matter is addressed by applying the Newton-Raphson iterative scheme. The system of equation then yields:

$$\begin{aligned} &\left(\mathbf{C}|_m^{t+\Delta t} + \Delta t\, \mathbf{K}|_m^{t+\Delta t} + \Delta t \frac{\partial\, \mathbf{K}|_m^{t+\Delta t}}{\partial \mathbf{U}}\, \mathbf{U}|_m^{t+\Delta t} - \Delta t \frac{\partial\, \mathbf{F}|_m^{t+\Delta t}}{\partial \mathbf{U}}\right) \Delta \mathbf{U}|_{m+1}^{t+\Delta t} \\ &= \Delta t\, \mathbf{F}|_m^{t+\Delta t} - \Delta t\, \mathbf{K}|_m^{t+\Delta t}\, \mathbf{U}|_m^{t+\Delta t} - \left(\mathbf{S}|_m^{t+\Delta t} - \mathbf{S}|^t\right) \end{aligned} \tag{B.27}$$

in which the solution of the linear system is $\Delta \mathbf{U}|_{m+1}^{t+\Delta t} = \mathbf{U}|_{m+1}^{t+\Delta t} - \mathbf{U}|_m^{t+\Delta t}$.

Eq. B.27 includes two additional terms, predicting the effects of a variation of **U** on the variations of **K** and **F**. For simplification purposes, the third-order tensor $\partial\mathbf{K}/\partial\mathbf{U}$ was neglected. The main contribution of the Newton-Raphson method is the addition of the second-order tensor $\partial\mathbf{F}/\partial\mathbf{U}$, which considerably facilitates the convergence.

Similarly to the other coefficients of Eq. B.27, it is first calculated at the elementary level before assembling in the general system.

$$\frac{\partial \mathbf{F}^e}{\partial \mathbf{U}^e} = \begin{bmatrix} \int_{\Gamma^e} \mathbf{N} \frac{\partial g}{\partial p_c} \mathrm{d}\Gamma & \int_{\Gamma^e} \mathbf{N} \frac{\partial g}{\partial T} \mathrm{d}\Gamma \\ \int_{\Gamma^e} \mathbf{N} \frac{\partial q}{\partial p_c} \mathrm{d}\Gamma & \int_{\Gamma^e} \mathbf{N} \frac{\partial q}{\partial T} \mathrm{d}\Gamma \end{bmatrix} \tag{B.28}$$

where the derivatives of the external flows to the independent variables can be derived analytically. Supposing that the surface transfer coefficients do not depend on the variables p_c and T:

$$\begin{aligned} \frac{\partial g}{\partial p_c} &= -\beta \frac{p_v}{\rho_l R_v T} \\ \frac{\partial g}{\partial T} &= \beta \frac{p_v}{R_v T^2} \left(\frac{p_c}{\rho_l} - L_{lv} \right) \\ \frac{\partial q}{\partial p_c} &= (c_v T + L_{lv}) \frac{\partial g}{\partial p_c} \\ \frac{\partial q}{\partial T} &= -\alpha + c_v \beta \left(p_{v,a} - p_v \right) + (c_v T + L_{lv}) \frac{\partial g}{\partial T} \end{aligned} \tag{B.29}$$

B.1.2.4 Adaptative time stepping

As the variations moisture permeability can span over several orders of magnitude between dry and near-saturated conditions, moisture transfer tends to occur at highly varying paces. In presence of a liquid phase, moisture content variations are fast and time steps in the order of seconds are required for convergence. This is particularly the case for materials of high permeability or fractures that require sub-second time steps. Since the model is required to cover year-long simulations as well, a constant time step is not possible for reasons of computational costs. The algorithm therefore includes a dynamic time stepping procedure, adapting the size of each time step Δt according to the number of iterations of the previous step m:

$$\Delta t^{i+1} = \min \left[\Delta t^i \ \min \left(\frac{m_{max}}{2m}, 2 \right), \Delta t_{max} \right] \tag{B.30}$$

where m_{max} is the maximal authorised number of iterations and Δt_{max} is the maximal time step.

B.1.3 Numerical integration

As pointed out earlier, the element matrices are calculated by integration over the surface of the elements Ω^e. As this can not be done analytically, the Gauss-Legendre quadrature is used for a numerical integration. The principle of the method is the approximation of the integral of a function f over an n-dimensional domain Ω by

a weighted summation of the value of this function at a set of integration points [DUN 85]:

$$\int_{\Omega} f(\mathbf{x})\,\mathrm{d}\Omega = \sum_{i=1}^{N} w_i f(\mathbf{x}_i) \tag{B.31}$$

where the weights w_i and the coordinates of the points $\mathbf{x}_i$ are independent of the function f. N is the total number of integration points on the domain: a higher number of points yields a better approximation of the real solution.

B.1.3.1 Linear element

The external load vectors **F** are calculated by integration over the edges of the elements. The one-dimensional quadrature for the numerical integration of a function f between two nodes of coordinates x_1 and x_2 reads:

$$\int_{x_1}^{x_2} f(x)\,\mathrm{d}x = \frac{x_2 - x_1}{2} \sum_{i=1}^{N} w_i f\left(\frac{x_2 - x_1}{2} x_i + \frac{x_1 + x_2}{2}\right) \tag{B.32}$$

In the present work, this summation is performed using 4 quadrature points. The coefficients x_i and w_i are given in Tab. B.2.

x_i	w_i
$-\frac{1}{35}\sqrt{525+70\sqrt{30}}$	$\left(18-\sqrt{30}\right)/36$
$-\frac{1}{35}\sqrt{525-70\sqrt{30}}$	$\left(18+\sqrt{30}\right)/36$
$\frac{1}{35}\sqrt{525-70\sqrt{30}}$	$\left(18+\sqrt{30}\right)/36$
$\frac{1}{35}\sqrt{525+70\sqrt{30}}$	$\left(18-\sqrt{30}\right)/36$

Table B.2: Gauss-Legendre coefficients for 1D integration

B.1.3.2 Triangular element

The capacity matrices, permeability matrices and mass conservation vectors are calculated by integration over triangular surfaces. In that case, the two-dimensional quadrature reads:

$$I = \iint_{T} f\left(x,y\right)\mathrm{d}x\mathrm{d}y = \sum_{i=1}^{N} w_i F\left(s_i,t_i\right)\left|\mathbf{J}_i\right| \tag{B.33}$$

where x and y are the global coordinates, s and t are local coordinates tied to the edges of the triangle (see Fig. B.1), and $|\mathbf{J}|$ is the value of the Jacobian determinant. The function F is defined so that

$$f\left(x,y\right) = F\left(s\left(x,y\right),t\left(x,y\right)\right) \tag{B.34}$$

s_i	t_i	w_i
0	0	1/40
1/2	0	1/15
1	0	1/40
1/2	1/2	1/15
0	1	1/40
0	1/2	1/15
1/3	1/3	9/40

Table B.3: Gauss-Legendre coefficients for the unit triangle

The quadrature is performed with 7 points, of which coefficients and local coordinates in each triangle are given in Tab. B.3.

The global coordinates (x_i, y_i) of the integration points can be calculated from their local coordinates (s_i, t_i) by:

$$\begin{pmatrix} x \\ y \end{pmatrix} = \begin{bmatrix} x_1 & x_2 - x_1 & x_3 - x_1 \\ y_1 & y_2 - y_1 & y_3 - y_1 \end{bmatrix} \begin{pmatrix} 1 \\ s \\ t \end{pmatrix} \tag{B.35}$$

where (x_1, y_1), (x_2, y_2) and (x_3, y_3) are the global coordinates of the tiangle vertices. The Jacobian matrix reads:

$$\mathbf{J} = \begin{bmatrix} \dfrac{\partial x}{\partial s} & \dfrac{\partial x}{\partial t} \\ \dfrac{\partial y}{\partial s} & \dfrac{\partial y}{\partial t} \end{bmatrix} = \begin{bmatrix} x_2 - x_1 & x_3 - x_1 \\ y_2 - y_1 & y_3 - y_1 \end{bmatrix} \tag{B.36}$$

B.2 Algorithm

The presented procedure for the resolution of the transport equations was integrated into the newly developped *HAMDAM* simulation code (*Heat and Moisture transfer in DAMaged media*) written with the *Matlab* software, of which general structure is presented on Fig. B.1.

The code starts with an initialisation module, in which the user sets the conditions of the simulation:

- Geometry of the problem: size, number of nodes, type of elements (linear or quadratic triangular);

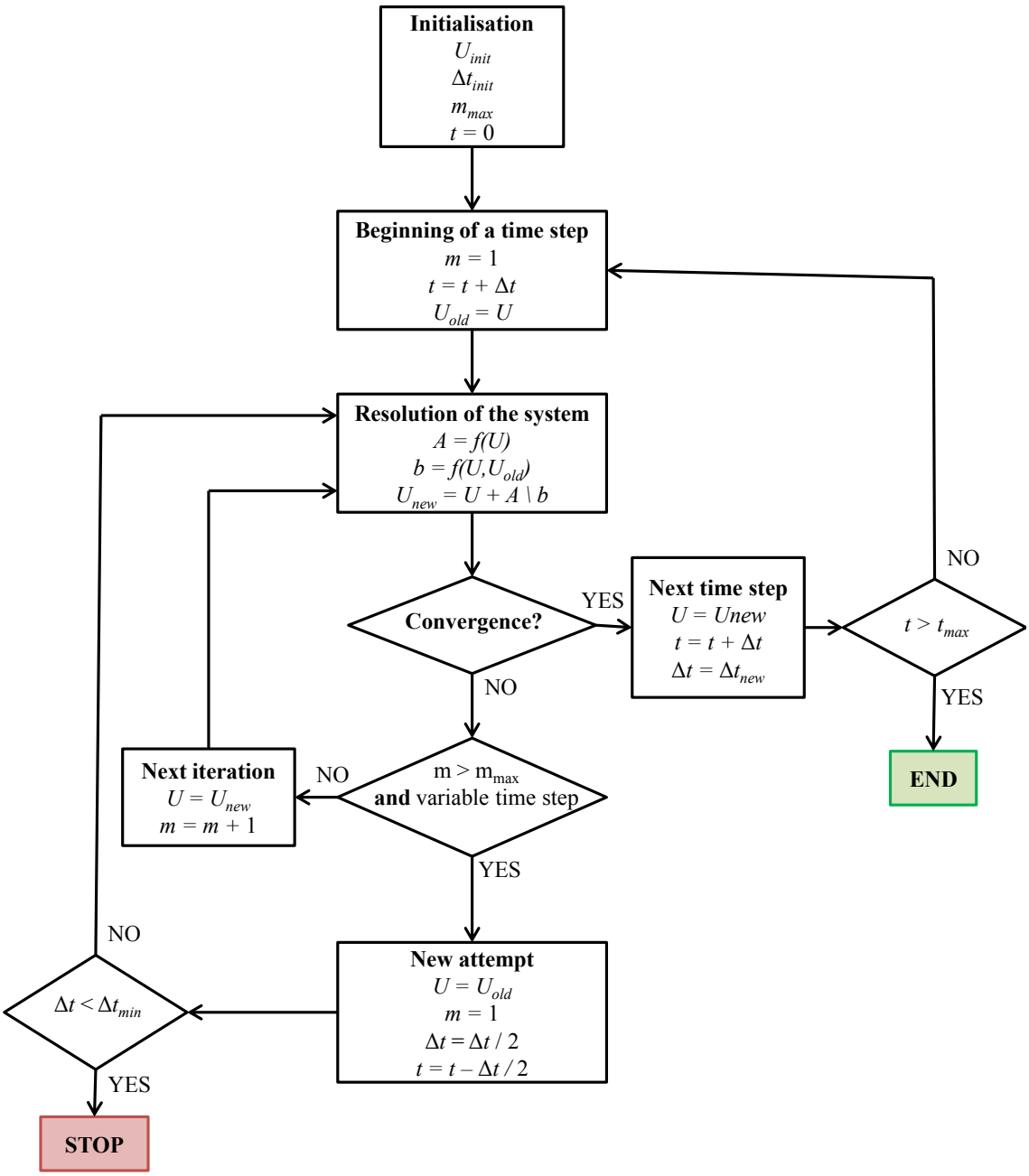

Figure B.1: Algorithm of the finite-element simulation code

- Boundary conditions on each of the 4 edges of the domain: type of boundary (insulation, constant value or convection), input of constant atmospheric conditions or of a climatic data file;
- Initial conditions: distributions of the initial capillary pressure and temperature over the domain;
- Temporal setup: choice of the initial, minimal and maximal values of the time step, of the maximal authorised number of iterations per time step, and of the total simulation time.

After the complete definition of the problem, the initial solution vector $\mathbf{U}|^{t=0}$ is first set with the nodal values of the initial capillary pressure and temperature fields. The algorithm presented on Fig. B.1 then proceeds as follows:

- Beginning of a time step: the number of iterations and time of simulation are updated. The solution vector of the previous time step is saved for use in the calculation of the moisture conservation vector.
- Resolution of the system: all element matrices are calculated using the value of the solution vector calculated at the previous time step $\mathbf{U}|^{t}$ and at the previous iteration of the current time step $\mathbf{U}|_{m}^{t+\Delta t}$. These matrices are then assembled into the equation system B.27 for the calculation of the new solution vector $\mathbf{U}|_{m+1}^{t+\Delta t}$.
- Convergence: the convergence criteria are calculated by comparing $\mathbf{U}|_{m+1}^{t+\Delta t}$ with $\mathbf{U}|_{m}^{t+\Delta t}$ (see Eq. B.26. This is not performed at the first time step of an iteration.
- If convergence is reached, the solution vector is saved. The amplitude of the next time step is calculated according to the number of iterations. The code then proceeds to the beginning of a new time step, unless the end of the simulation has been reached.
- If convergence is not reached at the end of an iteration, the code proceeds to a new iteration within the same time step.
- If the number of iterations exceeds the authorised value m_{max}, and if the user has chosen the adaptative time stepping procedure, the code considers that convergence may not be reached. A new attempt is made, reducing the amplitude of the time step by half. If this reduction causes Δt to reach a value lower than the authorised minimum Δt_{min}, the code stops: it is considered that convergence cannot be reached with the defined conditions of the problem.

Once the end of the simulation time is reached and the last time step is converged, the value of the solution vector at each time step, along with the amplitude of the heat and moisture boundary transfer, are saved. A post-processing module then allows the user to display and quantify any phenomenon or quantity in relation with the problem.